GRAPHENE TRANSISTORS FOR LABEL-FREE BIOSENSING

By

Bing Li

A thesis submitted to Plymouth University, in partial fulfilment of the degree of

DOCTOR OF PHILOSOPHY

Department of Computing, Mathematics and Electronics

Faculty of Science and Engineering

March 2016

Abstract

The discovery of monolayer graphene by Manchester group has led to intensive research into a variety of applications across different disciplines. As a monolayer of carbon atoms, graphene presents a high surface to volume ratio and a good electronic conductivity, making it sensitive to its surface bio-chemical environment. This project investigated the fabrication of electronic biosensors using different graphene-based materials. It included the production of graphene, the fabrication of electronic devices, the chemical functionalisation of graphene surface and the specific detection of target bio-molecules.

This project first investigated the production of graphene using three different methods, namely mechanical exfoliation, physical vapour deposition and electrochemical reduction of graphene oxide. With respect to the physical vapour deposition method, the production of large area transfer-free graphene from sputtered carbon and metal layers on SiO_2 substrate has, for the first time, been achieved. The relationship between growth parameters and the quality of resultant graphene layer has been systematically studied. In addition, a growth model based on the detailed analysis of morphological structures and properties of graphene film was simultaneously proposed. Optical microscopy, Raman spectroscopy and atomic force microscopy were used for the evaluation of the number, the quality and the morphology of resultant graphene layers in each method.

To investigate the performance of graphene electronic devices, field effect transistors were fabricated using both exfoliated and chemical vapour deposited graphene. A novel technique for graphene patterning has been developed using deep ultraviolet baking and an improved photolithography method. A new shielding technique for the low damage deposition of Au electrodes on graphene has also been developed in this project. The

practical challenges of device fabrication and performance optimisation, such as polymer residue and contact formation, have been studied using Raman spectroscopy and the Keithley 2602A multichannel source meter.

For the functionalisation of graphene, a number of chemicals were investigated to provide linking groups that enable binding of bio-probes on the graphene surface. Hydrogen peroxide and potassium permanganate have been demonstrated to have the capability of immobilising oxygen-containing groups onto graphene. The levels of oxidation were estimated by energy dispersive analysis and Fourier transform infrared spectroscopy. In addition, aminopropyltriethoxysilanes and polyallylamine have exhibited good efficiency for immobilising amino groups onto graphene. The resultant graphene was characterised by X-ray photoelectron spectroscopy and cyclic voltammetry measurements.

Graphene electrodes modified with electrochemically reduced graphene oxide were developed for the first time which exhibit significantly improved redox currents in electrochemical measurements. Using single stranded DNA immobilised via π-π bonds as probes, these electrodes showed a limit of detection of 1.58×10^{-13} M for the human immunodeficiency virus 1 gene. In parallel, human chorionic gonadotropin sensors were developed by immobilising its antibodies on 1-pyrenebutyric acid N-hydroxysuccinimide ester functionalised graphene field effect transistors. These field effect transistors have been demonstrated to exhibit a quantitative response toward the detection of 0.625 ng/ml antigen.

In summary, the fabrications of two types of graphene-based biosensors for the detection of specific DNA sequence and human chorionic gonadotropin have been achieved in this project. Their sensitivity, selectivity, reproducibility and capability of multiple biomarker detection need to be further improved and explored in future work.

The outcomes of this project have provided not only ready-made biosensing platforms for the detection beyond these two targets, but also novel techniques applicable to the development of multidisciplinary applications beyond biosensor itself.

List of Abbreviations

0D, 1D, 2D, 3D - 0 dimensional, 1 dimensional, 2 dimensional, 3 dimensional

ABS - acrylonitrile butadiene styrene

AFM - atomic force microscope

Al_2O_3 - aluminium oxide

APTES - aminopropyltriethoxysilanes

cDNA - complementary DNA

CMOS - complementary metal–oxide–semiconductor

CR-GO - chemical reduced graphene oxide

CV - cyclic voltammetry

CVD - chemical vapour deposition

DI - deionised

DUV - deep UV

DCC - dicyclohexylcarbodiimide

DPV - differential pulse voltammetry

dsDNA - double stranded DNA

EDX - Energy-dispersive X-ray spectroscopy

FET - field effect transistor

FTIR - Fourier transform infrared spectroscopy

$Fe(OH)_3$ - iron(III) oxide-hydroxide

$FeSO_4 \cdot 7H_2O$- ferrous sulphate-7 hydrate

FWHM - full width at half maximum

GO - graphene oxide

hCG - human chorionic gonadotropin

H_2O_2 - hydrogen peroxide

HFO_2 – hafnium (IV) oxide

H_2SO_4 - sulfuric acid

HMDS - hexamethyldisilazane

HNO_3 - nitric acid

HOPG - highly oriented pyrolytic graphite

IPA - isopropyl alcohol

KCl - potassium chloride

$K_3Fe(CN)_6$ - potassium ferricyanide

$KMnO_4$ - potassium permanganate

$K_2S_2O_8$ - potassium persulfate

LoD - limit-of-detection

LoR - lift-off resist

NaOH - sodium hydroxide

$NaAlO_2$ - sodium aluminate

Na_2ZnO_2 - sodium zincate

NH_3-ammonia

$(NH_4)_2S_2O_8$- ammonium persulfate

NO_2- nitrogen dioxide

NMR - nuclear magnetic resonance

OLED - organic light-emitting diode

rGO - reduced graphene oxide

PAA - polyallylamine

PANSE - 1-pyrenebutyric acid N-hydroxysuccinimide ester

PET - polyethylene terephthalate

PBS - phosphate-buffered saline

PECVD - plasma enhanced CVD

PMMA - poly (methyl methacrylate)

P_2O_5 - phosphorus pentoxide

PVD - physical vapour deposition

RF - radio frequency

RTP - rapid thermal process

RSD - relative standard deviation

SD - standard deviation

SEM - scanning electron microscope

SiO_2 - silicon dioxide

STM - scanning tunnelling microscope

ssDNA - single stranded DNA

TEM - transmission electron microscopy

TLM - transfer length measurement

UHV - ultrahigh vacuum

UV - ultraviolet light

XPS - X-ray photoelectron spectroscopy

Contents

Table of Figures

List of Tables

Acknowledgement

It is with utmost sincerity that I express my gratitude to all of those who have supported me throughout my Ph.D. research. This unique experience has greatly expanded my knowledge and skills for further research.

First and foremost, I would like to thank:

Prof. Genhua Pan, my first supervisor. I really appreciate him for getting me through my Ph.D. studies, both inspiring and guiding me throughout my research work.

Prof. Neil Avent, my second supervisor, for providing the access to Biomedical and Healthcare Sciences laboratory and the useful discussions on the biological experiments in my project.

Dr. Shakil Awan, my third supervisor, for giving me precious opinions and suggestions on the electronic measurement in my project.

I would also like to thank:

Dr. David Jenkins for sharing his experience and proofreading my thesis.

Mr. Nick Fry, technician in the Wolfson Nanomaterials and Devices Laboratory, for his technical support with device fabrication and measurement.

Dr. Tracey Madgett and Dr. Paul Waines, technicians in the Centre for Biomedical Research, for their technical support and suggestions on the biological experiment in my project.

Dr. Glenn Harper, technician in the Electronic Microscope Centre, for helping me on using SEM and SEM image analysis.

Dr. Roy Lowry and Mr. Andrew Tonkin, in School of Geography, Earth and Environmental Sciences, for helping me on CV measurement, FTIR characterisation and corresponding data analysis.

Last but not the least, I would like to thank my parents, friends, and those who were directly and indirectly involved in this project for their supports and encouragements all through my studies. To each of the above, I would like to extend my deepest appreciation.

Author's Declaration

At no time during the registration for the degree of Doctor of Philosophy has the author been registered for any other university award.

This Ph.D. study was financed with the aid of School of Computing, Mathematics and Electronics, Plymouth University, China Scholarship Council for the U.K. Ph.D. scholarship for the research grant. A programme of advanced study was undertaken, which included supervised cleanroom operation instruction and an introduction of safety.

Internal Contacts: Dr. Guido Bugmann, Plymouth University.

External Contacts: Dr. Daniele Doneddu, Swansea University.

Word count of main body of thesis: 43853

Signed: _____

Date: _____

Chapter 1 Introduction

1.1 The Need for Graphene Biosensors

Health diseases and conditions such as cancer, cardiovascular disease, stroke and dementia have become major burdens on healthcare systems, globally affecting millions of people. Therefore, clinical monitoring and diagnostic systems have attracted a huge amount of research interest in future healthcare. Biosensing technology has been a growing industry for several decades and is continuously expanding to meet this need. Currently, a very large sensor market including blood glucose, human chorionic gonadotropin (hCG) and other hormone monitoring is well established. However, there is still a large number of health conditions that cannot be diagnosed and reported in time before they become fatal using current commercial process. Therefore, the development of existing biosensing platforms towards early diagnosis, lower detection limits, higher sensitivity, better selectivity and reproducibility, in body fluids or in vivo, is required.

Current biosensing technology mainly relies on fluorescent dye labelled probes, which react with specific target molecules present in blood, urine or saliva. The detection is by exposing the sample to a monochromatic laser and achieved by capturing the corresponding emission signal. This requires an expensive and time-consuming dye labelling process and complicated laser excitation/detection instruments.

Graphene, being a 2 dimensional (2D) material, has been regarded as a “dream material” since its experimental discovery in 2004 by the Manchester group led by Andre Geim and Kostya Novoselov. Its unique chemical and physical properties, such as high electronic and thermal conductivity, 2D nature, intrinsically high surface to volume ratio and chemical inertness, have been believed to be capable of yielding biosensors with extremely high sensitivity and a low limit-of-detection (LoD) in the biosensor and

are compatible to current commercial fabrication technologies. Therefore, compared with the conventional biosensors, graphene-based biosensors have the potential to exhibit improved sensing performance with a lower commercial cost.

1.2 Outline of this Thesis

The aim of this work is to develop a biosensing platform utilising the unique properties of graphene, which could potentially lead to a better sensing performance and be compatible with industrial applications. This thesis is split into two distinctive parts. The background review section, which includes Chapters 2 and 3, provides a literature review on the production of graphene, fabrication of graphene-based devices and graphene-based biosensing technology. The experimental section, which includes Chapters 4 to 8, describes the experimental detail and results in the production of different types of graphene on silicon dioxide (SiO_2), the fabrication of a graphene-based field effect transistor (FET) and electrodes, a number of methods for chemical functionalisation of graphene and the assembly of a graphene-based DNA/hCG biosensor.

The outline of this thesis is presented as follows:

Chapter 2 and 3 reviews the current state of graphene in all aspects of biosensor fabrication. It focuses on graphene and its physical/chemical properties, the production and transferring of large area graphene, covalent and noncovalent functionalisation of graphene and graphene-based applications. In particular, different types of graphene-based biosensors have been introduced together with their definitions, structures, categorisations, sensing mechanisms, sensing parameters along with their advantages and disadvantages.

Chapter 4 describes the experimental techniques and methods used in this work. It mainly includes the techniques used in the preparation of the substrate, the growth of graphene from sputtered materials, the production of micro-exfoliated graphene, the fabrication of graphene FETs, the functionalisation of graphene with different oxidants or linkers and the assembly of a DNA/hCG sensor. The experimental setup and working mechanisms of equipment used for different characterisation have also been outlined.

Chapter 5 presents the results of exfoliated graphene and graphene grown from sputtered materials. The surface coverage, quality, grain size of graphene grown at different carbon/metal ratios and varied growth conditions has been systematically characterised and investigated. A model for the growth of transferrable or transfer-free graphene has been proposed.

Chapter 6 shows the results of the fabrication of graphene-based electronic devices. A novel shielding technique for the fabrication of graphene FETs has been developed. Compared with the normal method, the improvements in the success rate of fabrication and the electronic performance of the resultant devices prepared by the novel sputtering deposition have been demonstrated. Two different methods for cleaning the various residues/adsorbents have also been demonstrated.

Chapter 7 discusses chemical methods used for the functionalisation of graphene. It consists of the hydroxylation of graphene with hydrogen peroxide (H_2O_2), the hydroxylation of graphene with $KMnO_4$, the amination of graphene oxide (GO) with aminopropyltriethoxysilanes (APTES) and the amination of GO with polyallylamine (PAA). Also, the superiority of using PAA/ reduced graphene oxide (rGO)/graphene modified electrodes in enhancing the reduction current of hydrogen peroxide has been demonstrated.

Chapter 8 covers the results of the assembly and characterisations of two types of biosensors, namely DNA sequence sensors and hCG immunosensors. The quantitative sensing parameters, such as LoD, dynamic range and selectivity of DNA sensor have been provided. In parallel, the qualitative detection of hCG using 1-pyrenebutyric acid N-hydroxysuccinimide ester (PANSE) modified rGO electrode has been demonstrated.

Chapter 9 summaries the major progress and results of this work, highlights the contribution of this work to knowledge and proposes the potential future work to biosensing technology.

Appendix presents the list of journal & conference publications related to this project and the detailed patterns of lithography photomasks designed in this work.

Chapter 2 Graphene and its Production

2.1 Graphene

2.1.1 Definition and Structure of Graphene

Graphene is a single atom thick 2D film which consists of sp^2- hybridised carbon atoms, that can be regarded as a basic building block of 3 dimensional (3D) graphite, 1 dimensional (1D) carbon nanotubes and 0 dimensional (0D) fullerenes [1, 2], as shown in Fig. 2-1. It can also be considered as an indefinitely extended aromatic molecule, which is the ultimate case of polycyclic aromatic hydrocarbons.

In a graphene lattice, each carbon atom connects the adjacent three carbon atoms via δ electrons having a bond length of 0.142 nm. The delocalised π band is formed by the non-bonded electrons in $2p_z$ orbits, which are perpendicular to the graphene plane and interact with those from other adjacent carbon atoms [3].

Figure 2-1 has been removed due to Copyright restrictions.

Figure 2-1. The relationship between graphene and 0D, 1D, 3D materials (left), and simulated structure of graphene sheet (right) [4, 5].

2.1.2 Graphene Properties

2.1.2.1 Physical Properties

Graphene shows unique optical properties due to its single atom thickness. For white light (390 - 700 nm) passing through a graphene monolayer, the transmission is 97.7%. For n layers, the transmission decreases by 2.3% with every additional layer of graphene, up to 5-10 layers beyond which bulk graphite properties are restored [6]. Graphene on SiO_2 substrate shows a different colour with different number of layers due to their refractive index, which has directly led to the discovery of graphene and the identification of the number of graphene layers in 2004 [2, 7]. Since then, more extraordinary properties of graphene have been unearthed [8], such as electron mobility of 10^6 $cm^2 \cdot V^{-1}$ s^{-1} at room temperature [9] (around 40000 cm^2 V^{-1} s^{-1} on SiO_2 substrate [10]), ultralow resistivity [1], ultrahigh breaking strength of 1 TPa and tensile strength of 125 GPa [11], anomalous quantum hall effect [12], controllable doping level [13], behaviour of massless Dirac fermions [14, 15], unusual band structure (as shown in Fig. 2-2) [16, 17], high thermal stability and conductivity [18], various electronic transport performance in armchair or zig-zag edge orientation [19], high transparency at certain wavelengths [20, 21], high chemical resistance [22], long spin diffusion length at room temperature [23].

Figure 2-2 has been removed due to Copyright restrictions.

Figure 2-2. Band gap for monolayer and bilayer graphene [17] (π is valence band, π^* is conduction band and E_D is energy gap).

2.1.2.2 Chemical Properties

In the graphene lattice structure, carbon atoms bond to each other via δ electrons and a highly dense electron cloud forms both above and below the plane, leading to not only chemical stability [24], but also the possible chemical activities in cyclo-additions, Click reactions and carbine insertion reactions [25, 26], with the destruction of the sp^2-hybridised structure. Through a harsh oxidation treatment with an assistance of an ultrasonic bath, e.g. modified Hummer's method [27], graphite bulk can be exfoliated into graphene and randomly modified by carboxyl groups, hydroxyl groups and epoxy groups, leading to solubility in different solvents [28]. The edge of graphene and graphene derivatives have proven to be more chemically active than the planar surface [29]. Thus, depending on the specific requirements, the resultant GO can be further converted to graphene amide or partially reduced to graphene by amination agents or deoxidiser [30]; Because of the incredibly high surface to volume ratio, graphene has also been considered as an ideal material for hydrogen storage [31]. Each hydrogen atom can be bonded to one carbon atom via the π electrons, which leads up to a 7.7% H-mass distribution, and released through an annealing process [32]. In parallel to post chemical modification, graphene can also be chemically doped during the growth process, e.g. F atoms turn graphene from a conductor to insulator [33]. B, N atoms lead to the p-type or n-type graphene, respectively, which may impact the semiconductor industry in the longer term [34-36].

These unique physical/chemical properties have changed the name of graphene from "an academic material" to "a wonder material of the 21st century". It is believed that graphene could be a promising successor of silicon for the post Moore's law era [1, 16, 37], with a wide range of technological applications in electronics [38], photonics [39, 40], biosensor and chemical sensor [41, 42], energy storage [43], spintronics [44-46], quantum computing [47].

2.2 Production of Large-area Graphene

Graphene was first produced [2] with a method called mechanical exfoliation on a 300 nm doped Si/SiO_2 substrate, against the "common wisdom" [1, 48-50] by the Manchester group in 2004. This special Si/SiO_2 substrate not only electrically isolates the graphene film but also provides a route for its visual identification, which makes the characterisation of graphene's physical and chemical properties possible. In their work [2], a very high mobility, up to 10^4 $cm^2/V{\cdot}s$ with a strong ambipolar electric field effect and ballistic transport at submicron levels at room temperature has been observed. Although the theoretical study of graphene has been reported for over 60 years [1] and the initial efforts to produce graphene with mechanical exfoliation method dates back to 1990 [51, 52], it was only possible to produce graphite flakes consisting of 50 to 100 layers until 2004. So far, our understanding of graphene is at a very early stage. To integrate this wonder material into commercial applications, the production of high quality, large-scale graphene on compatible substrates is one of the key requirements. Extensive efforts aiming to achieve this goal have been made since the experimental discovery of graphene [2]. This section reviews the state-of-art techniques for the production of high quality, large-area graphene films.

The techniques for the production of large-area graphene which have been most commonly used, can be categorised into three types [53]: epitaxial growth from single crystal SiC, chemical vapour deposition (CVD) growth on transition metals and physical vapour deposition (PVD) growth using solid carbon sources. These techniques are all based on the same growth mechanism, which is the decomposition of carbon-containing materials at an elevated temperature and the re-crystallisation of the sp^2-hybridised graphene lattice on the catalytic surfaces. However, the specific growth materials and growth conditions, such as carbon sources, growth temperature, environment pressure, heating and cooling rates, growth time, types and crystal sizes of

the catalytic surfaces, vary from one method to the other, which may lead to different quality of the resulting graphene. In this section, the characteristics of each method are discussed together with their advantages and disadvantages.

2.2.1 Epitaxial growth from single crystal SiC substrates

The mechanisms of carbon graphitisation on SiC have been investigated for over 40 years [54, 55]. However, until 2004, the same year as the discovery of mechanically exfoliated graphene [2], the epitaxial production of an ultrathin graphite layer was reported by Berger and his co-workers using thermal decomposition of 6H-SiC (0001) and re-crystallisation of carbon in an ultrahigh vacuum (UHV) [37], which was believed as the first technique for the production of large-area graphene. The epitaxial growth of monolayer graphene was subsequently reported by the same group in 2006 [16]. The growth requires a single crystalised SiC substrate to be heated to a temperature ≥ 1200 °C in a UHV chamber. Si atoms on the surface of SiC were sublimed, whilst C atoms were left behind due to the higher vapour temperature [55-57]. Because of the minor mismatch between the SiC (0001) and graphene lattices, the remaining C atoms were able to re-crystallise into a graphene layer at the cooling down stage [37, 58].

Epitaxial graphene grown on single crystal SiC has been found not to be self-limiting. The substrate type (Si or C terminated), the annealing temperature [59, 60] and the vacuum condition [61] all have been proven essential to the number of layers, quality and properties of the resulting graphene film. On the C-terminated face, graphene is preferred to form with more layers, usually more than 10. The first few layers adjacent to the substrate show an electron-doped characteristic together with a random orientation, whilst the subsequent layers on the top are not as much doped as those with a random crystal orientation [62]. In this case, the resultant graphene presents an electron mobility of 10^4 - 10^5 $cm^2 V^{-1} s^{-1}$ with a corresponding carrier density of 10^{13} cm^{-}

^{2}. In contrast, the number of graphene layers grown on the Si-terminated face is more controllable and uniform [62], although in this case, the graphene shows a lower carrier mobility (10^{2} - 10^{3} cm^{2} V^{-1} s^{-1}) and carrier density (10^{12} cm^{-2}), which has been proven to be due to the absence of an electron-doped interface [63].

The major advantage of epitaxial growth is that graphene forms directly on top of the insulating SiC substrate; therefore, post-transfer of the resultant graphene film to another insulating substrate is not required, providing a unique platform for exploring the one-step fabrication of electronic devices, such as FETs and integrated electronic circuits. So far, epitaxial growth of graphene has attracted major interest from leading commercial organisations in the field [64]. Devices, such as graphene transistors operating at 100 GHz [65] and graphene integrated circuits operating at up to 10 GHz [66] have been reported by International Business Machines Corporation.

However, the quality of epitaxial graphene needs to be improved to meet the industrial requirements for electronic applications. Particularly, epitaxial graphene presents a terraced morphology instead of an atomically smooth layer on top of the single crystal SiC substrate [16], as typically shown in Fig. 2-3 [61], leading to a degradation of electronic performance. In addition, the high cost of the single crystal SiC substrate limits its large-scale applications in industries. The very high growth temperature in UHV can be another limitation.

Figure 2-3 has been removed due to Copyright restrictions.

Figure 2-3. Terraced morphology of epitaxial graphene on single crystal SiC substrate and the terrace step height measured by atomic force microscope (AFM). The left AFM image is from graphene formed on 6H–SiC (0001) substrate. The middle AFM image shows terraces adjusted at the same height. The right profile shows the height of terraces and small depressions of around 0.5 nm and 1 nm amplitude at the very edge of the macro-step [61].

2.2.2 Chemical Vapour Deposition

After the epitaxial method, one of the game changing achievements in the production of large-area graphene is the CVD method [67-69] using short-chain hydrocarbons as the carbon source, such as methane and ethylene [70-74], on a catalytic surface, such as Ni [21, 75, 76], Ru [77-79], Ir [80], Au [81], Cu [67], Pt [82], Rh [83, 84], Pd [85, 86] and Fe [87]. Short-chain hydrocarbon gases have been used as a carbon source for the production of carbon nanotubes [88, 89] for a long time. During that period, although the growth of few layer graphite or even monolayer graphite using CVD have been discovered, for example, on Pt (111) by Land et al [90] and on TiC (111) by Nagashima et al [91], no results in the characterisation of its electron transport properties of the resultant film have been reported.

In the typical CVD method, a poly crystalline, or amorphous metal sheet [92, 93] or film [94, 95], which acts as a catalytic surface, is subjected to a pre-annealing process (800-1000 °C) in a vacuum to obtain large crystalline grains. The gaseous carbon source

is introduced onto the surface of the metal film, hydrocarbon first is adsorbed onto this catalytic surface and then decomposes into carbon atoms and forms the graphene lattice during the cooling down process. Different theories have been reported to explain the growth mechanisms of CVD graphene on the surface of transition metals. The earlier theory assumed the growth of graphene was subjected to an epitaxial process on the hexagonal or other crystallographic surface, such as Co (0001) [96], Ni (111) [97], Pt (111) [96], Ru (111) [98], Ir (111) [99]. However, according to many recent findings in the growth of CVD graphene on a number of polycrystalline metals, the surface catalytic effect is more well-known [69], although the precise catalytic mechanism remains unknown. The growth process of CVD graphene is believed to depend on the carbon solubility of the substrate metal. For those metals having relatively higher carbon solubility at the high temperature, such as polycrystalline Ni [21, 75, 76], the carbon atoms are firstly dissolved and absorbed in the metal, forming a solid solution. Then during the cooling down process, carbon atoms segregate from the solid solution due to the decreased solubility of carbon at a lower temperature and precipitate (or surface segregate) on the surface of the catalytic metal, forming a few layer graphene on top of it. It is worth noting that “segregation” refers to the separation of carbon atoms within the metal layer, while the “precipitation” refers to the diffusion and deposition of carbon atoms onto the catalytic surface (known as “surface segregation), which includes the recrystallisation of carbon atoms. For those metals having relatively low carbon solubility at high temperatures, such as polycrystalline Cu [67-69], dissolution and segregation of carbon atoms within the metal layer is limited or, at least, is not the dominant process due to a limited number of carbon atoms in the metal layer. In this case, carbon atoms re-crystallise into a graphene lattice directly on the surface of the catalytic metal. These two different growth mechanisms on Ni and Cu have been experimentally demonstrated by Li and his co-workers [69] using a carbon isotope

labelling technique, as shown in Fig. 2-4. The growth process of graphene on Ni is presented in Fig. 2-4 (a). After the carbon isotope labels are sequentially introduced and randomly mixed up in the Ni layer during the heating process, the segregation and precipitation happened to all carbon atoms in the Ni, which in turn leads to a random distribution of carbon isotope labels in the graphene lattice. The growth process of graphene on Cu is shown in Fig. 2-4 (b). In contrast, the carbon isotope labels in the graphene lattice are distributed in the same sequence that introduced carbon isotope labels, indicating the surface precipitation is dominant, otherwise the isotope labels would have a random distribution, the same as shown in Fig. 2-4 (a).

Figure 2-4 has been removed due to Copyright restrictions.

Figure 2-4. Isotope labelling illustration of CVD graphene growth mechanisms. (a) On Ni and (b) Cu, respectively [69].

The essential parameters for the production of better graphene include hydrocarbon concentration/flow rate [100], annealing time/temperature [73], metal grain size [101, 102] and cooling rate [75]. However, the contribution of these parameters to the quality of the resultant graphene may vary from one growth model to another. The growth of graphene based on the first mechanism leads to the formation of graphene with more

layers particularly at the area around grain boundaries or where there are regions of smaller grains, which is attributed to the excessive surface segregation or precipitation of carbon. In this case, the fast cooling rate is effective to obtain few layers or even monolayer graphene [21, 75, 76]. In contrast, graphene growth via the second mechanism has been believed to be a self-limiting process. Once the metal surface is fully covered by a graphene monolayer, the catalytic effect of the metal layer degrades, in turn leading to monolayer graphene (bilayer graphene is obtained instead of the monolayer at atmospheric pressure [103]). A longer annealing time is then helpful for the production of monolayer graphene with a higher surface coverage [67-69]. Graphene grown on Cu and Ni have both been well explored; however, the results so far indicate that graphene growth on Cu is more promising for electronics applications. For example, monolayer graphene grown on Cu with a 95% surface coverage has been achieved together with a crystalline grain size of 1000 μm. The electronic mobility of graphene has reached up to 10^4 $cm^{-1}/V \cdot s$ at room temperature [67-69].

Figure 2-5 has been removed due to Copyright restrictions.

Figure 2-5. Typical surface morphology of CVD graphene on Cu substrate. (a) 2D and (b) 3D AFM images, showing the inherent non-flat topography with an r.m.s. roughness of 3-6 nm. Scale bar is 500 nm in (b) [104].

Figure 2-6 has been removed due to Copyright restrictions.

Figure 2-6. Scanning tunnelling microscope (STM) morphology analysis of graphene grown on Cu with different crystalline states. (a) Crooked wrinkles on amorphous Cu substrate and its height profile. (b) and (c) show striped ripples and wrinkles evolving along the boundaries from crystalline to noncrystalline states. (d) Ripples appearing on step boundaries of crystalline Cu. (e) Sketch map showing the positions of wrinkles and ripples with substrate states of (a) to (d) [105].

Only a few publications on the surface morphology of CVD graphene have been reported. According to these references, graphene grown on the surface of a Cu substrate always presents a non-flat nature [104, 106, 107]. Typical surface morphology of CVD graphene on Cu foil is characterised with AFM, as shown in Fig. 2-5. After the sublimation and the re-crystallisation of Cu grains at high temperature, Cu substrate shows an inherent non-flat nature. The terrace and rippling morphology of graphene can be seen together with a typical r.m.s value of 3-6 nm, which is actually a rubbing of the non-flat Cu underneath. This is one of the major contributions to the terraces and ripples of transferred graphene on SiO_2 substrate. In addition, the non-flat morphology of graphene has been found to be closely related to the difference of thermal expansion coefficients between Cu substrate and graphene [105], as shown in Fig. 2-6. Compared with that of well-crystallised Cu substrates, Cu in the amorphous or transition state

shows a greater difference in thermal expansion coefficient than the graphene grown on top of it, leading to a larger contraction of Cu substrate during the thermal quenching, which in turn leads to the formation of larger wrinkles on the graphene film. Although graphene grown on well-crystallised Cu substrate prefers to form a flat morphology on the top surface of each terrace, it shows ripples (0.5 nm high) or wrinkles at the step area, which is attributed to the small difference of thermal expansion coefficients between Cu and graphene. Similar problems have been found with graphene grown on Ni substrate [106], except the absence of rippling morphology caused by metal sublimation (because of the much weaker sublimation of Ni film at the same growth temperature). Typical AFM images of graphene before and after transferring from a Ni film onto a SiO_2 substrate are shown in Fig. 2-7. The graphene has also been found to be a rubbing of Ni morphology underneath. Each grain more or less wraps around the hemispherical Ni grain underneath and deep trenches form between adjacent grains. After the Ni support layer is etched away, the non-flat graphene film falls onto the SiO_2/Si substrate, leading to the formation of single wrinkles around the hemispherical grain boundaries and bi-wrinkles between the adjacent hemispherical grains. It is notable that grains here are rubbings of Ni grains underneath instead of the crystal grains of graphene. Also, the wrinkles caused by the thermal expansion between the Ni substrate and graphene are at least a few times larger than those caused by the hemispherical Ni grains.

Figure 2-7 has been removed due to Copyright restrictions.

Figure 2-7. AFM analysis and longitudinal section profile of CVD graphene grown on Ni/SiO_2 stack, before (left) and after (right) transfer. The dotted circle in left AFM image refers to an individual Ni grain while two adjacent lines refer to a trench between Ni grains. The dotted circle and the two adjacent dotted lines in right AFM image refer to a closed wrinkle and bi-wrinkle after transfer, respectively. Longitudinal section profiles illustrate the surface-morphology-preserved after transfer of graphene from Ni to a SiO_2/Si substrate [106].

As CVD graphene has to be produced on top of the transition metals, a post-transferring process from metal to the other substrate, such as SiO_2/Si substrate [70, 76, 108-110] or polyethylene terephthalate (PET) film [111, 112], is required for the fabrication and characterisation of graphene-based applications. Poly (methyl methacrylate) (PMMA)-based wet-transfer is the most commonly used method for research purposes. Graphene grown on the metal substrate is covered by a spin-coated PMMA layer and then etched using HCl or ferrous sulphate-7 hydrate ($FeSO_4 \cdot 7H_2O$), to dissolve the metal layer from the back side. Once the metal layer is fully etched away, the graphene/PMMA layer floating on the etchant solution can be picked up onto the other arbitrary substrate without introducing any visible cracks or wrinkles [21], which is attributed to the

hydrophobicity of PMMA and the high breaking strength of graphene. To transfer high quality, large-area graphene for graphene applications on an industrial scale, such as touch screen displays [111], flexible heaters [113], solar cells [114, 115], roll-to-roll transfer based on the PET/epoxy film [109] has recently been proposed and achieved by Sony. By integrating Joule heating, CVD growth, gravure coating, ultraviolet light (UV) bonding and spray etching, a result of 100 m long, high quality graphene on PET/epoxy film has been recorded [107]. Additionally, for large-area, high quality graphene growth with CVD method, a number of findings have been reported on using different metal alloys, such as Ni-Cu [116], Ni-Au [117] and Ni-Mo [118, 119].

2.2.3 Growth from Solid Carbon Source

In addition to CVD, the other transition metal-based technique for large-area high quality graphene production has been reported using solid carbon sources. It shares the same growth mechanism with CVD method: polycrystalline Ni [120], Cu [121] or Co [74] deposited onto SiO_2 in vacuum are used as the catalyst and solvent, while solid carbon-containing materials atop or underneath the metal, such as amorphous SiC or C, are used as carbon source. After a rapid thermal process (RTP) step in either a vacuum or a protective atmosphere at a temperature up to 1100 ^{o}C, carbon atoms can be dissolved and re-crystallised into a graphene lattice. Both the catalytic metal layer and the carbon-containing material can be deposited onto the heat-proof substrate by physical vapor deposition such as sputtering [122, 123], thermal evaporation [124], vacuum arc [125], molecular beam epitaxy [126] or ion implantation [127, 128]. Spin-coated PMMA [121] or other carbon-containing polymers such as poly acrylonitrile [129], trimethoxy phenylsilane [130], polystyrene [131], poly (2-phenylpropyl) methysiloxane [132], acrylonitrile butadiene styrene (ABS) [133], have also been explored. A one-step material deposition has been demonstrated for the growth of graphene using carbon impurities embedded in the metal or alloy targets [134]. Due to

the same growth mechanism with CVD graphene, a post-transfer process from the metal layer to the insulator is required for the fabrication and characterisation of graphene-based applications.

Graphene growth from solid carbon sources was first achieved in 2009 by annealing e-beam evaporated Ni onto single crystal SiC substrates at 750 °C [120], which is much easier to achieve than the epitaxial method. Later in the same year, a method of using plasma enhanced CVD (PECVD) deposited amorphous SiC and sputtered Ni films was reported for the growth of graphene at a RTP temperature of 1100 °C, which waived the high cost of single crystal SiC substrates [135]. Since then, growth of wafer-scale graphene has been reported with using a number of different materials, such as Ni/SiC [136, 137], Ni/C [123, 125], Ni/PMMA [124, 132, 138], Cu/PMMA [121, 139], NiCu/C [140, 141]. In this method, the essential parameters for the growth of large-area high quality graphene are the ratio of the metal/carbon source and the cooling rate. With optimal growth parameters, the quality of graphene is then mainly dependent on the grain size of the poly crystalline metal, although the type of carbon source has an effect on the resultant graphene to some extent. Graphene growth on the larger metal grains prefers to be monolayer or few layer, whilst multilayer graphene is likely to be obtained from those areas with smaller grains and at grain boundaries. The multilayer characteristic can be attributed to the overlap of metal grains, which produces overlapped graphene. Therefore, whether graphene grown on each metal grain is self-limiting remains arguable [142]. The major disadvantage of graphene growth from solid carbon sources is that large-area high quality graphene cannot be grown uniformly, at present, due to the polycrystalline nature of catalytic metal underneath.

2.2.4 Transfer-free and Direct Growth on Dielectric Substrates

For the fabrication of graphene-based electronic devices, graphene has to be grown on or transferred onto the insulating substrate. However, as discussed earlier in 2.2.2 and 2.2.3, direct growth of graphene on an insulating substrate is unlikely to be achieved with CVD or growth with solid carbon source. In order to use graphene produced by these techniques for device fabrication, a PMMA-based post-transfer process is required, as introduced in 2.2.2, which not only increases the commercial cost but also introduces polymer residues and damage to the graphene film. To address these issues, two techniques of graphene growth have been developed: transfer-free growth [142] and direct growth [129] of graphene on insulator substrates.

For the transfer-free growth of graphene, two methods have so far been developed: complete evaporation [94, 143] and post-etching [142] of the catalytic metal layer after the crystallisation of graphene. Due to a decreased sublimation temperature in UHV, the catalytic metal layer in the "evaporation method" can be evaporated, leading to a graphene layer grown atop of it falling onto the dielectric surface. This method was first reported by Ariel Ismach and his co-worker within a CVD process [94]. The Cu film on top of SiO_2 substrate can be fully evaporated or de-wetted into finger-like patterns after 15 mins to 7 hours annealing at 1000 °C and at a low pressure (100-500 mTorr), leaving inhomogeneous graphene behind on the substrate. A p-type doped behaviour has been recorded together with a carrier mobility of ~600 $cm^2 V^{-1} s^{-1}$ and a gate modulation around 3 on this corresponding graphene FET. With the post-etching method, Gao and his co-workers have achieved transfer-free growth of graphene from sputtered Cu by a CVD method [144]. By pre-treatment of the substrate with nitrogen plasma, bubble seeds can be planted in the SiO_2 layer, which then generate bubbles during the chemical etching process. These resultant bubbles can join those trapped under the graphene film and act together as capillary bridges with a strong negative pressure, resulting in the

graphene remaining on the original substrate after the removal of the Cu layer [144], as shown in Fig. 2-8 (a). In this case, the graphene obtained is weakly n-type doped and shows a carrier mobility of 3800 $cm^2 V^{-1} s^{-1}$, which is comparable to that of CVD graphene. The effectiveness of this approach has been proven by its control experiment without the pre-treatment of the substrate, leading to the delamination of the graphene layer from the substrate after Cu etching.

Figure 2-8 has been removed due to Copyright restrictions.

Figure 2-8. Schematic illustration of face-to-face transfer-free graphene production. (a) Mediated by capillary bridges and (b) control experiment without pre-planted N_2 seeds [145].

The interface of catalytic metal and SiO_2 has been believed to be chemically unfavourable for graphene growth [142]; however, direct growth of graphene on a SiO_2 substrate has been achieved. With a 10 nm spin-coated polymer layer (PMMA) as carbon source and a 50 nm Ni layer as solvent and catalyst, few-layer graphene has been obtained directly on the SiO_2 substrate after 1 min RTP at 1000 °C [129]. The quality of the resultant graphene is strongly dependent on the carbon sources used, which may be attributed to the decomposition and residue conditions. Similar results with using different carbon sources and catalytic metal (or metal alloys), such as CH_4/Cu, ABS/Ni, trimethoxy phenylsilane/Ni or Cu/Ni (containing trace amorphous carbon), have been reported [20, 132, 138, 141]. By adjusting the parameters of graphene growth, low-

defect wafer-scale graphene with bilayer coverage of 70% and the monolayer coverage of 20% has been recorded directly onto SiO_2 substrates. Although the quality of graphene grown with this method cannot meet the requirement of application fabrication so far, the key achievement of this method, which is very promising for the future, is that graphene is grown directly on the atomically flat insulator substrate. In contrast, the major disadvantage of this growth method is that carbon atoms prefer to segregate through the grain boundaries or micro voids of the metal layer (shown in Fig. 2-9 (a) [20, 146]), leading to the randomly distributed ridges on graphene film (shown as dark blue area in Fig. 2-9 (b)). A relatively high D band and G/2D band intensity ratio can be seen from a Raman spectrum taken from the ridge area (shown in Fig. 2-9 (c)), indicating the more defective and multilayer nature of graphene around the ridges. The corresponding FET devices show a lower carrier mobility ranging from 150-700 $cm^2\ V^{-1}\ s^{-1}$ and heavily p-doped characteristic compared with those devices fabricated with high quality graphene.

Figure 2-9 has been removed due to Copyright restrictions.

Figure 2-9. Transmission electron microscopy (TEM), optical and Raman analysis of graphene grown at the interface of metal/SiO_2. (a) TEM image of the longitudinal section showing grain boundary and void. (b) Optical image of graphene ridges formed at 160 °C for 2 min on SiO_2. (c) Typical Raman spectra acquired from the graphene ridge labelled by a black dot in b [20].

Due to the same diffusion-segregation growth mechanism, the thickness of the metal layer and the ratio between the metal and carbon sources are believed to be the most important parameters for the production of high quality large-area graphene with both transfer-free and direct growth on insulating substrate. A lower carbon to metal ratio is favoured leading to a lower surface coverage of graphene and the potential disconnection between top-surface graphene and substrate; in contrast, a higher carbon to metal ratio may result in the de-wetting of the layer before graphene growth and excessive segregation of amorphous carbon after the growth, in turn leading to a mixture of multilayer graphene/amorphous carbon.

The production of wafer-scale graphene using metal-free PECVD was pioneered by Zhang and his co-workers in 2011 [147] on various insulating substrates. After that, the direct growth of wafer-scale monolayer graphene on Ge substrates was achieved by Wang and his co-workers very recently [148]. In this method, hydrocarbon radicals were first introduced onto the surface of a Ge substrate together with a H_2/CH_4 ratio of 50:0.1, at a temperature ranging from 800-910 °C. The carbon atoms decomposed from the hydrocarbon and bonded with each other and the graphene grains interlinked together by collision under the catalytic effect of Ge, leading to the formation and extension of the graphene layer on the surface of the Ge substrate. The positively shifted Dirac point can be observed together with a carrier mobility of 800-900 $cm^2 V^{-1} s^{-1}$ from its resultant FET device, which is comparable to that of CVD graphene. To improve its electronic properties, wafer-scale wrinkle-free single-crystal monolayer graphene grown on a hydrogen-terminated Ge (110) substrate was achieved [149]. The growth mechanism of single-crystallised graphene is attributed to the atomic arrangement of single-crystal Ge, which enables unidirectional alignment of graphene grains merging into a graphene film with the same orientation. Compared with graphene produced on polycrystalline Ge substrates, a much higher carrier mobility, up to 10^4 $cm^2 V^{-1} s^{-1}$ has

been observed due to the decreased electron scattering at defective grain boundaries and wrinkles. Due to an extremely low solubility of carbon in Ge under equilibrium conditions, graphene grown with this method has been believed to be a self-limiting process.

2.2.5 Conclusions

Different techniques for the production of large-area high quality graphene have been developed since the experimental discovery of graphene. Epitaxial graphene grown on single crystal SiC substrate is a wafer scale method for the production of large-area graphene directly on semi-conductive substrates, although the cost of substrates and growth temperature is very high, and the non-flat terraced nature limits its application. CVD graphene grown on transition metal films, particularly on Cu and Ni, is another promising approach for the production of large-area high quality graphene. With very good transfer compatibility to arbitrary substrates, it has been used for a number of applications, such as touch screen displays, e-paper and organic light-emitting diodes (OLEDs). Although CVD growth is more commercial than the epitaxial method, its high growth temperature and the requirement of the post-transfer process make this method in need for further development. Graphene growth from solid carbon source and transfer free growth are the other two achievements for the production of large-area graphene, although further improvements of these methods are required to make them practical for industrial device applications. Each growth method developed so far has its advantages and limitations. The main challenge is the development of a wafer scale production technique for atomically flat and low defect single crystal graphene directly onto insulating substrates. Although graphene is unlikely to be used for the fabrication of commercial high-performance applications in the near future, its superior physical/chemical properties have already been proved promising by proof-of-concept devices and sensors [150].

Chapter 3 Graphene Functionalisation & Applications

3.1 Functionalisation of Graphene

Since the experimental discovery in 2004 [2], graphene has attracted tremendous interest due to its unique properties. However, developments of graphene-based applications have been limited due to its low solubility, zero band gap and chemical inertness. To overcome some of these limitations, chemically covalent or non-covalent functionalisation of graphene with organic or inorganic molecules can prevent the agglomeration of layered graphene in the solvent phase. This leads to its higher solubility and provides active functionalities on the graphene surface to tune its physical/chemical properties to meet the requirements of different applications. Therefore, understanding graphene chemistry and knowing how functional groups attach onto and modify graphene are necessary for the further development of graphene applications.

Chemical functionalisation of graphene has been widely explored to meet the requirements of electronic and biosensing applications [30, 151]. In this section, state-of-the-art techniques for chemical functionalisation of pristine graphene and graphene derivatives, especially those commonly used for the fabrication of graphene biosensors, have been reviewed in detail. According to the different mechanisms, they could be categorised into covalent or non-covalent methods. Covalent functionalisation is based on breaking sp^2-hybridised carbon in pristine graphene lattice using methods such as oxidation [27] and binding of dienophiles, or attachment of functionalities through oxygen-containing functionalities existing on the surface of GO through the esterification or silanisation with APTES [25]. Non-covalent functionalisation is achieved via the interaction of π-π bonds, hydrophobic bonds or Van der Waals forces. The ultimate purpose of chemical functionalisation of graphene in this work is to

achieve chemically active graphene, which is capable to bond or interact with other biomolecules.

3.1.1 Covalent Functionalisation

Graphene has an sp^2-hybridised 2D structure, which refers to the hybridisation of one *s* orbital and two *p* orbitals and results in three energetically equivalent sp^2 orbitals. The remaining *p* orbital forms a π bond with *p* orbitals from other carbon atoms, which is perpendicular to the plane of the graphene sheet and is responsible for the interaction between graphene layers. In a typical covalent functionalisation, the break of sp^2-hybridised C-C bonds and re-hybridisation of sp^3-C-C bonds results in the presence of free radicals or dienophiles. These introduce chemically active functionalities into the graphene lattice or at the end of the graphene sheet, which are capable to interact with other molecules.

3.1.1.1 Oxidation of Pristine Graphene

The first technique for the production of functionalised graphite dates back to 1859 [152]. By reacting a mixture of potassium chlorate and highly concentrated nitric acid (HNO_3), graphite oxide was obtained using a combination of extended bath sonication and careful centrifugation. This method is of high risk and needs care at all stages due to the strong oxidation used. To make this method safer, faster and more effective, a technique was developed between 1898 and 1957 by Staudenmaier, Hofmann and Hummers using different oxidants [153-155]. Although, Hummers method can achieve a higher oxidation level (27.92 wt% oxygen), it was found that the oxidation is incomplete, due to the GO-shell graphite-core structure. Hummers method has been optimised by a peroxidation process using a mixture of sulfuric acid (H_2SO_4), $K_2S_2O_8$ and phosphorus pentoxide (P_2O_5) [156] and considered as the most effective technique for the large-scale production of GO (known as modified Hummer's method) [27, 157,

158]. The precise mechanism of Hummer's method has not been confirmed so far (likely to be that of sp^2 C-C bond being attacked by free radicals), but the outwardly functional groups on graphene plane have been proposed and confirmed by the results of nuclear magnetic resonance (NMR) [159] and Fourier Transform Infrared Spectroscopy (FTIR) [160]. One of the most well-known GO models was proposed by Lerf and Klinowski as shown in Fig. 3-1 below. The plane of a graphene sheet is randomly decorated by hydroxyl groups (-OH) and epoxide groups (C-O-C) with the opening of C=C bonds, whilst the periphery of the graphene plane is functionalised by a small amount of carboxylic groups and carbonyl groups [161, 162]. In this case, the hydrophobic inert graphene is turned into highly hydrophilic GO with numerous reactive sites on both sides of the graphene sheet, which in turn provides the possibility of reacting with other biomolecules dispersed in aqueous solutions [163]. The advantage of the modified Hummer's method is its high efficiency of oxidation, which is indicated by the weight percentage of oxygen atoms in GO. However, the disadvantage is that all chemicals involved are strong oxidizing agents and the reaction itself is very harsh as well, limiting this approach towards the functionalisation of electronic devices (thin metal film can be easily oxidised, damaged or no longer attached to the substrate).

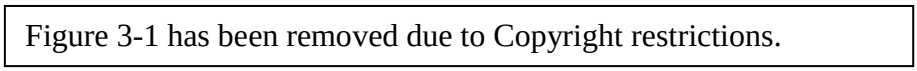

Figure 3-1. Typical atomic structure of graphene oxide [164].

3.1.1.2 Addition of Free Radical to *sp*^{2}-hybridised Carbon

In order to achieve the single-type functionality terminated graphene and to further understand the mechanism of covalent functionalisation, more selective methods have been developed recently. In 1894, Fenton reported a method which used a mixture of H_2O_2 and ferrous iron salt (Fe^{2+}, to act as a catalyst) to degrade various organic compounds [165]. This was later developed as a method for introducing hydroxyl groups into graphene-like structures, such as graphene, graphite and carbon nanotube [166-168]. Through a catalytic decomposition of H_2O_2 at room temperature, hydroxyl radicals (HO·), which are believed to be one of the most powerful oxidants [169], are generated constantly. Unsaturated sp^2-hybridised carbon bonds and the defective sites, existing in the plane of the graphene sheet, are synchronously attacked by the hydroxyl radicals through an electrophilic addition reaction. This results in the introduction of large quantities of hydroxyl groups onto the surface of the graphene (a limited amount of –COOH and quinone groups (C=O) on the rim of graphene sheet), the reaction equation is described as:

$$Fe^{2+} + H_2O_2 \rightarrow Fe^{3+} + HO\cdot + OH^-$$

(1)

$$Fe^{3+} + H_2O_2 \rightarrow Fe^{2+} + HOO\cdot + H^+$$

(2)

$$Fe^{2+} + HO\cdot \rightarrow Fe^{3+} + OH^-$$

(3)

Compared with Hummers' method, a negligible amount of carboxyl (-COOH) and quinone groups are introduced onto the surface of graphene. However, similar to Hummer's method, the original *sp*^{2}-hybridised graphene lattices are significantly disordered by radical attack during Fenton reaction, which is consistent with the

introduction of oxygen-containing functionalities [167]. Therefore, the electronic properties, such as the conductivity of hydroxylated graphene, decrease sharply compared with pristine graphene. In addition to the Fenton Reaction, other hydroxylation methods, such as hydroxylation with sodium hydroxide (NaOH), $KMnO_4$ [170], sodium aluminate ($NaAlO_2$) [171] or sodium zincate (Na_2ZnO_2) [172], which have normally been used on organic chemistry, have been attempted and developed to achieve hydroxyl terminated graphene. However, these methods have not been widely used due to the limited hydroxylation efficiency.

Tour and his co-workers reported a method of adding nitrophenyl groups onto a graphene channel by heating up diazonium salts together with pristine graphene [173]. The diazonium salt has a general molecular structure of $R\text{-}N_2^+X^-$, where R stands for an organic part like aryl and X is an anion. The mechanism of functionalisation is that the sp^2 hybridised carbon atoms in the graphene lattice are attacked by the highly reactive free radicals generated during heating and then covalently bonded with those radicals. Similar to the oxidation functionalisation above, the conductivity of the corresponding graphene sheet drops sharply after functionalisation, which is attributed to the conversion of the sp^2 to an sp^3 hybridised structure. After that, Niyogi and his co-workers demonstrated that the attachment of nitrophenyl onto graphene introduced a controllable band gap, providing graphene a huge potential in semiconductor applications [174]. The ratio between sp^2 and sp^3 hybridised carbon atoms, which can be calculated by the intensity ratio of the D band and G band in Raman spectroscopy, can, therefore, be used to evaluate the level of the functionalisation process.

3.1.1.3 Immobilisation of Functionalities onto Graphene Oxide

Graphene oxide can be considered as a monolayer of carbon atoms connected through sp^2 or sp^3-hybridised C-C bonds with each other, which may randomly bond with

oxygen containing functionalities such as hydroxyl, epoxy, carbonyl, and carboxyl functional groups. The hydroxyl and epoxy groups are distributed on the both sides of basal graphene plane while the carbonyl and carboxyl groups are distributed at the edge or defective site of the graphene sheet. Therefore, GO provides the potential to react with chemicals, which can react with both carbon atoms in graphene lattice and the oxygen containing functionalities distributed on graphene. Due to the extensive experience accumulated on the chemistry of oxygen-containing groups above, GO has been commonly chosen as the initial material for the production of graphene derivative and the fabrication of graphene-based devices [163].

The method of GO functionalisation with APTES (or APTS) was first reported by Yang and his co-workers [25] by heating up the mixture of GO, dicyclohexylcarbodiimide (DCC, act as a catalyst) and APTES to 70 °C for 24 h. The mechanism is that the silane moieties bonded to the surface of GO through a nucleophilic displacement reaction occurred between epoxy groups from GO and amino groups from APTES, as shown in Fig. 3-2. In the presence of water, APTES molecules are subject to a hydrolysis condensation with each other and form a layered structure on the surface of GO. The key evidence of this successful chemical functionalisation include: the presence of a band at 1059 cm^{-1} in FTIR spectrum and Si2p bands at 102.6 eV and 98.6 eV in X-ray photoelectron spectroscopy (XPS), which indicates the existence of silicon atoms in Si-O-C and Si-O-Si bonds. The shift of the Os1 band in XPS from 532.7 eV to 531.8 eV after APTES functionalisation indicates the presence of oxygen atoms in Si-O-C and Si-O-Si bonds.

Figure 3-2 has been removed due to Copyright restrictions.

Figure 3-2. Demonstration of reaction between GO and APTES.

In contrast, another mechanism for the functionalisation of GO with APTES has been proposed recently [166]. In the presence of water, ethoxy groups in APTES molecules subject to a hydrolysis reaction, result in a Si-OH functionalities terminated surface. These Si-OH functionalities react with the hydroxyl groups from both GO and hydrolysed the APTES molecules themselves, and in turn, result in Si-O-Si bonds, forming an inhomogenous multi-molecular layer on the surface of GO, as shown in equation (4) below. However, in the absence of water, ethoxy groups in APTES molecules directly react with the surficial hydroxyl groups from GO. In this case, the resultant condensed layer is relatively uniform and has fewer layers, as shown in equation (5) below. It is worth noting that these two reactions practically occur at the same time, as the trace water in chemicals is impossible to remove.

$$H_2N - CH_2CH_2CH_2 - Si(OR) - OH + HO - C \rightarrow H_2N - CH_2CH_2CH_2 - Si(OR) - O - C + H_2O \quad (4)$$

$$H_2N - CH_2CH_2CH_2 - Si(OR)_2 - OR + HO - C \rightarrow H_2N - CH_2CH_2CH_2 - Si(OR) - O - C + ROH \quad (5)$$

Where R = H or C_2H_2O.

Polymers containing chemically active species, such as hydroxyl, amino groups, can also be immobilised onto the surface of GO through a covalent bond. In such a hybridised composite, the electrical conductivity and the chemical inertness are mainly attributed to the structure of graphene while its chemical properties and mechanical properties are attributed to the particular bonded polymer. In biosensing applications, polymers that can provide abundant amino or carboxyl groups, are preferable in the fabrication of this polymer-graphene composite. PAA is one of the long alkyl molecule containing abundant reactive amino groups, which are able to react with epoxy groups on the surface of GO. In this reaction, a three-membered epoxy group was attacked by nucleophiles (amino groups in PAA molecules here) and subjected to a ring opening reaction, resulting in the formation of C-N bonds [175]. This mechanism is supported by the increase of the peak at 1500 cm^{-1} in the FTIR spectrum and the sharp decrease of the C1s peak at 286.7 eV in the XPS spectrum, which are indicators of the formation of a C-N bond and the breaking of epoxy rings, respectively. The advantages of this method are: a monolayer or few-layer GO fragments can be cross-linked with each other easily by the covalent C-N bonds and the non-covalent interaction between negatively charged GO and positively charged PAA. Therefore, the preparation procedure of this composite is simple and easy (simply by dropping PAA solution onto the surface of GO) compared with those complicated purification/functionalisation (such as electro polymerisation) and the resulting composite is relatively more stable [176]. In addition, the functionalisation of GO with PAA is more effective in providing the reactive amino groups as each PAA molecule contains a large number of amino

groups and only a small amount of them are used for immobilizing themselves onto the surface of GO.

3.1.2 Noncovalent Functionalisation

To make graphene hydrophilic, soluble in more nonpolar/polar solvents, able to provide various functionalities whilst its structure can be maintained, the noncovalent functionalisation has been carried out for the modification of graphene. Compared with the covalent functionalisation, the noncovalent functionalisation of graphene is achieved mainly through π-π interactions between graphene and the target molecules (or Van der Waals's force between graphene and molecules), and thus, its physical and electronic network will not be disturbed [177]. As mentioned earlier, carbon atoms bond with each other through the three energetically equivalent sp^2 orbitals and the remaining *p* orbital makes a contribution to the π bond, which is perpendicular to the plane of the graphene sheet. The π-π interaction is one of the most important noncovalent driving forces which refers to the attraction of the negatively charged π electron clouds with similar electron densities (the π-π interaction also exists through induction interactions, even if one of the systems is electron-rich and the other is electron deficient, such as the negative charge transfer from benzene to hexafluorobenzene).

Noncovalent bonds are weaker than covalent bonds as it is further from the positively charged atomic nucleus, and the species noncovalently bonded onto the surface of graphene always leads to doping in graphene, which can be monitored by sweeping the gate voltage vs source-drain current in a FET device. In a typical I_D-V_G characterisation curve, it should exhibit a Dirac point at 0 V, however in practice, the Dirac point is negatively or positively shifted due to particularly bonded absorbents from the air or organic residues remaining from the fabrication process [178]. Annealing in a vacuum or inert gas such as Ar is preferred in desorbing absorbents from the surface of graphene,

which in turn reduces the doping level. However, the electronic performance, such as mobility, degrades as annealing brings graphene closer to the supporting substrate SiO_2 [179].

Noncovalent functionalisation of GO with single stranded DNA (ssDNA) has been reported by Liu and his co-workers [180] by simply incubating an ssDNA solution with GO for 24 hours. Due to the strong π-π interaction between the sp^2-hybridised carbon in GO structures and adenine, guanine, thymine and cytosine in ssDNA molecules, which all contain ring structures, ssDNA shows a strong tendency to flatly bond onto the surface of GO. Besides π-π interactions, hydrogen bonds between DNA molecules and oxygen-containing functionalities on the surface of GO act as a secondary driving-force and enhance the binding. In subsequent work, Xu and his co-workers reported a simple 3D self-assembly method for the production of DNA-GO multifunctional hydrogels with the same binding mechanism (π-π interaction) [181]. By heating up a mixture of equal volume solutions of GO and double stranded DNA (dsDNA) with various concentrations to 90 °C for 5 mins, the dsDNA molecules were subjected to an unwinding process and the corresponding ssDNA noncovalently bonded onto the surface of GO, resulting in DNA-GO hydrogels. The resulting DNA-GO hydrogels showed unique mechanical strength, environmental stability (no form change after being immersed in strong acid for one week) and high dye-adsorption (nearly 100% adsorption after 24 hours). Also, as bonded ssDNA molecules are capable of hybridising with its complementary DNA (cDNA), these stable DNA-GO composites have potential applications for catalysis, optoelectronics, FETs and biosensors.

3.2 Graphene Applications

Although it is unlikely that graphene can soon be integrated into current logic circuits as channel material due to the absence of a bandgap, a wide range of graphene-based

applications has been proposed and developed in labs since its experimental discovery. The properties or form of graphene used varies from one application to another according to the specific requirements. For example, the large area monolayer graphene without defects is required in the application of graphene FETs, while for some other applications such as energy storage devices and graphene modified electrodes, a graphene nano platelet with some defects is ideal. The major achievements in the application of graphene in electronics and sensing technology have been reviewed in detail below and a summary of the unique properties of graphene for particular applications is shown in Table 3-1 accordingly.

Table 3-1. A summary of properties of graphene for particular applications

	Electrical conductivity	Breaking strength	Surface/ volume ratio	Transpar-ency	Thermal conductivity	Chemical inertness	Elasticity
Transistor	√	×	×	×	×	√	×
Transparent & flexible conductor	√	√	×	√	×	√	√
Sensor	√	×	√	×	×	√	×
Energy storage	√	×	√	×	×	√	×
Paint	√	×	√	×	√	√	×
Field Emission	√	×	×	×	×	√	×
Battery	√	×	√	×	×	√	×

3.2.1 Graphene Transistor

So far, halving the FET size every 18 months is the most successful concept in the development of logic circuits following Moore's law since 1965 [182]. However, after a considerable exploration of conventional Si-based complementary metal–oxide–semiconductor (CMOS), the International Technology Roadmap for Semiconductors has announced that it will approach the limit around 2020. This can be attributed to the inhomogeneity of device fabrication, quantum effects and difficulties in heat dissipation with increasing density of device integration. Therefore, for the further development of FETs, it is crucial to investigate new materials, potentially providing smaller geometry

size, lower resistance, higher mobility and higher thermal conductivity to realise a replacement of conventional Si.

Graphene has attracted intensive research on the development of electronic transistors due to its 2D nature and unique electronic band structure calculated by Wallace from a tight-binding model in 1947 [50, 65] (as shown in Fig. 3-3). Two connected Dirac cones normally describe this band structure with a linear energy-momentum dispersion relation. The Fermi level (E_D) is proposed at the point where the valence and conduction bands meet, which is also known as a Dirac point or neutrality charge point. Both occupied valence and unoccupied conduction bands present a density of states of zero, making graphene a zero band-gap semiconductor. As a consequence of this, the Quantum Hall Effect can be observed at room temperature with a low magnetic field, making graphene a very promising candidate in the development of next generation semiconductors.

Figure 3-3 has been removed due to Copyright restrictions.

Figure 3-3. Electronic dispersion in the honeycomb lattice.

A typical graphene-based FET includes: a gate, which is insulated from the channel area by a dielectric layer (also known as barrier); a channel region, which is a graphene film connecting the source electrode and the drain electrode, as shown in Fig. 3-4 (right) below. By controlling the voltage applied between the gate and the source, the

conductivity of the channel can be modulated. The first and most important breakthrough of graphene FETs was achieved by Manchester in 2004, using the model shown in Fig. 3-4, right. Due to the incompatibility of back-gated FETs with other practical components, the top-gated FET has since been developed using exfoliated, CVD and epitaxial graphene as channel materials and SiO_2, aluminium oxide (Al_2O_3) and hafnium (IV) oxide (HFO_2) as the dielectric layer, as shown in Fig. 3-4 left. On the other hand, radio frequency (RF) transistors have also been developed and optimised. Lin and his co-workers from IBM first reported a 240 nm gate RF transistor fabricated with few layer epitaxial graphene in 2010 [65]. The cut-off frequency was up to 100 GHz, which was higher than those of the best silicon FET with similar gate length, was obtained together with a mobility value of 1520 $cm^2\ V^{-1}\ s^{-1}$. At the same time, by using a 1-2 nm thick HFO_2 as a dielectric layer, a top-gated graphene nanoribbon FET has now been reported with a recorded on-off ratio of 70 [183].

For the application of graphene-based FETs, the most crucial problem is the absence of a bandgap. There are four main methods that have been proposed and achieved for the opening of a bandgap: narrowing the channel width down to the nanometre scale, also known as using graphene nanoribbons [184]; replacing the monolayer graphene with a bilayer one [185]; applying a strain to monolayer graphene sheet [186] and modifying the surface of graphene with chemical functionalities [187]. Whichever methods above are used, the degradation of the electronic performance of pristine graphene will result due to the structural change of graphene. The most important advantage of graphene in the electronic application is its high mobility at room temperature. The mobility reported from pristine graphene on a SiO_2/Si wafer, which was prepared with mechanical exfoliation, generally ranges from 10000 to 15000 $cm^2\ V^{-1}\ s^{-1}$ with an upper limit of 70000 $cm^2\ V^{-1}\ s^{-1}$ [188]. Furthermore, without the effects of impurities, wrinkles and substrate, a mobility of 200000 $cm^2\ V^{-1}\ s^{-1}$ has been recorded [189].

Compared with the exfoliated graphene, the graphene produced with CVD and epitaxial method shows mobility up to 3700 $cm^2\ V^{-1}\ s^{-1}$ and 5000 $cm^2\ V^{-1}\ s^{-1}$, respectively.

Figure 3-4 has been removed due to Copyright restrictions.

Figure 3-4. Structural diagram of a conventional top-gated FET using graphene (left) and a graphene-based back-gated FET (right).

3.2.1.1 I_d-V_g Characterisation

$I_{source\text{-}drain}$-$V_{gate\text{-}source}$ characterisation (known as I_d-V_g characterisation in this thesis) is determined by plotting the current measured between source and drain electrodes versus the voltage applied between source and gate electrodes. Due to the zero bandgap nature of monolayer graphene, a typical graphene FET exhibits ambipolar behavior in I_d-V_g characterisation, in which the charge carrier change from electrons to holes (or from holes to electrons) reaches a minimum level at the Dirac Point, as shown in Fig. 3-5. In the region around the Dirac Point, both holes and electrons have their contribution to charge carriers, whilst in the region relatively far from the Dirac Point, charge carriers consist of only holes or electrons, which show a relationship of $n_{e,h} = \alpha V_g$ with applied back gate voltage (α is the injection rate of back gate charge). The source-drain current can be described by the equation below for low source-drain voltages (V_{ds}<V_{gs}-V_0) [190]:

$$I_d = (W/L)\mu C_{ox}\left(\left(V_g - V_0\right)V_d - 0.5V_d^2\right) \quad (6)$$

where W and L are the width and length of the channel respectively, μ is the mobility of charge carriers at low-fields which can be calculated by:

$$\mu = \sigma/qn$$

$$= (I_d * L)/(V_d * W * C_{ox} * (V_g - V_0)) \quad (7)$$

Where n is the carrier concentration, q is the elementary charge, σ is conductivity for the linear range of I_d-V_g characterisation, C_{ox} is the geometrical capacitance which can be expressed as $C_{ox} = (\mathcal{E}_r * \mathcal{E}_0)/d$, d is the thickness of the dielectric layer and V_0 is the voltage at the Dirac Point.

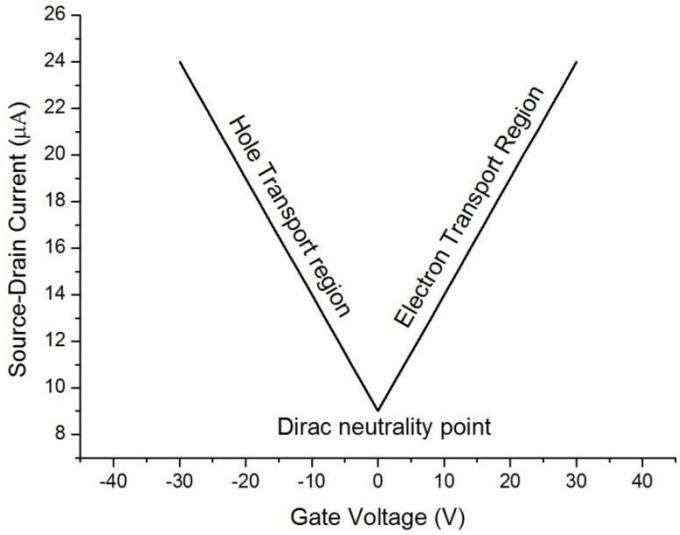

Figure 3-5. Ideal source-drain current versus source-gate voltage.

3.2.1.2 Total Resistance Measurement

Due to the low resistive nature of graphene, an ohmmeter in the circuit loop measures the total resistance of the graphene channel and the connecting wires in the conventional two wire resistance measurement, which leads to an inaccurate reading of the real graphene resistance. To solve this problem, four wire (also known as Kelvin) resistance measurement has become the most commonly used method for the accurate evaluation of graphene resistance. In a typical four wire measurement, the current is taken from the

circuit loop, which has the same reading at all the points, and the voltage drop is measured just across the graphene channel, which avoids the effects from connecting wires, as shown in Fig. 3-6 (a) and Fig. 3-6 (b).

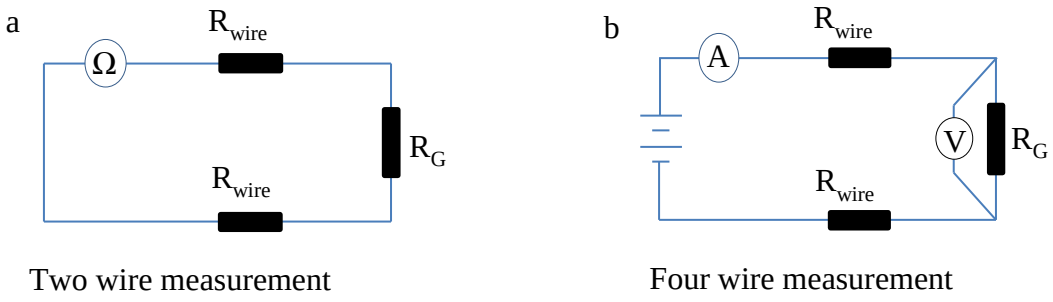

Two wire measurement Four wire measurement

Figure 3-6. Two wire and four wire measurement. (a) circuit loop comparison of two probes measurement and (b) four probes measurement.

3.2.1.3 Contact Resistance Calculation

The total device resistance of a graphene FET consists of the graphene channel resistance and the contact resistance. The channel resistance is determined by the quality of the graphene and the interaction between the graphene and the supporting substrate, which cannot be changed easily. However, the contact resistance, which mainly depends on the structural damage and the interaction at the graphene-metal interface, can be reasonably reduced, resulting in improved electronic performance. Therefore, a feasible method for the calculation of contact resistance is required.

One of the most commonly used methods for the calculation of contact resistance is the transfer length measurement (TLM), which contains any resistance independent with the channel length. The TLM method is based on the equation:

$$R_{total} = 2R_m + 2R_c + \rho_{ch}(d/W) \quad (8)$$

Where R_m is the resistance due to the metal contact, R_c is the contact resistance and ρ_{ch} is the channel resistivity. In most cases, R_m is very small compared with R_c, therefore,

R_m can be ignored. The R_c, therefore, can be determined by plotting the measured total resistance versus their channel length accordingly (all other parameters are kept constant). At the zero length point, the total resistance equals twice that of the contact resistance, as the schematic diagram shows in Fig. 3-7 (a).

For quick and convenient evaluation of contact resistance, an alternative method is extracting the contact resistance at high V_g in the R-V_g curve [191], where the resistance of the graphene channel was found to be stable and negligible compared with contact resistance. Therefore, the total resistance measured equals twice the contact resistance, as the schematic diagram shows in Fig. 3-7 (b).

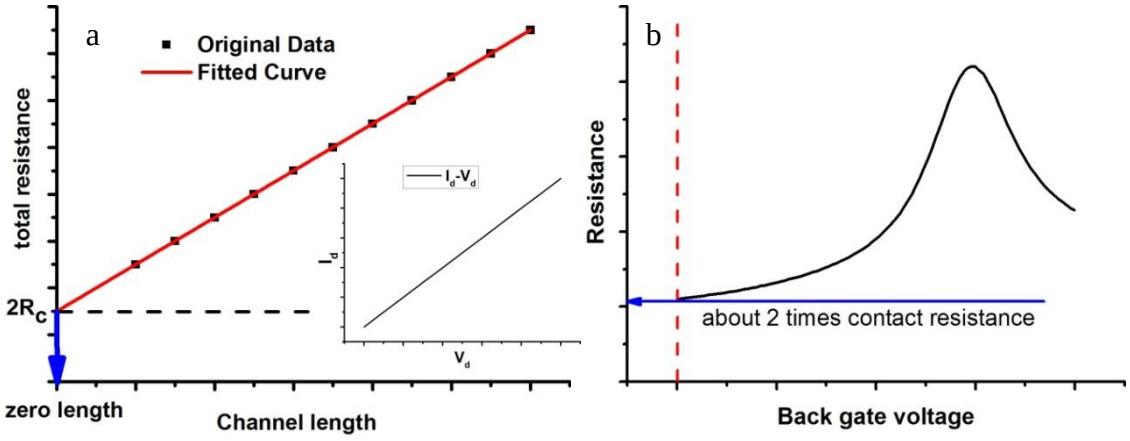

Figure 3-7. Contact resistance calculation. (a) Calculation of contact resistance with TLM method and (b) extraction of contact resistance at the high V_g region.

3.2.2 Graphene-based Sensors

Graphene has the potential to convert any physical stimulation, such as molecules physically absorbed or chemically bonded onto it into a change of an electronic signal. This change, which gives graphene a promising prospect in the application of sensing technology, can be attributed to the change of carrier concentration occurred on graphene caused by the surrounding field or those molecules performing as electron donors/acceptors. To date, graphene has therefore been considered for a variety of

sensor applications, from the measurement of the magnetic field to DNA base sequence and from monitoring the pressure applied to particular the environmental conditions (such as pH, humidity).

One of the earliest successful cases is a graphene gas sensor reported by Schedin and his co-workers, which presented a limit of nitrogen dioxide (NO_2) detection down to a single molecule absorbed onto graphene [192]. According to their report, the functionality of this gas sensor can be fully recovered by a vacuum annealing at 150 ˚C or illumination under UV for a short time after the detection of specific target substances. Compared with the detection mechanism of ammonia (NH_3), which is a donor of electrons to graphene, the mechanism of NO_2 or 2, 4-dintrotoluene detection is attributed to hole conduction, as each NO_2 molecule receives one electron from graphene. Therefore, by immobilizing specific functionalities onto the surface of graphene, the graphene gas sensor with a high selectivity for the specific substance can be achieved. A LoD of 5 ppm NO_2, NH_3 and 28 ppb 2, 4-dintrotoluene have later been reported by another group [193]. In another reference, the surface of graphene was chemically functionalised with Pd nanoparticles [194], and, this sensor was able to detect H_2 from the strong affinity between Pd and H_2 molecules.

Another break through is the fabrication of graphene-based heavy metal sensors. The detection of Pb^{2+} and Cd^{2+} by a Nafion-graphene modified electrode has been reported by Li and his co-workers, showing a LoD of 0.02 μg/L for both of them, which is a significant improvement compared with the conventional mesoporous carbon or carbon nanotube modified electrodes [195]. In parallel, Yao and his co-workers reported a graphene/sponge-based pressure sensor [196]. The mechanism of this conductive sponge-based pressure sensor is that the change of the graphene absorbed sponge leads to a macroscopic change in the conductivity under a certain pressure.

A biosensor is a device for the detection of particular biomolecules, which appear in the biological system together with other substances. Biosensors are one of the key topics of this thesis. Conventional devices designed for monitoring various parameters can be simply replaced by one graphene-based sensor to achieve the same purpose. However, the development of graphene-based sensors is still in its infancy due to the reasons below. The commercial production of large area high quality graphene has not been widely developed; chemical functionalisation always introduces defects into pristine graphene sheets, which degrade the electronic performance of graphene to some extent; the physical or chemical mechanism at the interface of graphene and target molecules, which plays an essential role in sensing devices, has not been fully understood so far.

3.3 Graphene-based Biosensors

3.3.1 Definition and Structure of a Biosensor

A biosensor is an analytical device for the detection of a specific analyte, which normally contains a biochemical receptor, an integrated physical transducer and a signal processor [197], as shown in Fig. 3-8. The biochemical receptor can be nucleic acid (DNA/RNA/base) [198], antibody/antigen [199], protein (enzymes), organelles, cells [200] or tissue, which are able to interact with the target biomolecules specifically and generate a biochemical signal simultaneously. The transducer is integrated with the biological receptor to convert the biochemical signal into another signal which can be processed or recorded, such as a FET device [42], an electrode [201], nanoparticles [202], magnetic labels or fluorescent labels [203]. The signal processor (also known as biosensor reader), which can accept a signal from the transducer and output into a readable data form, is usually custom designed to suit the specific biosensing system. The ultimate purpose of the development of a biosensor is to carry out a fast, reliable, accurate test at the point of concern where the sample was produced.

Figure 3-8 has been removed due to Copyright restrictions.

Figure 3-8. Elements of a typical biosensor. (a) biological receptor. (b) physical transducer. (c) Signal processor (biosensor reader) [204].

3.3.2 Fluorescence Biosensors

Conventional biosensing or immunoassay techniques mainly rely on the fluorescent dye labelled probes which can interact with specific molecules existing in blood or other body/non-body fluids [205]. The detection is achieved through laser excitation of fluorescent labels and capture of the fluorescent emission process, which is a slow, expensive and complicated technique. Very recently, graphene-based fluorescence biosensors have been explored and developed by Chang and his co-workers using a different principle of detection [206]. In a typical graphene-based fluorescence biosensor, graphene mainly performs as: a substrate, which can weakly bond with fluorescent dye labelled aptamer (short DNA sequence) or ssDNA due to its hydrophobic nature and π-π interactions between graphene and substances [207] and a quencher of fluorescent signals due to the fast electronic transference from fluorescent dye to graphene sheet. Therefore, when the fluorescent dye labelled probe molecules are

added into the system (weakly attached to graphene sheet), quenching of the fluorescent signal can be observed, as shown in Fig. 3-9 (a). Whilst the target molecules are added into the system, the labelled probe molecules are released from the surface of graphene due to the stronger interaction between the specific probe-target pair, which in turn restores the fluorescent signal [198, 208, 209], as shown in Fig. 3-9 (b). With this method, a detection limit of 31 pM [206] thrombin and 2.0 nM DNA [41] have been reported, respectively. It is notable this system can also be modified and used as a multi-functional device or virus sensor simply by introducing the multi fluorescence labelled DNA [208] or the specific functional groups (such as $–NH_2$) [210] onto the graphene sheet, respectively.

The major attraction of this method is the high throughput due to its fast response time and the strong signal generated; however, the probe labelled with a fluorescent dye requires pre-treatment and preparation, leading to extra cost and work. Also, to collect fluorescent signals of sufficient intensity for an accurate analysis, fluorescent biosensors are difficult to miniaturize to meet the requirement of in vitro applications.

Figure 3-9 has been removed due to Copyright restrictions.

Figure 3-9. The principle of graphene-based fluorescence biosensors [198].

3.3.3 Electrochemical Biosensors

Electrochemical biosensors are specially designed for the analysis of electroactive systems or the detection of electroactive biomolecules. In this sensing system, graphene

mainly plays a role as a conductor for receiving or donating electrons due to its high surface to volume ratio (provide more edges, defects and basal plane area) and fast electron transfer ability [211]. A typical electrochemical sensing system normally includes: a working electrode, which is functionalised with graphene (or derivatives) and specific biological probes; a counter electrode, which constitutes an electrical circuit with the working electrode; and a reference electrode, aiming to provide a constant potential during the measurement, as shown in Fig. 3-10. The basic principle is that the electroactive molecules in the electrolyte can be reduced or oxidised at different specific electronic potentials, which donate or receive electrons from the surface of the working electrode (showing redox peaks). Once the target molecules bond with probes on the surface of the working electrode, the electroactivity of the working electrode will be reduced or increased, this will either obstruct or promote electron transport, leading to the decrease or increase of those redox peaks.

The advantages of this graphene-based electrode include wide potential windows [212], electrochemical inertness in solutions [150] and good electrochemical activity. However, one of the challenges for biosensor applications is that the biological probe molecules cannot be directly bonded onto the surface of pristine graphene in most cases due to the absence of hydrophilic functionalities on graphene. In addition, only a very limited number of electroactive sites are available on the surface of pristine graphene, which limits the sensitivity of the resulting biosensor [213]. GO, graphene decorated with randomly distributed oxygen-containing functionalities on both sides of the plane, has also been widely reported as a biosensor material due to its high chemical and electrochemical activity [214] [213, 215]. However, these oxidised areas on the GO plane break the long-range conjugated network and π-electron cloud, leading to a degradation of carrier mobility and conductivity [216]. Tremendous work has so far been carried out to develop different materials with an aim to achieve the merit of high

conductivity and chemical/electrochemical activity on the same electrode [202, 217]. Among these materials, rGO is believed to be one of the best candidates due to its reasonably reduced number of functionalities [164], a large number of remaining electroactive sites [218] and structural similarity with graphene. However, the conductivity of a thick rGO layer on a normal glassy carbon electrode can never be comparable to pristine graphene [219] and deleterious chemicals are always used during rGO production [220, 221].

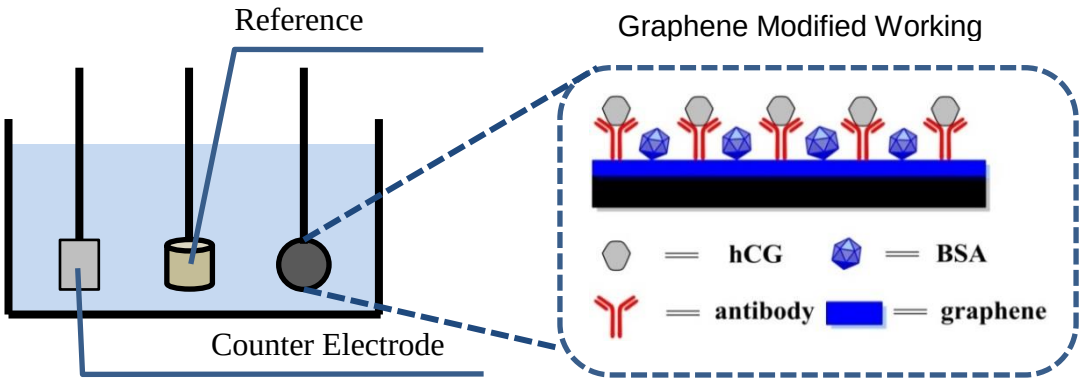

Figure 3-10. Structural diagram of electrochemical antigen biosensor.

According to the specific detection mechanisms, electrochemical biosensors can be categorised into the following types: voltammetric/amperometric biosensors which apply a sweep/constant potential to the working electrode versus the reference potential and monitors the changes of current caused by reduction/oxidation reactions on the surface of working electrode [222]. The main advantages of this method are its commercial cost and the high reproducibility. Potentiometric biosensor is designed for measuring the changes of electronic potential while there is no or negligible current. Conductometric biosensors measure the conductivity change of the sample solution as the composition of the solution keeps changing during the reduction or oxidation reactions [223]. Impedimetric biosensors (also known as Electrochemical Impedance Spectroscopy) measure the changes in resistivity or capacitance at the working electrode.

The graphene glucose sensor, which was firstly reported by Shan and his co-workers [224], is considered as the most famous and commercial electrochemical biosensor so far. Glucose was recognised and oxidised to gluconic acid by the glucose oxidase enzyme immobilised on the surface of a graphene working electrode. The resultant electron is transferred to oxygen, which is therefore reduced to H_2O_2 [225], resulting in a redox peak at -0.5 V. Using this method, a linear response from 2 to 14 mM glucose was recorded together with a good reproducibility. After that, this method has been modified and improved by a few groups using chemical reduced graphene oxide (CR-GO) [226], graphene/chitosan composite [201] and graphene/gold nanoparticle/chitosan [227]. A LoD of 0.6 μM has so far been recorded.

Graphene electrochemical DNA sensors are mainly designed for the detection of a certain DNA sequence or mutation sites in DNA molecules. One strategy for DNA mutation detection is achieved by monitoring the direct oxidation of DNA bases at different electronic potential during the electrochemical process. Zhou and his co-workers reported this CR-GO-based DNA sensor [226] in 2009. By carrying out differential pulse voltammetry (DPV) measurements with a CR-GO working electrode, four types of DNA bases, either free status or in DNA chains, can be separated at their corresponding potential. The other common strategy for DNA sequence detection is immobilizing the known ssDNA onto the surface of a graphene electrode, which is able to hybridise with its cDNA to affect the electroactivity of the electrode, in turn leading to a change in the electronic response. In addition to glucose and DNA biosensors, graphene has also been used for the detection of H_2O_2 [226], nicotinamide adenine dinucleotide [228] and heavy metal ions [195].

3.3.3.1 Cyclic Voltammetry (CV) Measurement

CV measurement is one of the most universal methods for the electrochemical analysis, which has been widely used in inorganic chemistry, organic chemistry and chemical biology [229]. A typical measurement unit is shown in Fig. 3-10. It consists of the following components: the working electrode, where the electrochemistry of interest takes place, is chemically or physically functionalised by graphene and bio-molecules. The counter electrode (also known as auxiliary electrode or assistant electrode), which is made of inert materials such glassy carbon, provides an electrical current circuit together with working electrode. The reference electrode, in this work, is an Ag/AgCl electrode, which aims to provide a stable and well-known electrode potential. The electrolyte consists of an (or a pair of) electrochemical active substance, such as 5 mM potassium ferricyanide ($K_3Fe(CN)_6$), and a supporting substance, such as 1 M potassium chloride (KCl). The triangular excitation potential sweeps from the initial point toward either positive or negative to the switch point and then returns to the initial point as the end of one cycle, as an example shown in Fig. 3-11 (a). The scan rate can be calculated from the slope. CV characteristics are determined by plotting the cycled potential applied between the working and the reference electrodes versus the current measured between the working and counter electrodes, as shown in Fig. 3-11 (b).

At the beginning of this electrochemical procedure, the potential is scanning negatively from the initial potential of 0.8 V, as indicated by the arrow. When the potential is sufficiently negative, a reaction $Fe(CN)_6^{3-} + e = Fe(CN)_6^{4-}$ starts to occur (from b to E_{pc}) until the $Fe(CN)_6^{3-}$ at the surface of electrode gets diminished (c). At the switch point, the potential starts to scan toward positive from -0.4 V. When the potential is sufficiently positive, a reaction $Fe(CN)_6^{4-} - e = Fe(CN)_6^{3-}$ starts to occur (from e to E_{pa}) until the $Fe(CN)_6^{4-}$ at the surface of electrode starts to diminish. The intensity of the

redox current reflects the electroactivity of electrode. The concentration ratio of $Fe(CN)_6^{3-}$ and $Fe(CN)_6^{4-}$ at a certain potential can be expressed as:

$$E = E°_{Fe(CN)_6^{4-},Fe(CN)_6^{3-}} + (0.059/1)log(\frac{Fe(CN)_6^{3-}}{Fe(CN)_6^{4-}}) \quad (9)$$

Where E° is formal reduction potential of the electroactive pair, which can be found in the references.

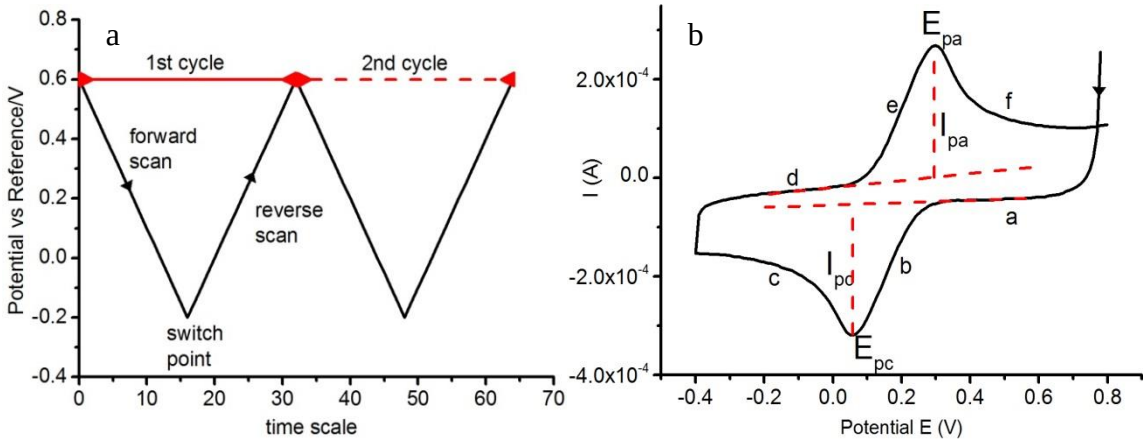

Figure 3-11. CV measurement. (a) Excitation potential of CV measurement and (b) a typical CV characteristic obtained with a scan rate of 100 mV/s and a scan range of -0.4 to 0.8 V.

3.3.3.2 Differential Pulse Voltammetry (DPV) Measurement

DPV measurement is another commonly used method for the electrochemical analysis. It can be carried out using the same components as in CV measurements and the resulting current is measured as a function of time (or potential) between the working and the reference electrodes. However, the potential applied in a DPV measurement is varied with fixed pulses of small constant amplitude. The base potential is a constant during one pulse period, but changes from one pulse to another in small steps (Step E). Constant pulse amplitude is kept throughout the whole measurement with respect to the base potential. Each current reading is determined by the current change measured

between two points, which are the one just before a pulse and the other one at the end of the same pulse, as shown in Fig. 3-12 (a). By plotting all the current readings versus their base potential accordingly, DPV characteristics can be obtained, as shown in Fig. 3-12 (b). In comparison with CV measurement, the background current, which does not change significantly between two pulses, has been subtracted; therefore, the detection sensitivity of using DPV measurement for the same substance is normally higher than that of CV measurement.

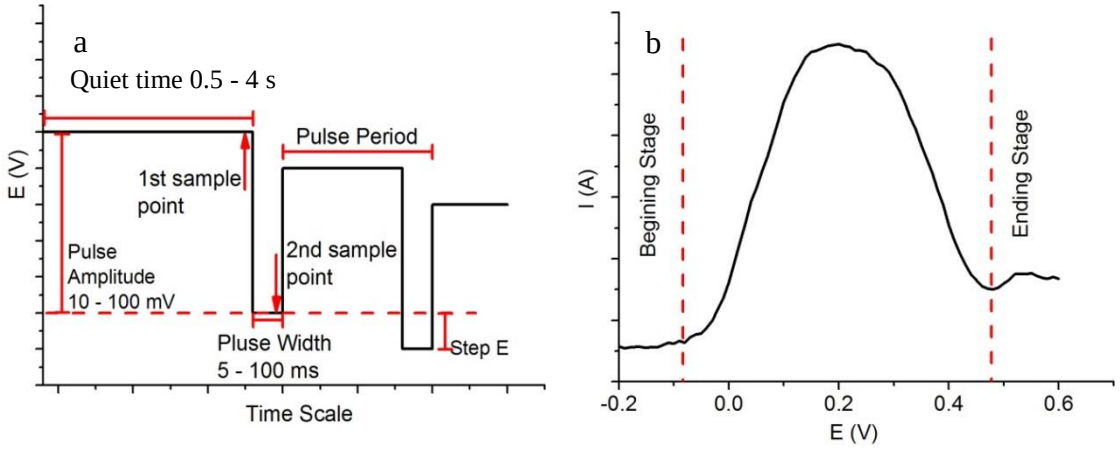

Figure 3-12. DPV measurement. (a) Excitation potential of DPV measurement and (b) a typical DPV characteristic obtained with a scan range of -0.2 to 0.6 V.

3.3.4 Field Effect Transistor-Based Biosensor

In this sensing system, graphene, as a 2D material, provides some advantages, such as high electron transfer speed, high area to volume ratio and the possibility of being chemically functionalised, which make the graphene-based FET perfect for detecting charged molecules. The surface of the graphene channel is normally pre-functionalised with the specific "bioreceptor" molecules (such as antibody, enzyme or amino acid), which enable the detection of specific target molecules. The principle of the graphene FET biosensor is that once a target molecule binds onto the conductive channel which has been pre-modified by various molecules or functional groups, a change in the

charge carrier density results, in turn leading to a change in the conductivity of the biosensor [230], as shown in Fig. 3-13. Therefore, graphene FET biosensors are capable of highly sensitive and selective detection of target analyte, such as DNA and antigen [230, 231]. As a milestone, Mohanty and his co-workers reported a graphene FET-based biosensor in 2008 [42] by oxidizing the graphene surface. DNA molecules or negatively charged bacteria can then be linked or absorbed onto the surface of the graphene via the peptide bond or Coulombian force, providing a LoD of 0.175 μg/μL for DNA and single bacterium, respectively. Following this, CVD graphene FET biosensors have been widely reported and improved for the detection of nucleotides and ssDNA with showing a resolution of a single base [232] and a limit of detection of 0.01 nmol/L [232, 233], respectively. They also found that the graphene channel can also be modified by nanoparticles or corresponding antibodies to achieve the detection of immunoglobulin G (lgG) [234], immunoglobulin E (lgE) [235] or cancer biomarkers [236].

One of the most significant breakthroughs is that the operation of a graphene FET has been achieved in solution instead of under high vacuum or atmospheric conditions. By taking the advantage of a solution top gate, the electronic characteristics of soluble biomolecules can be monitored in real time without considering the thickness of the substrate [237] or losing the activity of the biomolecules [232]. Ang and his co-workers first reported a solution top gate graphene FET pH sensor with a fast response time and low signal-noise ratio [238]. Based on his work, the detection of pH and the physical absorption of protein [231] have been achieved by the Ohno group with the electrolyte gated graphene FET, and the specific detection of immunoglobulin E protein has later been achieved by pre-immobilisation of Immunoglobulin E aptamers onto graphene [235]. Nevertheless, further investigation of the effects on electronic performance from the solid/liquid interface and the liquid gate is still required.

In parallel to the development of the detection in liquid, detection in a living cell has also been carried out very recently. Cohen-Karni reported that a graphene FET, which is combined with both graphene and a silicon nanowire and interfaced to an electrogenic cell [239], could record conductance signals from spontaneously beating embryonic chicken cardiomyocytes with a signal to noise ratio >4. Furthermore, they found the peak to peak width shows a positive correlation with the area of the graphene FET, indicating that the data measured is averaged from many points across the interfaced cell membrane. In the following work, Hess and his co-worker developed a technique for action potential detection by coating living HL-1 cells (electrogenic cells) onto FET arrays fabricated with large area CVD graphene [240]. A similar high signal to noise ratio together with large transconductive sensitivity presents a promising future for graphene FET-based biosensors.

Figure 3-13 has been removed due to Copyright restrictions.

Figure 3-13. Label-free biosensing for bacterium attachment and DNA hybridisation using FET-based platform. After the binding of (a) bacterium, (b) ssDNA and dsDNA, graphene conductivity increases. Inset 1-4 in (a): A LIVE/DEAD test conducted on GA or electrode. Inset in (b): fluorescence analysis of dsDNA attached on graphene using confocal microscopy, W is wrinkles [42].

3.3.5 Sensing Parameters

Sensitivity: It refers to the change of the output signals when measuring a certain change of the substance concentration. The sensitivity of steady calibration is determined by plotting steady values versus C or log (C/C°), where C is the concentration of the substance and C° refers to a reference concentration. Similarly, the sensitivity of transient calibration is determined by plotting (d_{value}/d_t) versus C or log (C/C°), where d_{value} is the change of output signal within a time period of d_t. In both of these cases, the sensitivity needs to be calculated within the linear range of the characteristic curve. It is also notable that the sensitivity, which is based on the measured value, differs from the LoD, which takes the noise in the signal into account and is calculated from the fitted curve.

LoD: It relates to the difficulty to precisely measure a certain analyte with a concentration close to zero. The adequate amount of analyte has to be provided to produce a signal which can be distinguished from the noise signal in zero concentration samples. LoD is the minimum quantity of substance or the lowest concentration of substance likely to lead to a reliable signal change at which detection is feasible [241]. The most common method of LoD estimation is known as:

$$\text{LoD} = \text{the mean value} + \text{nSD} \tag{10}$$

As shown in Fig. 3-14, where the mean value and standard deviation (SD) are calculated from repeating measurements of blank sample and n is normally > 2 or even > 10 to provide a more conservative value.

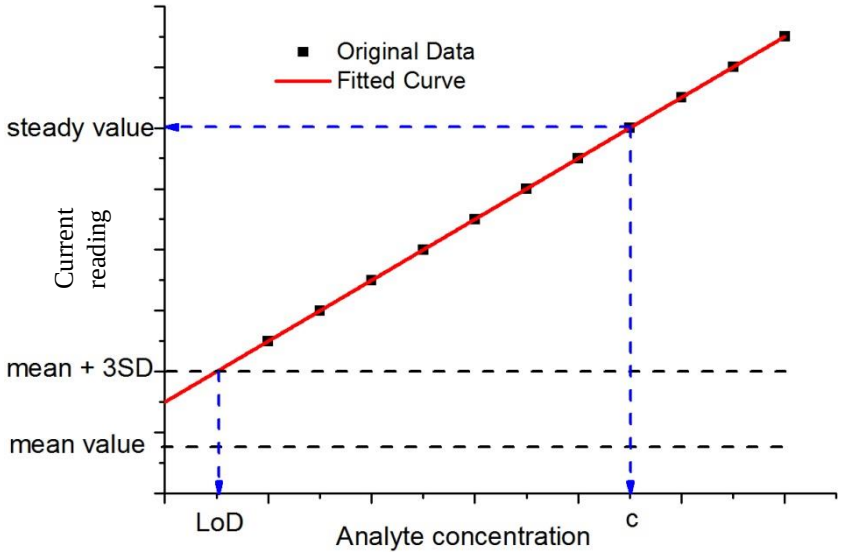

Figure 3-14. Diagram illustration of LoD and sensitivity.

Selectivity: it is the ability to distinguish a specific target analyte from a mixed media or solution. This is the key characteristic of a biosensor and achieved by using complementary DNA chains, antigen-antibody pairs or specific protein-target cells. Two major methods have so far been proposed for the determination of biosensor selectivity. The first method is achieved by separately measuring the target substance against the interfering substance under the same experimental conditions. Then, selectivity is defined as the ratio of the signal generated from the target substance alone and the one from that interfering substance alone at the same concentration with the target substance. The second method is carried out by adding a certain interfering substance with an expected concentration into the solution of the target substance with a medium concentration. Then, the selectivity is defined as the change percentage of the biosensor response compared with the solution of the sole target substance.

Response Time: it is defined as the necessary time to reach 90% of the steady state response [242]. There are three major factors affecting the response time: the transport rate of the analyte through different layers of the electrode or in the electrolyte; the

activity of the biological recognition pair, such as the activity of the antigen towards its antibody and the mixture of state/conditions of the sample into the measurement unit.

Reproducibility (stability of signal, also known as precision): reproducibility refers to the signal shifts or scatters between a series of individual continuously cyclic measurements with the constant conditions, which are within the usable range of this sensor. The reproducibility is normally evaluated by SD, which are expressed as:

$$\sigma = \sqrt{\left(\frac{1}{N}\right) \sum_{i=1}^{N} (x_i - \mu)^2} \tag{11}$$

Where mean value $\mu = (1/N) \sum_{i=0}^{N} x_i$, or can be evaluated by the relative standard deviation (RSD), which is expressed as:

$$c_v = \sigma/\mu \tag{12}$$

Where σ is SD and μ is the mean value calculated above.

3.3.6 Conclusion

A number of different chemical reactions for graphene functionalisation, including both covalent and non-covalent methods, have been presented. The detailed functionalisation mechanisms have been discussed together with their advantage and disadvantage for the fabrication of graphene-based biosensors. By taking advantage of the outstanding properties of graphene, various graphene-based applications have thus been pioneered and developed. In this section, the most commonly developed types of graphene biosensors have been reviewed. The comparisons of their structures, detection mechanisms, applications are also carried out. Fluorescence biosensors provide a fast response time and a strong signal output; hence, high throughput can be achieved. However, the extra work on labelling the probe molecules and the difficulty in the miniaturisation of the device slows down the development of this biosensor.

Electrochemical biosensors provide a commercial way for the detection of electroactive molecules with high reproducibility, but its compatibility with current industry needs to be further developed. FET-based biosensors present an electronic performance, good compatibility with current semiconductor industry and low commercial cost, therefore, it has been believed to be the most promising biosensor.

Although some impressive progress has been made, none of the current techniques of graphene biosensor fabrication can meet the requirement of industrial-scale production at present. The major obstacle is the inhomogeneous nature of graphene obtained by different methods, such as the number of layers and the defect density, which will cause heterogeneity of the measurement baseline from device to device. Therefore, the production of large area, high quality graphene is urgently required for the further development of graphene-based biosensors. Besides, most of the reported sensing techniques are carried out in ideal media instead of the real clinical samples, such as blood, urine, tissue, and thus, the practical biosensor needs to be explored. The possible challenges of graphene-based biosensors can also be the improvement of the sensitivity and LoD, selectivity, response time and the repeatability of detection along with the commercial cost.

Chapter 4 Experimental Techniques

4.1 Techniques in Graphene Production with Sputtered Materials

4.1.1 Sputtering Deposition

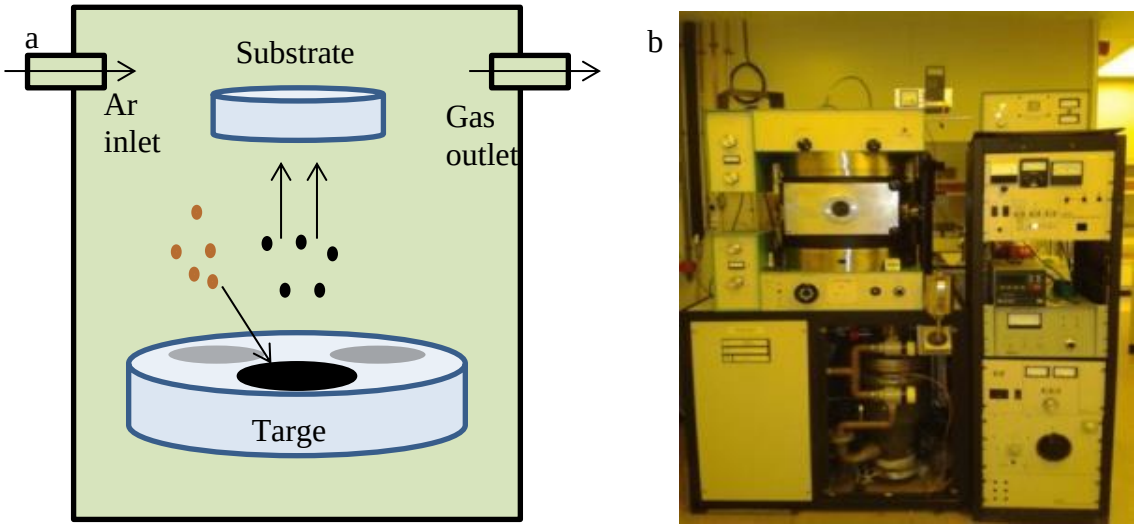

Figure 4-1. Sputtering deposition unit. (a) Schematic of conventional sputtering coating technique and (b) an optical image of the three targets 8'' sputtering machine.

The sputtering machine is one of the major tools used for the precise deposition of thin films in semiconductor industries. The required base pressure is set to be < 5 x 10-7 Torr in this work. 20 mins plasma cleaning for each target and 3 mins plasma cleaning for the substrate are carried out to remove the contaminant or oxide on their surfaces. Then, the chamber need to be pumped down again to the required base pressure waiting for material deposition. Liquid nitrogen is used for the cooling of the diffusion pump. The material targets have a typical purity of >99.99%.

During the sputtering process, the target is bombarded by the energetic atoms (either Ar or N ions in this project). After the momentum exchange between ions and target atoms, atoms from the surface of the target are ejected towards the substrate surface as the

collision energy is much higher than the binding energy between target atoms, as shown in Fig. 4-1. For materials such as carbon, Ni, SiC, an Ar pressure of 3-3.5 mTorr and a discharge power of 300 W has been proven to be optimal; whilst an Ar pressure of 4 mTorr and a discharge power of 200 W were chosen for Au, Ag and Cr deposition. Most of the atoms of the target materials deposit onto the substrate via relatively straight trajectories, however, Au atoms sputter with more random trajectories, which causes difficulties in the later lift-off process. In all cases, water cooling to the substrate holder is applied throughout the deposition process to help prevent the overheating of resist on substrate (see lithograpy process in 4.2.2), as this may cause hardening of the lift-off resist at the substrate surface and also helps to minimise the damage from the impact of local high temperature particles in the plasma.

4.1.2 Rapid Thermal Annealing

The RTP can be carried out either in the vacuum chamber of sputtering machine or in the commercial RTP unit. The details of heating and cooling curves of both systems are shown in Fig. 4-2 (a). For the RTP carried out in the same vacuum chamber as the sputtering deposition, a homemade heating component containing two 500 W halogen lamps is employed. Oxidation of the metal film and graphene grown at high temperature is minimised as there is no atmospheric oxygen introduced during this process. For the RTP carried out in the commercial rapid thermal processor, not only a faster and more controllable heating rate up to 100 °C/s but also a rapid cooling capability is achievable due to its eleven 1.5 kW halogen lamps and a cold chamber wall design, respectively. In both cases, the temperature of the sample was monitored by a thermal-couple installed on the back of the substrate holder (a highly doped SiO2 wafer) and to avoid the oxidation of graphene during and after graphene growth at high temperature, high purity Ar was introduced into the chamber as protective gas at least one hour before and throughout the whole RTP. Also, to obtain good quality graphene, the samples needed

to be annealed immediately after the deposition of the metal materials, because the surface oxidation and adsorption has negative effects on the growth of the graphene. In both systems, no significant difference in the quality of graphene was found, when all other parameters were kept constant and no oxidation occurred. 120 s annealing time was applied to all samples in this work so that the effects caused by the different temperatures of annealing could be investigated.

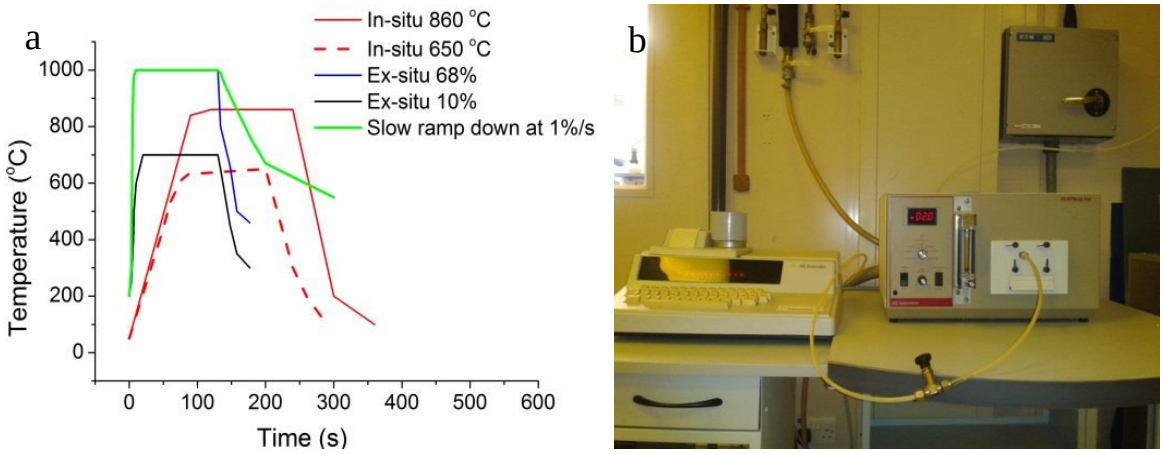

Figure 4-2. Rapid thermal processor. (a) Typical heating and cooling curves of the RTP in sputtering machine and commercial thermal processor, green curve overlapped with the blue one from 0-120 s. (b) Optical image of the ex-situ RTP unit.

4.1.3 Etching of Metal Film

The metal layer, such as Cu or Ni, together with their soluble salt that was produced during the RTP on the samples can be etched away by immersion into 1:3 HCl aqueous solutions. Too strong a solution of HCl would generate many bubbles during the etching, which cause damage to the graphene or even lifts off the graphene from the substrate; whilst over diluted HCl requires a much longer etching time. This etching time varies from 1h to overnight depending on the thickness of the metal layer. After HCl etching, the samples were gently rinsed with deionised (DI) water three times, followed by an

oven bake at 110 °C for 20 mins to remove the HCl residues and the water absorbed by graphene.

4.2 Techniques in Production of Exfoliated Graphene

4.2.1 Blocking of Surficial hydroxyl Groups

The surface of the SiO_2 wafer is normally terminated with hydroxyl groups, which is hydrophilic, due to its production techniques and the storage conditions. This hydrophilic surface has a strong interaction with water adsorbed from the air, which leads to poor adhesion when the photoresist is spun onto it, in turn leading to a failure later in the lithographic process. To increase the adhesion between the photoresist and the substrate, two methods for removing and blocking of the surficial hydroxyl groups have been explored.

4.2.1.1 Plasma Etching

The SiO_2 wafer is loaded into the vacuum chamber of the sputtering machine and pumped for 2 hours to get rid of gaseous absorbent and water on the surface of the substrate. Then, a 3 mins plasma etch is carried out using a discharge power of 50 W and an Ar pressure of 3-3.5 mTorr to remove the surficial hydroxyl groups, as described in 4.1.1. The etching rate of SiO_2 here is less than 0.2 nm/min and thus no significant effects can be introduced to the optical identification of graphene on such wafers described in 4.7.1. After plasma cleaning, the wafer can be kept in the vacuum chamber until shortly before the next process to minimise contamination prior to graphene transfer.

4.2.1.2 Hexamethyldisilazane Blocking

Hexamethyldisilazane (HMDS) is a common primer used for increasing the adhesion between the SiO_2 wafer and the photoresist. To block the surficial hydroxyl groups, the

SiO_2 wafer is sealed in a stainless steel container with 3 drops of HMDS and heated up to 120 °C for 2 hrs. During this process, a very thin layer of $Si(CH_3)_3$ is chemically bonded with the hydrophilic surface, turning it to a hydrophobic surface [243, 244] which the photoresist can more readily stick onto. The wafer is then thoroughly rinsed with 99.99% purity ethanol and blown dried with N_2. No negative effects have been found for the optical identification of graphene on this type of wafer. The blocking mechanism is shown in Fig. 4-3. It is important to note that HMDS cannot be spin-coated as using this method the HMDS would be too thick. In this case, the ammonia on the surface of the wafer can diffuse into the photoresist spun on it, leading to the crosslink between the photoresist molecules and, in turn, resulting in the potential failure in later lithographic processes.

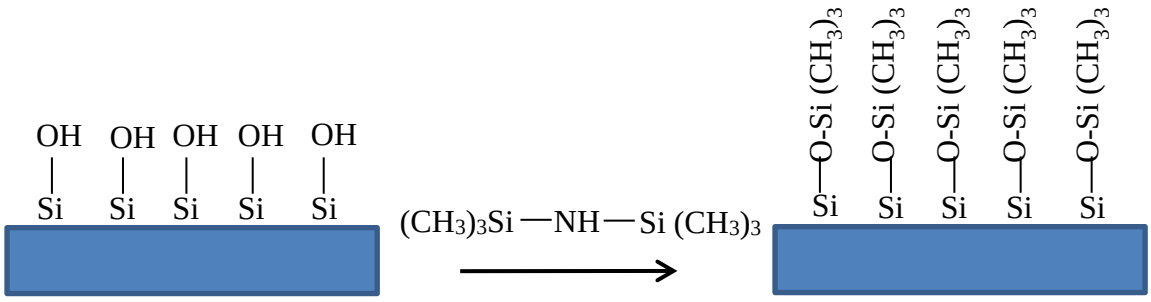

Figure 4-3. The schematic reaction between surficial hydroxyl groups and HMDS.

4.2.2 Mask Aligner and Photolithography

Photolithographic techniques using a mask aligner have been commonly used to create the micrometre-sized structures in the semiconductor industry for many years. In this project, all the patterns on the SiO_2 substrate were created using these techniques.

As 1.5 x 1.5 cm substrates are used in this work, a 4-inch SiO_2 wafer must firstly be diced into these sizes. A diamond tipped pen is used to scribe the backside of the wafer into 1.5 cm squares and then the wafer is turned over onto a flexible surface where

pressure is applied with a metal ruler to break the wafer into separate substrates. To remove the particles resulted from the dicing process and other contaminates physically attached to the SiO_2 substrate surface, the substrates are cleaned for 15 mins in warm acetone in an ultrasonic bath. This is followed by a further 10 mins in isopropyl alcohol (IPA) and 10 mins in DI water. As acetone cleaning always leaves residues on the substrate after it gets dried, following IPA and DI water cleaning steps have been found necessary in avoiding the acetone residues remaining. Finally, the substrates are dried using a nitrogen gun and baked in the oven at 110 °C for 1 h to remove any residual water that may remain on its surface (this procedure is referred as the standard cleaning in this thesis).

After drying, a uniform layer of photoresist is spin-coated onto the polished side of SiO_2 substrate using a speed of 3000 rpm for 20-30 s, as shown in Fig. 4-4 (b). One minute pre-baking of the resulting substrate is carried out at 100 °C on the hot plate to solidify the photoresist by removing its solvents. To pattern the resist, the substrate is exposed to UV on the mask aligner for 5 s or 10 s for photoresist 1805 or 1813, respectively, as shown in Fig. 4-4 (c). Next, the substrate is immersed in the photoresist developer for about 25 s and rinsed with DI water for 30 s to produce the pattern, as shown in Fig. 4-4 (d). Post-baking at 110 °C for 30 mins is required to completely dry the water on the surface of the substrate. After sputtering deposition, as shown in Fig. 4-4 (e), the substrate is cleaned in the ultrasonic bath with photoresist remover and then rinsed with DI water so that the sacrificial layer can be completely peeled off, leaving the required pattern, shown in Fig. 4-4 (f).

The chemical principle here is: UV exposure leads to denaturation of the photoresist and the denatured positive photoresist can be dissolved and washed away in the photoresist developer, exposing the SiO_2 substrate where the metal film will deposit. The indentured positive photoresist is dissolved in the photoresist remover so that the metal

film on top of the photo resist can be peeled off. As UV is a hazard, proper eye protection is required.

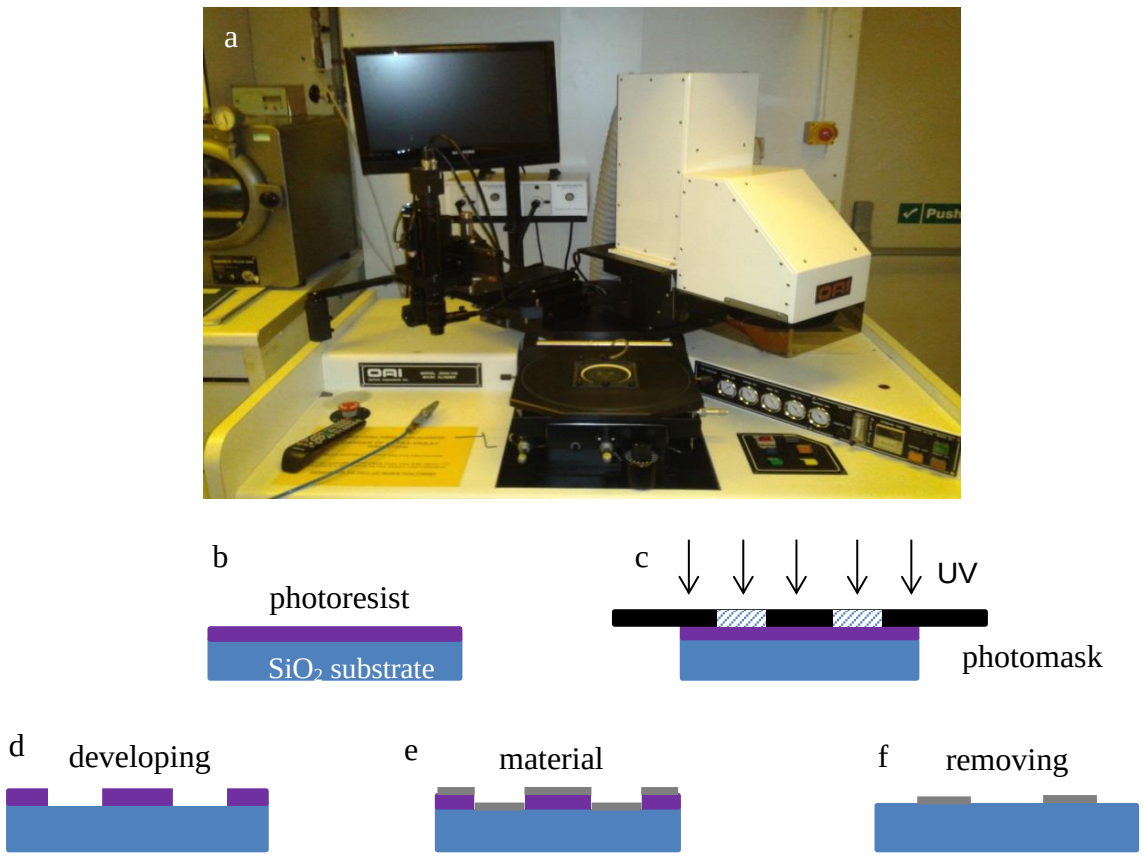

Figure 4-4. Mask aligner in lithography technique. (a) Optical image of the mask aligner and (b-f) schematic of photolithography and lift-off process in Cleanroom.

4.2.2.1 Photomask Design

Photomasks for the fabrication of graphene devices are home designed with L-Edit. Fig. 4-5 (a) shows the mask designed for the fabrication of exfoliated graphene devices, which contains one numeral-marker square for substrate mapping and three four-probe device squares with the different channel length of 5, 10 and 15 µm, as indicated by the numbers. Fig. 4-5 (a1) and (a2) presents the central area of one device pattern with a channel length of 5 µm and the dimension of one number for substrate mapping, respectively. Fig. 4-5 (b) shows the mask for the fabrication of CVD graphene devices, which consist of four squares for substrate mapping, channel shaping, contact

deposition and window opening. Fig. 4-5 (b1) and (b2) shows the zoom-in patterns for graphene channel shaping and contact deposition. The minimum feature for all the patterns is 2 µm. The photomasks are manufactured on 4'' soda lime glass using Cr as a UV blocking material by Compugraphics International Ltd, UK.

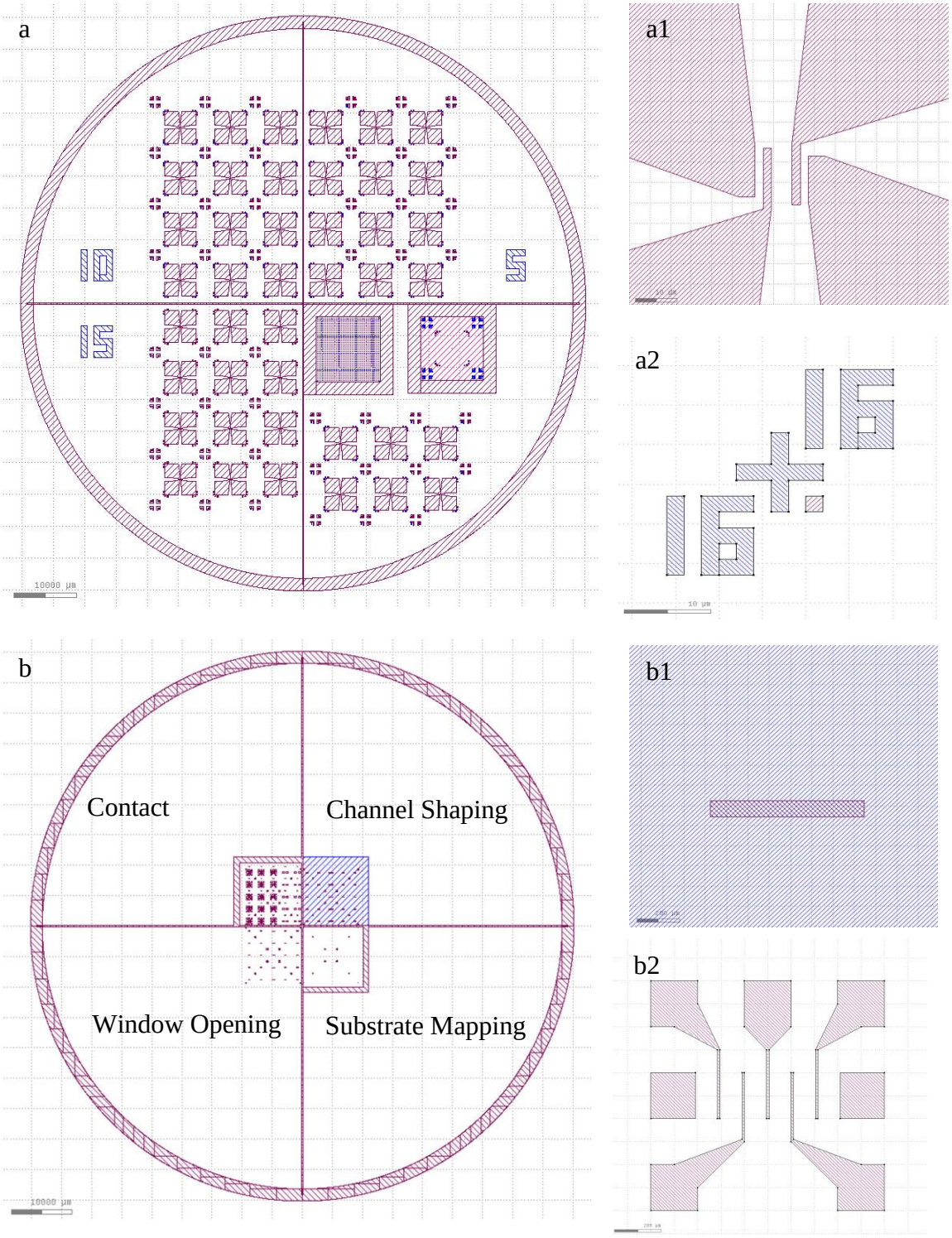

Figure 4-5. A home designed photomask for device fabrication. (a) For exfoliated graphene devices and (b) CVD graphene devices.

4.2.3 Substrate Mapping

Due to the requirements of graphene identification with an optical microscope [245], exfoliated graphene is normally produced on the doped silicon substrate with 300 nm SiO_2 atop (known as SiO_2 substrate in this thesis). However, the exfoliated graphene has an area up to a few hundred micrometres, which is difficult to be recognised on SiO_2 substrate. To locate the exfoliated graphene, the SiO_2 substrate needs to be mapped with the unique numbers throughout its whole surface before transferring exfoliated graphene onto it.

The number-marker square on the photomask designed for substrate mapping is shown in Fig. 4-5 (a), which consists of 400 numbers within 1 x 1 cm (20 rows x 20 columns). Conventional photolithograph and sputtering deposition, as introduced in 4.1.1 and 4.2.2, are carried out to create the numbers with 50 nm Ni (or 30 nm Cu). Afterwards, the chemical cleaned substrates are subjected to a plasma cleaning process in the sputtering machine, which helps to thoroughly remove the potential contamination and enhance the adhesion between the graphene film and the SiO_2 substrate. Plasma cleaning lasts 3 mins at 50 W with an Ar pressure of 3-3.5 mTorr, after which the substrates are kept in the vacuum chamber before transferring graphene onto it.

4.2.4 Mechanical Cleavage

One piece of shiny flat highly oriented pyrolytic graphite (HOPG) is put onto Scotch tape (3 cm x 10 cm) and gently pressed with the back of tweezer to make sure the large flat area of HOPG is attached tightly onto the tape. The major bulk of the graphite is peeled off, leaving a thin graphite layer on the tape. This piece of graphite is subjected

to repeatedly folding and splitting to achieve increasingly thinner pieces until most of the Scotch tape is covered by graphite flakes. To thin the graphite flakes further, the second piece of Scotch tape is attached to the first one, then repeat the mechanical cleavage above. It is important to use a different area of the tape for each peeling action so that each action is effective and there is sufficient area covered by graphite/graphene. In addition, the initial graphite bulk should have a big flat surface instead of uneven one to provide a better chance of producing a larger graphene film.

4.2.5 Transfer of Exfoliated Graphene

A piece of plasma cleaned SiO_2 substrate is taken out of the vacuum chamber, one at a time, and placed onto the tape where there is a matt finish. The exfoliated graphene on tape is pressed onto the polished side of the SiO_2 substrate. After 3-5 hours in contact with the substrate, the tape is pulled off carefully and the substrate is sent back into the vacuum chamber in case of impurity adsorption. The transferred graphene on SiO_2 substrate can then be characterised by an optical microscope, Raman spectroscopy and AFM. Here, it has been found that using a thermal annealing procedure before pulling off the tape produces larger size graphene and enhances the adhesion between the graphene and the substrate, however, this procedure results in more glue residues on graphene and SiO_2 substrate, which cannot be easily removed.

4.3 Processing of CVD Graphene

4.3.1 Transfer of CVD Graphene

The wet transfer procedure of CVD graphene is shown in Fig. 4-6. The commercial CVD graphene grown on both sides of Cu foil purchased from Graphene Supermarket (ltd) was firstly cut into the required size. Then, a layer of PMMA with a thickness about 500 nm was spin-coated (about 1000 rpm) onto one side of the Cu foil to ensure

the graphene film was visible during the transfer procedure in solution and also to protect the potential damage from HNO_3 and mechanical transfer. Graphene grown on the other side of Cu foil was etched away by immersing this one-side PMMA-coated sample into 10% HNO_3 aqueous solution for 2 mins and then the sample was thoroughly rinsed with DI water to remove the HNO_3 residue. By immersing this sample into 0.1 M ammonium persulfate ($(NH_4)_2S_2O_8$) aqueous solution (or 0.7 mol/L iron nitride) for 12 hours, the supporting Cu foil was completely dissolved, resulting in a visible graphene/PMMA film floating on the surface of etchant solution. Then, the graphene/PMMA film was gently rinsed with DI water to remove the etchant residue. One piece of plasma pre-cleaned SiO_2 substrate (or arbitrary substrate) was chosen to carefully pick up this graphene/PMMA film from DI water with the assistance of a fine needle. The graphene/PMMA film on SiO_2 substrate was dried with a nitrogen gun and then subjected to an annealing process at 220 °C for 5 mins to promote a stronger interaction between the graphene and SiO_2 substrate. This sample was then immersed into warm acetone (about 60 °C) for about 30 mins to remove PMMA layer and then sequentially rinsed with isopropanol and DI water to remove acetone residues. The N_2 gun was used again with a small flow rate to dry the water. The dried graphene samples were kept in the vacuum chamber at room temperature to prevent the absorption of air.

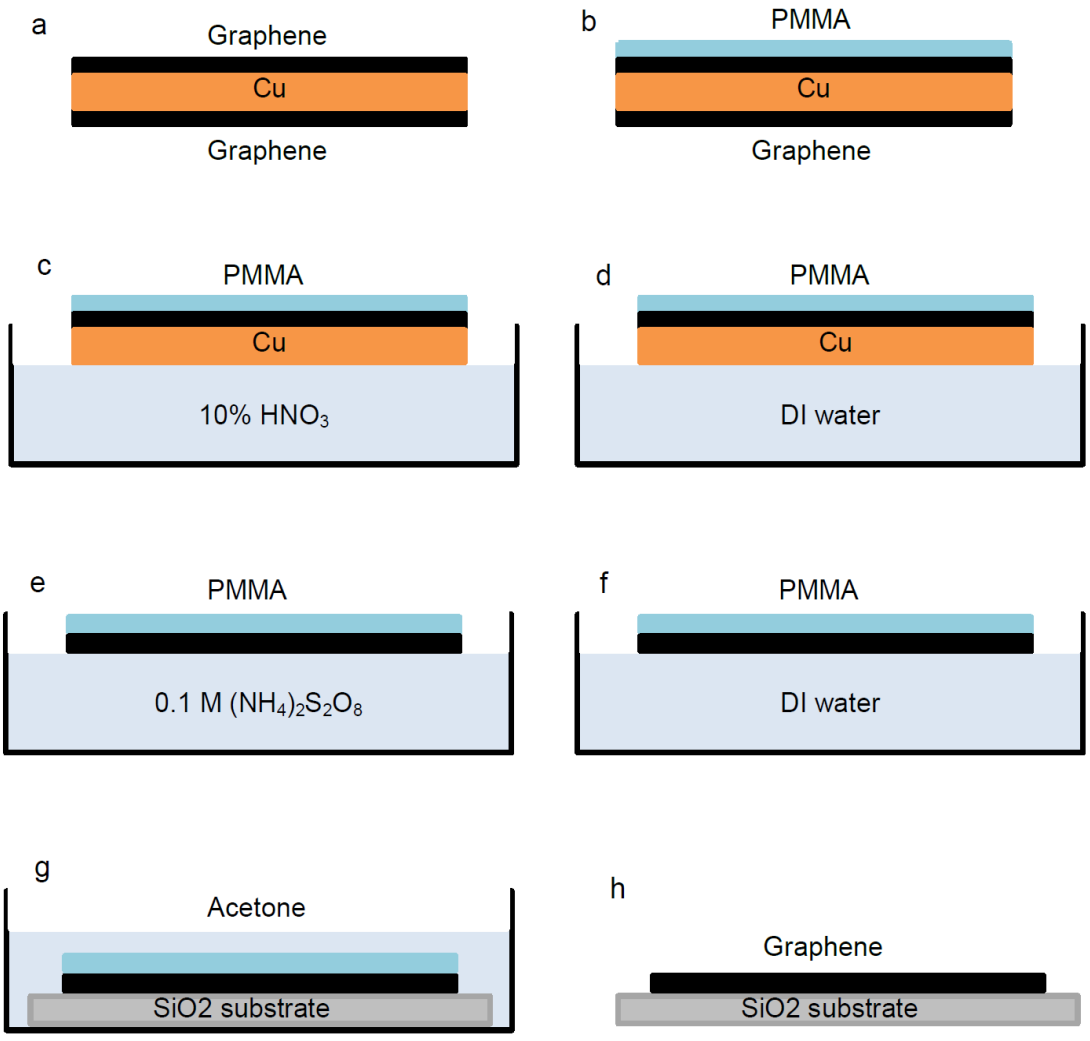

Figure 4-6. Schematic of wet transfer procedure of CVD graphene.

4.3.2 Novel Graphene Shaping Technique using Ion-milling Etching

Instead of using an oxygen plasma asher, in this work, a modified etching method using an ion-miller has been achieved for the patterning of CVD graphene. Graphene on SiO_2 substrate was successively spin-coated by 500 nm lift-off resist (LoR) and followed by post-baking at 175°C for 5 mins. The sample was then spin-coated by another layer of photoresist with the same thickness. The key step of using modified ion-milling method for the graphene patterning is to bake the sample at 180°C for about 1 h under a deep UV exposure, which helps with the removal of the photoresist after ion-milling. The discharge power and current were optimised to 100 W and 30 mA respectively. To

further prevent the photoresist crosslinking and ensure its removal, the 100 s milling time was split into five multi-stages with 1 min cooling between each two stages. Then, standard lithography as previously described in 4.2.2 was used for the formation of the electrodes. Water cooling and a thermal conducting shim between the substrate and its holder were also found to be essential to achieve successful fabrication.

4.4 Techniques in Graphene Devices Fabrication

4.4.1 Modified Photolithography and Lift-off

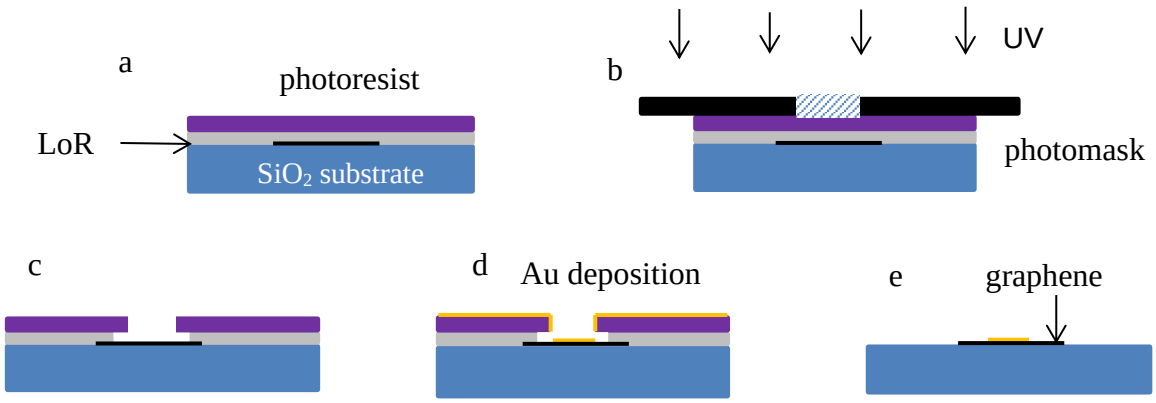

Figure 4-7. Schematic of modified photolithography and lift-off process.

To produce successful graphene transistors, Au contacts need to be patterned on graphene without causing any significant damage to the graphene. However, the ultrasonic bath used in the conventional lift-off process removes not only the unwanted metal film but also the graphene layer. To overcome this problem a modified lithography and lift-off process together with a novel sputtering deposition (introduced in 4.4.2) was developed for the fabrication of Au contacts on graphene.

After the standard cleaning process, the samples were kept in the vacuum chamber of the sputtering machine for 1 hour to get rid of gaseous and water absorbents on the surface of graphene. A SiO_2 substrate is spin-coated with LoR at 3000 rpm for 30 s with a resulting thickness of 0.5 μm and then placed in a fan oven to dry at 175 °C for 5 mins.

After it cools down to room temperature, the substrate is spin-coated with a layer of photoresist at 3000 rpm for 30 s to create a sandwich structure (0.5 μm thick), as shown in Fig. 4-7 (a). Then exposure using UV (Fig. 4-7 (b)), followed by the developing process (Fig. 4-7 (c)) are carried out as described earlier in 4.2.2. Because the dissolution rate of LoR in photoresist developer is slightly faster than that of photoresist, undercuts in the photoresist are created after the developing process. This helps to avoid the physical connection between the Au film on photoresist and the Au film on the substrate occurring during sputtering, which prevents the Au on photoresist from remaining on the substrate after lift-off process. The undercut distance is about 0.2 μm after developing, which is not only able to overcome difficulties in removing the unwanted Au film, but also helpful to achieve better-defined contact edges.

4.4.2 Novel Method for Sputtering Deposition of Au Contacts on Graphene

4.4.2.1 Shielding Tube Production

The novel sputtering deposition of the Au contacts was performed using a shielding tube as shown in Fig. 4-8 to prevent deposition of the Au atoms onto the sidewall of the photoresist edges. The shielding tube is home designed and produced using aluminium in local workshop. As the diagonal size of individual graphene FET is 7 mm, the inner diameter of the protective aluminium tube is designed to be 14 mm to ensure that the contact pattern can be fully covered by sputtered Au. The height of this aluminium tube is 20 mm and it is clipped on top of the Si substrate during the deposition process. In this case, although the sputtered Au atoms deposit through trajectories toward substrate, only a small portion of ejected atoms can go through the metal tube, the deposition rate is much slower than that without using the shielding tube.

4.4.2.2 Deposition Parameter Control

Au with a thickness of 30–50 nm was sputtered onto graphene as the contact material. A 2 x 10^{-7} Torr base vacuum and 4–20 mTorr Ar pressures were chosen depending on the particular samples. Water cooling was applied to the back of the substrate throughout the deposition process. The finished device has four Au contacts designed to align with four contact probes during testing. These have an overall size of 5 × 5 mm and a 2 μm graphene channel length which was chosen for all devices measured in this section.

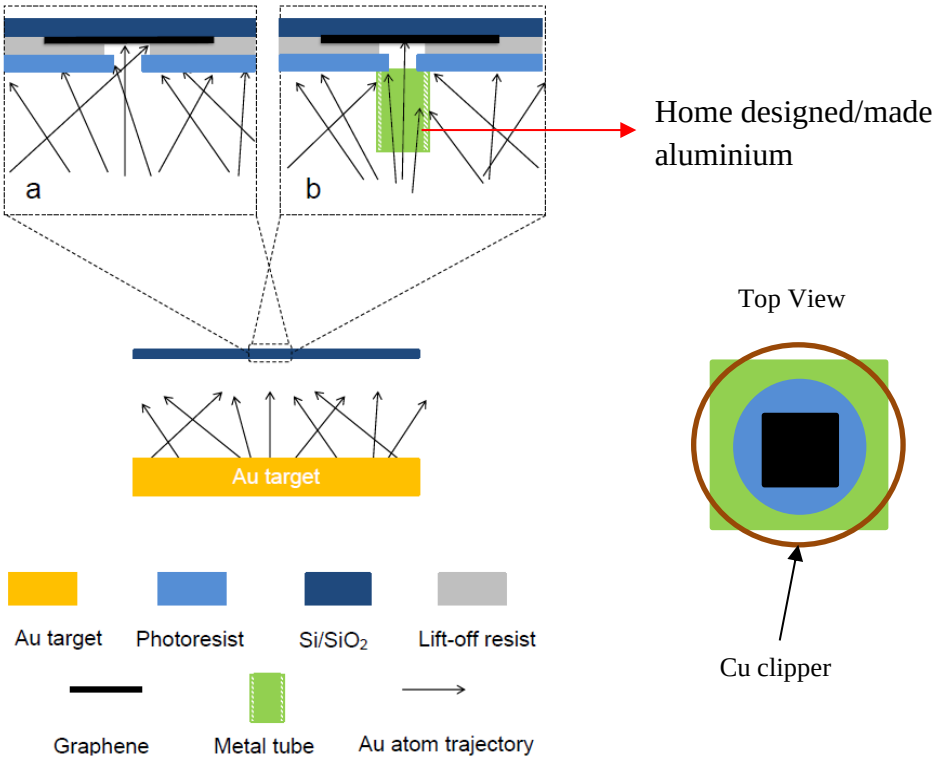

Figure 4-8. Schematic illustration of (a) conventional and (b) novel sputtering deposition. The dimension of green metal tube is 14 mm inner diameter and 20 mm height.

4.4.3 Post-cleaning Procedures

A post-cleaning procedure without ultra-sonication (in warm acetone for 1-2 h, in IPA for 1 h and DI water for 30 mins successively) was found to be essential to minimise the

negative effects from the polymer residues remaining on graphene channel after the fabrication. This process is referred as the standard post-cleaning in this project.

In addition, another two methods of post-cleaning were developed, which are: thermal annealing in Ar in a separated atmospheric chamber at 300 °C and thermal annealing in the vacuum chamber of the sputtering machine with a home-designed filament.

4.4.4 Contacts Formation with Thermal Evaporator

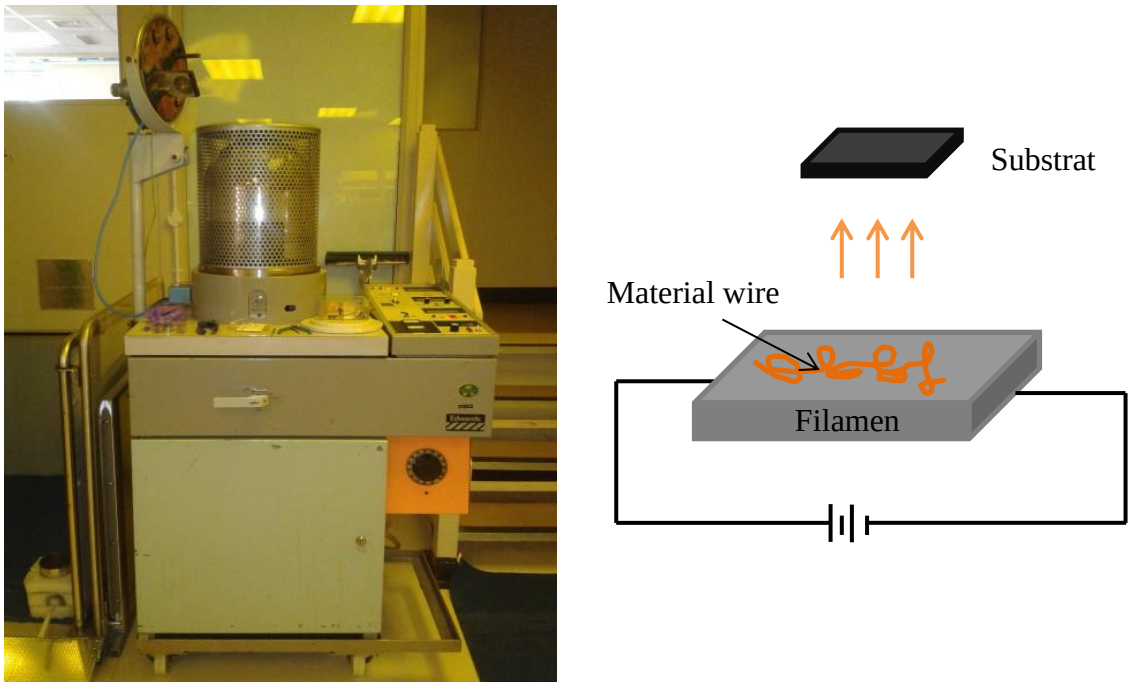

Figure 4-9. Thermal evaporator. (a) Optical image and (b) Schematic illustration of Edward's thermal evaporator.

To evaluate the effects on the structural and electronic performance of graphene FETs introduced by sputtered Au contacts, an Edwards 306 thermal evaporator was used to deposit the Au contacts on the graphene channel and the results compared in Chapter 6. Here, evaporation is achieved by tuning the voltage applied between two terminals of a tungsten boat holder containing Au. Once the Au has melted and evaporated, the metal vapour rises and deposits onto the surface of the substrate. It is worth noting that the

adhesion between the evaporated material and substrate is less than that between sputtered material and substrate.

4.5 Techniques for Functionalisation of Graphene Surface

4.5.1 Hydroxylation of Graphene Channel

4.5.1.1 Fenton Reaction

Hydroxylation of graphene can be achieved through the Fenton Reaction [168, 246], as introduced in 3.1.1. The catalyst of this reaction, which is 0.025 g $FeSO_4 \cdot 7H_2O$, is incrementally added into 20 ml of 30% H_2O_2 in a glass beaker. Graphene powder is then added into the solution for 30 mins. The pH value is maintained at 4-5 to avoid the precipitation of iron(III) oxide-hydroxide ($Fe(OH)_3$), which will lead to the decomposition of H_2O_2 with a by-product of O_2. Modest shaking is applied in case of the local overheating and the splash of chemicals as the Fenton Reaction is highly exothermic. After the reaction, hydroxylated graphene is collected by 10 mins centrifugation at a speed of 5000 rpm and rinsed thoroughly with DI water to remove salt residues. The Fenton reaction shows a high hydroxylation rate towards the modification of graphene powder. However, it cannot be used for the modification of graphene FET due to the harsh nature and a large amount of gas generated, which could damage both the graphene channel and the Au contacts on top of it.

4.5.1.2 Hydroxylation with Potassium Permanganate

To overcome the disadvantage of the Fenton reaction, hydroxylation of graphene with $KMnO_4$ has been developed. A 0.2 M $KMnO_4$ solution is prepared with a balanced pH value of 10. Graphene powder or a graphene FET is immersed into this solution for 4 h at 4 °C, followed by thorough DI water rinsing to remove $KMnO_4$ residues.

4.5.2 Modification with Graphene/rGO Dual-layer

GO aqueous solution, which contains >80% monolayer GO with an overall concentration of 0.5 mg/ml, was produced by Hummer's method as introduced in 3.1.1. A 3 mm diameter electrode modified with screen-printed graphene powder was chosen as the working electrode. To figure out the optimal GO concentration for the fabrication of a graphene/rGO electrode, GO was diluted to 0.05 mg/ml, 0.1 mg/ml, 0.15 mg/ml, 0.2 mg/ml, 0.25 mg/ml and 0.3 mg/ml by adding DI water and then carefully drop-casted onto the surface of the graphene modified electrodes with a volume of 20 ml respectively. The electrodes were dried at room temperature for 1 h to promote strong π-π interaction with graphene underneath. An Ag/AgCl and a carbon electrode were selected as the reference and the counter electrodes respectively. The electrochemical reduction of GO was achieved by a CV cycle in 10 mM $K_3Fe(CN)_6$ and 1 M KCl solution with an applied potential of 0.5 to -1.5 V and a scan rate of 100 mV/s. According to the reference [247], the reduction of GO occurred at a potential of -0.6 V and maximised at -0.87 V. Due to the optimised thickness of GO and the electrochemically irreversible nature of this reaction, the reduction of GO can be achieved by only one cycle at the potential above [247]. The resultant rGO/graphene double-layer electrodes need to be thoroughly rinsed with DI water and then dried at room temperature. To minimise the difference in the symmetry and intensities of redox currents between electrodes, the following key parameters need to be kept as constants: the concentration and quality of GO solution drop-casted onto the surface of graphene electrode, the area of hydrophobic polymer insulated on working electrodes and the number of reduction cycles [247]. For the fabrication of rGO modified electrode, the GO layer was directly reduced on top of a carbon working electrode following the procedures above.

4.5.3 Amination of Hydroxylated Graphene

4.5.3.1 Amination with 3-aminopropyltriethoxysilylpropylamine

For the fabrication of antigen biosensors, the surface of the hydroxylated graphene electrode needs to be further functionalised and terminated with amino groups, which could bond with antibodies to provide a platform for antigen detection. The mechanisms of functionalisation with APTES have been introduced in 3.1.1. The electrode surface terminated with hydroxyl groups is immersed into 1% (V/V) APTES ethanol solution for 10 mins, then rinsed thoroughly with ethanol and followed by oven baking at 120 °C for 4 mins. The GO layer in the structure of graphene/GO/APTES was electrochemically reduced to rGO in ferricyanide system with the same methods used in 4.5.2.

4.5.3.2 Amination with Polyallylamine

After the coating of the GO layer, 20 µl PAA with a concentration of 2 % (V/V) was dripped onto the surface of the GO modified electrode and then was left in a moist container for 1 h to promote chemically/physically reacting with negatively charged GO underneath. The unreacted PAA was gently rinsed with DI water and the electrode was dried at room temperature for 1h before use. The GO layer in the structure of graphene/GO/PAA was electrochemically reduced to rGO with the same method in 4.5.2.

4.5.4 Reduction of H_2O_2 with graphene/rGO/PAA modified electrode

An H_2O_2 aqueous solution with a concentration of 30% (w/w) was diluted to 0.05 M by adding phosphate-buffered saline (PBS) buffer with a pH of 7.1. Blank PBS buffer of 20 µl was added onto the surface of electrodes modified with graphene, rGO, PAA and graphene/rGO/PAA respectively as references. Then, the surface of the electrodes were

rinsed with DI water three times and dried in air at room temperature. 0.05 M H_2O_2 of 20 µl in PBS buffer was then dripped onto the electrodes accordingly. The scan potential ranged from 0.2 V to -0.6 V and the scan rate was 100 mV/s.

4.5.5 Modification with 1-Pyrenebutyric acid N-hydroxysuccinimide Ester

To obtain a bioactive surface, which the antibody molecules can bond to, PANSE has been used to functionalise the graphene electrode without introducing defects into the graphene lattice [248]. A 2 mM PANSE solution is prepared by adding 0.0385 g PANSE powder into 5 ml methanol with modest shaking for 5 h. The graphene modified electrode is immersed into this resulting solution and sealed tightly for 2 h at room temperature, followed by methanol rinsing to remove excess PANSE. The mechanism is: the PANSE molecule consists of a four-benzene ring end (as shown in the red structure in Fig. 4-10), which can be immobilised onto the surface of graphene via the non-covalent π-π bond, leaving the bioactive end free-standing in solution.

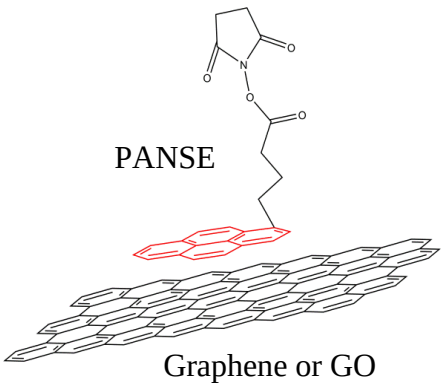

Figure 4-10. Schematic of the interaction between PANSE and the graphene plane.

4.6 Assembly and Characterisation of Biosensor

4.6.1 Fluorescence Analysis of DNA hybridisation on rGO

The lyophilised oligonucleotide was prepared and diluted in PBS buffer with a pH value of 7 as stockers. For the fluorescent analysis: the concentration of 6-carboxyfluorescein

(FAM)-labelled probe ssDNA was further diluted down to 50 nM [208] in PBS buffer and 30 µl of this ssDNA solution was chosen as the reference. 10 µl 300 nM target cDNA and 10 µl blank PBS buffer were added into two same mixtures of 10 µl 50 nM ssDNA and 10 µl 0.05 mg/ml GO solution, respectively. To enable the hybridisation between the probe ssDNA its cDNA on the surface of GO, the concentration of cDNA added here, therefore, needs to be at least five times more concentrated than that of the probe ssDNA. Compared with the hybridisation between free-standing ssDNA and cDNA in solution, a much longer time up to 1 h is required for the restoration of the fluorescent signal due to the bonding competition existing between GO/ssDNA and ssDNA/cDNA. After 1 h reaction, a volume of 20 µl was sampled from three tubes above and dried on the freshly cleaned glass slides at room temperature. The fluorescent images were recorded with Nikon Eclipse 80i Microscope, as introduced in 4.7.7.

4.6.2 Electrochemical Analysis of DNA hybridisation

For the electrochemical analysis: 10 µl probe ssDNA with a concentration of 10^{-6} M was added [214] onto the surface of the rGO/graphene double-layer electrode and kept at 35 °C for 30 min to achieve a ssDNA terminated electrode surface. The ssDNA weakly bonded onto the surface of the electrode or free-standing in solution was removed by rinsing the electrode surface with nuclease free water for 15 times. 10 µl of the target cDNA with the concentration ranging from 10^{-12} M to 10^{-7} M were dripped onto the surface of ssDNA terminated electrodes at room temperature for 1 h. Then the weakly bonded or free-standing cDNA on the electrode surface was thoroughly rinsed away with the nuclease free water before the electrochemical analysis. The electroactivity of the electrode surface at each step were monitored by CV and DPV measurements.

4.6.3 Fabrication of hCG biosensor

The fabrication of rGO modified electrode used the same procedure with 4.5.2, except the screen-printed graphene layer. The electrode was then immersed into 2 mM PANSE methanol solution for 1 h at room temperature, followed by 3 times methanol rinsing. 10 µl of the antibody solution with a concentration of 100 µg/ml was then dipped onto the surface of rGO modified electrode and incubated at room temperature for 2 h. Then, the surface of the electrode was rinsed with PBS buffer and 20 µl of bovine serum albumin (BSA) solution with a concentration of 0.5 mg/ml was dripped onto the surface of the electrode to block the free amino functionalities which may non-specifically bind with hCG. After 30 mins, the electrode was again rinsed with PBS buffer to remove free-standing BSA. These electrodes can be stored at 4 °C waiting for use. The label-free detection of hCG was achieved by dripping 20 µl hCG solution onto the surface of biosensor prepared above. The hCG solution with different concentration ranging from 0.05 to 50 ng/ml were prepared by diluting 1 µg/ml stocker in PBS buffer. The mixture was left at room temperature for 2.5 h to ensure antibody/antigen binding. The electrodes were rinsed by PBS buffer before any characterisation.

4.7 Characterisation Techniques

4.7.1 Identification of Graphene with Optical Microscope

As the properties of graphene change with increasing number of layers, a high throughput and precise technique for determining the number of graphene layers is essential for the exploration of graphene. However, the conventional characterisation instruments, such as AFM, Raman and TEM, not only show inefficiency for the fast graphene identification but also can potentially damage the graphene crystal lattice.

By taking the advantage of the refractive index enhancement on 285 nm (with a maximum 5% error, 300 nm is common) SiO_2 substrate, graphene with a different number of layers shows different colours and contrasts to each other under a normal white light source [7, 245]. And according to theoretical calculations and experimental results, the contrast for monolayer reaches up to 12% for green light, making graphene visible to the naked eye. The identification of monolayer and bilayer graphene needs to be assisted by Raman spectrum analysis first because the colour varies from lab to lab. Once the monolayer is identified, it can be used as a reference for other cases.

The Olympus BH2 optical microscope is equipped with 4 objective lenses (5 X, 10 X, 20 X, 50 X), two-eyepieces (10 X) and connected with a high-resolution monitor, as shown in Figure 4-11. The intensity of the white light source can be controlled at 12 levels.

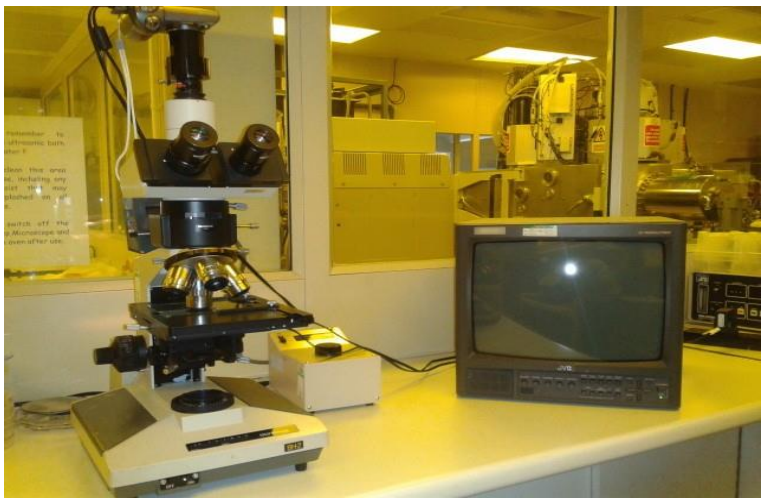

Figure 4-11. Optical microscope BH2 (Olympus, Japan).

4.7.2 Atomic Force Microscope

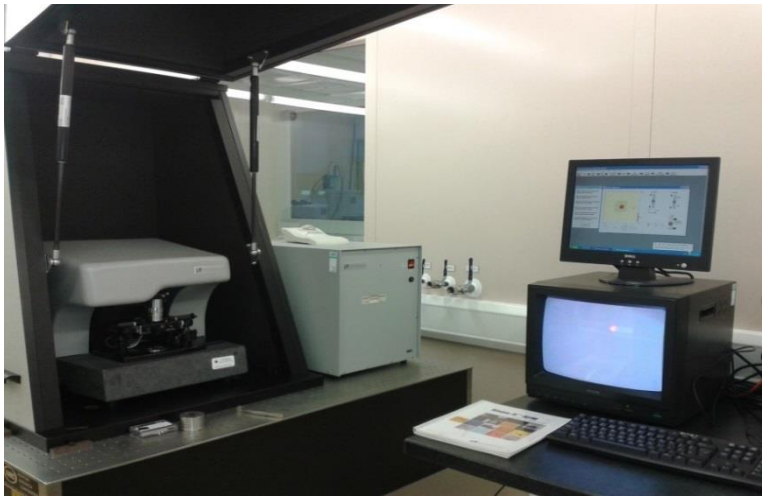

Figure 4-12. Optical image of AFM (PACIFIC NANOTECHNOLOGY).

AFM consists of the following four components, which are an electronic controller, a mechanical measurement unit and a PC with corresponding software. The cantilever tips of AFM used in this project are purchased from Nano World. Typical technical data of non-contact cantilever is: 4 μm thick, 125 μm length, 30 μm width, using a resonance frequency of 320 kHz and force constant of 42 N/m. The arrival amplitude varies from 900-1100 mV and the typical resolution of the image is 256 points. A Nano-R controlling software is mainly used for the characterisation of graphene morphology in this project. During the probe scans cross the sample surface, a constant force is maintained and applied onto the probe. By recording the Z direction movement, a 3D morphology of sample surface can be imaged.

AFM also is used as one of the foremost methods for the identification of single layer graphene. However, for the measurement of graphene thickness, especially down to a few layers of graphene, the offset may vary from 0.5-1 nm due to AFM probe-graphene-substrate interactions and the corrugated wrinkle which keeps graphene sheet thermally

stable [249, 250]. The formula to evaluate the number of graphene layers from an AFM measurement is:

$$\mathrm{N} = \frac{P - X}{0.34} + 1$$

Where N is the number of graphene layers

P is the measured thickness (nm)

X is the measured thickness of monolayer graphene.

4.7.3 Raman Spectroscopy

4.7.3.1 Mechanism

Raman spectroscopy is the most accurate, non-destructive and high-performance tool for the characterisation of graphene with different layers and qualities. A typical system contains a monochromator, optics, photodetector and monochromatic light, which is chosen as the excitation light source in the system. After laser excitation, most of the photons are elastically scattered from the surface of the analyte, however, a small portion of those are scattered inelastically, which is reflected as the change of wavelength or wave number. According to those changes caused by the molecular rotation and vibration, the properties and chemical bond structure of the substance can be determined. The shift in wavelength, also known as the Raman shift, is presented as the wavenumber, as:

$$\Delta\omega = (\frac{1}{\lambda_0} - \frac{1}{\lambda_1})$$

Where $\Delta\omega$ is the Raman shift with an unit of cm^{-1}

λ_0 is the wavelength of excitation light source

λ_1 is the wavelength of Raman Spectrum

4.7.3.2 Experimental Setup

Raman spectroscopy analyses are carried out with an XPLORA HORIBA system integrated with an OLYMPUS BX41 microscope (equipped with 10 X, 100 X objective lenses and 10 X eyepieces), as shown in Fig. 4-13. Typical acquisition parameters for the characterisation of graphene are shown below (unless stated otherwise):

532 nm green laser source, 100 mW with a diameter of 1 μm

100 X objective lens

Scan range: 1100 to 3000 cm^{-1}

Exposure time: 5-60 s upon particular sample

Grating: 1200 T

Filter: 10-25% in case of damage to graphene lattice

Slit: 100 μm

Hole: 100 μm

Scan area: upon particular sample

4.7.3.3 Raman Characteristic of Graphene

From a view of a graphene research related instrument, the most important abilities of Raman spectroscopy is to determine the number of graphene layers, disorder or defects, the presence of edge boundaries. Relevant information can be extracted from the positions (quoted as wavenumber, unit cm^{-1}), intensities and shape of a few prominent bands.

A typical Raman spectrum of graphene contains three major bands: the D band centred around 1350 cm^{-1}, the G band centred around 1580 cm^{-1} and the 2D band centred around 2700 cm^{-1}. The D band indicates the presence of disorder or edge site within the graphene plane and intensity of this band is related to the disorder level. This band is attributed to the second order Raman scattering process in the sp^3 hybridised carbon bonds. The G band comes from the in-plane vibration of C-C bond; therefore, it is very sensitive to the stress change caused by the change of the number, symmetry and crystallinity of graphene layers. The position of the G band shifts as a function of the number of graphene layers; however, this is not preferable for the accurate determination of graphene layers [251]. The 2D band, which is known as the G' band (G-prime) but has no relationship with the G band, is a result of the second order of zone-boundary phonons, same as the D band [252]. However, the 2D band can be found in both well-crystalised graphene and defective graphene. The full width at full width at half maximum (FWHM) of the 2D band is related to the number of graphene layers and the components of the 2D band are particularly important for the determination of the number of graphene layers: the 2D band of monolayer graphene can be Lorentz fitted by only one single symmetric band but four for bilayer graphene.

More practically but less accurately, the intensities ratios of D/G and 2D/G can be used to evaluate graphene quality (defect density) and the number of layers, respectively. Compared with graphite or few layer graphene, the most significant characteristics of monolayer graphene with good quality is that its spectrum shows an invisible D band, a sharp and symmetrical 2D band together with a G/2D intensity ratio < 0.7 and the FWHM value < 45 cm^{-1}. With the increase of graphene layers, both the intensity of a negatively shifted G band and the G/2D intensity ratio increase, while the 2D band becomes wider and asymmetrical (comprising more sub-bands). With the increase of defect or disorders densities, both the D band and D/G intensity ratio increase. These

trends fit up to 5-10 layer graphene and become hardly distinguishable for graphene with more layers.

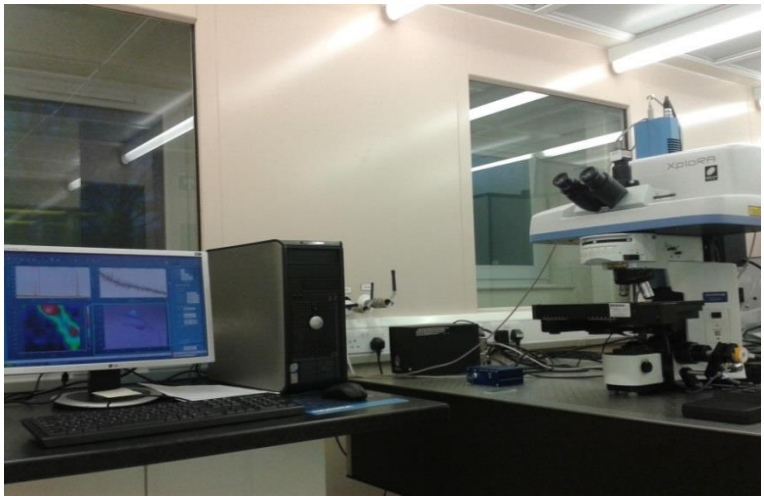

Figure 4-13. XPLORA Raman analysis system with an OLYMPUS BX41 microscope in Cleanroom (HORIBA, UK).

4.7.4 Characterisation with Keithley 2602A Two Channel Source Meter

The characterisation of electronic performance of graphene devices is carried out with using a Keithley 2602A Source Meter interfaced with a Cascade Microtech MPS 150 probe station, as the optical image shown in Fig. 4-13 (a). A Keithley 2602A is a two-channel source-measure unit with a high current resolution of 1 pA at the range of 100 nA. The output voltage is from -40 to 40 V. The output voltage or current are programmed with TSP Express software.

4.7.4.1 I_d- V_g Characterisation

The mechanism of I_d-V_g characterisation has been introduced in 3.3.4. The setup for measuring a graphene FET fabricated on SiO_2 substrate (as shown in Fig. 4-13 (a)): the source-drain voltage can vary from 10 mV to 2 V while the back gate voltage sweeping from -40 V to 40 V maximum depending on the particular measurement. A source-drain voltage of 10 mV and a back gate voltage of 20 V are chosen for the first measurement

for any device in order to avoid the current damage to the graphene channel. The time point is set at 100 ms with at least 100 data points and back gate leakage, which is normally < 10^{-9} A needs to be double checked before measurement.

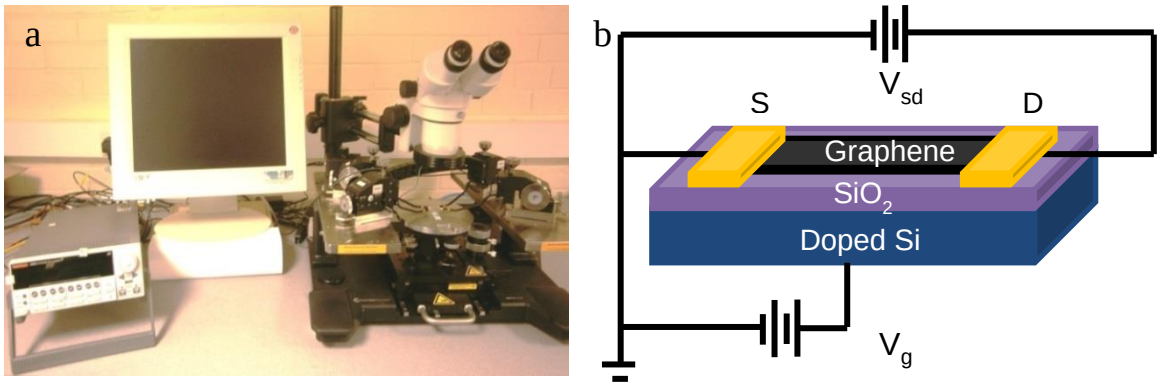

Figure 4-14. Electronic setups for graphene FET measurement. (a) Optical image of Keithley 2602A and Cascade Microtech MPS 150 Probe Station and (b) the sketch of a typical I_d-V_g measurement.

4.7.4.2 CV and DPV Measurements

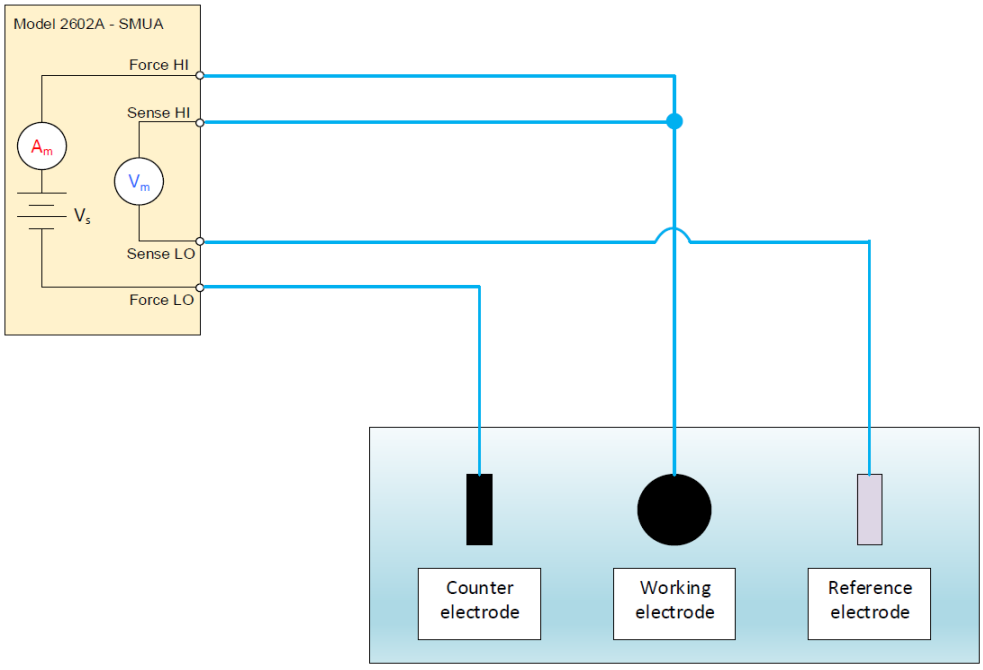

Figure 4-15. Schematic of the CV measurement setup with Keithley 2602A.

CV and DPV measurements, as introduced in 3.3.3, are two of the most versatile approaches developed for analysing the electroactive molecules in solution. They both are carried out with home designed connections with a Keithley 2602A source meter as shown in Fig. 4-15. 10 mM ferricyanide and 1 M KCl are chosen as the electroactive substance and the supporting electrolyte, respectively. It is worth noting that the supporting electrolyte needs to be at least 100 times more concentrated than the electroactive substance; otherwise, the system cannot be under equilibrium to see fast transfer kinetics. For CV measurements: a liner-sweeping triangular potential from 0.8 to -0.4 V is applied on working electrode against the standard potential from a reference electrode and acts as an excitation signal. Scan rates of CV measurements were varied from 30 mV/s to 200 mV/s in the characterisation of the rGO-graphene double-layer electrode and the scan rate of 100 mV/s was chosen for the rest of this project unless otherwise stated. For DPV measurements: The scan potential ranged from 0.8 V to 0.4 V. The pulse period for the DPV measurement was 0.4 s, pulse width was 0.12 s, pulse amplitude was 50 mV, step potential was 10 mV and quiet time was 2 s.

4.7.5 Scanning Electron Microscope (SEM)

Figure 4-16. JEOL JSM-7001F field enhanced SEM.

SEM characterisation is performed with a JEOL JSM-7001F ultra-high resolution FE-SEM, as shown in Fig. 4-16. An analyte is loaded in the vacuum chamber and the surface is cross-scanned by the electron beam. This SEM system equipped with a Schottky Electron Gun, an acceleration voltage range of 0.5 kV-30 kV, a magnification range of 10 – 500000 X and a resolution down to 1.2 nm at a power of 30 kV. During the analysis, an electron beam is focused onto the surface of the sample, which results in the generation of secondary electrons, backscattered electrons, X-rays photons, Auger electrons and cathodoluminescence. By detecting the secondary electrons, the topographical data and elemental information can be obtained. Meanwhile, by analysing the X-ray photons, the elemental information of the sample can be recorded (energy dispersive analysis by X-rays, EDX).

4.7.6 X-Ray Photoelectron Spectroscopy

XPS is one of the most powerful techniques for analysing the elemental composition and chemical state of the sample surface. XPS analysis was performed using a Kratos AXIS ULTRA equipped with an a mono-chromated Al kα X-ray source (1486.6 eV) operated at 10 mA emission current and 12 kV anode potential (120 W). The ULTRA was carried out in the fixed analyser transmission (FAT) mode with a pass energy of 80 and 20 eV for wide survey scans and high-resolution scans respectively (Nottingham University). During the scanning, input photons are absorbed by the first few nanometre material, resulting in the emission of the core electrons, which has the unique binding energy for different elements. By analysing the binding energy and their corresponding intensities, elemental information can be quantitatively obtained together with their chemical states. It is to be noted that XPS has no response to hydrogen and helium.

4.7.7 Florescence Microscope

Fluorescence analysis of dye labelled DNA molecules was carried out with a Nikon Eclipse 80i Microscope. This fluorescence microscope is equipped with five objective lenses (5 X air, 10 X air, 40 X air, 60 X oil, 200 X oil) and two 10 X eyepieces. It is capable of exciting the sample with different wavelength lasers, which are blue (485 nm), green (525 nm) and red (650 nm), and block the source laser with corresponding filters. The white light is provided by a halide metal lamp and the images can be recorded at a resolution of 1392 x 1040.

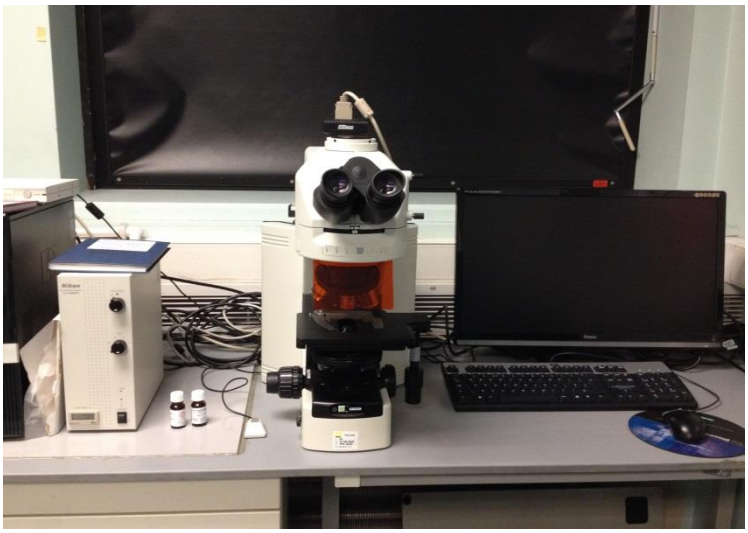

Figure 4-17. Nikon Eclipse 80i fluorescence microscope.

4.7.8 Fourier Transform Infrared Spectroscopy

Infrared spectroscopy refers to the light with wavelength from 700 nm to 1 mm. Within this range, photons can be absorbed by the IR-active analyte molecules, which vibrate in a number of different mode. The FTIR characteristics of a certain analyte reflect its inner chemical structure. In this work, a Perkin Elemer Benchtop FTIR was used for the chemical component analysis. Before the analysis, the analyte needs to be mixed and ground with 0.2 g KBr powder. The fine mixture is compressed into a tablet with about

10 T weight on top and placed in a dark chamber for measurement. The acquisition time is 30 s and the range of measurement is 400 – 4000 cm^{-1}.

Chapter 5 Novel Method for Graphene Production

5.1 Introduction

Graphene has attracted huge interest due to its unique performance in a wide range of applications since its discovery. To date, many different methods for the production of graphene have been proposed and achieved, as reviewed in Chapter 2. In this chapter, the results of conventionally exfoliated graphene on SiO_2 substrate are briefly presented together with their corresponding optical and Raman analysis, indicating the good repeatability of this method and the high quality of the resultant graphene. In addition, this chapter will mainly focus on the novel production method for large area transfer-free graphene grown from sputtered carbon and metal layer on SiO_2 substrate. Compared with previous work, our investigations have proven that a Ni film, acting as the catalytic agent and the buffer, cannot be fully evaporated either in a high vacuum chamber or in an atmospheric environment. Also, the interface of a Ni layer and the SiO_2 substrate has been found unfavourable for the formation of graphene. The systematic exploration of this growth method has led to discover that large area graphene can be obtained directly on the SiO_2 substrate when the thickness of the Ni is thinner than 100 nm. A growth model based on the detailed analysis of morphological structures and properties of graphene films is simultaneously proposed. This in-depth study of graphene growth paves a new way to the further development of graphene production and related device fabrication.

5.2 Experimental

5.2.1 Materials and Instruments

DI water

Dicing tape, 100 m x 25 cm *(Loadpoint, UK)*

4-inch Si (500 µm) wafer with 300nm SiO_2 atop *(Siltronix, US)*

IPA, general purpose grade *(BDH chemicals LTD, UK)*

Acetone, general purpose grade *(BDH chemicals LTD, UK)*

Graphite Flakes, 10-20 mm *(NGS, Germany)*

Mask aligner J500/VIS *(OAI optical associates Inc)*

Vacuum spinner 14E *(DAGE PRECIMA INTERNATIONAL)*

6-inch Ni target, 99.99% purity *(Kurt J. Lesker, US)*

6-inch SiC target, 99.99% purity *(Kurt J. Lesker, US)*

8-inch C target, 99.99% purity *(Kurt J. Lesker, US)*

Oxygen free nitrogen, N_2 *(BOC, UK)*

Pure argon, Ar *(BOC, UK)*

Liquid nitrogen *(BOC, UK)*

Ultrasonic Cleaner *(CBEST, US)*

Hotplate SH8 *(STUART SCIENTIFIC)*

Hydrochloric acid 37%, laboratory regent grade, HCl in this report *(Fisher scientific, UK)*

Three targets sputtering machine 8-inch *(Nordiko Limited, UK)*

Three targets sputtering machine 6-inch *(Nordiko Limited, UK)*

4-inch Si (500 µm) wafer with 90nm SiO_2 atop *(Siltronix, US)*

Rapid thermal processor, 210T-03 *(Heatpulse, UK)*

Fan Oven *(WTB binder, Germany)*

5.2.2 Production and Characterisation

The pre-preparation of SiO2 substrates for the production of exfoliated graphene from graphite bulk was detailed in 4.2. The deposition of material layers for the production of graphene with sputtered materials was carried out with normal sputtering technique, as detailed in 4.1. Samples were then subjected to an RTP either in-situ or ex-situ. Details of the heating and cooling curves of these two systems are given 4.1.2. The metal layer of as-prepared samples was etched in HCl solution to obtain transferable or transfer-free graphene, as detailed in 4.1.3.

The quality and the number of graphene layers were evaluated by a combination of optical microscopy and Raman spectroscopy, as detailed in 4.7.1 and 4.7.3. Surface morphologies and roughness were characterised by an optical microscope and AFM, as detailed in 4.7.2. Electronic characteristics of graphene FETs were measured with a Keithley 2602A multichannel source/measurement meter under ambient environment conditions.

5.3 Results and Discussion

5.3.1 Characterisation of conventionally exfoliated graphene with different Layers

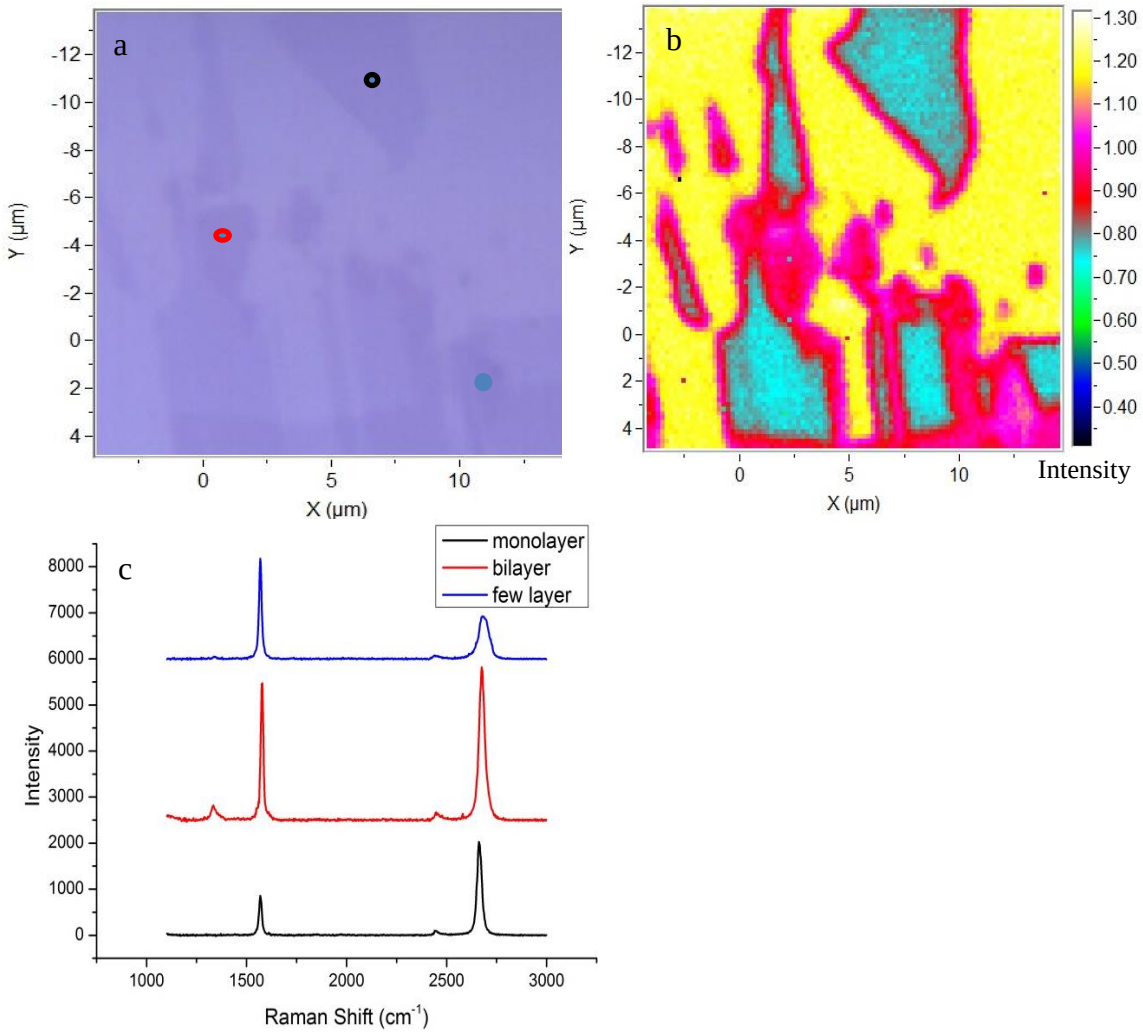

Figure 5-1. Characterisation of exfoliated graphene with a different number of layers on SiO_2 substrate. (a) Optical image of exfoliated graphene with a different number of layers. (b) Raman mapping of G/2D intensity ratio of the same area and (c) individual Raman spectrum from corresponding colour coded points in (a).

Fig. 5-1 presents an optical image of exfoliated graphene with different layers on SiO_2 substrate together with its corresponding Raman mapping (G/2D intensity ratio) and individual Raman spectrum. In Fig. 5-1 (a), the contrast difference between graphene

with different layers can be identified with the naked eye, where the darker area implies more graphene layers; however, the lightest pink colour, which relates to the monolayer graphene, varies from one lab to another and it, therefore, needs to be confirmed by Raman spectroscopy as a reference for the further optical determination of graphene with more layers. For the cyan area in Fig. 5-1 (b), where the black curve in Fig. 5-1 (c) is taken from, the typical G band and 2D band can be seen at 1573 cm^{-1} and 2664 cm^{-1}, respectively. The G/2D intensity ratio of 0.41 and the 2D FWHM value of 24.5 cm^{-1} are shown together with an invisible D band, suggesting the monolayer nature and well-crystallised lattice. For the red area in Fig. 5-1 (b), where the red curve in Fig. 5-1 (c) is taken from, both the G band and the 2D band are upshifted (1585 cm^{-1} and 2678 cm^{-1}) compared with those of monolayer graphene. The increased G/2D intensity ratio of 0.91 can be observed together with a weak D band around 1350 cm^{-1}, indicating this bilayer graphene has been slightly damaged by the exfoliation process. Also, its 2D band consists of two individual components instead of a single band in the monolayer, if it is fitted with a Lorentzian curve. The spectrum of the pink area in Fig. 5-1 (b), which is the blue curve in Fig. 5-1 (c), show a further increased G/2D intensity ratio of 1.3 and a upshifted 2D band at 2702 cm^{-1} which consists of more complicated sub-peaks, indicating the nature of few layers of graphene or graphite. From the G/2D intensity ratio mapping, it can also be seen that the monolayer is relatively uniform in the central area, whilst the edges have a higher D band which is related to the polarisation, relative position of the laser spot and the amount of disorder [253].

5.3.2 Novel Growth Process and Typical Results of Sputtered Graphene

Fig. 5-2 shows the growth procedure of graphene from sputtered materials. A SiO_2 wafer is coated by the carbon source layer and the metal film in the sequence of either substrate/SiC/Ni (Fig. 5-2 (a)) or substrate/Ni/SiC (Fig. 5-2 (b)). All targets were 6 or 8 inch in diameter and had a typical purity of 99.99%. After the deposition of all the

materials, the sample stack undergoes an RTP at a temperature varying from 650 °C to 1000 °C. Whichever the deposition sequence of these two layers is, graphene has always been found on top of the stack, as shown in Fig. 5-2 (c). The Ni (containing Ni-silicide or Ni-carbide) layer is etched away by an HCl aqueous solution, as shown in Fig. 5-2 (d). For the sample with a Ni thickness of 100-500 nm on top, shown as Fig. 5-2 (e), the graphene film comes off the SiO_2 wafer and floats on the surface of etchant solution after HCl etching, which can be scooped up with any arbitrary substrate [120, 135, 254]. In contrast, as shown in Fig. 5-2 (f), graphene is maintained on the original dielectric substrate when the Ni layer is thinner than 100 nm.

Figure 5-2 has been removed due to Copyright restrictions.

Figure 5-2. Schematic illustration of graphene growth from sputtered material. (a) and (b) show the sputtering deposition of different materials in the different sequence. (c) Graphene obtained on top of the stack after annealing. (e) and (f) show the samples with different Ni thickness result in transferable and transfer-free graphene after etching (d), respectively [142].

Fig. 5-3 (a) presents a comparison of Raman spectra of exfoliated monolayer graphene (blue) and that of graphene obtained from S1 (red), which is prepared in the structure of the substrate/50nm SiC/500 nm Ni and annealed at 1000 °C for 2 min in the ex-situ system. It can be seen that both exfoliated graphene and graphene grown from sputtered material show a FWHM value of the 2D band < 35 cm^{-1} and G/2D ratio < 0.5, indicating

the monolayer nature of graphene [61, 67, 252]. Also, no observable D band can be seen around 1350 cm^{-1} in the red spectrum, suggesting that graphene grown from sputtered materials has a comparable defect level with that of exfoliated graphene [61]. A Raman mapping of the FWHM across an area of 750 x 500 μm from S1 is shown in Fig. 5-3 (b). In the light of the FWHM value, a 40% surface coverage of monolayer graphene has been achieved within this area.

Figure 5-3 has been removed due to Copyright restrictions.

Figure 5-3. Raman analysis of sputtered and exfoliated graphene. (a) Raman spectra of graphene grown from sputtered materials (red) and that of monolayer exfoliated graphene on SiO_2 substrate. (b) FWHM mapping of the 2D band across an area of 750 x 500 μm on S1.

5.3.3 Dependence on Growth Parameters

To optimise the growth parameters and obtain graphene with better quality and higher surface coverage, the effects of RTP conditions, layer thicknesses and deposition sequences to the resultant graphene are discussed in this section.

Fig. 5-4 (a) shows the Raman spectra of S1 and S2, which have the same SiC and C thicknesses, but a reversed deposition sequence to each other (sub/500 nm Ni/50 nm SiC for S2). Both of these two samples have been annealed at two RTP temperatures of 1000 °C and 700 °C. For the spectrum of S1 annealed at 1000 °C, it shows the typical

characteristics of monolayer graphene with a low defect density. However, the spectrum of S2 annealed at the same temperature shows an increased FWHM value of the 2D band, the G/2D intensity ratio and D band, indicating more defects and layers have been introduced in the resultant graphene. The other two Raman spectra shown in Fig. 5-4 (a) are obtained from S1 and S2 annealed at a lower temperature of 700 °C. The FWHM values of the 2D bands are found to be 45.8 cm^{-1} and 55.2 cm^{-1}, suggesting a bilayer or tri-layer nature respectively. Again, S1 exhibits slightly better Raman characteristics with a smaller FWHM value and negligible D band intensity at this temperature. On the other hand, the darker are as which are covered by graphene can be optically distinguished from the lighter area which are covered by amorphous carbon in the camera shots shown in Fig. 5-4 (b) and (c). As a comparison, the sample S2 (Fig. 5-4 (c)) has a much higher graphene surface coverage of 90% than that of SiC underneath the Ni (40% surface coverage in Fig. 5-4 (b)). This is attributed to a relative high carbon concentration at the Ni surface and a slow dispersion of carbon in Ni during the heating up process, in turn leading to more sufficient carbon source for the formation of graphene during the cooling down process. Fig. 5-4 (d) and (e) shows morphological AFM images of S1 and S2 annealed at 1000 °C, respectively, indicating that the carbon-containing Ni films of the both samples have re-crystallised with different grain size during the RTP procedures. These results suggest that: S1 structure tends to produce graphene with the higher quality but with lower surface coverage; S2 has a negative effect to the size of Ni grain after annealing; and the samples annealed at higher temperature prefer to produce graphene with better quality.

Figure 5-4 has been removed due to Copyright restrictions.

Figure 5-4. Dependence of deposition sequence and annealing temperature. (a) Raman spectra of S1 and S2 annealed at 1000 °C (blue and light green curves) and 700 °C (dark green and red curves) respectively. (b) and (c) camera shots show distinctions with and without graphene on S1 and S2 respectively. (d) and (e) AFM images (amplitude contrast) of S1 and S2.

Fig. 5-5 (a) shows two typical Raman spectra of S3 (sub/50 nm SiC/200 nm Ni), which are annealed at 680 °C (red) and 1000 °C (blue), respectively. Fig. 5-5 (a. 1) and (a. 2) show the surface morphology of S3 after annealing at 680 °C. The large number of triangular nano-grains with a typical size of 20–30 nm indicates an incomplete re-crystallisation process. Its corresponding Raman spectrum took atop shows the FWHM

of the 2D band ~74.1 cm^{-1} and a G/2D ratio of 1.77, demonstrating graphene grown on this type of grain has a multilayer nature [252]. The D/G intensity ratio of 0.17 also suggests that the graphene film contains considerable nano-grains and defects [255]. As a comparison, S3 prepared with the same deposition parameters but annealed at 1000 °C, produces a bilayer graphene film with the typical FWHM of 2D ~ 47 cm^{-1} and a G/2D intensity ratio of 0.96. The corresponding AFM image in Fig. 5-5 (a. 3) shows a better re-crystallisation of the carbon-containing layer with bigger grain sizes of 0.5–1.5 μm. Compared with S1, a conclusion can be drawn that the samples prepared at the same RTP temperature with thicker Ni films (500 nm) favour the growth of higher quality monolayer graphene if Ni is on top of SiC. Also, the results here confirm a conclusion that the higher annealing temperature is preferred for the re-crystallisation of a carbon-containing Ni film and the formation of graphene, leading to a better graphene quality.

The characteristics of S4 (sub/2.5 nm C/40 nm Ni), which is prepared with a thinner carbon/Ni layer and annealed at 1000 °C, are shown in Fig. 5-5 (b). The amorphous carbon is used as the carbon source here because no significant difference in resultant graphene has been observed between the samples employing either SiC or C. In this case, the G/2D ratio of 1.15, D/G ratio of 0.26 and a FWHM value of 57 cm^{-1} have been observed, indicating the bi- or tri-layer layers graphene with low-level defects and nano-crystalline. The AFM image of S4 shows a grain size smaller than 1 μm and the mean grain size of the sample is approximately 500 nm (detailed analysis shown in Fig. 5-6).

Fig. 5-5 (c) shows Raman spectra of S1 annealed at the same temperature of 1000 °C for 2 min but processed with reduced cooling rates (intensity decrease) of 2 %/s (red) and 1 %/s (blue), respectively. Compared with the samples annealed at 15 %/s in Fig. 5-4 (a), much wider 2D bands and higher D bands can be identified, indicating graphene formed in this case has more layers and defects. According to the analysis of a large number of samples, it has been proven that the heating rate is not as crucial as a faster

cooling rate to the formation of monolayer graphene on Ni, which agrees with the results by Yu et al. [75].

Figure 5-5 has been removed due to Copyright restrictions.

Figure 5-5. Raman spectra of as-grown graphene from samples with different RTP systems/conditions and Ni layer thicknesses. (a) Raman spectra of S3 with RTP temperatures of 680 °C and 1000 °C, AFM images of S3 annealed at 680 °C are given in (a. 1) and (a. 2), at 1000 °C shown in (a. 3). (b) Raman spectrum of S4 annealed at 1000 °C. AFM of S4 is given in (b. 1). (c) Raman spectra of S1 processed with different cooling rates.

5.3.4 Distribution of Grain Size and Analysis of Surface Roughness

The atomically flat graphene film with a low defect density is essential for the fabrication of graphene-based applications, such as electronic devices and sensors [256]. However, graphene produced by the current mass-production techniques is far from

perfect due to the high density of defects, edges, chemical impurities and grain boundaries [257]. Although improvements have been made to obtain graphene with these ideal qualities, it remains a major challenge [258]. In the method of graphene grown from sputtered materials, the quality of resultant graphene strongly depends on the grain size and the surface morphology of re-crystallised Ni film after thermal annealing. The distribution of grain size (in diameter) of S1, S2 and S4 are determined by the AFM topographic images over a surface area of 10 x 10 μm and shown in Fig. 5-6. The average grain sizes of S1 and S2 are found to be 939 nm and 564 nm, as shown in Fig. 5-6 (a) and (b) respectively. It can be attributed to the C layer on top of Ni that has a negative effect on the grain size enlarging during the re-crystallisation [259]. S4, which consists of a much thinner Ni (40 nm) and C layer (2.5 nm), shows a half average grain size compared with S1, indicating that a thinner Ni layer prefers to re-crystallise into smaller grains, as shown in Fig. 5-6 (c). In addition, Fig. 5-6 (d) is the distribution of grain size measured on the CVD graphene on Cu over a surface area of 10 x 10 μm. No difference of grain size can be found between the commercial CVD graphene on Cu from Graphene Supermarket and the graphene grown in conjunction with sputtered Ni.

Figure 5-6 has been removed due to Copyright restrictions.

Figure 5-6. Grain size distribution of graphene grown on top of (a) S1, (b) S2, (c) S4 and (d) CVD graphene grown on Cu sheet. Scan range cross over a surface area of 10 x 10 μm. The corresponding AFM images are shown in Fig. 5-7.

The distribution of grain size of S3 has been observed at the similar order of magnitude to S4 (transfer-free graphene). It is worth noting that the grain sizes measured by AFM here actually refers to the grain size of the metal film on where the graphene was grown, instead of the grain size of graphene crystals, which can only be identified with atomic resolution. According to Raman mapping which shows the inhomogenous signal around the grain boundaries of the metal film, it is inferred that the grain size of graphene crystals are restricted by the grain boundaries of the Ni film as the graphene crystals are unlikely to grow across the grain boundaries of the Ni film, or bridging the adjacent Ni grains without introducing any defects. This is consistent with Huang *et al*'s work [260] that the grain size of the graphene crystals of CVD graphene on Cu are much smaller than those on a Cu film as dislocation always occurred in graphene crystals grown on large Cu grains.

The morphology images of samples in Fig. 5-6 are shown in Fig. 5-7 together with the analysis of surface roughness. It can be seen that all the graphene samples have uneven surface morphologies with typical mean roughness values ranging from 10~30 nm and 10 points heights up to 200 nm. This phenomenon is attributed to the re-crystallisation of a carbon containing metal layer at the elevated temperature (up to 1000 °C) and the graphene morphology is a rubbing of the metal morphology where it grows. For S1 shown in Fig. 5-7 (a), which has the same layer thickness with S2 (shown in Fig. 5-7 (b)) but reversed deposition sequence, shows a higher roughness, confirming that a C layer on top of Ni has a negative effect on the formation of bigger grains. Compared with S4 shown in Fig. 5-7 (c), it can be seen that samples with the thicker Ni layer on top show higher roughness, which is also a confirmation of the conclusion drawn from grain size analysis. Both the grain size and roughness of Fig. 5-7 (c) and Fig. 5-7 (d) are remarkably similar, implying that our result has competitive flatness with graphene prepared by CVD methods.

Figure 5-7. AFM analysis of surface morphology and roughness of graphene grown on (a) S1, (b) S2, (c) S4 and (d) CVD graphene grown on Cu sheet. Scan range cross over a surface area of 10 x 10 μm.

5.3.5 Transferrable and transfer-free graphene

As the Ni film cannot be fully evaporated during or after the graphene growth, the samples need to be immersed into an HCl aqueous solution to remove the Ni, Ni-silicide or Ni-carbide layers, as introduced in 4.1.3. For the sample with a thicker Ni layer (> 100 nm), the graphene film could come off the original SiO_2 substrate and floats on the surface of the HCl solution. Due to the ultrahigh breaking strength of the graphene film, it can be picked up by another arbitrary substrate without introducing any visible cracks. For the sample with a thinner Ni layer (< 100 nm), the graphene film can be maintained on the original SiO_2 substrate and, therefore, no post-transfer process is required for the fabrication of devices on SiO_2. According to the observation, the etching of the Ni film occurred at all of the sample edges, grain boundaries and dislocations of graphene on the sample plane, as bubbles can be observed from all of these places. However, due to the good crystallisation of the graphene film, the side-way etching is dominated instead of top etching, in turn leading to a much longer etching period for those samples with a thinner Ni.

A comparison of transferrable and transfer-free graphene is provided in Fig. 5-8. A typical Raman spectrum of graphene transferred onto the SiO_2 substrate (S2, can be S1) is shown in Fig. 5-8 (a). Compared with the spectrum of S2 before etching, only the intensity of the D band is slightly increased, which may be attributed to the nano-sized damage introduced during the transfer process. Its corresponding optical image is shown in Fig. 5-8 (a. 1). There is no crack that can be seen with the naked eye, indicating that the graphene film is of good quality on a macroscale. 2D and 3D AFM images (amplitude contrast) of the same sample are presented in Fig. 5-8 (a. 2) and (a. 3) respectively, showing the grain sizes ranging from 0.5–1.5 μm together with its uneven morphology. It also can be seen that graphene is formed or wrapped around Ni grains, which means that the morphology of graphene is actually a rubbing of the Ni surface

underneath. This rigid sheet, which contains a flat area on each grain top and the curved or vertical surface around the overlap of grain boundaries, can float off the original substrate once the Ni layer underneath is etched away. According to the analysis of surface roughness in Fig. 5-7, there is no significant difference in the surface morphology or roughness between the as-grown graphene, transferred graphene and CVD graphene on Cu [258] or on Ni [102], which is mainly due to a similar re-crystallisation process of the metal grains at similar temperatures of graphene growth. As mentioned earlier, the actual graphene grains are much smaller than those of the metal grains [260] for CVD graphene on Cu film. Malola *et al.* [257] also have reported that graphene grain boundaries are topological defects with a disordered character, which can be characterised by trends in energy, structure, chemical reactivity, corrugation heights and dynamic properties as a function of lattice orientation mismatch. Therefore, graphene grown from sputtered Ni shows similar characteristics like CVD graphene, implying two types of grain boundaries formed during the graphene growth on metal surfaces. The grain boundaries of graphene on the large metal crystal surface is caused by the dislocation of carbon atoms during the graphene growth [260], and the grain boundaries caused by the multiple nucleation sites across the metal film [102] and the physical separation of the metal grains. The latter one results in the uneven graphene morphology as shown by AFM images. As both of the film roughness and grain boundaries can potentially degrade the electronic properties of device applications, a major challenge is the growth of defect-free and atomically flat single crystal graphene films [256, 258].

Fig. 5-8 (b) shows a typical Raman spectrum and an optical image of transfer-free graphene from S4 after the removal of the Ni layer in HCl. Its corresponding 2D and 3D AFM images are shown in Fig. 5-8 (b. 2) and Fig. 5-8 (b. 3), respectively. For the transfer-free graphene, the Raman spectrum shows comparable quality with that of as-

grown S4 shown in Fig. 5-5 (b), except an increased D band, which indicates nano-sized damage occurred during in the etching process. From Fig. 5-8 (b. 2) and (b. 3), it can be seen that the surface morphology of the graphene is also a rubbing of the morphology of the Ni layer underneath. However, compared with transferred S2 onto SiO_2 substrate, the etched S4 shows smaller grains and lower roughness, which corresponds to the conclusion from Fig. 5-5. For this sample, the most important achievement is that the graphene remained on the original substrate, after the Ni film is etched away in HCl, demonstrating that the adhesion between graphene and the substrate is much stronger than the buoyant force caused by graphene hydrophobicity.

To understand the reason how graphene can either come off or remain on the original substrate with the different Ni thickness, more detailed studies have been carried out. The Raman spectra and AFM images of S1-S4 taken before the chemical etching are compared with their corresponding results obtained after the chemical etching. For the specific sample S4, the top graphene layer is removed by sputtering before immersing the samples in HCl. As the four samples show similar results, only one typical result is given in Fig. 5-8 (c). The Raman spectrum (upper blue curve) before chemical etching is shown together with its corresponding AFM image (Fig. 5-8 (c. 1)), which present a typical graphene signature with the re-crystallisation grains. The bottom spectrum (red curve) is taken from the S4 substrate surface after the removal of the graphene and the Ni layer, showing relative weak but wide D and G bands around 1350 cm^{-1} and 1600 cm^{-1}, respectively, a typical signature of nanocrystalline graphite [261, 262]. It can be seen that the structure of nc-G on the substrate reflects the morphology of the bottom surface of the Ni layer (shown as nc-G in Fig. 5-8 (c. 2)). These results demonstrate that graphene always grows on the top surface and leaves a nc-G layer on the substrate whatever the deposition sequence of materials and the thickness of the layers. In the consideration of a diffusion-segregation (or precipitation) mechanism [100, 263], it is

believed that the precipitation of carbon atoms from Ni during the RTP cooling down phase is isotropic, which means that carbon atoms precipitate on both the top and bottom surfaces. However, graphene forms only on the top surface and wraps around Ni grains while a layer of carbon does precipitates at the interface between Ni and SiO_2, which is attributed to the loss of the catalytic function of the Ni layer caused by the unfavourable chemistry at the Ni/SiO_2 interface. Therefore, for samples with the thicker Ni layer, there is no physical connection between the graphene on top of the Ni and nc-G layer on the substrate once the Ni layer is etched away, and consequently, graphene floats off the substrate because of its hydrophobic nature. However, for samples with thinner Ni (in the range of < 100 nm), graphene around Ni grain boundaries can come down to the substrate and join the nc-G layer during the re-crystallisation and weak de-wetting process, which performs as anchors between the graphene film and the original substrate. The rest of the graphene grown on top of the flat grains falls onto the substrate and keeps this morphology as its physical structure.

Figure 5-8 has been removed due to Copyright restrictions.

Figure 5-8. Characterisations of the transferred graphene and transfer-free graphene. (a) Raman spectrum of graphene of S2 transferred to the SiO_2. a.1, a.2 and a.3 are the optical micrograph, AFM amplitude contrast and AFM 3D images of the sample, respectively. (b) Raman spectrum of transfer-free graphene from S4, retains on the original substrate after the removal of Ni in HCl. b.1, b.2 and b.3 are its relative optical micrograph, AFM amplitude contrast and AFM 3D images, respectively. (c) AFM image and Raman spectra of the top graphene layer and the substrate surface after the removal of graphene by sputter-etching and the removal of Ni layer by etching in acid.

5.3.6 AFM comparison of grain morphology of conventionally transferred CVD graphene and graphene grown from novel sputtered films

Fig. 5-9 shows the AFM amplitude contrast and 3D grain topography of CVD graphene grown on Cu foil (Fig. 5-9 (a)) and graphene grown from a sputtered Ni/C stack (S1, Fig. 5-8b), after transferring onto the SiO_2 substrates respectively. Although the two

samples are grown on different metal layers, the morphologies of them are remarkably similar; indicating the transferred graphene from sputtered materials has very comparable quality on flatness.

Figure 5-9 has been removed due to Copyright restrictions.

Figure 5-9. AFM amplitude contrast and 3D topography of transferred (a) CVD graphene and (b) graphene grown from sputtered Ni/C stack on the SiO_2 wafer.

5.3.7 Novel Growth Model of Sputtered Graphene

In light of these above observations, a growth model of graphene grown from different Ni thicknesses is proposed, as shown in Fig. 5-10. Fig. 5-10 (a) shows that when the Ni layer is thick enough (> 100 nm), graphene can grow on relatively large and smooth Ni grains, which form during the RTP. For each individual Ni grain, monolayer graphene grows uniformly on top of the surface and around the grain (a.1). In this case, the Raman characteristics of monolayer graphene can be detected as shown in Fig. 5-3 (a). However, in practice the size of the Ni grain is affected by many factors and the growth of uniform graphene is difficult to achieve around grain boundaries as explained in Fig. 5-8. There is only 40% coverage of monolayer graphene that can be achieved discontinuously. A layer of nc-G is also formed at the interface of the Ni and SiO_2 substrate due to the isotropic precipitation of carbons atoms, as the Raman results

shown in Fig. 5-8 (c). The adhesion between nc-G and the substrate is strong enough to withstand the ultrasonic bath; however, graphene floats off the substrate after the etching of Ni, as there is no physical connection between them (a.2). Fig. 5-10 (b) presents the case of the growth of transfer-free graphene when smaller Ni grains are re-crystallised during RTP. In this case, graphene cannot only grow around the Ni grain boundaries but also come down to the substrate due to the re-crystallisation and de-wetting, linking up graphene with the nc-G layer on the substrate (b.1). Because of the existing physical connections here, graphene can overcome the buoyant force caused by its hydrophobic nature and remain on the original substrate after chemical etching (b.2), as supported by AFM images and Raman spectrum shown in Fig. 5-8 (b) for S4. If the thickness of the Ni film decreases further to < 30 nm, as shown in Fig. 5-10 (c), a layer of discontinuous graphene can be found on the substrate, which is due to the same reasons explained in Fig. 5-10 (b). The abundance of nucleation sites and an insufficient Ni layer result in smaller Ni grains overlapping with each other, which in turn result in graphene grains overlapping with each other, as shown in Fig. 5-8 (b) and (c). Around these overlaps, although graphene on each Ni grain is likely to be monolayer, it may produce a Raman spectrum of a bilayer or few layers of graphene. The higher percentage of overlapped graphene, the more spectra looks like multilayer graphene, makes the interpretations of these Raman results more complicated than that of evenly exfoliated graphene on a SiO_2 substrate. Therefore, under the optimised conditions, it is a matter of debate that graphene growth can be self-limiting on individual Ni grains. The multilayer Raman spectra could be due to the contribution of overlapped graphene grains. However, more detailed studies need to be carried out to clarify this hypothesis.

Figure 5-10 has been removed due to Copyright restrictions.

Figure 5-10. Schematic illustration of the graphene growth model. (a) Sample with Ni thickness >100 nm: (a. 1) graphene grows on top of Ni and replicates the morphology of Ni grains while a nc-G layer is formed at the Ni-SiO_2 interface. (a. 2) a transferable monolayer graphene sheet is obtained after the etching of Ni. (b) Sample with Ni thickness from 30–100 nm: (b. 1) graphene on top of the Ni can grow through the grain boundaries and join the nc-G layer on the substrate. (b. 2) Graphene remains on the original substrate after the etching of Ni. (c) Smaller Ni grains in grain boundaries: (c. 1) monolayer graphene also grows around these small Ni grains. (c. 2) The resultant graphene shows overlapped grains across the grain boundaries, which is caused by the overlapped structure of the Ni layer after re-crystallisation [142].

5.4 Conclusions

The production of graphene with mechanical exfoliation on a SiO_2 substrate has been successfully repeated. The unique optical properties and good quality of the resultant exfoliated graphene have been confirmed by the optical contrast comparison and Raman spectroscopy, respectively. Compared with graphene produced by other methods, e.g. CVD or epitaxial graphene from SiC, exfoliated graphene possesses the best lattice quality and uniformity.

A novel technique for either large area transferable or transfer-free graphene grown from sputtered materials on a SiO_2 substrate has been developed. Graphene is always obtained on top of the Ni layer while a layer of nc-G is obtained on the surface of a SiO_2 substrate, which is believed to be as a result of isotropic precipitation of carbon atoms from the Ni layer and the unfavourable chemistry at the Ni-SiO_2 interface for the graphene growth. The results are comparable with CVD samples at the surface morphology and roughness, which are caused by the re-crystallisation of the Ni film and the robust nature of graphene. Transfer-free graphene can be produced on the SiO_2 substrate with the chemical etching of the Ni layer, if the thickness of Ni ranges from 30-100 nm, paving the way to a novel production technique of large area graphene on the dielectric substrates. A growth model has been proposed to demonstrate the relationship between graphene states and the Ni layer thickness. Graphene grown on individual Ni grains may be self-limiting with a catalytic mechanism, as no connection between the graphene formation and the Ni crystal orientation has been observed. The overlapped graphene boundaries, which are caused by the Ni grain boundaries, bring complications in the interpretation of the Raman data. To meet the requirement of the industrial application, a profound challenge, is the solution to the uneven morphology of the graphene film caused by metal layer re-crystallisation and the optimisation of graphene growth conditions.

Chapter 6 Fabrication and Characterisation of Graphene FET Devices

6.1 Introduction

Due to its unique physical and chemical properties, graphene has attracted a huge amount of research interest since 2004 [2]. To fully understand its unique properties and apply them to the industrial scale production for biological, electrical and thermal applications [34, 42, 264, 265], a non-destructive method for the fabrication of electronic contacts on a graphene film is required. Many methods have so far been proposed and achieved in laboratories, such as electron beam evaporation (e-beam evaporation) [93], CVD [266] and thermal evaporation [38]. However, among them, thermal evaporation is believed to be the only non-destructive method to achieve this purpose. Sputtering deposition, as the most favorable deposition technique in the current semiconductor industry, it has a number of advantages such as high throughput, diverse material choices. However, defects and disorders are always introduced into the graphene by the energetic sputtering flux, resulting in performance degradation of graphene-based devices [267-270]. Moreover, the fabrication of Au contacts on graphene has been found unlikely to be achieved by the conventional lift-off technique without post-cleaning in ultra-sonication due to the difficulties in removing the unwanted sputtered Au films. However, to minimise the potential damage to the graphene film, ultra-sonication should be avoided in the fabrication procedures of graphene devices [271].

To reduce graphene damage caused by the deposition of sputtered Au films during device fabrication, some improved sputtering configurations have been proposed [272, 273]. It has been confirmed that either the flipping substrate or the deposition with low

incidence could effectively reduce the damage to graphene. However, both the flipping substrate configuration and the low deposition angle makes the lift-off process unlikely to be achievable, therefore, no electronic devices and measurements can be fabricated or provided in those reports [264]. Although chemisorbed metal, such as Ni, has also been used as a contact material to achieve lower resistance after performing a post-annealing process [274, 275], the mechanism here is to promote the chemical/physical interaction between the graphene and metal contact instead of reducing the damage to the graphene.

In addition, for the fabrication of biosensor with CVD graphene, the graphene has to be geometrically designed and patterned to meet the size requirement. Prior to this work, the scalable patterning of graphene was normally achieved by oxygen plasma etching, which made it the most commonly used technique in the industry of graphene microfabrication [276, 277]. Some other techniques, such as focused ion beam etching [278, 279] and photocatalytic patterning [280], have also been reported. In contrast, ion-milling and sputtering, as the main preferred high throughput dry etching tools in the semiconductor industry, have not been reported. Due to the thermal effect of a sacrificial polymer layer, the removal of polymer afterward has become a difficulty.

In this chapter, a novel shielding technique for the deposition of Au contacts on graphene by sputtering was developed. As far as is known, this is the first method for fabricating electronic Au contacts on graphene film without introducing difficulties in the lift-off process. To minimise the damage, both Ar pressure and discharge power for the deposition of Au have been systematically studied and optimised. In contrast to those devices fabricated with conventional sputtering configuration, the devices fabricated using the shielding technique and optimised deposition parameters show an increased success rate of device fabrication from 17% to 90%. Also, their corresponding two-probe contact resistivity ($R_{contact}$) and total device resistivity (R_{total}) have been found significantly decreased down to 1.04 and 2.4 kΩ μm, respectively. In addition,

absorption effects to the electronic performance, which are mainly from organic residues generated during fabrication and gaseous molecules during the electronic measurement, have been systematically presented and analysed, providing the optimisation of the performance of graphene FETs.

A novel scalable manufacturing technique to precisely pattern CVD graphene on a SiO_2 substrate using improved ion-milling and lift-off process was reported for the fabrication of graphene-based electronic devices. The transferred CVD graphene was successively spin-coated by lift-off resist (LoR) and photoresist. Then the sample was subjected to a thermal baking process under deep ultraviolet light (DUV) to decrease the thermal effect caused by ion-milling afterward. The quality of the resulting patterned graphene was characterised by Raman spectroscopy and optical microscope. The mechanism of this technique was explained by cross-section analysis using SEM.

6.2 Experiment

6.2.1 Materials and Fabrication Instruments

Microposit remover 1165 *(Rohm and has electrical materials Europe, UK)*

Microposit developer 351 *(Rohm and has electrical materials Europe, UK)*

Lift-off Resist 3B *(Rohm and has electrical materials Europe, UK)*

Mask aligner J500/VIS *(OAI optical associates Inc)*

4-inch Au target, 99.99% purity *(Kurt J. Lesker, US)*

Hotplate SH8 *(STUART SCIENTIFIC)*

Vacuum spinner 14E *(DAGE PRECIMA INTERNATIONAL)*

Thermal evaporator *(Edwards 306, UK)*

Ion Miller *(Edwards, UK)*

DUV light *(UVP, UK)*

Three targets sputtering machine 6-inch *(Nordiko Limited, UK)*

Fan Oven *(WTB binder, Germany)*

4-inch Si (500 μm) wafer with 300nm SiO_2 atop *(Siltronix, US)*

6.2.2 Procedures and Characterisation

Graphene samples were prepared with mechanical exfoliation from HOPG, as introduced in 4.2. LoR and photoresist were spin-coated with the modified photolithography and lift-off process in 4.4.1. The sputtering deposition of Au contacts was carried out using a shielding tube as introduced in 4.4.2. The transfer of CVD graphene was achieved following the process introduced in 4.3.1 and the patterning of CVD graphene was achieved through the steps in 4.3.2.

The quality and the layer number of graphene were evaluated by a combination of optical microscopy, AFM and Raman spectroscopy, as introduced in 4.7.1, 4.7.2 and 4.7.3, respectively. Surface morphologies of the FET devices were characterised by the optical microscope, AFM and SEM, as introduced in 4.7.1, 4.7.2 and 4.7.5. The quality of graphene films underneath the Au contacts and in the channel area was evaluated by Raman Spectroscopy equipped with a 532 nm laser. Electronic characteristics of graphene FETs were measured with the Keithley 2602A multichannel source/measurement meter under ambient environmental conditions, as introduced in 4.7.4.

6.3 Results and discussion

6.3.1 Fabrication of Au Contacts on Exfoliated Graphene

The normal sputtering configuration and the modified sputtering configuration with a shielding tube are shown in Fig. 6-1 (a) and (b) respectively. In the normal configuration, Au is deposited not only onto the sample plane but also onto the side walls of photoresist and bridge over the LoR undercuts right through to the surface of the graphene. These bridges act as anchors linking up Au contacts onto graphene and unwanted Au films on the photoresist, resulting in difficulties in removing the unwanted Au films in the lift-off process. An optical image of a device fabricated with normal sputtering configuration is shown in Fig. 6-1 (c). It can be seen that the top left and bottom left contacts are linked up with each other by the Au film, leading to a short circuit in electronic measurements. Also, the Au ribbon with a typical size down to few micrometers can be seen suspended at the edges of contacts, which may have a physical contact with the graphene channel, leading to a fluctuation in $R_{contact}$ in electronic measurements. This poorly defined contact edge became worse when the pattern came down to the few micrometer or nanometer scale.

To address this phenomenon, a shielding tube has been proposed and added into the normal sputtering configuration, as shown in Fig. 6-1 (b). This aluminum tube acts as a shield and is mounted on top of the photoresist patterns. The size of the inner bore is designed to be only slightly larger than that of the photoresist patterns, which can prevent excessive Au atoms depositing onto the side walls of the photoresist. In this case, only the portion of Au atoms ejected via the relatively perpendicular trajectories could reach the surface of the patterned substrate, leading to the finely defined patterns without introducing difficulties in the lift-off process, as shown in Fig. 6-1 (d). As a result of using this shielding technique, the success rate of the lift-off step (with no Au

bridges and ribbons between contacts or at the edges of contacts) increased from 17% to nearly 90%.

The typical Raman spectra of as-exfoliated graphene (black) and the graphene underneath the Au contacts sputtered with optimised parameters (red) are shown in Fig. 6-1 (e). It can be observed that the intensity ratio of the D to G band has slightly increased from 0.01 to 0.04 after the deposition sputtered Au on top, indicating that very limited defects or disorders can be introduced into the graphene lattice during this process. It corresponding I_d-V_g (black) and R-V_g (red) characteristics have been presented in Fig. 6-1 (f). From its I_d-V_g curve, a modulation of the channel conductivity around 4 and a R_{total} of 15.6 kΩ μm can be observed when the V_{sd} = 500 mV, presenting a good electrical characteristic of the exfoliated graphene device, which is in accordance with previous reports [15, 76]. The Dirac point, where the minimum conductivity presents, can be seen positively shifted to 19 V. This p-type doped phenomenon is caused by both polymer residues generated in the transfer process and gaseous adsorbents from air trapped on or underneath the graphene channel. The contact resistivity can be calculated from its corresponding R-V_g curve. Because at high negative V_g region, where two $R_{contact}$ dominate the R_{total} [191], the channel resistance is negligible and only less than a 5% discrepancy of $R_{contact}$ can be found compared with those values extracted with more complicated methods such as the TLM and curve fitting methods, the $R_{contact}$ of 5.4 kΩ μm therefore can be treated as the resistivity reading at high negative region of R-V_g curve. In this work, the minimum $R_{contact}$ has been found to be 1.04 kΩ μm, which is much lower than the $R_{contact}$ measured from those devices fabricated with normal sputtering configuration and even competitive with those prepared with e-beam evaporation [281], confirming the superiority of the modified sputtering in improving the electronic performance.

Figure 6-1 has been removed due to Copyright restrictions.

Figure 6-1. A comparison of device fabricated by normal and modified sputtering. (a) Normal and (b) modified sputtering configurations. (c) and (d) optical images of the devices fabricated with normal and modified sputtering configurations, respectively. (e) Raman spectra of as-exfoliated graphene (black) and graphene underneath the sputtered Au contact (red). (f) I_d-V_g (black) and R-V_g (red) characteristics of a graphene FET, V_{sd} = 500 mV. Au contacts in (e) and (f) are sputtered with the modified configuration at a discharge power of 20 W and Ar pressure of 20 mTorr.

6.3.2 Comparison of effect on graphene by Au with different deposition conditions

In this section, the damage to graphene caused by Au sputtered under different conditions has been systematically studied by Raman spectroscopy and its effects to the corresponding electronic characteristics have also been investigated by I_d-V_g measurements. Fig. 6-2 (a) shows a comparison of damage to graphene introduced by an Au film sputtered at different Ar pressures of 4, 8 and 20 mTorr with a constant discharge power of 50 W. It can be seen that the D/G band intensity ratio has increased

to 1.08 and the 2D band became negligible when Au was sputtered at an Ar pressure of 4 mTorr, as the black spectrum shows in Fig. 6-2 (a). By increasing the Ar pressure to 8 mTorr, the all characteristic bands of graphene, which are located at 1350 cm^{-1}, 1580 cm^{-1} and 2680 cm^{-1}, can be observed together with a D/G intensity ratio of 2.1 and a G/2D intensity ratio of 1.2, as the red spectrum shows in Fig. 6-2 (a). After the Ar pressure was further increased to 20 mTorr, the relative height of the G and the 2D bands maintained whilst the D band significantly decreased, in turn leading the D/G intensity ratio to decrease from 2.1 to 0.62, as the blue spectrum shows in Fig. 6-2 (a). From these results, it can be concluded that the higher Ar pressure during Au deposition is preferable and results in the less damage to the graphene, which is in accordance with Chen's conclusion [272]. The bombardment of high-speed energetic Au atoms occurred when they arrive at the graphene, which causes the amorphisation of the sp^2-hybrided graphene lattice [261],this is believed to be the major reason for the damage to graphene. The increased Ar pressure is preferred as it leads to more interparticle collisions, which result in more disordered trajectories and reduced energy of the sputtered species and in turn leads to the moderated damage to the graphene. After the deposition of Au at this increased Ar pressure, the graphene lattice has been changed into nanocrystalline graphite (nc-G phase) [282]. However, as a sacrifice for less damage to graphene, the deposition rate of Au was decreased from 11 to 0.6-0.7 nm/min when the Ar pressure was increased from 4 to 20 mTorr with the same discharge power of 50 W. Therefore, there is a limit of Ar pressure for using this method to moderate the damage, above which the deposition of Au is not commercial and practical.

Fig. 6-2 (b) shows a comparison of damage to graphene introduced by an Au film sputtered at the same Ar pressures but with a constant discharge power of 20 W. When the pressure of Ar increased from 4 to 8 and 20 mTorr, the intensity ratio of the D and G bands gradually decreased from 3.36 to 1.22 and 0.08 respectively. Compared with

those samples fabricated at the same Ar pressures as in Fig. 6-2 (a), it can be seen the D/G intensity ratio in all the three cases are correspondingly lower, indicating that the decreased discharge power is also helpful to reduce the damage caused by sputtered Au. This is attributed to the less energetic bombardment of Au atoms ejected with less energy, which is not enough to break the C-C bonds in the graphene lattice. Using both an optimised Ar pressure and the discharge power, a very limited number of defects and disorders were introduced into graphene film underneath the sputtered Au contacts with an indicator of a negligible D band, as shown in the blue spectrum in Fig. 6-2 (b).

Fig. 6-2 (c) provides a comparison of R-V_g characteristics of devices fabricated with and without optimised sputtering parameters. When the Au contacts are deposited onto a graphene channel with a 50 W discharge power of and a 4 mTorr Ar pressure, as shown in the black spectrum in Fig. 6-2 (c), a R_{total} of 26 kΩ μm and a calculated $R_{contact}$ of 10 kΩ μm can be seen together with a positively shifted Dirac point around 35 V on its corresponding R-V_g curve. When the Au contacts are fabricated with an optimised discharge power of 20 W, as shown in the red spectrum in Fig. 6-2 (b), the R_{total} and $R_{contact}$ decreased to 16 and 5.6 kΩ μm respectively whilst showing a positively shifted Dirac point at 20 V. In contrast, using both an optimised discharge power of 20 W and Ar pressure of 20 mTorr at the same time, as shown in the blue spectrum in Fig. 6-2 (c), a further decreased R_{total} of 3.4 kΩ μm and $R_{contact}$ of 1.04 kΩ μm can be observed with a positively shifted Dirac point at 10 V. From these results it can be confirmed that the Au sputtered on top of graphene as contact material could introduce serious damage to the graphene lattice, which in turn result in the higher $R_{contact}$ and R_{total} and higher doping level. As a method to address this issue, the relatively higher Ar pressure and lower discharge power are favorable, resulting in less damage to the graphene during the deposition of the Au contact, which could avoid the degradation of graphene's unique electronic properties.

Figure 6-2 has been removed due to Copyright restrictions.

Figure 6-2. Raman spectra of graphene underneath the sputtered Au film and the electronic characterisation of corresponding devices. Raman Spectra of graphene underneath the Au deposited at a discharge power of (a) 50W and (b) 20W with three different Ar pressures respectively. (c) R-V_g characteristics of devices prepared with different sputtering conditions.

6.3.3 Fabrication success rate and total device resistance

After the characterisation of 75 graphene FETs fabricated with different configurations and sputtering conditions, the success rate of device fabrication, which refers to the ratio of devices with no Au bridges and ribbons between contacts or at the edges of contacts / total devices fabricated, together with their R_{total} and $R_{contact}$ have been presented in Fig. 6-3. When the Au contacts are fabricated with the normal sputtering, a low fabrication success rate of 17%, a R_{total} range of 540 kΩ µm - 2 MΩ µm and a $R_{contact}$ range of 260 - 940 kΩ µm can be seen due to difficulties in the lift-off process. As an improvement of using a shielding tube, the fabrication success rate was significantly increased to 90% with the R_{total} and $R_{contact}$ decreased to 26 - 400 kΩ µm and 10 -180 kΩ µm, respectively. Using both an optimised sputtering configuration and deposition parameters, not only a high fabrication success rate of 90% was achieved, but also a further reduced $R_{contact}$ down to 1.04 kΩ µm was obtained, which is much lower than that of devices fabricated with the normal sputtering technique and competitive with that of devices fabricated with the e-beam technique [38, 267]. An overview of the success rate, R_{total} and $R_{contact}$ of devices fabricated with different sputtering configurations and parameters have been summarised in Table 6-1. It is noted that the conclusion might be contradictory to that of other works [274, 275], which is due to the different metal materials used in the fabrication of the electronic contacts. Metals used for the formation of electronic contact can be categorised into physisorbed, such as Au as in this chapter, and chemisorbed, such as Ti [283], Pd, Ni or Cu in those references, which could chemically interact with those defects and disorders distributed within the graphene plane during annealing, leading to a much lower contact resistance [284]. The Au contact is inert with graphene even at the elevated temperature [284], therefore the decreased total resistivity and contact resistivity in this work can only be attributed to the reduced damage to graphene underneath the metal. Also, according to these measurements, no particular dependence

has been found between conductivity modulation/carrier mobility and the Au deposition conditions within the range of the discharge power of 20-50 W and the Ar pressure of 4-20 mTorr. This is because the conductivity modulation depends on many factors, such as the quality and state of the graphene channel, the interaction between the substrate and the graphene and the amount of residues on the graphene, the contribution from graphene underneath the Au contacts is only one of these many factors.

Figure 6-3 has been removed due to Copyright restrictions.

Figure 6-3. Statistics of total resistance and contact resistance of devices fabricated with normal configuration (group 1), using shielding tube (group 2) and with both a shielding tube and optimised sputtering parameters (group 3).

Table 6-1. Summary of success rate, total resistivity and contact resistivity of devices fabricated with different configurations and sputtering parameters.

Table 6-1 has been removed due to Copyright restrictions.

Because the Keithley 2602A is setup in the ambient environment, most of the as-fabricated devices show positively shifted Dirac points, locating from 5 to 20 V, which can be attributed to the doping effect caused by polymer residuals generated during the fabrication process, water and O_2 absorbed on the graphene channel [2, 3, 49, 285].

6.3.4 Effects of annealing in vacuum to graphene transistors

Fig. 6-4 (a) shows Raman spectra obtained before and after the thermal annealing in a vacuum of 10^{-7} mTorr (all the devices were measured under ambient conditions without specific illustration throughout this report). As previously reported [252], the spectrum of graphene mainly comprises three peaks. The 2D peak around 2680 cm^{-1} corresponds to the second order of boundary phonons. The G peak around 1580 cm^{-1} is due to C-C sp^2 bond stretching, and the D peak which is invisible for perfect graphene, can be induced by defects or disorders. Here, no significant difference can be found between the G bands, 2D bands and G/2D intensity ratios of two curves shown in Fig. 6-4 (a), indicating no structural changes occur during the annealing process. However, compared with the one obtained before annealing in a vacuum, the intensity of the D band and its corresponding integral area decreased after annealing, implying that defects

or disorders caused by the fabrication process have been repaired or removed to some extent. Fig. 6-4 (b), (c) and (d) show comparisons of I_d-V_g curves measured before and after annealing in a vacuum with source-drain voltages of 0.2, 0.5 and 1 V, respectively. This presents a trend that both mobility and gating efficiency increased. For example, mobility increases from 1600 $cm^2/V{\cdot}s$ to 3700 $cm^2/V{\cdot}s$ and gating efficiency increases from 1.8 to 2.3 as shown in Fig. 6-4 (b). Besides, the Dirac points shift from 40 V+ to around 18 V after annealing under vacuum, implying a decreased doping level, which is due to the partly evaporated absorbents, e.g. O_2, water, LoR and photoresist residues here [286] and improved metal/graphene or a substrate/graphene interface [274, 287]. The reason for non-zero Dirac points obtained before annealing are attributed to the same residues and absorbents on graphene channel as devices are measured under ambient conditions.

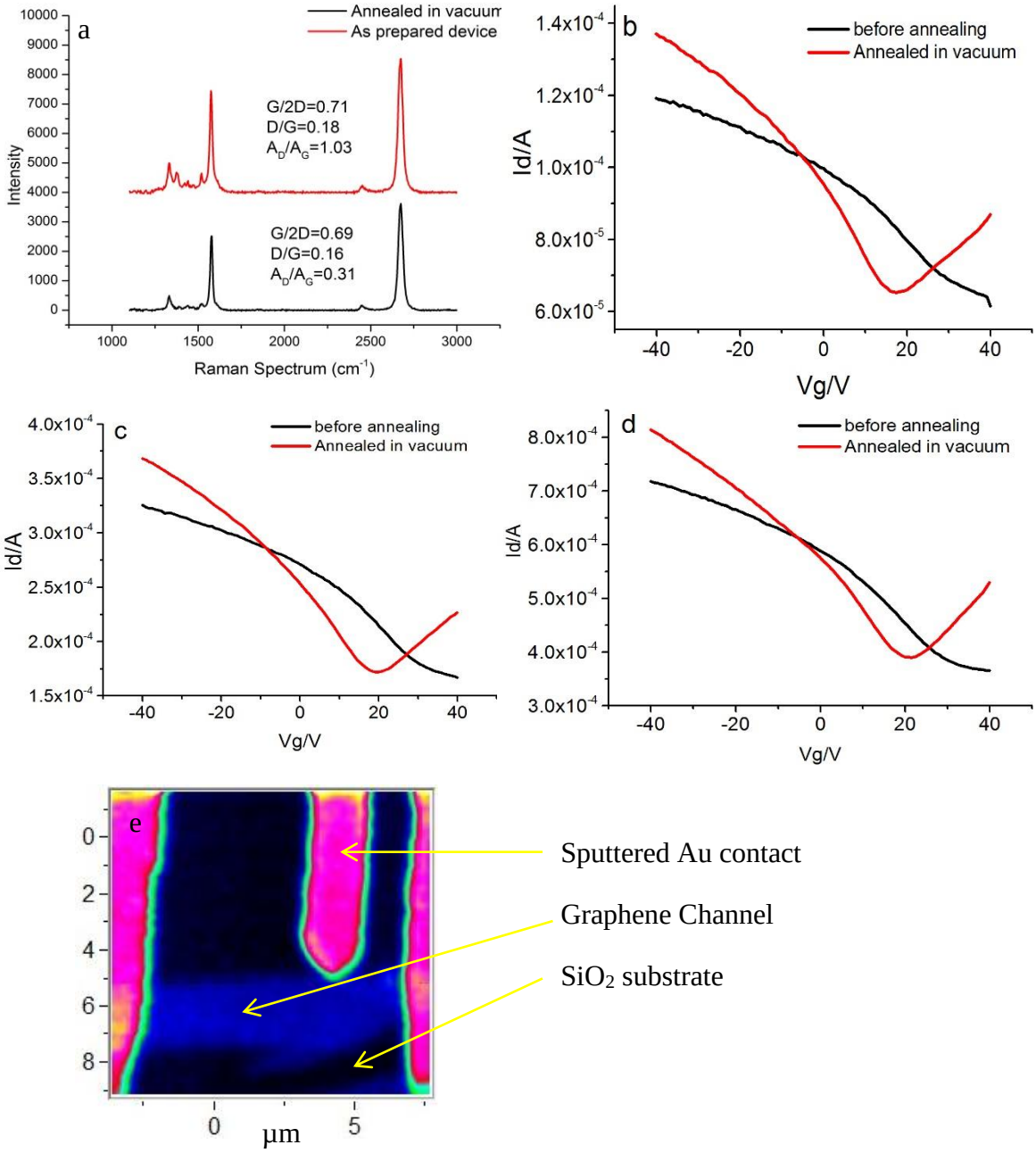

Figure 6-4. Effect of thermal annealing on the characteristics of graphene FET. (a) Raman spectra of a graphene channel before and after annealing in vacuum at 300 °C. (b), (c) and (d) I_d-V_g curves of FET measured before and after annealing in vacuum with a source-drain voltage of 0.2 V, 0.5 V and 1 V, respectively. (e) Raman mapping of 2D band on the device channel, unit µm.

Fig. 6-4 (e) present a Raman mapping of the 2D band of a device measured shown in Fig. 6-4, showing regular and uniform graphene channel, which indirectly proves the effectiveness of the fabrication process. To investigate the difference before and after

annealing in vacuum, the morphology of the graphene channel has been characterised by AFM, as shown in Fig. 6-5 (a) and (b). It can be seen that the thickness of exfoliated graphene on a SiO_2 substrate was about 1.4 nm before annealing and reduced to 0.8 nm after annealing, indicating the vacuum annealing compressed the dead space between the graphene and the substrate [286] and may enhance the interactions between the graphene and SiO_2 layer.

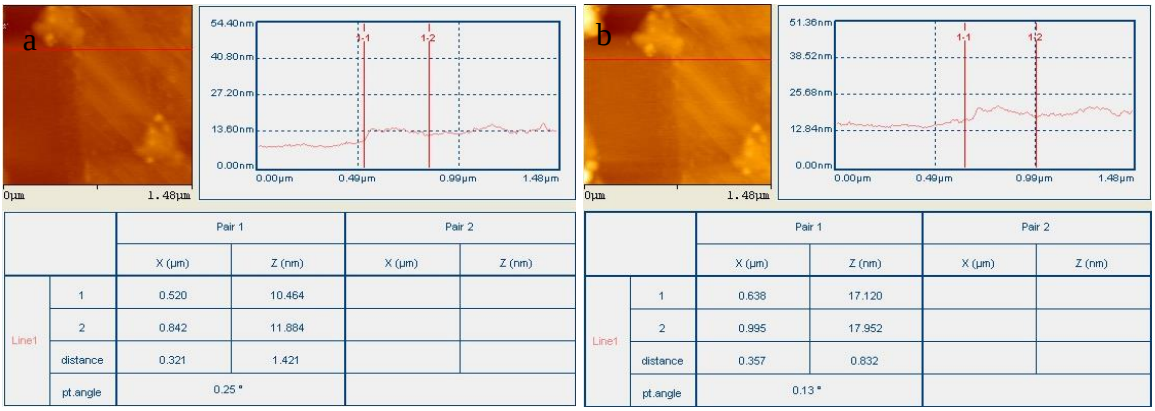

		Pair 1		Pair 2	
		X (μm)	Z (nm)	X (μm)	Z (nm)
Line1	1	0.520	10.464		
	2	0.842	11.884		
	distance	0.321	1.421		
	pt.angle	0.25 °			

		Pair 1		Pair 2	
		X (μm)	Z (nm)	X (μm)	Z (nm)
Line1	1	0.638	17.120		
	2	0.995	17.952		
	distance	0.357	0.832		
	pt.angle	0.13 °			

Figure 6-5. AFM image and thickness measurements of graphene channel (a) before and (b) after annealing in vacuum.

6.3.5 Effects of annealing in an Ar environment on a graphene transistor

To demonstrate the effects of annealing at atmospheric pressure, the high purity Ar gas was inlet to prevent the graphene getting oxidised and keeping the temperature at 300 °C for 3 h. As shown in Fig. 6-6 (a), the results of the Raman spectra are similar to those of annealing in a vacuum. The D/G band intensity ratio decreased from 0.07 to 0.03 and no significant change can be found with the G/2D band intensity ratio, confirming that thermal annealing in Ar can also repair the graphene crystals to some extent. However, in Fig. 6-6 (b), (c) and (d), it can be seen that the total resistance decreases nearly 50% compared with those of before annealing and the Dirac point shifts positively to 40 V+, implying the higher doping level caused by the accumulation of excess holes. These results coincide with previous reports [179]. The mechanism for

decreasing resistance is the same as those for annealing in vacuum, which is attributed to the partly evaporated absorbents but the different behavior of Dirac point have not been explained before. This will be discussed in relation to the data shown in Fig. 6-7.

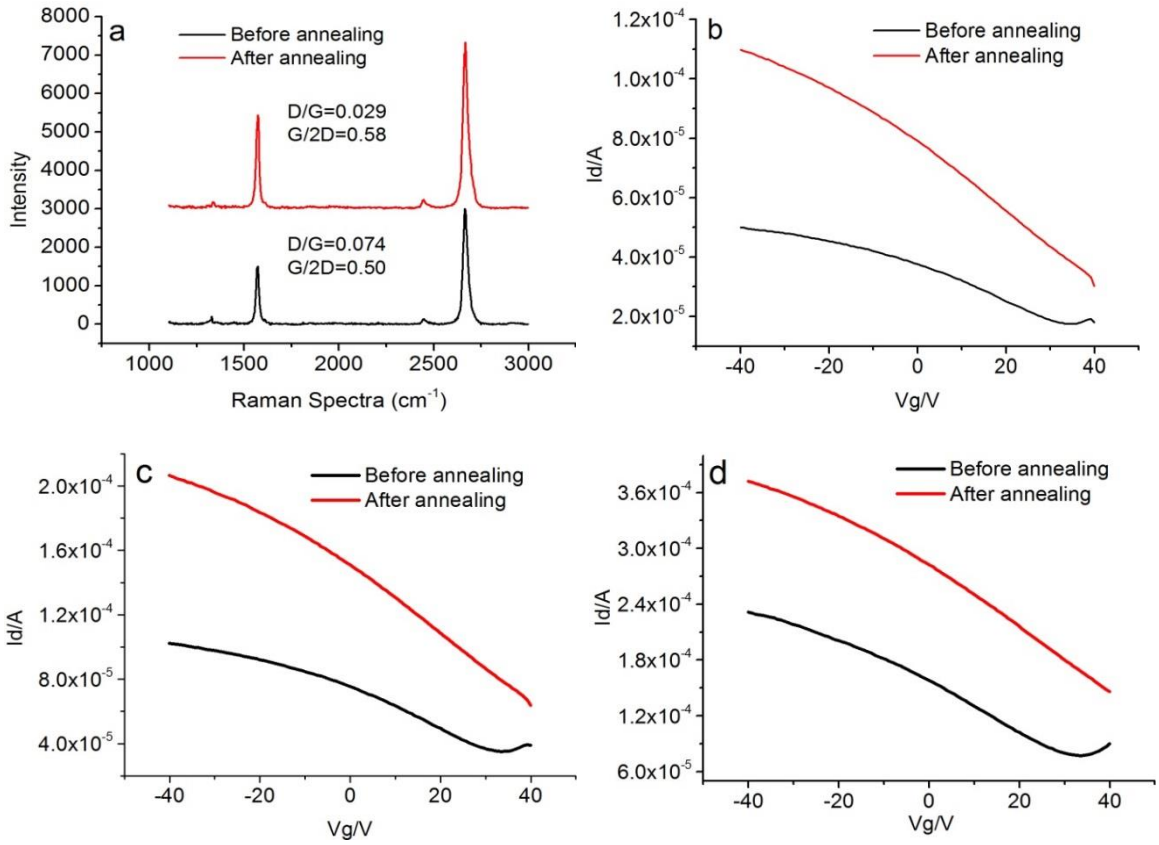

Figure 6-6. Raman Spectra of graphene before and after annealing in an Ar atmospheric pressure and the dependence of FET electrical property changes with annealing in Ar. (a) Raman Spectra of a graphene channel before and after annealing in Ar at 300°C for 3h. (b), (c) and (d) I_d-V_g curves of graphene transistors measured before and after annealing in Ar with a back gate voltage of 0.5V, 1V, 2V, respectively.

6.3.6 Post Cleaning

The sensitivity and activity of graphene channels have been considered as the most important characteristic for graphene-based sensors. Freshly prepared devices have been used to demonstrate the effects of chemical cleaning, exposure to air and vacuum

cleaning. Fig. 6-7 (a) shows Raman spectra obtained from an as-prepared graphene transistor (black) and those obtained after the chemical cleaning process (blue) and exposure to air (red), respectively. For as-prepared graphene, a low G/2D ratio (around 0.5) with a negligible D band indicates the high quality of this device. After the chemical cleaning processes or 4 h exposure in air, there is neither a visible D band nor changes of the G/2D band intensity ratio observed, indicating that no structural or electronic defect has been induced by adsorption and the cleaning processes. This is attributed to O_2 (or other gaseous molecules from air), water and photoresist molecules that are trapped or absorbed by a graphene channel t hrough Van der Waals' force (physically attached to a graphene channel), without breaking or affecting sp^2-hybridised C-C bonds. It can be seen in Fig. 6-7 (b) that the Dirac point shifts gradually towards a negative voltage with longer chemical treatment, indicating the reduced LoR and photoresist residues on graphene channels. Also, the Dirac point stops around 18 V after 2 hours of the chemical treatment, which is coincident with the previous report that the complete removal of polymer residues is impossible to achieve [286]. Fig. 6-7 (c) presents the effects of exposing air to graphene transistors. As a result of adsorption on a graphene channel, the Dirac point shift towards a positive voltage gradually and finally stop around 40 V. Compared with the positive shift caused by water and photoresist molecules, it can be restored by vacuum pumping as shown in Fig. 6-7 (d), confirming adsorption from air that are physically attach onto the graphene channel. This phenomenon, in a sense, explains how the transport characteristics measured after annealing in vacuum are different with those measured after annealing in Ar. (1) During the few hours of the pumping stage before the thermal annealing in a vacuum, absorbed gaseous molecules desorbed from the graphene channel. Water and organic molecules are partly evaporated by the following annealing stage. (2) In contrast, annealing at atmospheric pressure will not lead to desorption of gaseous molecules before thermal

annealing, which may react with organic residues or trap more gaseous molecules at high temperature, in turn results in a higher doping level.

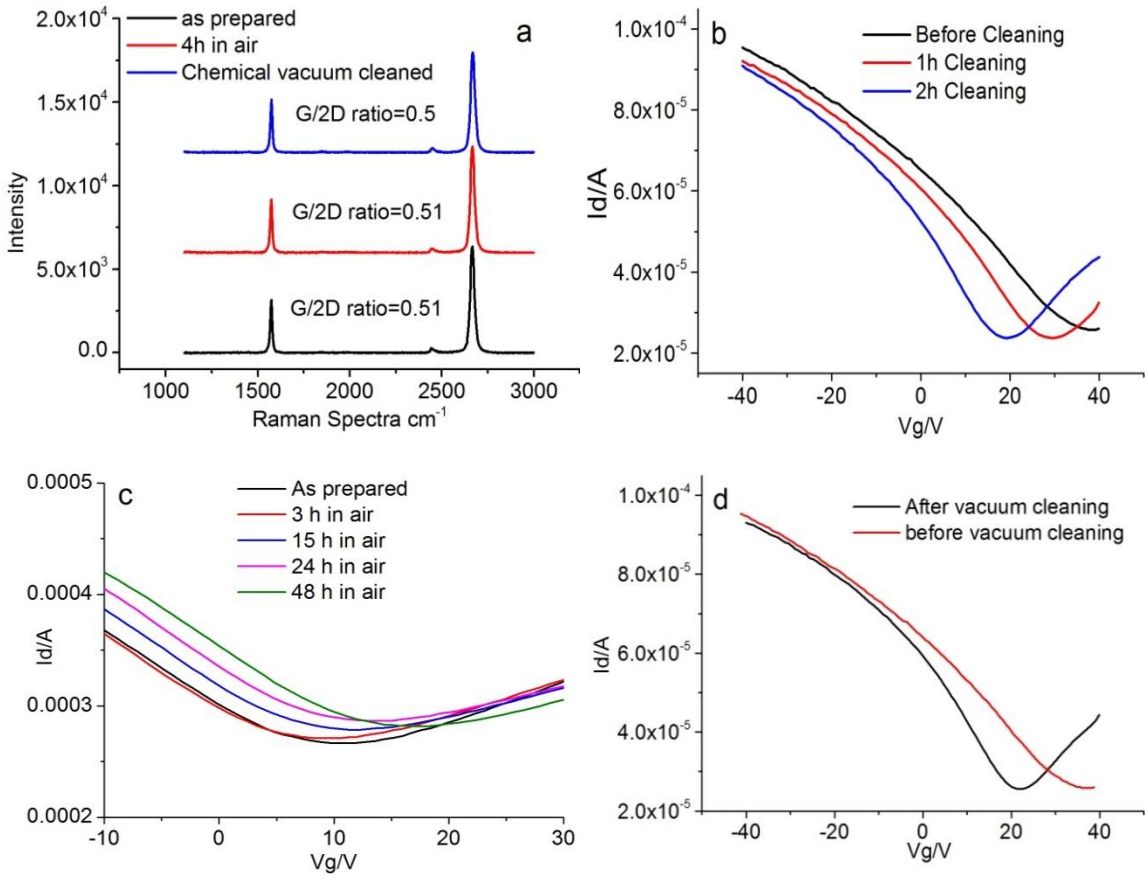

Figure 6-7. Dependence of electrical property changes with chemical cleaning and exposure in air. (a) Changes of Raman spectra caused by chemical cleaning and exposure in air, respectively. (b) Effect of the chemical cleaning process to I_d-V_g curves of graphene transistor, source-drain voltage is 500 mV. (c) Effect of exposure in air to I_d-V_g curves of graphene transistor, source-drain voltage is 500 mV. (d) Effect of vacuum cleaning to I_d-V_g curves of graphene transistor, source-drain voltage is 500 mV.

The SEM image from a graphene channel before and after a proper post-cleaning process is shown in Fig. 6-8. From Fig. 6-8 (a), it can be seen that the as-prepared graphene device is contaminated by a lot of nanometer scale particles, such as the residues of photoresist and fragments of graphite, which in turn affected the electronic

performance of one graphene FET. In contrast, after chemical vacuum cleaning, it can be seen that there are no observable particles adsorbed on the graphene channel, even as the magnification increases (as shown in Fig. 6-8 (b)). A protuberance, which forms at the edge of the Au contacts with nanometer scale cracks, can be identified and this is normally the reason leading to a lift-off problem in conventional sputtering configuration. The protuberance then spreads downhill to the graphene sheet showing a narrow gold ribbon, implying that Au atoms are deposited onto graphene via disordered trajectories.

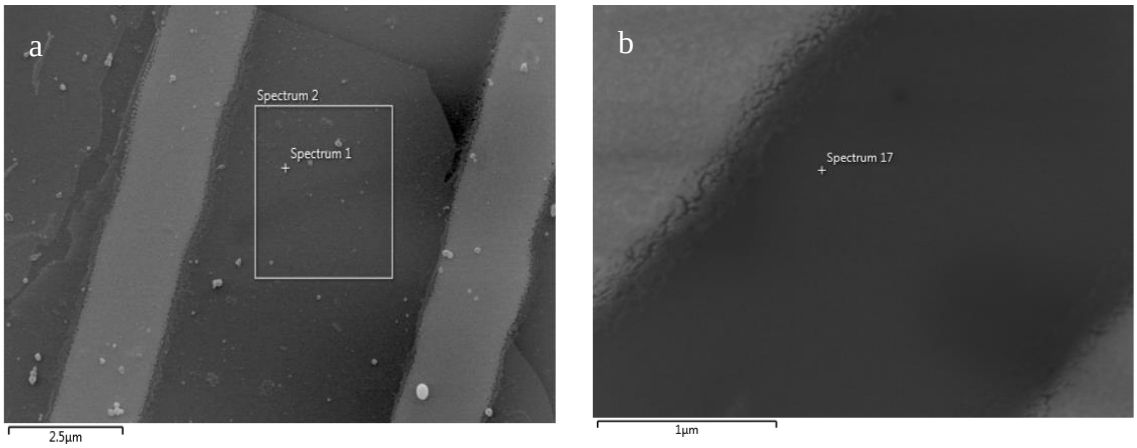

Figure 6-8. SEM image from the channel of a graphene FET (a) before and (b) after the post cleaning process. The scale bar is 2.5 µm in image (a) and 1 µm in image (b).

There are a few points that need to be clarified: (1) the estimation of mobility could introduce an uncertainty when the V_g is above 40 V, which is limited by our instrument. (2) Most of our as-prepared devices show positively shifted Dirac points, from 5 to 20 V, which is in line with effect caused by organic residuals, water and O_2 from the fabrication process [2, 3, 10, 285]. Devices showing higher doping level above are used to demonstrate the variation tendency of different treatment in this chapter. (3) As the Keithley 2602A measurement system is set up in ambient environment, the cleaned devices in this chapter still show slightly p-doped behavior which is caused by gaseous

absorption on graphene. (4) Compared with thermally evaporated contacts, the Cr layer, which have commonly been used to improve adhesion between Au and SiO_2 [283], has been found unnecessary in our configuration. This is attributed to room temperature sputtering which could minimise thermal expansion difference between the Au film and the Si substrate. The absence of Cr will be a novel way to enhance the performance of graphene transistors.

6.3.7 CVD Graphene patterned with Ion-milling Etching

The qualities of graphene patterned by the normal and the modified ion-milling etching have first been characterised by the optical microscope. Fig. 6-9 (a) shows the graphene channel patterned by the normal ion-milling and the lithography process. It can be seen that the unwanted graphene has been completely etched away; however, the photoresist and LoR used for masking purposes remained after the standard chemical cleaning process (shown as cyan colour in Fig. 6-9 (a)), which acts as an insulating layer on top of the graphene, leading to the failure of the device. To help in removing this resist layer, a magnetic stirring step has been applied during the lift-off process in the Photoresist Remover. Although it has helped in the removal of the resist layer to some extent (60% resist lifted off, as shown in Fig. 6-9 (b)), the quality of the resulting graphene channel is still far from acceptable for the fabrication of graphene electronic devices. In contrast, after the graphene was etched by the modified ion-milling process, the resist layer on the graphene channel can be completely removed by the standard lift-off process, as shown in Fig. 6-9 (c). In this case, neither the polymer residue nor visible cracks on the film can be optically seen throughout the whole channel area of the resulting electronic device after a thorough cleaning process, as shown in Fig. 6-9 (d).

The qualities of graphene patterned by the normal and the modified ion-milling etching have also been characterised by Raman spectroscopy. Compared with that taken from

graphene patterned by the modified ion-milling etching, a strong band around 1540 cm^{-1} can be seen in the Raman spectrum taken from graphene patterned by the normal method, as shown in Fig. 6-9 (e), indicating the existence of polymer residues. A high-resolution Raman mapping of the D band across a graphene channel area of 35 x 35 µm shown in Fig. 6-9 (d) has also been provided in Fig. 6-9 (f). The higher intensity dots showing red and yellow in colour are standing for the atomic damage within the graphene lattice, which has a similar defect density with that of graphene before patterning, indicating the non-destructive nature of this modified ion-milling etching technique.

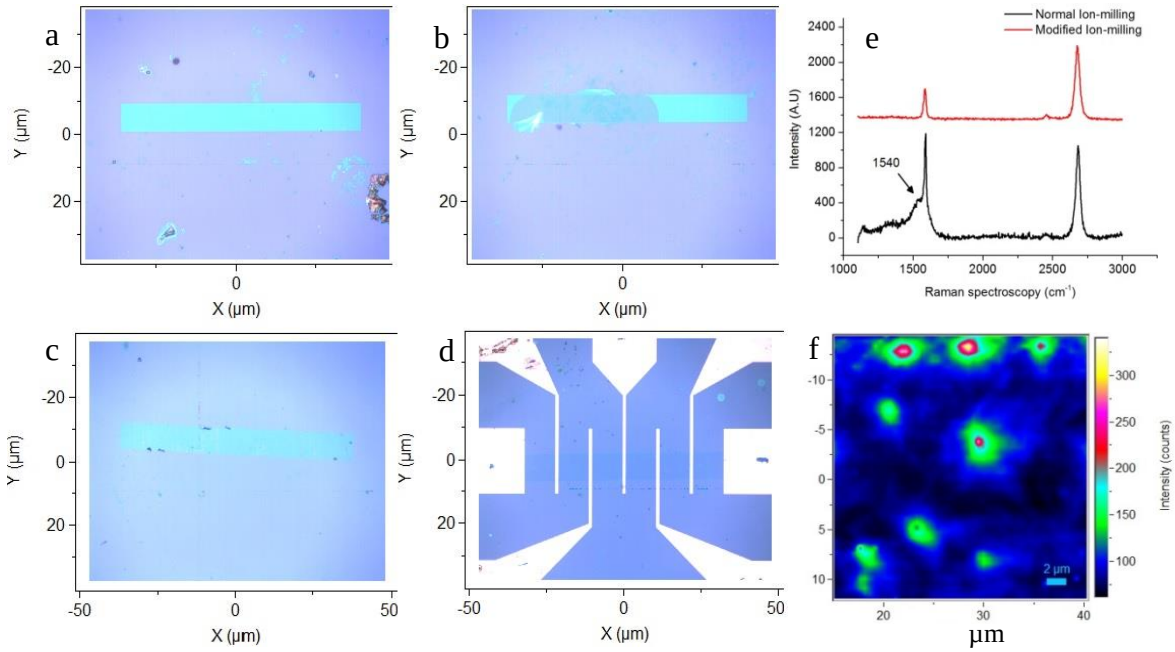

Figure 6-9. Optical and Raman characterisation of ion-milling patterned graphene. CVD graphene patterned by (a) normal, (b) stirring remover and (c) DUV baking ion-milling methods. (d) FET fabricated using graphene from (c). (f) Raman mapping of D band across 35 x 35 µm area, scale bar is 2 µm.

6.3.8 Cross-section Analysis of the UV Baking Effect

A comparison of the cross-section profiles of the photoresist-LoR bilayer with and without pre-DUV baking before ion-milling etching is provided in Fig. 6-10 to explain the mechanism of this successful lithography process. Fig. 6-10 (a) shows the cross-section image of ion-milled resist layer without pre DUV baking. Both of the photoresist and the LoR layer were rectangular with sharp edges after the developing process. However, it can be seen that after the ion-milling process, the edge of the photoresist has become rounded and the boundary between the photoresist and LoR is distinguishable, implying a melting and soften process of the photoresist during the ion-milling etching. In addition, there is an outer layer that can be seen on the surface of the photoresist, which comes down to the surface of the substrate along the side walls of the photoresist-LoR layer, as indicated by the arrows. As a contrast, the cross-sectional image of the ion-milled resist layer with pre DUV baking is presented in Fig. 6-10 (b). However, neither the hardened outer layer on the surface of the photoresist-LoR layer nor the visible photoresist-LoR boundary can be seen in this case, although the edge of photoresist was also softened and rounded.

The mechanism here is: the flow temperature of our photoresist 1805 G2 here is about 130 - 135°C. When the Ar ion is bombarding the surface of the photoresist without pre-DUV baking, the local temperature could reach a few hundred even thousand degree Celsius, which heats up the photoresist and leads to a thermal flow within the outer layer of photoresist. In this case, the outer layer of the photoresist, particularly at the edges, melts and then forms a hardened shell (thermally cross-linked photoresist), which goes right through to the SiO_2 substrate and links up the substrate, preventing the photoresist-LoR from lifting off in the later steps. In contrast, when the sample was exposed to DUV at 180 °C before the ion-milling etching, the whole photoresist layer becomes thermally cross-linked and hardened very quickly before it flows onto the SiO_2

substrate. This prevents the formation of a hard shell at the high local temperature during the ion-milling process and in turn maintains the integrity and strippability of the photoresist features. It is also notable that this pre-treatment can be transferred and applied to the plasma etching of graphene, such as sputtering etching.

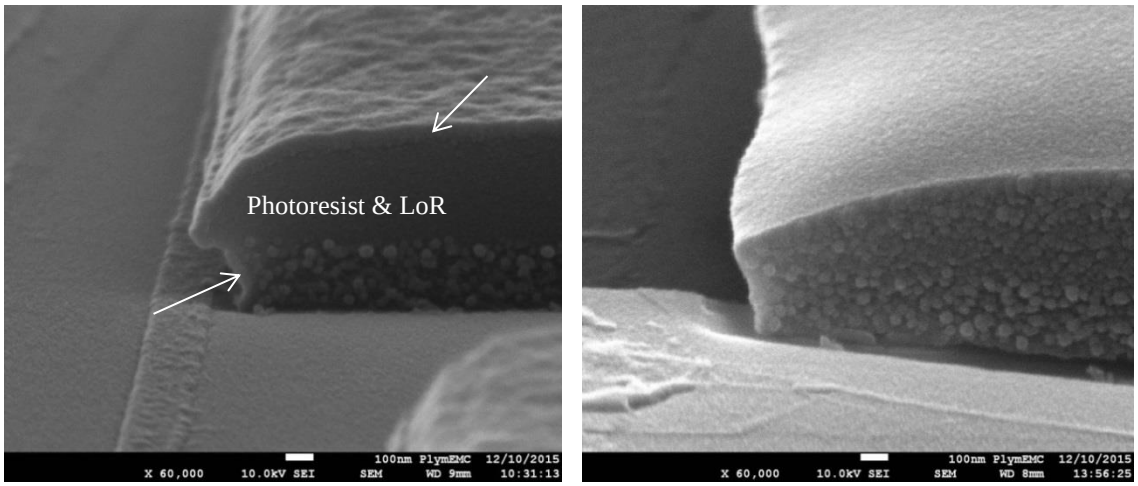

Figure 6-10. Cross-section analysis of photoresist-LoR layer (a) without and (b) with DUV baking before ion-milling process.

6.4 Conclusions

The superiority of using a shielding tube in the normal sputtering configuration to overcome the difficulties in the lift-off process during the practical fabrication has been demonstrated. The damage to the graphene caused by the sputtered Au at different Ar pressures and discharge powers has also been systematically investigated. By taking advantage of both an optimised sputtering configuration and deposition parameters, the success rate of device fabrication has been significantly improved; the graphene/Au junction at the electronic contacts has been better defined and also better electronic performance of resultant devices, such as lower R_{total} and $R_{contact}$, have been achieved. Although further work toward fully understanding the Au-graphene interaction and adhesive metal-graphene interaction is required, this technique has increased the choice

of deposition tools for the fabrication of the Au contacts on the graphene film. In addition, the mechanisms of removing of different residues with different methods have also been studied and the annealing in vacuum presents less negative effects to the properties of pristine graphene.

Also, the feasibility of using this novel ion-milling and lift-off process for the patterning of CVD graphene on a SiO_2 substrate has been illustrated. The mechanism of this technique has been attributed to avoiding the formation of the hardened outer layer, which linked up the photoresist layer and the substrate during the ion-milling process. The damage to graphene caused by this technique is minor, which is competitive with other patterning methods. This technique can also be applied to sputtering etching, which enlarged the tool choices for graphene patterning which made the fabrication of graphene devices more integrated with current semiconductor industries.

Chapter 7 Functionalisation of Graphene Surface

7.1 Introduction

Graphene-based nanocomposites have gained great research interest due to their large surface to volume ratio, high electrical conductivity, chemical inertness and biocompatibility [288-290]. For electrochemical applications, the electrocatalytic activities of the surficial materials on the working electrode are crucial. So far, electrodes modified with graphene [166], rGO [226], GO [157] and rGO/PAA nanocomposite [292] have been reported towards various applications, such as the detection of antigen, glucose, oxygen, DNA bases. However, the surface of pristine graphene is chemical and biologically inert in most cases, which is due to the absence of hydrophilic groups. Furthermore, the heterogeneous electron transfer between graphene and electrolytes in solution is at present regarded mostly to occur at the edges or defective sites on the graphene plane [293], which limits its application in the electrocatalytic analysis. Therefore, one of the key processes in the fabrication of electrochemical biosensor is to improve the functionalisation of the graphene surface [163]. The purpose of graphene functionalisation is to achieve a hydroxyl, carboxyl or amino terminated medium, which is highly hydrophilic and a compatible surface with most biomolecules so that probe molecules can be immobilised onto it by solvent-assisted techniques. The requirements of functionalisation are to obtain maximum chemically modified area and to retain the maximum outstanding electronic properties of graphene film.

In this chapter, the chemical hydroxylation of the graphene surface with two different methods have been developed and presented, respectively. The Fenton reaction, which used H_2O_2 and iron sulphate, has been successfully repeated, showing a high oxidation effect. However, the Fenton reaction is too harsh to be used for the functionalisation of

graphene electronic devices as the thin metal film can be seriously damaged by oxygen free radicals. A milder hydroxylation method using $KMnO_4$ has also been carried out, see 4.5.1.2. In this case, no observable damage has been found to the metal film, whilst the percentage of oxygen in the resultant hydroxylated graphene is lower. After hydroxylation, APTES and PAA have been used to achieve an amino functionalities terminated graphene surface, to where the antibody can bond. The graphene/rGO/PAA modified electrode shows an improved electrochemical activity for the reduction of H_2O_2. The resultant amino-terminated electrode can be used as a platform for oriented bonding to the –COOH functionalities in the Fc region of the antigen molecule, which provides a platform for the fabrication of the immunosensors.

7.2 Experiment

7.2.1 Materials and Instruments

Iron (II) sulphate ($FeSO_4$, catalytic agent), analysis grade *(Sigma Aldrich)*

H_2O_2 (30%), analysis grade *(Sigma Aldrich)*

$KMnO_4$, analysis grade *(Sigma Aldrich)*

APTES, 99% purity *(Sigma Aldrich)*

H_2O_2, 30% aqueous solution *(Sigma Aldrich)*

PAA, 20 wt% aqueous solution with molecular weight of 15,000 *(Sigma Aldrich)*

100 ml Beaker *(Fisher Scientific)*

Electronic balance with 0.0000 g sensitivity *(Sartorius BP1215, UK)*

Ethanol, 99.99% molecular biology grade *(Sigma Aldrich)*

DI water

Centrifuge with 3000 rpm speed *(Sigma 3-16KL, Germany)*

Vortex Shaker *(IKA VORTEX GENIUS 3, UK)*

7.2.2 Procedures and Characterisation

The production method of exfoliated graphene is detailed in 4.2. LoR and photoresist were spin-coated with the modified photolithography and lift-off process detailed in 4.4.1. The sputtering deposition of Au contacts was carried out using a shielding tube as detailed in 4.4.2.

For the hydroxylation, graphene flakes/powder was prepared from HOPG. One piece of HOPG (about 1 g) was firstly chopped by a scalpel to achieve small flakes. The resultant graphite flakes were added into 20 g/L sodium dodecyl sulphate (SDS) solution and kept exfoliating in the ultrasonic bath at 60 °C for 3 h. The graphene flakes/powder was then obtained through 3 times centrifugation/resuspension in DI water and dried in a vacuum oven (100°C). Both the Fenton reaction and hydroxylation with $KMnO_4$ were carried out following the mechanism and experimental details introduced in 3.1.1 and 4.5.1, respectively. The graphene/rGO modified electrode was introduced in 4.5.2. APTES and PAA were used for the Amination of hydroxylated graphene following the procedures introduced in 4.5.3 and 4.5.4.

For the reduction of H_2O_2, an H_2O_2 aqueous solution with a concentration of 30% (w/w) was diluted to 0.05 M by adding PBS buffer with a pH of 7.1. Blank PBS buffer of 20 µl was added onto the surface of electrodes modified with graphene, rGO, PAA and graphene/rGO/PAA respectively as references. Then, the surface of the electrodes were rinsed with DI water three times and dried in air at room temperature. 0.05 M H_2O_2 of 20 µl in PBS buffer was then dripped onto the electrodes accordingly. The scan potential in CV cycles ranged from 0.2 V to -0.6 V and the scan rate was 100 mV/s [292].

The quality of resultant graphene was evaluated by Raman spectroscopy, as detailed in 4.7.3. Surface morphologies of the FET devices were characterised by SEM, as detailed in 4.7.5. The chemical composition of the hydroxylated graphene was characterised by EDX, which is embedded in SEM, as detailed in 4.7.5. Chemical functionalities on top of graphene surface were characterised by FTIR, as introduced in 4.7.8. XPS was carried out following the details in 4.7.6. CV characterisation of the electrode was introduced in 4.7.4.

7.3 Hydroxylation with Hydrogen Peroxide

7.3.1 Raman Spectroscopy

Raman spectra obtained from pristine and hydroxylated monolayer graphene are shown in Fig. 7-1 (a), respectively. Compared with the one obtained from the pristine graphene, no observable difference in the relative intensities and positions of the G and 2D bands have been found from the spectrum obtained from the hydroxylated graphene. However, an increase of the D/G band intensity ratio from 0 to 0.13 can be observed, which indicates the defects or disorders have been introduced onto the graphene sheet. This is due to the electrophilic attacks of free HO· radicals, resulting in the opening of C=C bonds and partly losing of sp^2-hybridised structure [167]. Fig. 7-1 (b) presents the Raman mapping of the D/G band intensity ratio across the graphene channel (shown as dark blue color). It can be seen that the damage level is inhomogeneous across the mapped area, implying the concentration of –OH groups is inhomogeneously distributed. This may attribute to a different tension in the graphene sheet and the higher tension it has, the easier C=C bond breaks.

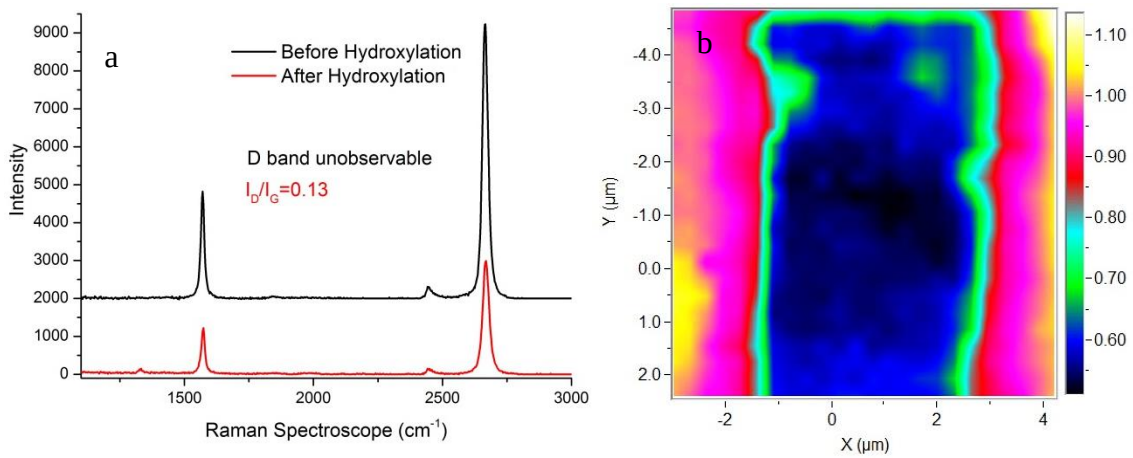

Figure 7-1. H_2O_2 Hydroxylated graphene. (a) Raman Spectra obtained before (black) and after (red) hydroxylation of graphene channel with H_2O_2. (b) Raman mapping of D/G band intensity ratio of FET graphene channel after the hydroxylation with H_2O_2.

7.3.2 SEM and EDX Characterisation

Energy Dispersive Analysis by EDX was used to investigate the hydroxylation of graphene with H_2O_2 from a view of the elemental composition. The acceleration voltage is set up at 5 kV to weaken the signals from the substrate and increase the proportion of element signals from surficially functionalities. A typical SEM image and EDX spectrum were taken from graphene channel (or SiO_2 substrate) which was subjected to the post cleaning process to avoid the signals from residues (shown in Fig. 7-2). As shown in Table 7-1, the points 1 and 2 were from pristine graphene and point 3 is from graphite flake (few layer graphene). The points 4 and 5 were from SiO_2 substrate as the references. The points 6, 7 and 8 came from graphene treated with Fenton Reaction for 30 mins. The relative atom number is calculated by equation:

$$\text{relative atom number} = \text{percentage of certain element}/\text{relative atomic mass}$$

It can be seen that data from the untreated graphene or the treated SiO_2 substrate show a similar O: Si atomic ratio of 1.84-1.86, which can be explained as a result of the

elemental ratio of SiO_2 substrate (the theoretical value of O: Si atomic ratio is 2). In contrast, an increase of O: Si atomic ratio from 1.85 to 1.96 can be observed from graphene channel treated by the Fenton Reaction, indicating the existence of hydroxyl groups on graphene surface (the increase of oxygen-containing groups here also include a very small percentage of carboxyl groups and carbonyl groups, however, hydroxyl group is dominant) [168]. The reasons of using O: Si atomic ratio instead of C: O atomic ratio is: the thickness of graphene, the dead space between graphene and SiO_2 substrate and the depth of electron beam went down are different for individual scanning, which result in the percentage of carbon element varies from one scanning to another. However, the O: Si atomic ratio of SiO_2 substrate should be constant as the molecular structure is homogeneous. In this case, no matter how the parameters mentioned above change, the “background” signal is kept as constant.

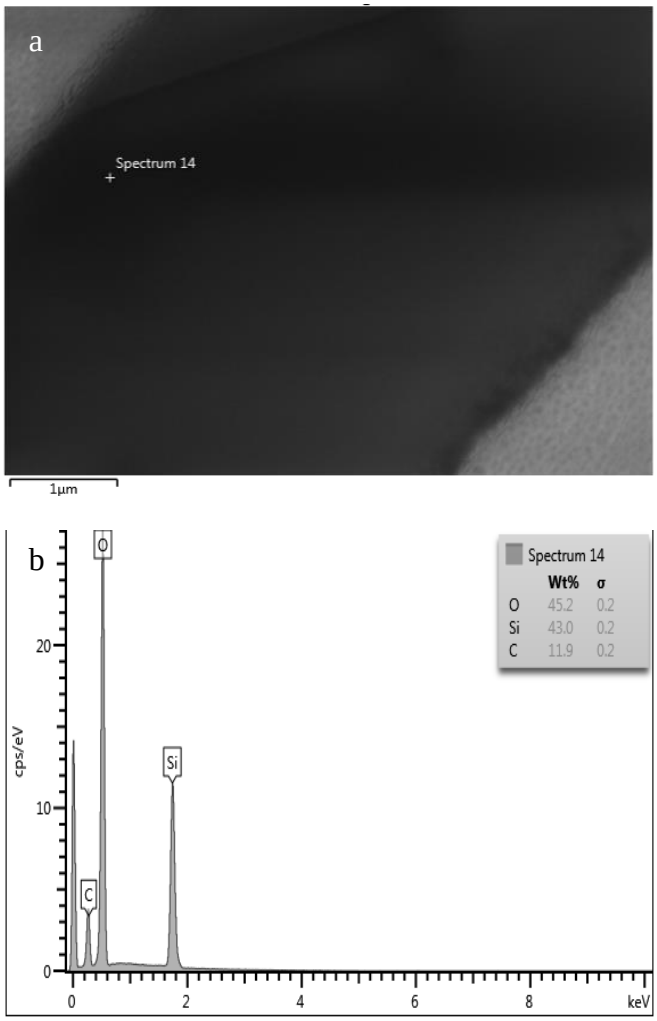

Figure 7-2. SEM analysis of hydroxylated graphene. (a) A typical SEM image of hydroxylated graphene channel and (b) corresponding elemental composition data. Scale bar in (a) is 1µm and error range is ±0.2% in (b). Referred as point 2 in Table 7-1.

Table 7-1. Elemental Analysis by EDX

Untreated graphene	Elements	Percentage (wt%)	Relative atom number	O: Si
Point 1	O	45.1	2.82	1.84
	Si	42.9	1.53	
	C	12		
Point 2	O	45.2	2.82	1.84
	Si	43	1.54	
	C	11.9		
Point 3 (flake)	O	36.6	2.29	1.86
	Si	34.4	1.23	
	C	29		
Treated SiO_2 wafer				
Point 4	O	49.8	3.11	1.85
	Si	47.1	1.68	
	C	3.1		
Point 5	O	48.2	3.01	1.77
	Si	47.9	1.71	
	C	3.9		
Treated graphene				
Point 6	O	41.3	2.58	1.96
	Si	36.9	1.32	
	C	21.8		
Point 7	O	44.5	2.78	1.93
	Si	40.5	1.45	
	C	15		
Point 8	O	40.8	2.55	1.96
	Si	36.4	1.30	
	C	22.8		

7.3.3 Fourier Transform Infrared Spectroscopy

FTIR is one of the most powerful techniques used to study the surface functionalities on graphene. Fig. 7-3 presents a comparison of FTIR spectra obtained before and after the Fenton Reaction. Compared to the spectrum obtained from pristine graphene, the increased peaks at 3428cm^{-1}, 1630cm^{-1}, 1380cm^{-1}, 1150cm^{-1} and 1040cm^{-1} are attributed to –OH stretching vibration, -C=O stretching vibration in quinone groups, -OH rocking vibration in carboxyl groups, -C-O stretching vibration in epoxy groups and C-O stretching vibration in alkoxy groups connected with carbon (initial peaks at 3428cm^{-1} and 1630cm^{-1} are attributed to water physically adsorbed on the sample surface and the C-C bond in graphene structure, respectively). From these results, it can be confirmed that a number of oxygen containing functionalities have been introduced onto the surface of graphene, which provide a possibility of the further attachment of bio-molecules.

The disadvantage of this technique is that the reaction is violent and strongly exothermic, peeling off the Au electrodes from the surface of the substrate and leading to damage to the devices. Therefore, an extra protective layer to an Au electrode is required using this technique.

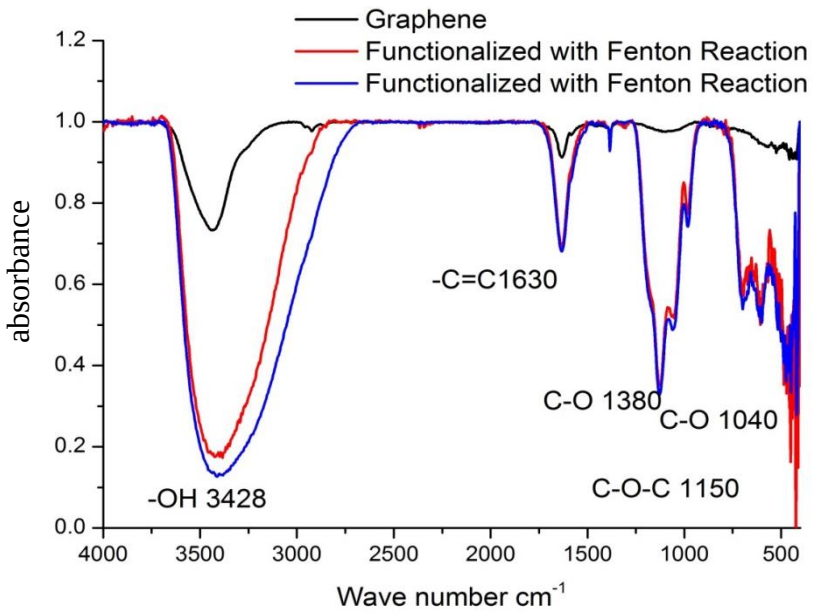

Figure 7-3. Comparison of FTIR spectra before (black) and after (red and blue) Fenton Reaction.

7.4 Hydroxylation with Potassium Permanganate

7.4.1 Raman Spectroscopy

Raman spectra obtained before and after the graphene hydroxylation with $KMnO_4$ are shown in Fig. 7-4. Similar with the results of the Fenton reaction, an increased I_D/I_G band intensity ratio can be seen together with the negligible changes in G and 2D bands, indicating that defects or disorders have been introduced onto graphene sheet.

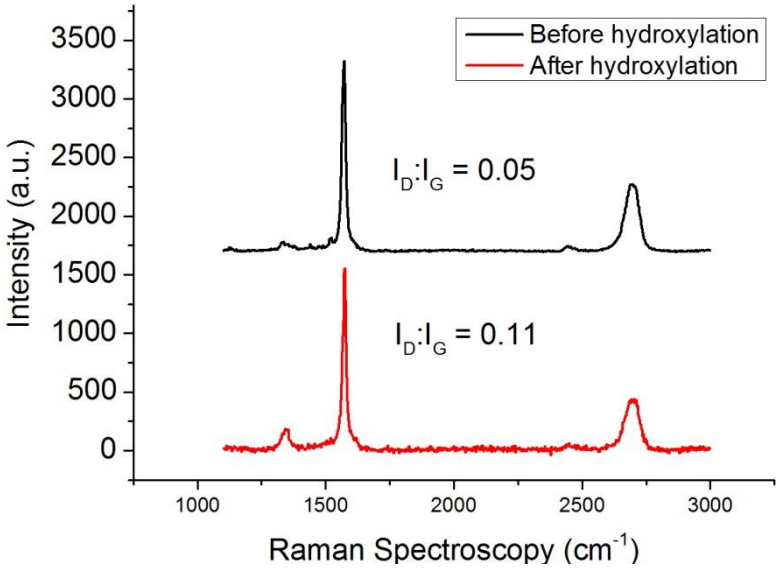

Figure 7-4. Raman spectra obtained before (black) and after (red) the hydroxylation with KMnO4.

7.4.2 EDX Characterisation

EDX was carried out to analyse the hydroxylation of a graphene surface with $KMnO_4$. An acceleration voltage of 5 kV was used to decrease the depth the electron beam goes into the sample. Six points and nine points were randomly chosen on the pristine graphene powder and the hydroxylated graphene powder with $KMnO_4$, respectively. It is worthwhile to note that the percentage of an individual element is shown as "atomic composition (at %)" in Table 7-2.

As shown in Table 7-2, the average O: Si atomic ratio slightly increased from 1.75 to 1.80 after the treatment of $KMnO_4$, indicating that the surface of graphene has been hydroxylated by the oxygen-containing functionalities. Again, there is a small portion of carboxyl groups and carbonyl groups existing except hydroxyl groups. The increase of oxygen is less than that in graphene hydroxylated by the Fenton Reaction, which can be explained by the lower effectiveness of $KMnO_4$ for the hydroxylation of graphene.

Table 7-2. Elemental Analysis of Hydroxylation Graphene with $KMnO_4$

Untreated graphene	Elements	Percentage (at%)	O : Si
Point 1	O	60.5	1.74
	Si	34.7	
	C	4.8	
Point 2	O	60.8	1.76
	Si	34.6	
	C	4.6	
Point 3	O	61	1.77
	Si	34.4	
	C	4.6	
Point 4	O	60.5	1.73
	Si	34.9	
	C	4.6	
Point 5	O	60.7	1.74
	Si	34.8	
	C	4.5	
Point 6	O	61	1.77
	Si	34.4	
	C	4.6	
Treated graphene			
Point 1	O	61	1.79
	Si	34	
	C	5	
Point 2	O	60.6	1.77
	Si	34.2	
	C	5.2	
Point 3	O	60.8	1.8
	Si	33.8	
	C	5.4	
Point 4	O	60.3	1.79

	Si	33.7	
	C	6	
Point 5	O	61.5	1.85
	Si	33.3	
	C	5.2	
Point 6	O	59.8	1.75
	Si	34.2	
	C	5.9	
Point 7	O	61.6	1.88
	Si	32.7	
	C	5.6	
Point 8	O	60.7	1.81
	Si	33.5	
	C	5.8	
Point 9	O	60.4	1.77
	Si	34.1	
	C	5.5	

7.4.3 Fourier Transform Infrared Spectroscopy

Fig. 7-5 shows a comparison of FTIR spectra obtained before and after graphene hydroxylation with $KMnO_4$. Compared to the spectrum obtained from pristine graphene, the peaks located at 3428 cm^{-1}, 1630 cm^{-1}, 1380 cm^{-1}, 1150 cm^{-1} and 1040 cm^{-1} have slightly increased, which are attributed the successful functionalisation of oxygen-containing groups (as detailed in 7.3.3). However, the effectiveness of hydroxylation with $KMnO_4$ is very limited, which is indicated by the small intensity difference of characteristic peaks before and after hydroxylation.

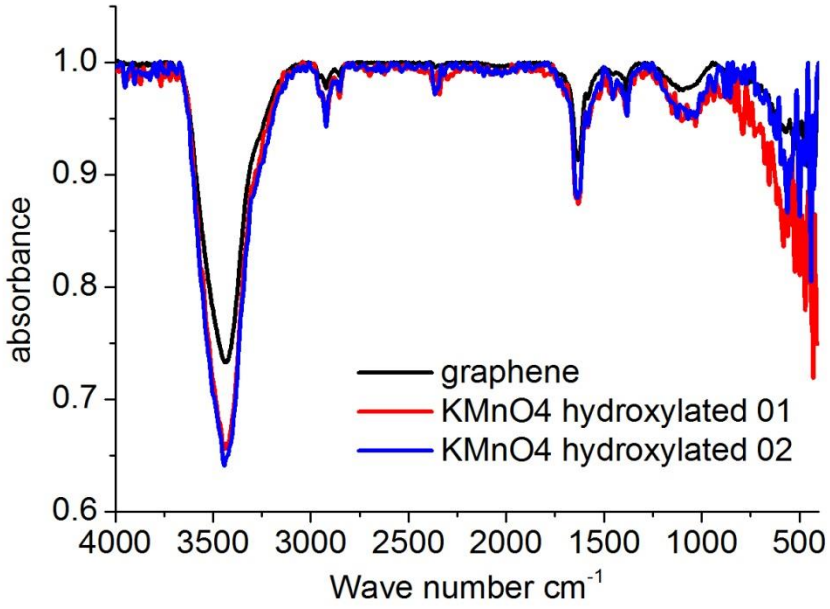

Figure 7-5. Comparison of FTIR spectra before (black) and after (red and blue) hydroxylation with $KMnO_4$.

7.5 Amination with APTES

7.5.1 XPS Characterisation

After the hydroxylation, the hydroxyl groups on the surface of graphene need to be converted into amino groups via an amination reaction, which provide the active sites for antibody to bond to. In this section, APTES has been used as the amination agents. The mechanism of amination and the experimental details have been introduced in 3.1.1 and 4.5.3.

XPS has been carried out for the semi-quantitative analysis of APTES amination, as spectra shown in Fig. 7-6. The black spectrum, which is obtained before the APTES treatment, shows the O (22.34%) and C (77.66%) in its elemental composition with undetected N and Si. In contrast, the red spectrum shows the O (27.38%) and C (67.53%) together with N (2.33%) and Si (2.76%), indicating the surface of hydroxylated graphene has been functionalised by the APTES molecules.

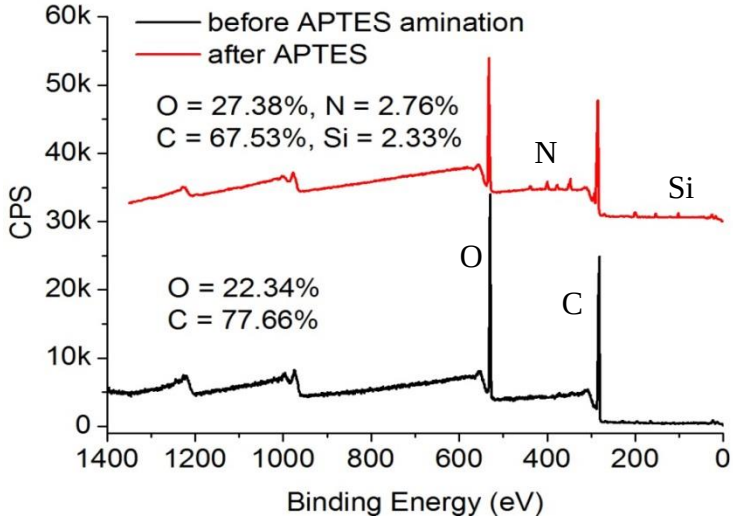

Figure 7-6. XPS analysis of graphene amination with APTES.

7.5.2 CV Characterisation

CV characterisation was carried out by using the working electrodes modified with hydroxylated graphene and APTES modified graphene respectively, as shown in Fig. 7-7. As a comparison before APTES amination, the I_{pc} decreased from 6.67 x 10^{-5} A to 5.16 x 10^{-5} A and the I_{pa} increased from -6.12 x 10^{-5} A to -5.32 x 10^{-5} A respectively, confirming that APTES has been immobilised onto the surface of hydroxylated graphene.

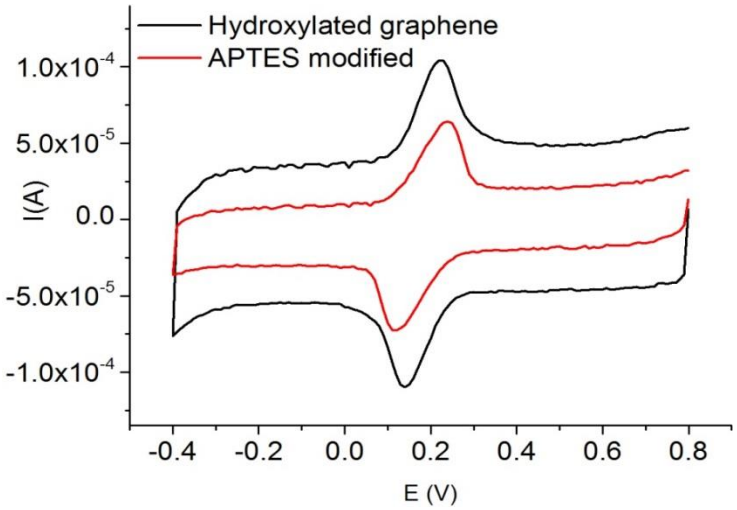

Figure 7-7. CV characteristics of hydroxylated and APTES modified graphene electrodes.

7.6 Amination with PAA and Electrochemical Performance for H_2O_2 Reduction

7.6.1 Fabrication of Graphene/rGO/PAA Tri-layer Electrode

A schematic illustration of the graphene/rGO/PAA tri-layer electrode assembly is shown in Fig. 7-8. The first stage of fabrication was to modify the graphene electrode with a thin layer of GO, thus yielding a large number of electroactive sites and –COOH functionalities on the surface of the electrode [294]. Then, PAA layer was assembled onto the top of GO via $–CONH_2$- bond and electrostatic adhesion, which not only provided a potential for immunosensor fabrication, but also acted as threads to crosslink GO films, preventing the graphene/GO layer coming off from the surface of the electrode during the electrochemical reduction. The graphene/GO/PAA electrode was subsequently subjected to the electrochemical reduction process to partially reduce the free oxygen-containing functionalities, which has not bonded with PAA but degrade the conductivity of the electrode.

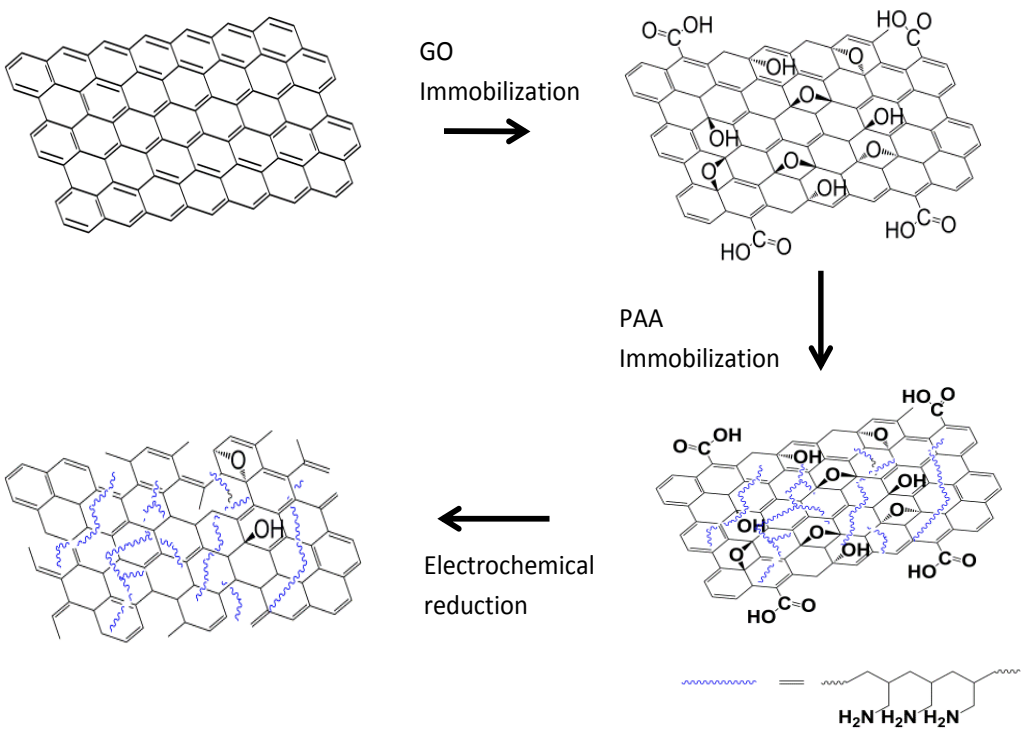

Figure 7-8. Schematic illustration of graphene/rGO/PAA tri-layer electrode assembly.

7.6.2 Characterisation of GO and PAA Modified Electrode

Raman Spectroscopy has been used to characterise the modification of GO and PAA layer on top of graphene. Fig. 7-9 (a) shows a comparison of Raman spectra obtained before and after the deposition of a GO layer on top of the surface of the graphene electrode. After the deposition of the GO layer, the increased intensity ratio of the D band to G band from 0.03 (red) to 0.98 (black) can be seen together with a significantly decreased 2D band, indicating that the number of defective sites on the surface of graphene/GO electrode has significantly increased [295]. However, compared with the spectrum obtained on graphene/GO electrode, no significant difference can be seen from that taken on graphene/GO/PAA electrode (shown as black in Fig. 7-9 (b)), which is due to the overlapped C-N/N-H characteristics at 1222 cm^{-1} and wide D band of GO centred at 1350 cm^{-1}. Fig. 7-9 (b) red shows the spectrum taken from a graphene/rGO/PAA tri-layer electrode. An increase of I_D/I_G from 0.94 to 1.35 can be

seen, which indicate that the GO has been effectively reduced during the electrochemical process [296].

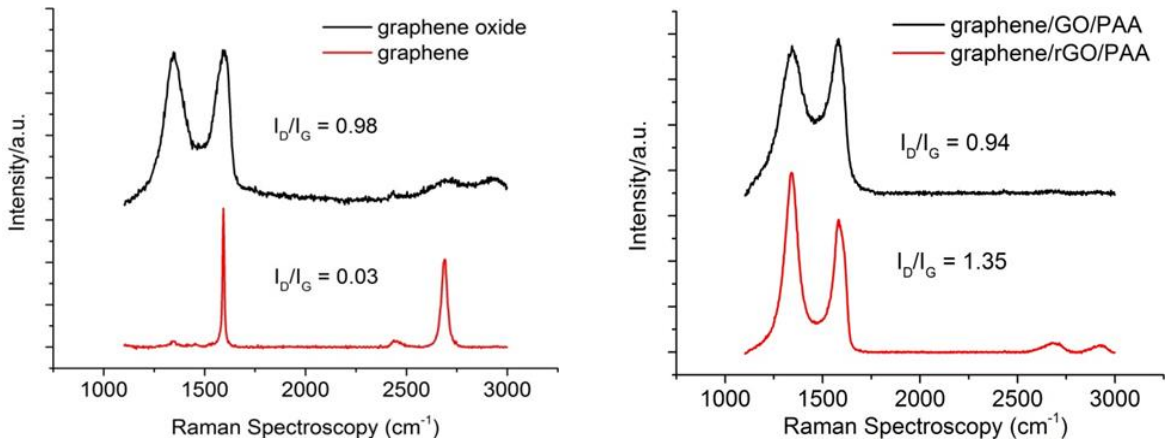

Figure 7-9. Raman characteristics of (a) graphene, graphene/GO (b) graphene/GO/PAA and graphene/rGO/PAA electrode, respectively.

XPS has been used to semi-quantitatively characterise the modification of GO and PAA layer. Fig. 7-10 (a) shows the wide survey spectra obtained from graphene and graphene/GO electrodes, respectively. A significantly increased O1s peak containing O-C=O at 531.5 eV, C-O at 532.9 eV and O-H at 534.5 eV (shown in inset Fig. 7-10 (a)) can be observed after the deposition of GO, indicating that the GO layer has been immobilised onto the surface of graphene electrode. Fig. 7-10 (b) shows the XPS characteristics of a graphene/GO/PAA tri-layer electrode before and after the electrochemical reduction. Both top and bottom spectra contain three main peaks, which are C1s located at 285.06 eV, N1s located at 401.08 eV and O1s located at 532.08 eV (K, Cl from electrolyte residues are not marked out on the spectra). The top spectrum shows N1s peak with an atomic ratio of 9.45%, indicating that PAA has been immobilised onto the surface of GO via amino bonding (-HN-CO-) and electrostatic forces. In comparison with the spectrum of a graphene/GO/PAA electrode, N1s from that of after electrochemical reduction process increased to 18.16 (at%), whilst O1s peak decreased from 14.92 (at%) to 7.06 (at%). The N1s regional high-resolution

spectrum of a graphene/GO/PAA modified electrode is shown in the inset of Fig. 7-10 (b). It consists of three major peaks centred at 401 eV, 399 eV and 397 eV, corresponding to N-H bond in PAA molecules, C-N bond in PAA-GO interface and PAA molecules, and Fe-CN from $K_3Fe(CN)_6$. From these results, it can be confirmed that GO has been effectively reduced whilst the PAA remained on the electrode surface. In addition, immobilisation of PAA caused some reduction effect to GO, which is in accordance with previous reports [297].

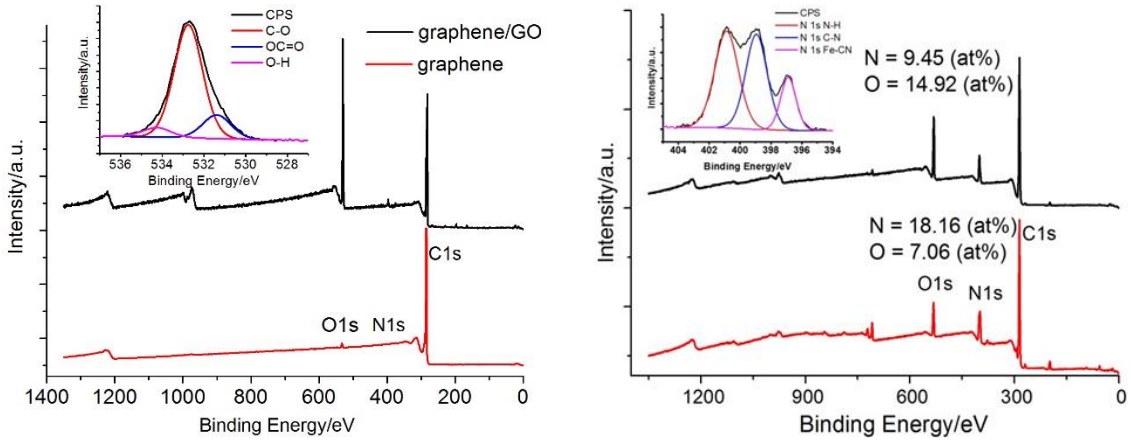

Figure 7-10. XPS analysis on differently modified electrodes. XPS characteristics of (a) graphene and graphene/GO (b) graphene/GO/PAA and graphene/rGO/PAA tri-layer electrode, respectively. Inset in (a): O1s spectrum of graphene/GO electrode, inset in (b): N1s spectrum of graphene/rGO/PAA tri-layer electrode.

7.6.3 Electrochemical Performance of Graphene/rGO/PAA Tri-layer Electrode in Ferricyanide

Fig. 7-11 (a) shows comparisons of the CV characteristics of four types of electrodes modified with graphene, graphene/GO, graphene/GO/PAA and graphene/rGO/PAA respectively. Compared with other electrodes, the superiority of using graphene/rGO/PAA tri-layer for electrode modification can be easily seen from this set of results. The CV curve of the graphene electrode (black curve) showed a cathodic

peak current (I_{pc}) value of 2.207 x 10^{-4} A and an anodic peak current (I_{pa}) value of -2.245 x 10^{-4} A. After the deposition of the GO layer, the redox currents intensities sharply decreased to 4.838 x 10^{-5} A and -4.844 x 10^{-5} A. And after PAA chemically/physically bonded onto the surface of GO, I_{pc} and I_{pa} were 2.116 x 10^{-4} A and -1.928 x 10^{-4} A. In contrast to all these, the graphene/rGO/PAA tri-layer electrode showed much higher values of I_{pc} and I_{pa} of 4.205 x 10^{-4} A and -4.485 x 10^{-4} A, respectively.

The decrease of current intensity after the deposition of GO is due to the stacking and bonding of GO onto the graphene surface, which is achieved via the interaction of π electrons provided by sp^2 hybridised carbon in the lattice of GO and graphene. The oxidised regions on the GO plane disturb the long-range conjugated carbon network and π-electron cloud, resulting in a degradation of electronic conductivity [216]. The increase of redox currents after the deposition of PAA layer was attributed to the electrostatic attraction between positively charged PAA molecules and negatively charged ferricyanide in the electrolyte solution. This leads to an enhanced redox process due to an accumulation of the electrolytes on the surface of the electrode; after the electrochemical reduction of GO, the redox currents again sharply increased due to the removal of oxygen-containing functionalities. The huge amounts of defects in a rGO layer inherited from GO acted as the electroactive sites to exchange electrons at the electrode interface and electrolytes. Therefore, compared with those electrodes modified with pristine graphene, graphene/GO and graphene/GO/PAA, the graphene/rGO/PAA tri-layer electrode had both a higher electron transport rate on the surface of the electrode and a higher electron exchange rate at the interface of electrode and ferricyanide system [298]. Quantitatively, the intensity of the redox current obtained on the graphene/rGO/PAA tri-layer electrode showed the increases of 99.8%, 826% and

132%, respectively, compared to that obtained on graphene, graphene/GO and graphene/GO/PAA modified electrodes.

The electroactive area of the differently modified electrodes was calculated using the Randles-Sevcik Equation [299]:

$$I = (2.69 * 10^5) A D^{1/2} n^{3/2} v^{1/2} C$$

where I is the redox current intensity with a unit of A, A stands for the electroactive area with a unit of cm^2, D stands for the diffusion coefficient of electroactive electrolyte in cm^2s^{-1}, n (which is 1 for $K_3Fe(CN)_6$) is the number of electrons transferred in the redox reaction, v and C are the scan rate in Vs^{-1} and the concentration of $K_3Fe(CN)_6$ in $molL^{-1}$, respectively. In this case, it can be found that the electroactive areas of corresponding electrodes above increased from 9.6 mm^2, 2.06 mm^2 and 8.22 mm^2 to 19.13 mm^2. Hence, the synergistic effect of using graphene/rGO/PAA in enhancing the electroactive area is significant.

Fig. 7-11 (b) shows the dependence of the redox peak currents on scan rates on a graphene/rGO/PAA tri-layer electrode. It can be seen all the CV characteristics presents highly symmetric redox peaks. The intensities of redox peak currents show a linear relationship with the square root of the scan rate (shown in the inset of Fig. 7-11 (b)), indicating this electron transport process was diffusion controlled and no adsorption phenomena for ferricyanide on the surface of the corresponding electrode, which was important for electrochemical applications.

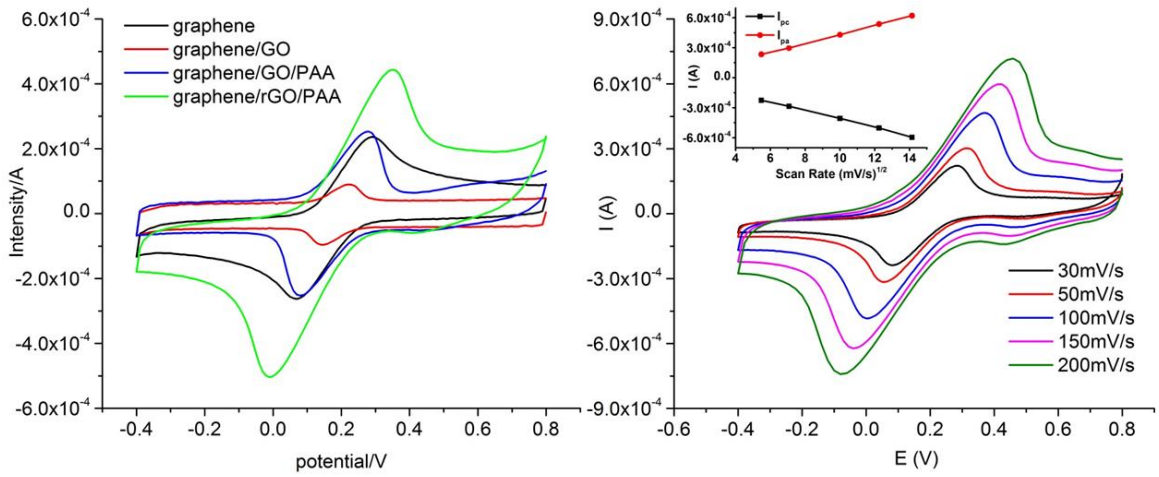

Figure 7-11. CV characteristics of (a) electrodes modified with graphene, graphene/GO, graphene/GO/PAA and graphene/rGO/PAA in 10 mM $K_3Fe(CN)_6$, respectively. Scan rate: 100 mV/s. (b) graphene/rGO/PAA electrode under the scan rates of 30, 50, 100, 150, and 200 mV/s. Inset: anodic and cathodic current peaks vs square root of corresponding scan rate.

7.6.4 Electrocatalytic Activity toward Reduction of H_2O_2

The electrocatalytic activities toward the reduction of H_2O_2 on different types of electrodes are monitored by the changes in reduction currents. Fig. 7-12 shows the CV characteristics of electrodes modified with graphene (black), rGO (blue), PAA (pink) and graphene/rGO/PAA (green) referenced to that of a plain glassy carbon electrode (red). The plain electrode showed the small reduction current with a value of 1.77 x 10^{-5} A at -0.6 V. When the electrode was modified with rGO or PAA, the reduction current at -0.6 V were recorded to be 6.48 x 10^{-5} A and 8.75 x 10^{-5} A, respectively. After graphene was deposited onto the surface of the carbon electrode, the reduction current increased to 2.59 x 10^{-4} A. In comparison with all these, the reduction current obtained on the electrode modified with graphene/rGO/PAA tri-layer increased to 3.32 x 10^{-4} A. This phenomenon was attributed to the structural changes of electrode surfaces. The rGO and PAA layer, which provided more electroactive sites on the surface of

electrodes, promoted the electrons transport, leading to higher reduction currents. However, due to their blocking nature the increased reduction currents were limited (3.66 and 4.94 times higher compared with the reduction current obtained on a glassy carbon electrode). As a result of the high conductivity, high surface to volume ratio and the electroactive sites at the edges of graphene, the reduction current increased 14.6 fold compared to that of bare glassy carbon. In contrast to these sole material modified electrodes, graphene/rGO/PAA tri-layer electrode exhibited a 411%, 279% and 28% increase in reduction current, indicating that graphene/rGO/PAA tri-layer electrode had much better electrocatalytic activity towards the reduction of H_2O_2.

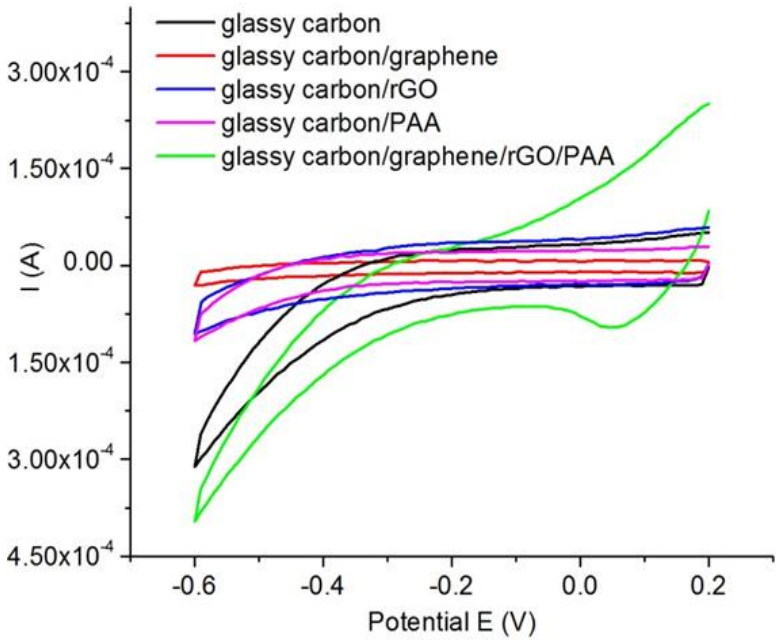

Figure 7-12. Cyclic voltammograms of electrodes modified with graphene, rGO, PAA and graphene/rGO/PAA tri-layer reference to a plain glassy carbon electrode (the concentration of H_2O_2 here is 0.05 M and the scan rate is 100 mV/s).

7.7 Conclusions

Two methods for the hydroxylation of graphene have been demonstrated using H_2O_2 and $KMnO_4$ respectively. The results are confirmed using Raman, EDX (SEM) and

FTIR. Hydroxylation with H_2O_2 presents a higher effectiveness than the method using $KMnO_4$; however, it causes more damage to the devices, leading to a failure of the devices. Hydroxylation with $KMnO_4$ has been proved to be a milder procedure; however, the effectiveness is low, in turn limiting the active sites where the antibody can bond to.

For the immobilisation of the antibody, hydroxyl needs to be converted into amino groups. Two methods for the amination of hydroxylated graphene using APTES and PAA have been demonstrated. From their XPS analysis, amination with PAA shows a higher effectiveness. In addition, an advance in using a graphene/rGO/PAA triple-layer structure to modify the electrode towards the electrochemical reduction of H_2O_2 in PBS buffer was presented. The rGO and PAA layers are immobilised onto the surface of graphene via –HN-CO- bonds and π-π bonds sp^2 hybridised carbon in the graphene lattice, respectively, which avoids using hazardous chemicals, complicated immobilisation process or instruments. The electroactive area of a rGO/PAA modified graphene electrode was significantly enhanced due to the synergistic effect between rGO, PAA and pristine graphene. The improved electron transfer performance is attributed to a combination of the huge amount of electroactive sites in rGO and the high conductivity of graphene. A much higher current towards the reduction of H_2O_2 in PBS buffer was observed from the graphene/rGO/PAA tri-layer electrode. The amino functionalities terminated electrode surface provides a potential for the fabrication of highly sensitive immunosensors.

Chapter 8 Assembly and Characterisation of Biosensors

8.1 Introduction

In this chapter, a novel rGO/graphene double-layer electrode-based label-free DNA biosensor has been proposed and fabricated. The GO layer, which aims to provide more electroactive sites, was directly immobilised onto the surface of a graphene electrode and electrochemically reduced to rGO through CV cycles. Due to its high conductivity and electroactivity provided by the graphene and rGO respectively, the rGO/graphene double-layer electrode presents substantially improved redox currents compared with the other electrodes. The probe ssDNA was afterwards immobilised onto the surface of rGO to detect its target cDNA. To the best of my knowledge, the unique interaction between dsDNA and rGO on a rGO/graphene double-layer electrode has not been reported before. In addition, a wide linear dynamic range together with a low detection limit for the label-free detection of the human immunodeficiency virus 1 (HIV1) gene has been achieved using this biosensor. Due to the waiver of deleterious target labelling, signal enhancing and complicated probe immobilisation process, this is a label-free DNA biosensor with low cost, high sensitivity and wide linear dynamic range, which will be very promising in genetic diagnosis and pathology [300, 301].

In addition, two types of hCG immunosensors based on the rGO modified working electrode and graphene FET have been demonstrated using PANSE as the linker agent between graphene and anti-hCG molecules. The PANSE layer was directly immobilised onto the surface of graphene by the π-π interaction between sp^2 hybridised carbon in the graphene lattice and benzene rings in the PANSE molecules. Using this PANSE linker, the antibody can be directly immobilised onto the surface of the electrode as probes without chemical activation for the detection of the complementary antigen, providing a novel and facile method for the fabrication of an hCG immunosensors. The qualitative

label-free detections of hCG in PBS at a very low concentration have been achieved using these two types of biosensors.

8.2 Experimental

8.2.1 Reagents

GO solution, 0.5 mg/ml >80% monolayer [27] (*Graphene Supermarket*).

Graphene working electrodes, 3 mm diameter *(Dropsens, Spain)*

HIV1 gene 5'-AGTCAGTGTGGAAAATCTCTAGC-FAM-3' (FAM is a carboxyfluorescein-based dye), lyophilised oligonucleotides *(Eurofins, UK)*

cDNA with sequence of 5'-GCTAGAGATTTTCCACACTGACT-3', lyophilised oligonucleotides *(Eurofins, UK)*

Non-complementary ssDNA with sequence of 5'-CGCCCTCTTCTTGTGGATG-3', lyophilised oligonucleotides *(Eurofins, UK)*

KCl, analyse grade *(Sigma Aldrich)*

$K_3[Fe(CN)_6]$, analyse grade *(Sigma Aldrich)*

PANSE, analyse grade *(Sigma Aldrich)*

Active human hCG full-length protein, 100 µg lyophilised powder (*Abcam, UK*)

Anti-hCG antibody, 0.02 mg/ml (*Abcam, UK*)

8.2.2 Procedures and Characterisation

The modification of a graphene electrode with electrochemically reduced GO has been introduced in 4.5.2. The fabrication of a graphene FET was achieved following the techniques and procedures introduced in 4.3. The modification of graphene (or rGO)

with a PANSE solution was carried out following the details in 4.5.5. The immobilisation of anti-hCG and the label-free detection of hCG were achieved following the details in 4.6.3.

The electrochemical analysis was carried out at room temperature with a Keithley 2602A multichannel source meter interfaced with a Cascade Microtech probe station MPS 150, as introduced in 4.7.4. The experimental details were introduced in 4.6.2. Fluorescence images were obtained from a Nikon 80i Epi-fluorescence microscope with a 489 nm excitation laser, as introduced in 4.7.7. The experimental details were introduced in 4.6.1. Raman spectra were obtained from an XPLORA HORIBA system equipped with a 532 nm laser and integrated with an OLYMPUS BX41 microscope, as introduced in 4.7.3. XPS analysis was carried out following the details in 4.7.6.

8.3 Fabrication of Label-Free DNA Biosensor

8.3.1 Schematic illustration of DNA biosensor fabrication

The procedure of the fabrication of a label-free DNA sequence biosensor is illustrated in Fig. 8-1. The graphene modified working electrode was firstly drop-coated by a layer of GO, which is afterwards chemically reduced to rGO through the CV scans. Then, the specific ssDNA probe is dripped and immobilised onto the surface of a rGO modified working electrode via π-π interaction to form a biosensing platform. This ssDNA immobilised biosensor, therefore, can be used for the label-free detection of its cDNA sequence and a difference in the electrochemical signal, in turn, will be as a result of the different amount of cDNA bonded onto the surface of working electrode.

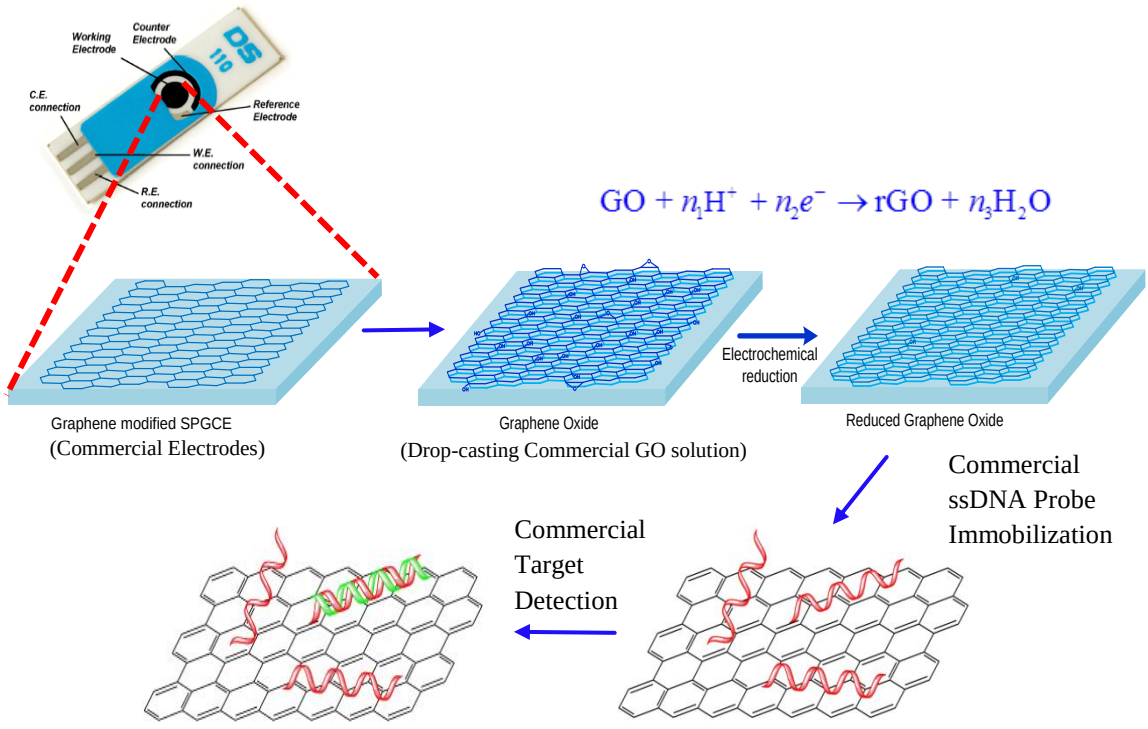

Figure 8-1. Schematic illustration of label-free DNA biosensor fabrication.

8.3.2 Optimisation of GO concentration

An essential requirement in fabricating rGO/graphene double-layer electrodes is to ensure a layer of relatively uniform GO showing good electrochemical reversibility on the surface of the graphene electrode, which can be monitored and estimated by the ratio of the anodic and cathodic peak currents (I_{pa}/I_{pc}) [302, 303]. GO is deposited and immobilised onto the surface of the graphene electrode by the interaction between π-electrons distributed both above and below the sheet plane of the GO and graphene. The CV characteristics of graphene electrodes modified with GO at different concentrations are presented in Fig. 8-2 (a). By increasing the concentration of GO from 0 to 0.3 mg/ml, the intensities of anodic currents show a 67.3% decrease from 2.27 x 10^{-4} A to 7.42 x 10^{-5} A, indicating that the GO, as an electrochemically insulating layer, has been successfully immobilised onto the graphene electrodes. Although more GO means more electroactive sites on the surface of the electrode, I_{pa}/I_{pc} decreases from

0.99 to 0.9 when the concentration of GO is 0.15 mg/ml, indicating that the uniformity and electrochemical reversibility of the corresponding electrode degraded significantly, as shown by the average of three measurements in Fig. 8-2 (b). Also, the increasing separation of redox peaks with the increase of the GO concentration can be observed as the other indicator of the degradation of electrochemical reversibility. From these results, it can be seen that 0.15 mg/ml of GO is preferable to form a relatively homogeneous GO layer on the surface of the graphene electrode with the balance of adequate electroactive sites.

The electroactive area of a GO modified graphene electrode can be calculated with the Randles-Sevcik equation [299]:

$$I = \left(2.69 \times 10^5\right) A D^{1/2} n^{3/2} v^{1/2} C$$

where I is the intensity of the redox current measured from CV characteristic in A. D is the diffusion coefficient of ferricyanide in cm^2s^{-1}. n is the number of electrons exchanged in the redox reaction, which is 1 here. v is the scan rate of CV measurement in Vs^{-1}, C is the concentration of electroactive substance in $molL^{-1}$ and A is electroactive area in cm^2. By using this equation, when the electrode is modified with 0.15 mg/ml of GO, the electroactive area decreased 54% compared with that of a bare graphene electrode, confirming the increased thickness of GO on the electrode surface, as the red curve shown in Fig. 8-2 (b). The drop of the electroactive area here is attributed to the unique structure of GO, which consists of the sp^2 hybridised graphene crystals and the randomly distributed defects, such as broken lattice and oxygen containing groups [304], which can block the transport of electron pathways between sp^2-hybridised area [216].

Figure 8-2. Optimisation of GO concentration. (a) CV characteristics of graphene electrodes modified with GO at different concentrations; (b) I_{pc}/I_{pa} intensity ratio (to the left Y axis) and electroactive area (to the right Y axis) versus GO concentrations.

8.3.3 Characterisation of rGO/graphene double-layer electrode

Fig. 8-3 (a) shows a comparison of Raman spectra taken from graphene, GO/graphene and rGO/graphene electrodes. When the graphene electrode is modified with GO, an increase of the I_D/I_G intensity ratio from 0.02 (blue) to 0.8 (black) can be seen together with a significantly decreased 2D band, indicating the introduction of a large number of defects and disorders onto the surface of electrode [295]. After the GO layer was electrochemically reduced to rGO, a further increase of the I_D/I_G intensity ratio to 1.28 (red) has been observed, indicating the effectiveness of this reduction process. The dependence between GO, rGO and their corresponding Raman spectra was reported by Lucchese et al [296]. The I_D/I_G intensity ratio, which has been found to be a function of the average distance between defects or disorders (D_f), increases with the increase of D_f from 0 to 4 nm, peaks at 4 nm, and afterwards decreases with the further increase of D_f. The distance between sp^2 hybridised area on GO increased within the range of 0 - 4 nm

after the reduction process, which is due to the partially removed oxygen-containing functionalities, leading to the increase of the I_D/I_G intensity ratio.

The electrochemical reduction of GO has also been semi-quantitatively characterised by XPS. A comparison of wide region XPS spectra taken from GO/graphene (black) and rGO/graphene electrodes (red) is presented in Fig. 8-3 (b). It can be seen that both spectra consist of strong C, O signals with the residue signals of K, Cl and N from the electrolyte. Compared with the spectrum taken from a GO modified graphene electrode, the intensity of the O peak has significantly decreased after the electrochemical reduction process. By extracting the different elemental sensitivities at 1486.6 eV, the atomic ratio of oxygen to carbon (O/C) decreased from 31% to 9%. The corresponding high-resolution C1s spectra are shown as insets in Fig. 8-3 (b). In the C1s spectrum taken from a GO/graphene electrode, as shown by the bottom inset, fitted by a dash-dot line, three major sub-peaks centred at 284.5 eV, 287 eV and 288.8 eV can be observed. They are attributed to sp^2 and sp^3 C-C bonds in graphene lattice, C=O bond in alkoxy and epoxy and HO-C=O bond in carboxyl respectively. In contrast, as shown by the top inset, fitted by a dash line, the intensities of all oxygen-containing group related peaks have decreased after the electrochemical reduction, particularly the one attributed to alkoxy and epoxy centred at 287 eV. These results suggest the GO layer has been effectively reduced and the graphene lattice has been restored to some extent. Compared to other violent or deleterious modification, it is notable that no extra damage has been introduced onto the graphene layer underneath the GO, which is helpful to maintain the unique electronic properties of graphene [166]. Therefore, the intensity of the redox currents is anticipated to increase using this rGO/graphene double-layer electrode in electrochemical characterisation.

Figure 8-3 has been removed due to Copyright restrictions.

Figure 8-3. Raman spectroscopy and XPS analysis of GO reduction. (a) Raman spectra of a bare graphene electrode, a GO/graphene electrode and a rGO/graphene electrode. (b) Wide region XPS spectra and their corresponding C1s high-resolution spectra taken from a graphene electrode modified with GO and rGO respectively.

Fig. 8-4 (a) shows the CV characteristics of four differently modified electrodes, namely graphene, rGO, GO/graphene and rGO/graphene electrodes. The superior performance in increasing the electroactive area using the rGO/graphene double-layer electrode can be clearly observed from this comparison. The CV characteristic obtained on a graphene electrode presents an I_{pa} of 2.204 x 10^{-4} A and an I_{pc} of -2.247 x 10^{-4} A, as shown by the black curve. When the electrode is modified with GO/graphene, the I_{pa} and I_{pc} have significantly decreased to 4.808 x 10^{-5} A and -4.809 x 10^{-5} A respectively, as shown by the green curve. When the carbon electrode is only modified with an rGO layer, an I_{pa} of 2.297 x 10^{-4} A and an I_{pc} of -2.303 x 10^{-4} A can be seen from its corresponding CV curve, as shown by the blue curve. By contrast, the much higher I_{pa} and I_{pc} values of 3.138 x 10^{-4} A and -2.966 x 10^{-4} A respectively were obtained on a rGO/graphene double-layer electrode, as shown by the red curve.

The increase of the redox currents can be attributed to a large number of defects and disorders inherited from the GO, which are randomly distributed within the rGO layer and acting as the electroactive sites for donating or receiving electrons between the electrode surface and the electrolyte [305]. Compared with those electrodes modified with rGO, pristine graphene or GO/graphene, the rGO/graphene double-layer electrode can provide not only a faster electron exchange rate at the interface of the graphene/glassy carbon but also a faster electron exchange rate at the interface of an electrode/electrolyte in ferricyanide system. Because of this reason above, the intensity of the redox currents measured on a rGO/graphene double-layer electrode shows an increase of 42%, 36% and 552% respectively, compared to those of devices modified with rGO, graphene and GO/graphene, as shown in Fig. 8-4 (a). The electroactive areas for rGO, graphene, GO-graphene, and rGO-graphene electrodes have been calculated to be 9.8 mm^2, 9.7 mm^2, 2.0 mm^2 and 12.8 mm^2 with the Randles-Sevcik Equation, respectively. Therefore, a significant synergistic effect in enhancing the electroactivity of the electrode can be achieved by using rGO/graphene for the modification of conventional electrodes.

The effects of different scan rates on CV characteristics of a rGO/graphene double-layer electrode are shown in Fig. 8-4 (b). It can be seen that all CVs present the highly symmetric anodic and cathodic currents, which can be linearly correlated with the square root of corresponding scan rates. These results suggest that a fast diffusion dominated the process rather than adsorption of an electroactive substance on the surface of the electrode, which are essential for electrochemical applications.

Figure 8-4 has been removed due to Copyright restrictions.

Figure 8-4. CV analysis of differently modified electrodes. CV characteristics of (a) graphene, GO, rGO and rGO/graphene electrodes with a scan rate of 100 mV/s, (b) rGO/graphene double-layer electrode measured at different scan rates of 30, 50, 100, 150, 200 mV/s. Inset: correlations between I_{pa} (red), I_{pc} (black) and the square root of corresponding scan rates.

8.3.4 Fluorescent analysis of DNA-GO interaction

The different interactions between the ssDNA/GO and dsDNA/GO are demonstrated by the fluorescent analysis below. A set of the fluorescent images taken from the dried sample of an FAM-labelled probe ssDNA (as a reference), the mixture of an FAM-labelled probe ssDNA and GO, and the mixture of hybridised dsDNA and GO is presented in Fig. 8-5. The strong fluorescent emission can be seen from the sample of a dried FAM-labelled ssDNA (30 µl of 50 nM) on a glass slide in the absence of GO under an excitation laser at 480 nm, as shown in Fig. 8-5 (a). In contrast, nearly 100% of the fluorescent emission was quenched in the presence of 10 µl of 0.15 mg/ml GO, indicating a strong bonding between ssDNA and GO [208], as shown in Fig. 8-5 (b). The fluorescent particle in Fig. 8-5 (b) is used as an indicator of the sample surface. In Fig. 8-5 (c), the fluorescence emission started to be visible again after 30 mins hybridisation between the target cDNA (10 µl of 300 nM) and the probe ssDNA,

indicating that the bonding between ssDNA and cDNA is stronger than that between ssDNA and GO.

The mechanism of fluorescence quenching is attributed to the strong π-π interaction between sp^2 hybridised carbon in graphene and DNA nucleobases, which could bring ssDNA closely attached to the surface of GO. Due to the unique long-range nanoscale energy transfer property of GO, when FAM-labelled ssDNA exposed under excitation laser, the released energy was transferred through the GO lattice instead of given out as fluorescent emission. After the hybridisation occurred between the probe ssDNA and its cDNA, DNA nucleobases are released from the GO surface and shielded in the duplex structure by the negatively charged phosphate backbone [198, 206, 208]. As a result, the distance between DNA nucleobases and the GO has increased, leading to the weakened interaction between DNA nucleobases and GO and, in turn, resulting in the restoration of the fluorescent emission. Therefore, if this happened on the GO-based electrode, there will be a difference in electrochemical response before and after hybridisation due to the different negativity on the electrode surface.

Figure 8-5 has been removed due to Copyright restrictions.

Figure 8-5. Fluorescent analysis of interactions between ssDNA/GO and dsDNA/GO. Fluorescent images taken on the dried samples of (a) probe ssDNA, (b) the mixture of probe ssDNA and GO, (c) the mixture of probe ssDNA, GO and

target cDNA. The wavelengths of excitation laser and emission signal are 480 nm and 520 nm respectively.

8.3.5 Label-free detection of HIV1 gene

CV measurement was used to qualitatively characterise the probe immobilisation and the label-free detection of an HIV1 gene on a rGO/graphene double-layer electrode. Fig. 8-6 shows the CV characteristics measured on a bare rGO/graphene double-layer electrode (black), ssDNA/rGO-graphene (red) electrode and dsDNA/rGO-graphene (blue) electrode respectively. The bare rGO/graphene electrode presents an I_{pa} of 2.55 x 10^{-4} A and an I_{pc} of -2.69 x 10^{-4} A in its CV characteristic. When the probe ssDNA was immobilised onto the surface of the rGO, the corresponding I_{pa} and I_{pc} decreased to 1.77 x 10^{-4} A and 1.97 x 10^{-4} A respectively. When the probe ssDNA hybridised with its cDNA, the I_{pa} and I_{pc} show further decreases down to 1.31 x 10^{-4} A and -1.55 x 10^{-4} A, respectively. In addition to the redox current change caused by DNA hybridisation, Fig. 8-6 the blue line also shows the other pair of redox peaks which can be attributed to the partially released dsDNA from the electrode surface and becomes negligible with a target concentration $\leqslant 10^{-8}$ M. These CV results are attributed to the changes in the bio-functional electrode surface: the probe ssDNA was immobilised onto the surface of the rGO/graphene electrode through π-π interaction between the purine/pyrimidine rings in the DNA nucleobases and the graphene lattice. In this case, the phosphate backbone of the DNA molecule, which is negatively charged, is forced to face away from the electrode surface [306], resulting in an electrostatic repulsion effect between the surface of the electrode and the negatively charged ferricyanide, in turn leading to a decreased redox currents. When the probe ssDNA hybridised with its cDNA on the surface of the electrode, they formed a duplex structure and shield the nucleobases inside of it, as explained in Fig. 8-5. It is worth noting, in this case, that the dsDNA is still weakly

interacting with the rGO instead of coming off and being "free standing" in the electrolyte [198, 307]. Most of the dsDNA molecules are maintained close enough to the surface of the electrode to result in a more negatively charged electrode surface, in turn leading to a further decreased redox currents. To minimise the interaction between the target cDNA and the rGO, the ssDNA is at least 10 times more concentrated than the cDNA, which could lead to a saturated status of the ssDNA on the surface of the rGO, and thus, the target cDNA mainly bonded to the probe ssDNA instead of bonding to the rGO via π-π bonds.

Figure 8-6 has been removed due to Copyright restrictions.

Figure 8-6. CV characteristics of a rGO/graphene double-layer electrode (black), ssDNA/ rGO/graphene electrode (red) and dsDNA/rGO/graphene electrode (blue). The concentration of the target cDNA is 100 nM and the scan rate is 100 mV/s.

DPV measurement was used to quantitatively estimate the sensitivity of this label-free DNA biosensor. Fig. 8-7 shows the dependence of DPV peak currents on the target concentration ranging from 10^{-7} M to 10^{-12} M. The linear relationship can be fitted by the following equation:

$$I_p = -3.22413\times10^{-6}\log(C) + 9.87262\times10^{-5}$$

where C is the concentration of the target cDNA in M and I_p is the intensity of DPV peaks. Based on the value of 3 times the standard deviation of the blank reference samples (n = 7), the highest LoD is calculated to be 1.58×10^{-13} M. By adding the non-complementary target DNA onto the surface of this DNA sensor, the change in redox current has been found to be only 7.7% of that caused by the target cDNA at the same concentration, indicating a reasonably good selectivity. The stability of this DNA sensor was evaluated by adding blank PBS buffer onto the surface of a working electrode and an increased redox current started to be seen after 3 hours' immersion. The reproducibility for the detection of the target cDNA at different concentrations was evaluated by measuring a limited number of parallel devices. The right inset in Fig. 8-7 shows the relative standard deviation (RSD) values of all the devices fabricated. By taking advantage of the large electroactive area inherited from GO and high electron transport rate from graphene, this rGO/graphene double-layer electrode-based DNA sensor presents a wider linear detection range and a lower LoD in contrast to polymer [308], carbon nanotube [185] or bare graphene quantum dot [309] modified DNA sensor. However, due to the limits of the fabrication procedure, further improvements towards sensor sensitivity [310], fabrication reproducibility [305] and stability [311] need to be carried out.

Figure 8-7 has been removed due to Copyright restrictions.

Figure 8-7. Dependence of DPV peak currents on the log(C/molL^{-1}) (logarithmic concentration of target cDNA). Insets: DPV characteristics of sensors hybridised with target cDNA ranging from 10^{-7} to 10^{-12} M with the corrected baselines and RSD (%) value of all devices fabricated.

8.4 Fabrication of Label-Free hCG Biosensor

8.4.1 Fabrication of Electrochemical hCG Biosensors with Graphene Electrode

A schematic illustration of the fabrication of a label-free electrochemical hCG biosensor is shown in Fig. 8-8. The first stage of fabrication is to immobilise PANSE, which consists of a hydrophobic pyrenyl moiety base and a bio-active ester head and is used as a linker molecule between the chemically inert graphene and anti-hCG, onto the surface of a graphene channel via π-π interaction. The immobilisation of anti-hCG molecules onto the graphene channel is achieved through a nucleophilic substitution reaction between the primary and secondary amino functionalities existing on the protein surface and the succinimidyl ester from PANSE. This nucleophilic substitution is self-activated, and therefore, no pre-treatment of the antigen with 1-ethyl-3-(3-dimethylaminopropyl) carbodiimide (EDAC)/ N-hydroxysuccinimide (NHS) chemistry is required. Based on

the different amount of hCG bonded onto the surface of a working electrode, a difference in the electrochemical signal will be produced in the label-free detection.

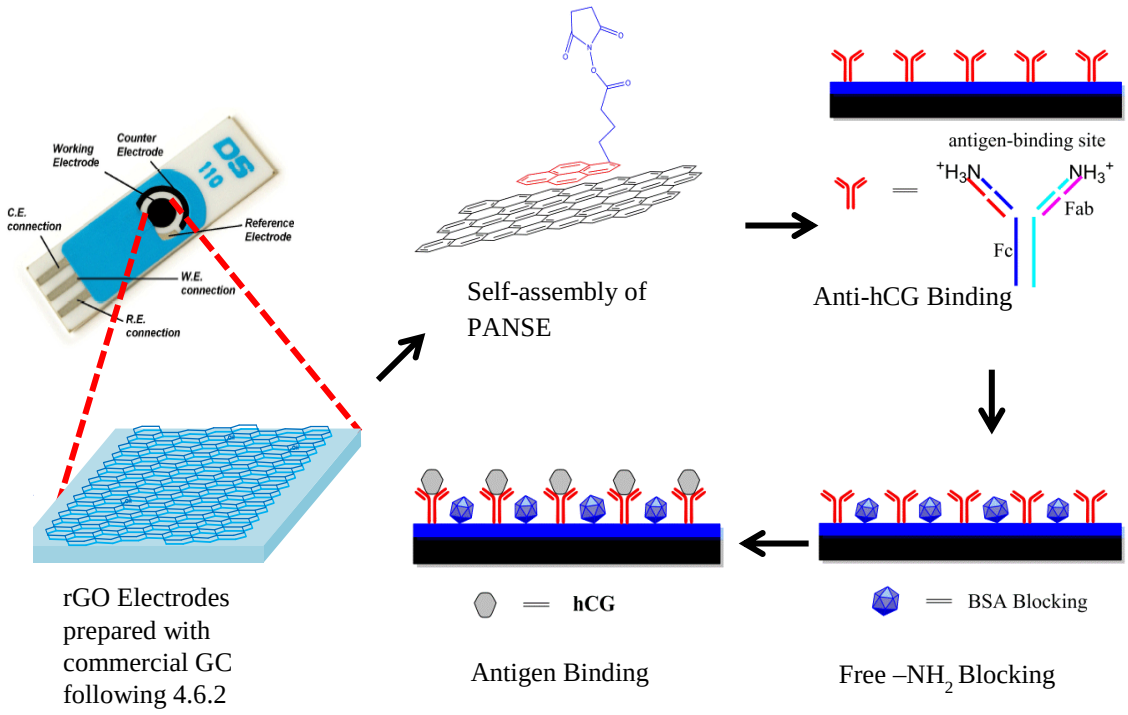

Figure 8-8. Schematic illustration of label-free electrochemical hCG biosensor fabrication.

XPS has been used for the confirmation of PANSE immobilisation, as shown in Fig. 8-9. Before the immobilisation of PANSE (Fig. 8-9 black), 98.49 (at %) C and 1.51 (at %) O can be seen with undetected N, implying the high purity of the graphene with oxygen trapped within it. After the immobilisation of PANSE, as shown in Fig. 8-9 red, a 1.4 (at %) increase of O has been observed together with 0.27 (at %) N. This is in accordance with the atomic ratio of C/O in the PANSE molecules, as shown in the inset of Fig. 8-9, confirming the immobilisation of PANSE on the surface of the electrode.

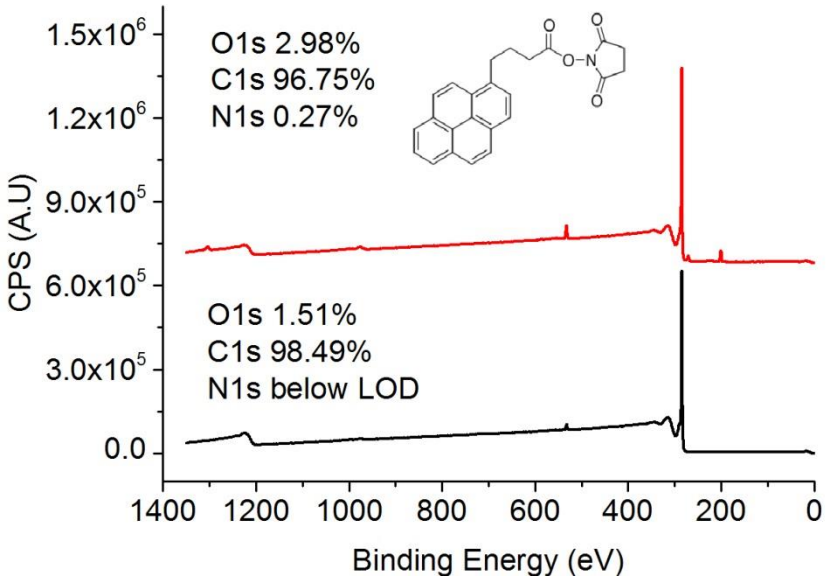

Figure 8-9. XPS spectra obtained before (black) and after (red) the immobilisation of PANSE.

The immobilisation of the probe antibody, free amino blocking and the detection of its complementary antigen on the rGO modified electrodes are monitored by the changes in CV redox currents. Fig. 8-10 shows the CV characteristics of a rGO/PANSE electrode (red), rGO/PANSE/antibody electrode (blue), rGO/PANSE/antibody/BSA electrode (pink) and a rGO/PANSE/antibody/BSA/antigen electrode (olive) with a reference to that of a plain rGO electrode (black). The plain rGO electrode shows the large redox currents with an I_{pa} value of 2.15 x 10^{-4} A and an I_{pc} value of -2.23 x 10^{-4} A. After the PANSE linker was immobilised onto the surface of the rGO, the redox peaks sharply decrease and separate. And after the immobilisation of the antibody and BSA, the redox peaks further decrease and separate. The CV characteristic of the rGO/PANSE/antibody/BSA/antigen electrode shows a pair of increased redox currents with a I_{pa} value of 3.76 x 10^{-5} A and a I_{pc} value of -1.32 x 10^{-4} A. These phenomena are attributed to the structural changes of the electroactive surface: as discussed in 8.3.2, due to the large number of electroactive sites in the rGO lattice, the rGO modified electrode presents the highest electroactivity compared with other electrodes in Fig. 8-

10. With the addition of the PANSE layer, the four-carbon chain, which acts as an insulating layer, has been introduced onto the surface of the electrode, leading to the sharp decrease of its electroactivity. After the immobilisation of the antibody and BSA, the redox currents further decreased due to their blocking nature. It also can be seen that the PANSE, antibody and BSA were unevenly distributed as shown by the increased separation of redox peaks. After the binding occurring between the antibody and antigen, an increase in the redox currents can be observed, which may be due to the positively charged hCG molecules.

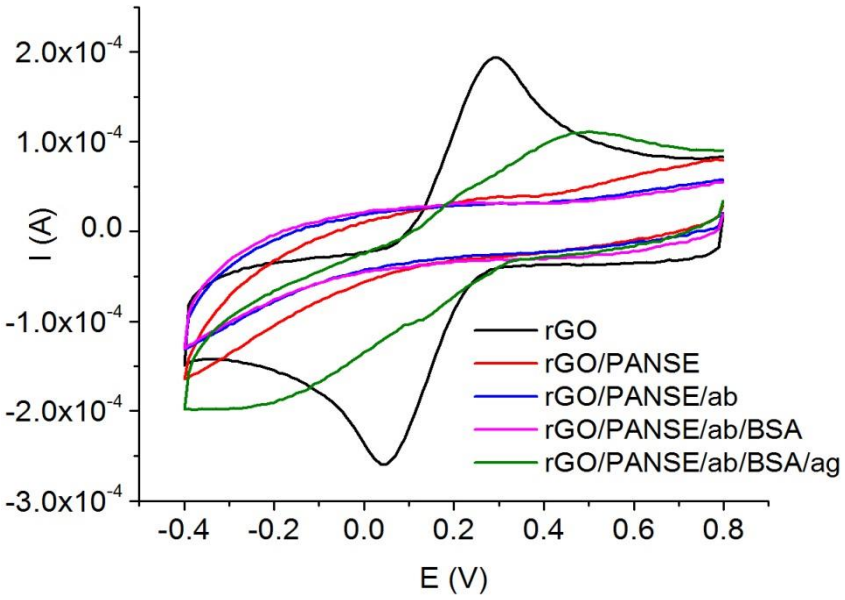

Figure 8-10. CV characteristics of the biosensor fabrication procedure and the label-free hCG detection.

8.4.2 Fabrication of Electronic hCG Biosensor with CVD graphene

A schematic illustration of the fabrication of a hCG biosensor is shown in Fig. 8-11. The first stage of fabrication is to transfer CVD graphene grown on top of a Cu foil onto the surface of a SiO_2 substrate following the wet transfer procedure. The patterning of a CVD graphene channel is achieved via the modified lithography and ion-milling process rather than conventional oxygen plasma etching, as introduced in 4.3.2. Then

from this step, PANSE and anti-hCG were successively immobilised onto the surface of a graphene channel following the same process for the fabrication of electrochemical hCG biosensors. Based on the different amount of hCG bonded with its anti-hCG on the surface of a graphene channel, a difference in the output of the electronic signal will be produced due to the changed resistance.

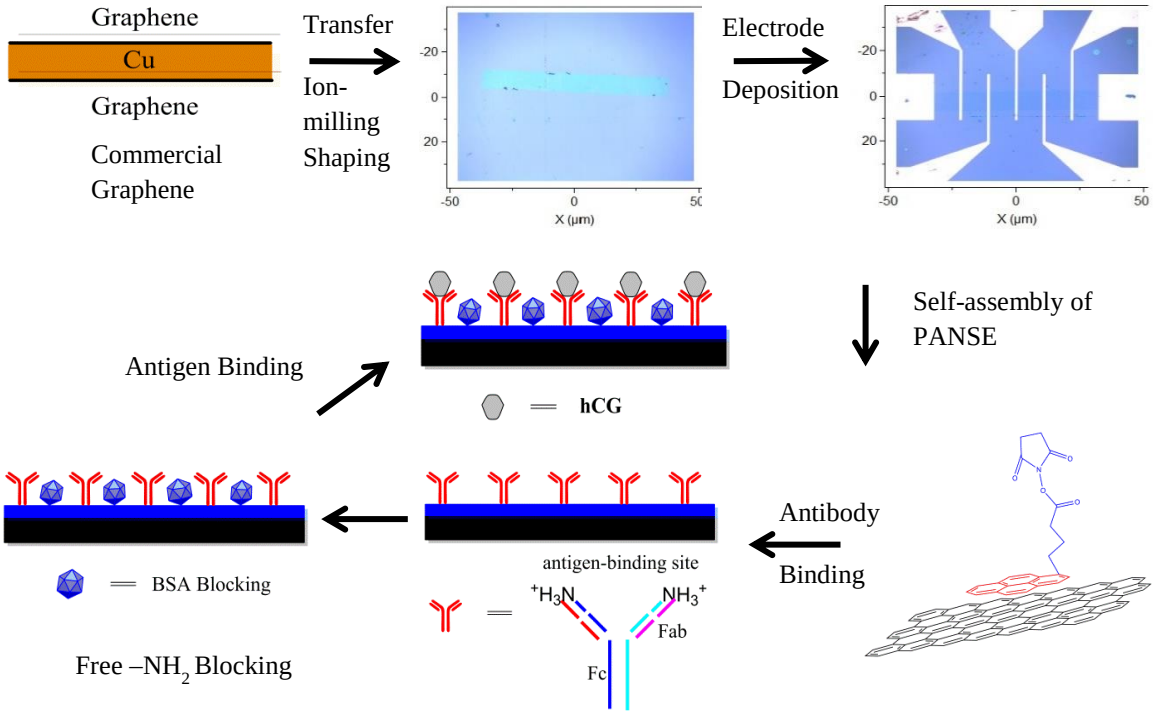

Figure 8-11. Schematic illustration of hCG biosensor fabrication.

Electronic characterisation has been carried out to monitor each step of electronic biosensor fabrication showing a label-free qualitative detection of hCG protein in PBS buffer. Fig. 10 (a) shows the I_d - V_d characteristics of the plain graphene FET, PANSE modified graphene FET, anti-hCG immobilised graphene FET and hCG bonded graphene FET. The lowest resistance with a value of 10.5 kΩ can be seen from the plain graphene FET (black). After the graphene was modified with a PANSE linker, the resistance almost doubled to 22 kΩ (red). After the anti-hCG was immobilised onto the surface of graphene, the resistance increased to 33.6 kΩ. With the specific binding of an hCG protein onto its antibody, the resistance further increased to 72 kΩ. This

phenomenon is attributed to the structural change of the graphene channel in electronic devices. Each carbon atom in the honeycomb-structured graphene lattice poesses a free electron, which forms the electron cloud on both sides of graphene with electrons from other carbon atoms, leading to a low resistivity in the electronic measurement [24]. After the immobilisation of the PANSE linkers via π-π stacking, the electron cloud is disturbed by this insulating material, which is in accordance with the conclusions drawn from Fig. 8-8 (b), leading to an increased resistance. With the addition of hCG onto the anti-hCG modified graphene channel, the hCG is chemically bonded with its antibody, which results in a further increased resistance due to the insulating nature of the hCG protein. The corresponding I_d - V_g characteristics of steps in Fig. 5 (a) have also been provided and shown in Fig. 10 (b1) - (b4). The Dirac point of plain graphene FET has been found around -2 V at the beginning and positively shifted to 30 V after adding PANSE, confirming the successful modification and p-type performance of PANSE. With the addition of anti-hCG and hCG, the Dirac point shifted to -20 V and then to +40 V (beyond the instrument limit), which not only presents a qualitative detection for hCG in PBS buffer but also illustrates the infeasibility of using the Dirac point as an indicator for the quanlitative detection of higher hCG concentrations (as the reproducibility of graphene FET devices is poor, when the device size comes down to micrometre scale). Therefore, the I_d-V_d characterisation is chosen for the later work quantitative detection of hCG in PBS.

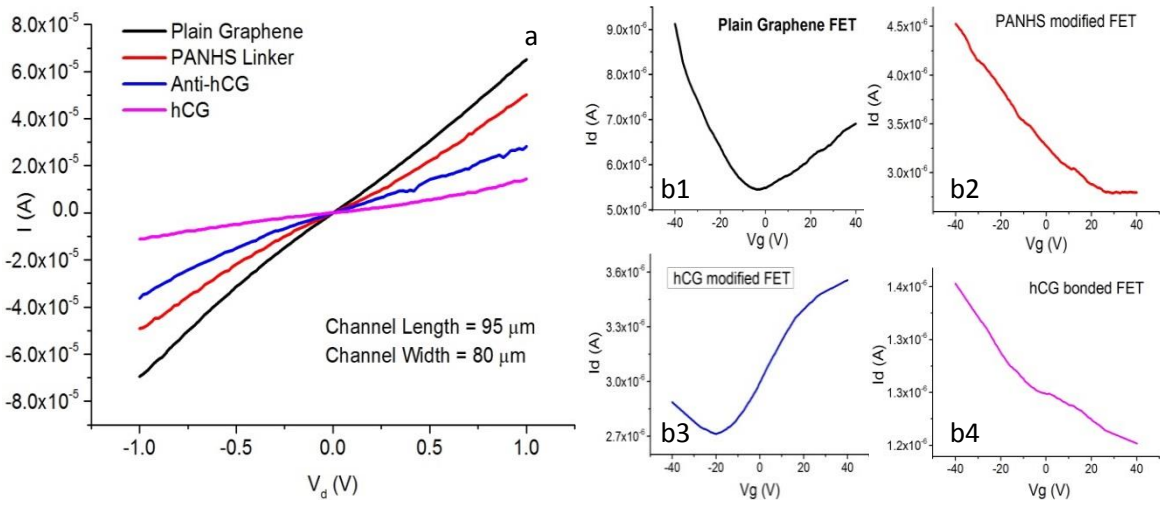

Figure 8-12. Qualitative label-free detection of hCG protein in PBS buffer. (a) I_d-V_d and (b) I_d-V_g characteristics of the plain graphene FET, PANSE modified FET, anti-hCG modified FET and FET after hCG bonded onto it (the concentration of hCG in PBS is 0.625 ng/ml).

8.5 Conclusions

The fabrication of a rGO/graphene double-layer electrode-based biosensor has been proposed and achieved for the label-free detection of DNA sequence. In contrast to bare graphene, rGO or GO/graphene modified electrodes, the rGO/graphene double-layer electrode shows a significantly increased peak current, which can be attributed to the large number of electroactive sites randomly distributed in the rGO layer and the high conductivity of the graphene underneath. Both the surface modification of the graphene electrode and the immobilisation of probes have been achieved via non-damage, non-deleterious and mild procedures, providing a convenient and commercial technique for the assembly of DNA biosensors. A wide linear range and a good sensitivity for the label-free detection of the HIV1 gene have been recorded on the resulting devices; however, the reproducibility, sensitivity and stability of this DNA sensor still need to be further improved. In parallel with a DNA sensor, the fabrication of two types of label-free hCG immunosensor has been achieved without requiring the pre-activation of the

antibody before its immobilisation, namely electrochemical hCG biosensor and FET-based electronic hCG biosensor. Although both of these two type of biosensors have exhibited a qualitative ability for the label-free detection of hCG at very low concentration (0.625 ng/ml), the modification of the electrode surface with PANSE and the reproducibility of biosensor need to be further improved. The quantitative detection of hCG is planned as future work.

Chapter 9 Conclusions and Further Work

9.1 Summary of Key Results

This project has investigated the use of different graphene-based materials for the fabrication of biosensors. The graphene was produced with both micro-exfoliation and from sputtered materials. Optical microscopy and Raman spectroscopy have been used to evaluate the number and the quality of the graphene layers. AFM and SEM have been used to evaluate the morphology and the thickness of resultant graphene layers. By tuning and optimizing the growth parameters, it has been found that the thicker Ni layer on top of the carbon source using a higher annealing temperature and a faster cooling rate were preferable to form graphene with fewer layers. In parallel, by systematically analysing the morphological structure and properties of resultant graphene grown on different Ni thickness, a growth model for transferable and transfer free graphene has been proposed and confirmed.

The fabrication of graphene FETs was investigated using photolithography, sputtering and thermal evaporation. Mechanical exfoliated graphene was selected as the channel material due to its best quality. Raman spectroscopy and I_d-V_g characterisation were used to estimate the damage to graphene from sputtered materials and the electronic properties of graphene. A novel shielding technique was developed for the sputtering deposition of Au contacts to overcome the difficulties in the lift-off process. This led to the increased success rate of fabrication from 17% to 90%, which is comparable with those fabricated by thermal evaporation. It has also been found that a higher Ar pressure and a lower discharge power were preferred to reduce the damage caused by sputtered Au. By using optimised fabrication parameters, $R_{contact}$ and R_{total} down to 1.04 and 2.4 kΩ μm, respectively, have been recorded. The effects of different absorbents/residues to

the electronic performance of graphene FET have been studied together with the corresponding removing methods.

Two methods of functionalising graphene to provide hydroxyl functionalities have been investigated using H_2O_2 and $KMnO_4$ respectively. EDX and FTIR were used to monitor and estimate the oxidation level of graphene. It has been found that oxidation with H_2O_2 shows the higher efficiency and more damage to graphene and metal contact, whilst oxidation with potassium permanganate presents a lower oxidation efficiency but less damage to the devices. APTES and PAA were used for the amination of hydroxyl groups functionalised graphene and the corresponding results were analysed with XPS, Raman and CV. In addition, improved electrocatalytic activity toward the reduction of H_2O_2 has been demonstrated with a graphene/rGO/PAA modified electrode.

The assembly of a label-free HIV1 gene sensor was demonstrated using the graphene/rGO double-layer electrode. The immobilisation of both GO and probe ssDNA was achieved by direct π-π stacking, which was confirmed with CV, Raman and XPS analysis. The unique interactions between ssDNA/rGO and dsDNA/rGO have been demonstrated by fluorescent and electrochemical analyses. It has been found that the enhancement of the electroactivity of a graphene electrode can be achieved by the synergistic effect between graphene and rGO. The interaction between a probe of ssDNA and rGO can be significantly weakened instead of released after adding its cDNA due to a stronger bonding between ssDNA/cDNA. Using this electrode, the label-free detection of an HIV1 gene has been achieved with showing an LoD of 1.58 x 10^{-13} M. In parallel, a label-free qualitative detection of hCG has also been achieved using a rGO/PANSE/anti-hCG modified electrode and FET-based sensing platform, respectively.

9.2 Further Work

Biosensors fabricated in this work were mainly using exfoliated graphene, screen-printed graphene and graphene electrochemically reduced from GO. To meet the requirements of industrial production, biosensor would need to be fabricated in high volumes. Therefore, the fabrication of biosensor using large area graphene needs to be systematically investigated (this work has been started and the initial qualitative results towards the detection of hCG protein have been presented in Chapter 8). The production method of transfer-free graphene on SiO_2, as discussed in Chapter 5, needs to be further developed to obtain wafer scale atomically flat and low defective single crystal graphene directly on SiO_2 or other insulating substrate, which could have a significant effect on the future graphene industry.

Most of the processing methods for the fabrication of graphene electronic devices in this work, such as sputtering and ion-milling, are based on the widely used techniques in the semiconductor industry, which may not be optimal for the fabrication of graphene devices. Therefore, the optimisation of these processing techniques and their corresponding parameters need to be carried out to enhance the performance of the resulting devices. The fabrication of a graphene hCG biosensor using ion-milling patterning has been started and the initial results have been shown in Chapter 8.

The label-free qualitative detection of hCG has been achieved in this project using CVD graphene-based FET sensing platform. To achieve the quantitative detection, this sensing platform needs to be further improved in following aspects. CVD graphene used in the FET fabrication needs to be further optimised and standardised to obtain graphene with more reproducible thickness and defects density. The single-channel sensing area in each device can be replaced by a channel-matrix, in which case the signal difference between individual devices would be averaged.

In this work, biosensors for the label-free detection of an HIV1 gene and hCG protein have been successfully developed. However, there are a large number of other diseases and health conditions for which can only be analysed using complicated lab-based methods. In addition, the current biosensor has very limited sensitivity and selectivity for the detection of biomarkers existing in the body fluid, such as plasma and saliva. Therefore, a CVD graphene-based biosensor for the label-free detection of a dementia biomarker in blood plasma is being investigated. The challenge will be the capability of specific detection of multiple dementia biomarkers in clinical blood plasma samples while maintaining a high sensitivity, selectivity and low commercial cost.

Appendix

1. Supporting Publications & Presentations

1.1 Journal Publications

- Bing Li*, Genhua Pan, Neil D. Avent, Kamrul Islam, Shakil Awan. A Simple Approach to Preparation of Graphene/Reduced Graphene Oxide/Polyallylamine Electrode and Their Electrocatalysis for Hydrogen Peroxide Reduction (accepted by *Journal of Nanoscience & Nanotechnology*).

- Bing Li*, Genhua Pan, Neil D Avent, Roy B Lowry, Tracey E Madgett, Paul L Waines. Graphene electrode modified with electrochemically reduced graphene oxide for label-free DNA detection, *Biosensors & Bioelectronics*, vol. 72, p. 313, 2015.

- Bing Li*, Genhua Pan, Nawfal Y Jamil, Laith Al Taan, Shakil Awan, Neil Avent. A Shielding Technique for Deposition of Au Electrical Contacts on Graphene by Sputtering, *Journal of Vacuum Science & Technology A*, vol. 33, p. 030601, 2015.

- Shakil Awan*, Genhua Pan, Laith M Al Taan, Bing Li, Nawfal Jamil. Radio-frequency transport Electromagnetic Properties of chemical vapour deposition graphene from direct current to 110 MHz, *IET Circuits, Devices & Systems*, vol. 9, p. 46, 2015.

- Bing Li*, Genhua Pan, Shakil Awan, Neil Avent. Techniques for Production of Large Area Graphene for Electronic and Sensor Device Applications, *Graphene and 2D Materials*, vol. 1, p. 2299, 2014.

- Genhua Pan*, Bing Li, Mark Heath, David Horsell, M Lesley Wears, Laith Al Taan, Shakil Awan. Transfer-free growth of graphene on SiO_2 insulator substrate from sputtered carbon and nickel films, *Carbon*, vol. 65, p. 349, 2013.

* Corresponding author

1.2 Conference Presentations

- Bing Li*, Genhua Pan, Neil D. Avent, Roy B. Lowry, Tracey E. Madgett, Paul L. Waines. Graphene electrode modified with electrochemically reduced graphene oxide for label-free DNA detection, Nano Korea 2015, Seoul, South Korea, 1st-3rd July, 2015.

- Genhua Pan*, Bing Li, Mark Heath, David Horsell, M Lesley Wears, Laith Al Taan, Shakil Awan. Transfer-free growth of graphene on SiO2 insulator substrate from sputtered carbon and nickel films, ImagineNano, Bilbao, Spain, 23th-26th April, 2013.

2. Lithography Designs

A number of different patterns have been designed and used for the shaping and fabrication of graphene devices. The patterns for the standard lithography and lift-off process were designed using L-Edit software and the photomasks were fabricated by Compugraphics International Ltd (UK) on soda-lime glass.

2.1 Designs for Exfoliated Graphene Device

The overview of the photomask designed for exfoliated graphene devices is shown in Fig. A-1. The quarters marked “5”, “10” and “15” stand for the channel length between the inner two probes and the right bottom quarter is designed for the substrate mapping before transferring graphene onto it.

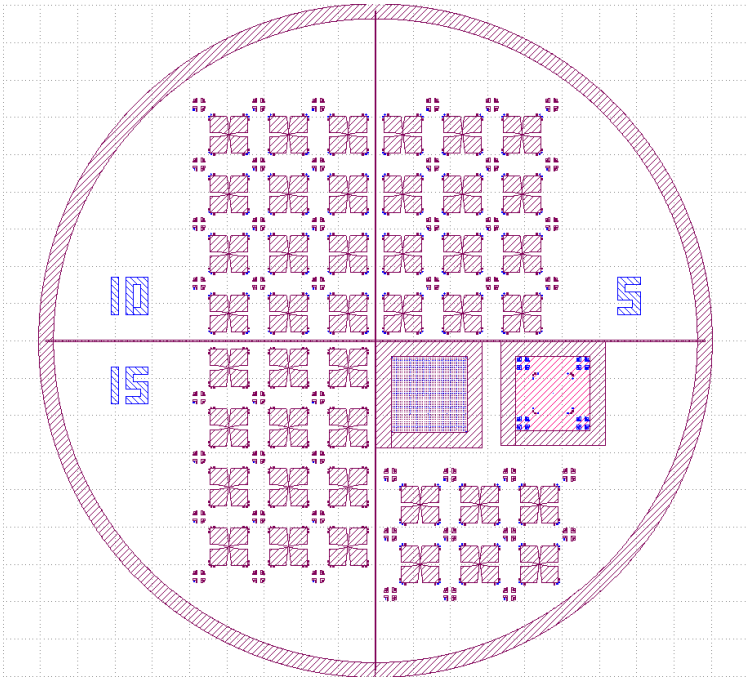

Figure A- 1. Overview of the photomask for the fabrication of exfoliated graphene devices.

The details of each quarter have been provided in Fig. A-2. Fig. A-2 (a), (b) and (c) show the corresponding zoomed in structures of those in Fig. A-1. The channel length varies from 5 µm to 15 µm, whilst the distance between the electrodes on the same side remains 2 µm. Fig. A-2 (d) shows an overview of the number matrix designed for the substrate mapping, which consists of 40 x 40 unique numbers across a 1 x 1 cm area. The further zoomed in structure has been shown in Fig. 4-5 (a2) in Chapter 4.

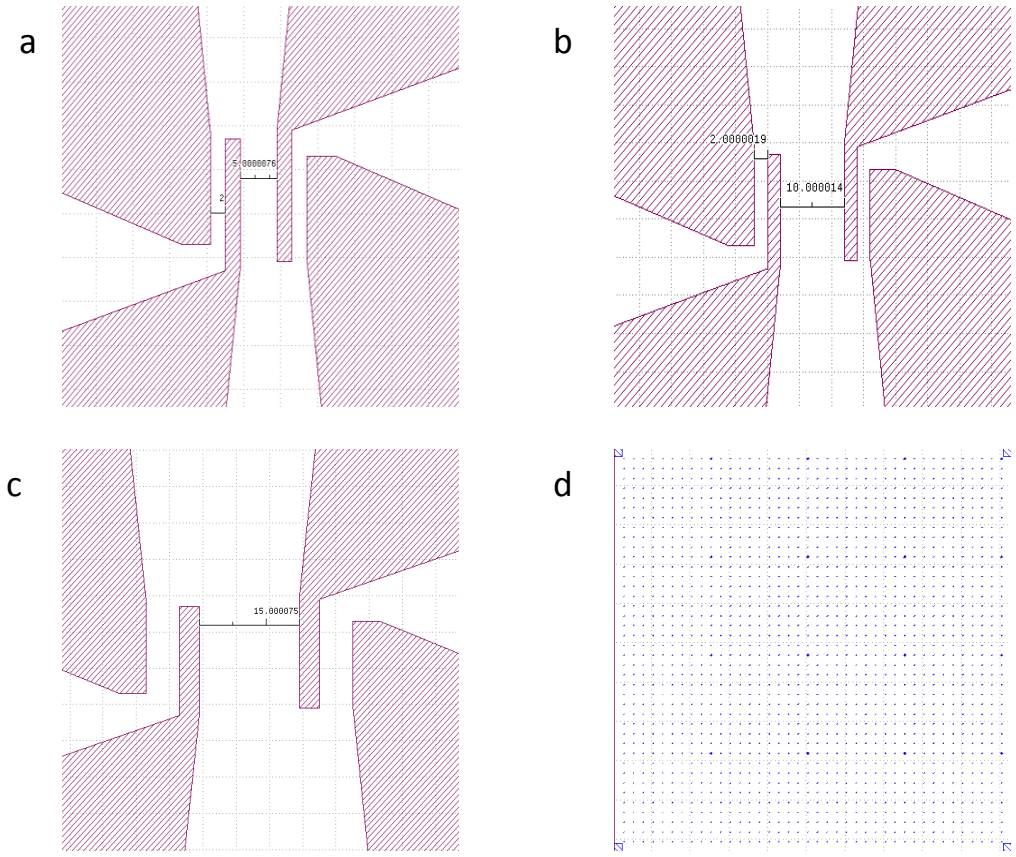

Figure A- 2. Details of the photomask for the fabrication of exfoliated graphene devices. (a), (b) and (c) show the designs for graphene FET with channel lengths of 5, 10 and 15 µm respectively, (d) shows the number matrix across an area of 1 x 1 cm.

2.2 Designs for CVD Graphene Devices

The overview of the photomask designed for the fabrication of a CVD graphene device has been presented and explained in Fig. 4-5 (b). The detailed patterns for the fabrication of the 2-electrode device with a channel length of 300 µm are shown in Fig. A-3. Fig. A-3 (a) shows the design for the shaping of a graphene channel with a length of 400 µm and a width of 80 µm. Fig. A-3 (b) shows the design for the deposition of a Cr/Au contact on a graphene channel and Fig. A-3 (c) presents the design for the formation of a polymer window on the surface of a graphene channel. The window length and width are designed to be 260 and 50 µm respectively.

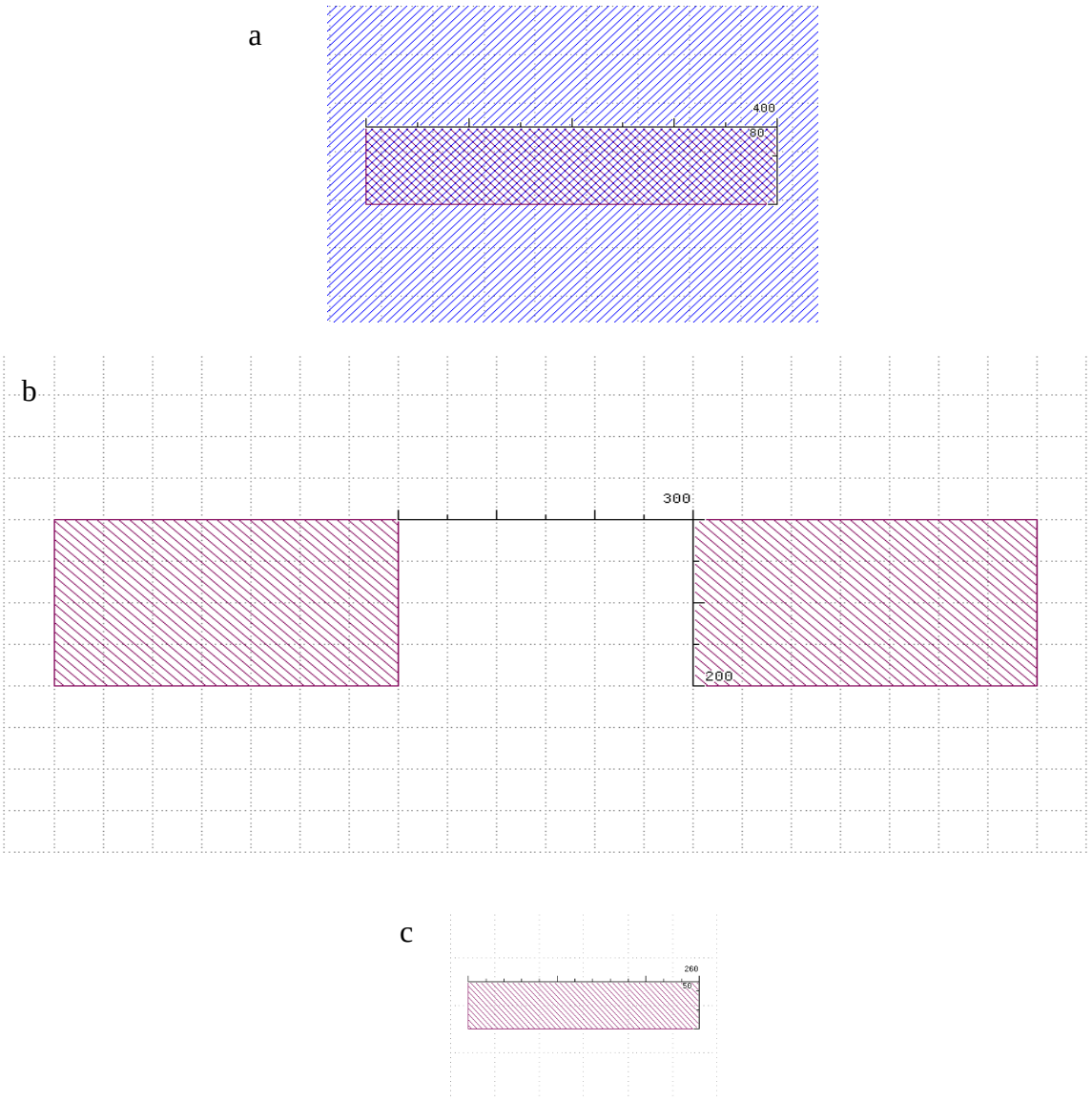

Figure A- 3. Designs for the fabrication of the 2-electrode device. (a), (b) and (c) are the designs for graphene shaping, electrode deposition and polymer window formation.

The detailed patterns for the fabrication of the 7-electrode device with the adjacent channel length of 95 µm are shown in Fig. A-4. Fig. A-4 (a) shows the design for the shaping of a graphene channel with a length of 720 µm and a width of 80 µm. Fig. A-4 (b) shows the design for the deposition of a Cr/Au contact on a graphene channel and Fig. A-4 (c) presents the design for the formation of a polymer window on the surface of a graphene channel. Each window has a length of 75 µm and a width of 50 µm.

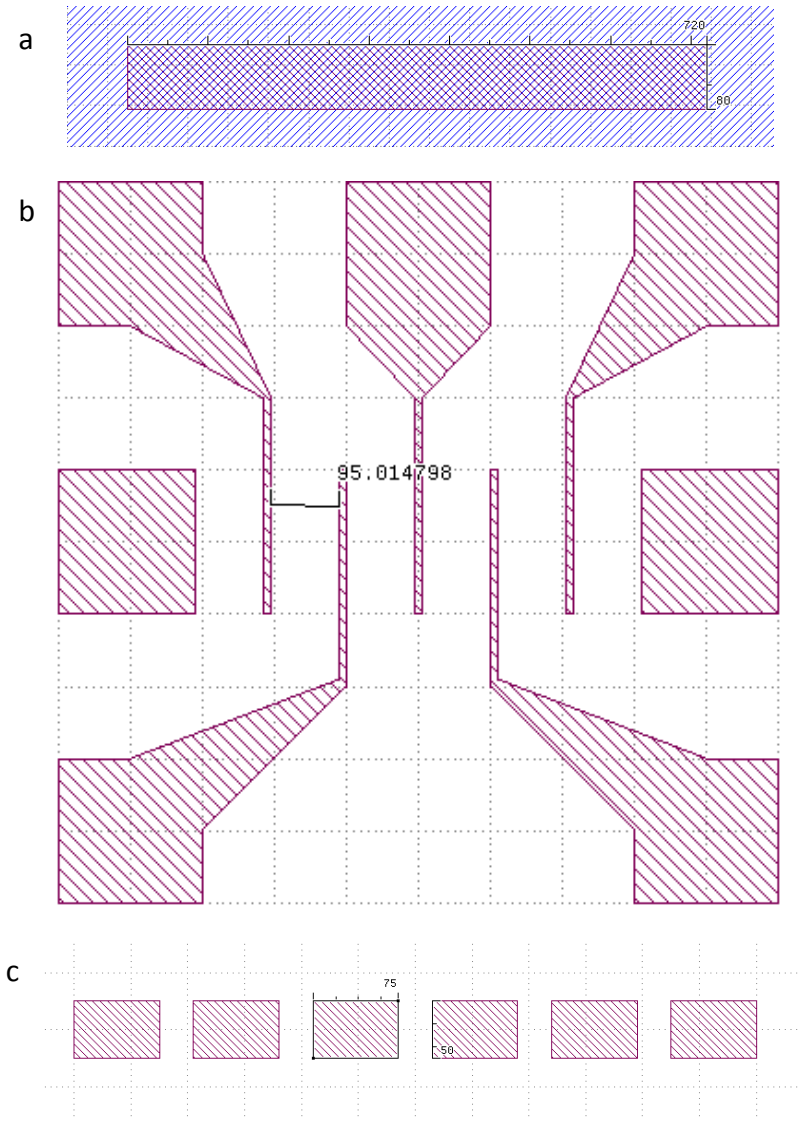

Figure A- 4. Designs for the fabrication of the 7-electrode device. (a), (b) and (c) are the designs for graphene shaping, electrode deposition and polymer window formation.

The detailed designs for the fabrication of an 8-electrode device and adjacent channel length of 95 µm are shown in Fig. A-5. Fig. A-5 (a) shows the design for the shaping of a graphene channel with a length of 400 µm and a width of 80 µm. Fig. A-5 (b) shows the design for the deposition of a Cr/Au contact on a graphene channel and Fig. A-5 (c) presents the design for the formation of a polymer window on the surface of a graphene channel. Each window has a length of 260 µm and a width of 50 µm.

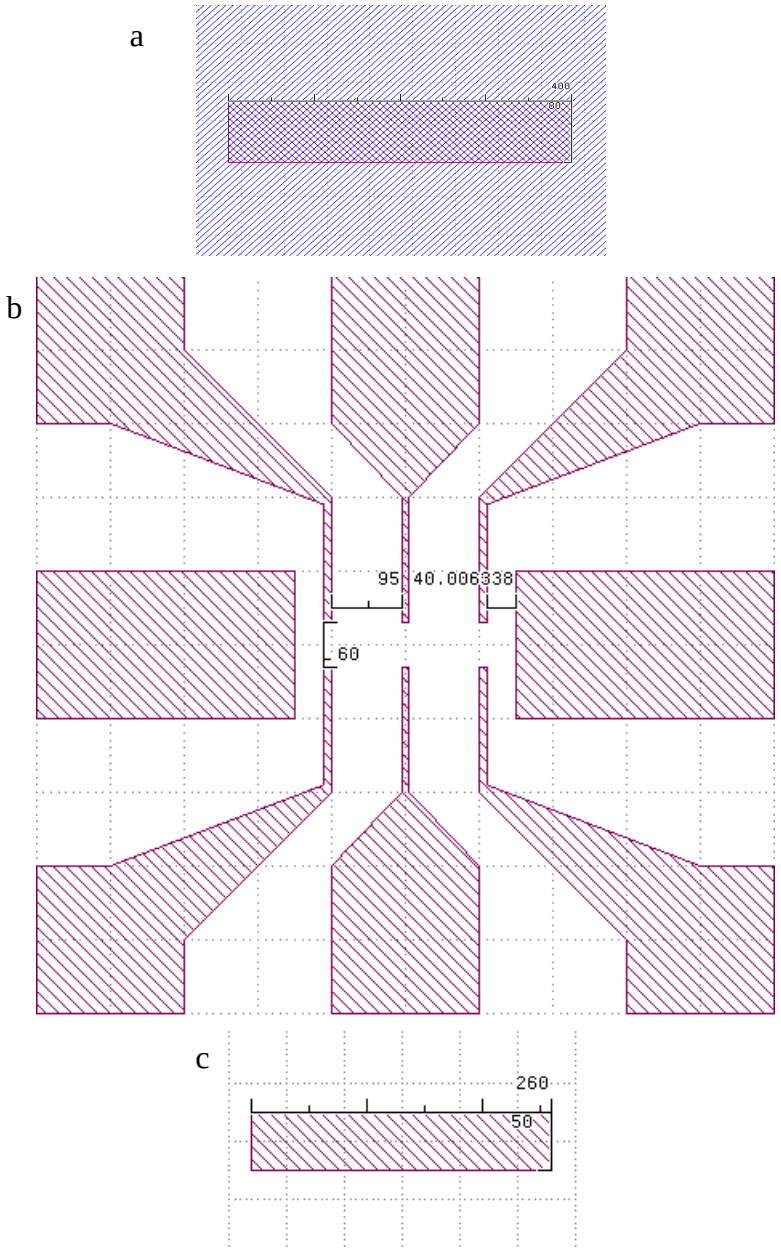

Figure A- 5. Designs for the fabrication of the 8-electrode device. (a), (b) and (c) are the designs for graphene shaping, electrode deposition and polymer window formation.

The corner designs for aligning the mask are shown in Fig. A-6. Fig. A-6 (a), (b), (c) and (d) are designed for aligning the quarter for substrate mapping, graphene channel shaping, electrode deposition and polymer window opening respectively.

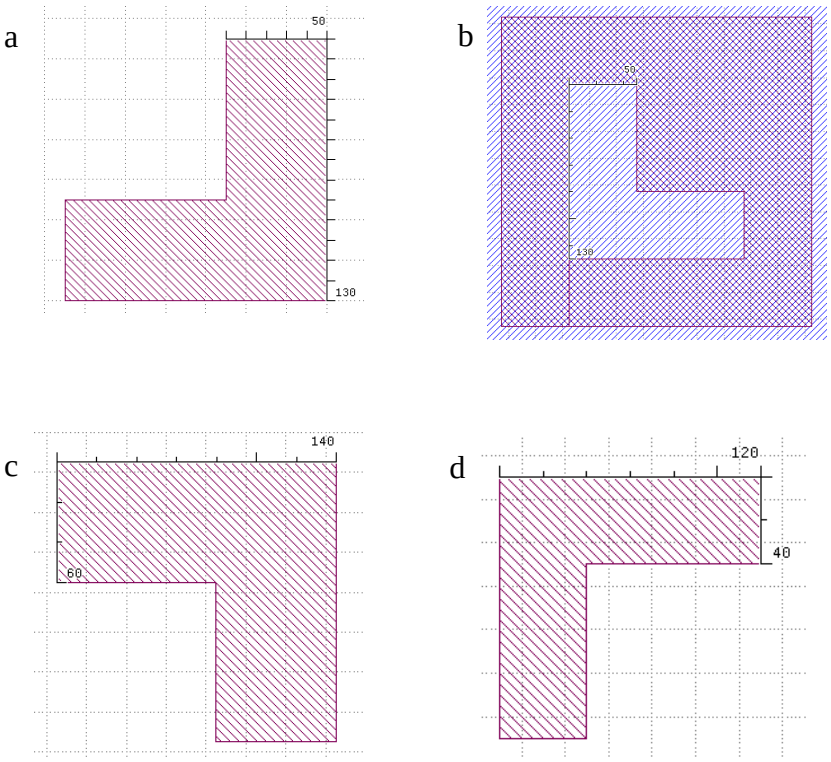

Figure A- 6. Markers for aligning the quarter for substrate mapping, graphene channel shaping, electrode deposition and polymer window opening respectively.

References

[1] A. K. Geim and K. S. Novoselov, "The rise of graphene," *Nature Materials,* vol. 6, p. 183, 2007.

[2] K. S. Novoselov, A. K. Geim, S. V. Morozov, D. Jiang, Y. Zhang, S. V. Dubonos, *et al.*, "Electric Field Effect in Atomically Thin Carbon Films," *Science,* vol. 306, p. 666, 2004.

[3] M. Ishigami, J. H. Chen, W. G. Cullen, M. S. Fuhrer, and E. D. Williams, "Atomic Structure of Graphene on SiO_2," *Nano Letters,* vol. 7, p. 1643, 2007.

[4] R. C. Thompson-Flagg, M. J. B. Moura, and M. Marder, "Rippling of graphene," *Europhysics Letters,* vol. 85, p. 46002, 2009.

[5] B. Garg, T. Bisht, and Y.-C. Ling, "Graphene-based nanomaterials as heterogeneous acid catalysts: a comprehensive perspective," *Molecules,* vol. 19, p. 14582, 2014.

[6] R. R. Nair, P. Blake, A. N. Grigorenko, K. S. Novoselov, T. J. Booth, T. Stauber, *et al.*, "Fine Structure Constant Defines Visual Transparency of Graphene," *Science,* vol. 320, p. 1308, 2008.

[7] Z. H. Ni, H. M. Wang, J. Kasim, H. M. Fan, T. Yu, Y. H. Wu, *et al.*, "Graphene Thickness Determination Using Reflection and Contrast Spectroscopy," *Nano Letters,* vol. 7, p. 2758, 2007.

[8] B. Li, G. Pan, S. A. Awan, and N. Avent, "Techniques for Production of Large Area Graphene for Electronic and Sensor Device Applications," *Graphene and 2D Materials,* vol. 1, p. 2299, 2014.

[9] K. I. Bolotin, K. J. Sikes, Z. Jiang, M. Klima, G. Fudenberg, J. Hone, *et al.*, "Ultrahigh electron mobility in suspended graphene," *Solid State Communications,* vol. 146, p. 351, 2008.

[10] J.-H. Chen, C. Jang, S. Xiao, M. Ishigami, and M. S. Fuhrer, "Intrinsic and extrinsic performance limits of graphene devices on SiO_2," *Nature Nanotechnology,* vol. 3, p. 206, 2008.

[11] C. Lee, X. Wei, J. W. Kysar, and J. Hone, "Measurement of the Elastic Properties and Intrinsic Strength of Monolayer Graphene," *Science,* vol. 321, p. 385, 2008.

[12] K. S. Novoselov, A. K. Geim, S. V. Morozov, D. Jiang, M. I. Katsnelson, I. V. Grigorieva, *et al.*, "Two-dimensional gas of massless Dirac fermions in graphene," *Nature,* vol. 438, p. 197, 2005.

[13] X. Wang, X. Li, L. Zhang, Y. Yoon, P. K. Weber, H. Wang, *et al.*, "N-Doping of Graphene Through Electrothermal Reactions with Ammonia," *Science,* vol. 324, p. 768, 2009.

[14] Y. Zhang, Y.-W. Tan, H. L. Stormer, and P. Kim, "Experimental observation of the quantum Hall effect and Berry's phase in graphene," *Nature,* vol. 438, p. 201, 2005.

[15] K. S. Novoselov, D. Jiang, F. Schedin, T. J. Booth, V. V. Khotkevich, S. V. Morozov, *et al.*, "Two-dimensional atomic crystals," *Proceedings of the National Academy of Sciences of the United States of America,* vol. 102, p. 10451, 2005.

[16] C. Berger, Z. Song, X. Li, X. Wu, N. Brown, C. Naud, *et al.*, "Electronic Confinement and Coherence in Patterned Epitaxial Graphene," *Science,* vol. 312, p. 1191, 2006.

[17] T. Ohta, A. Bostwick, T. Seyller, K. Horn, and E. Rotenberg, "Controlling the electronic structure of bilayer graphene," *Science,* vol. 313, p. 951, 2006.

[18] C. Jia, J. Jiang, L. Gan, and X. Guo, "Direct Optical Characterization of Graphene Growth and Domains on Growth Substrates," *Scitific Report.,* vol. 2, p. 707, 2012.

[19] A. H. Castro Neto, F. Guinea, N. M. R. Peres, K. S. Novoselov, and A. K. Geim, "The electronic properties of graphene," *Reviews of Modern Physics,* vol. 81, p. 109, 2009.

[20] C.-Y. Su, A.-Y. Lu, C.-Y. Wu, Y.-T. Li, K.-K. Liu, W. Zhang, *et al.*, "Direct Formation of Wafer Scale Graphene Thin Layers on Insulating Substrates by Chemical Vapor Deposition," *Nano Letters,* vol. 11, p. 3612, 2011.

[21] K. S. Kim, Y. Zhao, H. Jang, S. Y. Lee, J. M. Kim, K. S. Kim, *et al.*, "Large-scale pattern growth of graphene films for stretchable transparent electrodes," *Nature,* vol. 457, p. 706, 2009.

[22] H. J. Park, J. Meyer, S. Roth, and V. Skákalová, "Growth and properties of few-layer graphene prepared by chemical vapor deposition," *Carbon,* vol. 48, p. 1088, 2010.

[23] N. Tombros, C. Jozsa, M. Popinciuc, H. T. Jonkman, and B. J. van Wees, "Electronic spin transport and spin precession in single graphene layers at room temperature," *Nature,* vol. 448, p. 571, 2007.

[24] S. Chen, L. Brown, M. Levendorf, W. Cai, S.-Y. Ju, J. Edgeworth, *et al.*, "Oxidation Resistance of Graphene-Coated Cu and Cu/Ni Alloy," *ACS Nano,* vol. 5, p. 1321, 2011.

[25] H. Yang, F. Li, C. Shan, D. Han, Q. Zhang, L. Niu, *et al.*, "Covalent functionalization of chemically converted graphene sheets via silane and its reinforcement," *Journal of Materials Chemistry,* vol. 19, p. 4632, 2009.

[26] K. P. Loh, Q. Bao, P. K. Ang, and J. Yang, "The chemistry of graphene," *Journal of Materials Chemistry,* vol. 20, p. 2277, 2010.

[27] N. I. Kovtyukhova, P. J. Ollivier, B. R. Martin, T. E. Mallouk, S. A. Chizhik, E. V. Buzaneva, *et al.*, "Layer-by-layer assembly of ultrathin composite films from micron-sized graphite oxide sheets and polycations," *Chemistry of Materials,* vol. 11, p. 771, 1999.

[28] Y. Si and E. T. Samulski, "Synthesis of Water Soluble Graphene," *Nano Letters,* vol. 8, p. 1679, 2008.

[29] P. A. Denis and F. Iribarne, "Comparative Study of Defect Reactivity in Graphene," *The Journal of Physical Chemistry C,* vol. 117, p. 19048, 2013.

[30] V. Georgakilas, M. Otyepka, A. B. Bourlinos, V. Chandra, N. Kim, K. C. Kemp, *et al.*, "Functionalization of Graphene: Covalent and Non-Covalent Approaches, Derivatives and Applications," *Chemical Reviews,* vol. 112, p. 6156, 2012.

[31] C. Ataca, E. Akturk, S. Ciraci, and H. Ustunel, "High-capacity hydrogen storage by metallized graphene," *Applied Physics Letters,* vol. 93, p. 043123, 2008.

[32] D. C. Elias, R. R. Nair, T. M. G. Mohiuddin, S. V. Morozov, P. Blake, M. P. Halsall, *et al.*, "Control of Graphene's Properties by Reversible Hydrogenation: Evidence for Graphane," *Science,* vol. 323, p. 610, 2009.

[33] J. T. Robinson, J. S. Burgess, C. E. Junkermeier, S. C. Badescu, T. L. Reinecke, F. K. Perkins, *et al.*, "Properties of Fluorinated Graphene Films," *Nano Letters,* vol. 10, p. 3001, 2010.

[34] D. Wei, Y. Liu, Y. Wang, H. Zhang, L. Huang, and G. Yu, "Synthesis of N-Doped Graphene by Chemical Vapor Deposition and Its Electrical Properties," *Nano Letters,* vol. 9, p. 1752, 2009.

[35] T. B. Martins, R. H. Miwa, A. J. R. da Silva, and A. Fazzio, "Electronic and Transport Properties of Boron-Doped Graphene Nanoribbons," *Physical Review Letters,* vol. 98, p. 196803, 2007.

[36] A. Lherbier, X. Blase, Y.-M. Niquet, F. Triozon, and S. Roche, "Charge transport in chemically doped 2D graphene," *Physical review letters,* vol. 101, p. 036808, 2008.

[37] C. Berger, Z. Song, T. Li, X. Li, A. Y. Ogbazghi, R. Feng, *et al.*, "Ultrathin Epitaxial Graphite: 2D Electron Gas Properties and a Route toward Graphene-based Nanoelectronics," *The Journal of Physical Chemistry B,* vol. 108, p. 19912, 2004.

[38] B. Guo, Q. Liu, E. Chen, H. Zhu, L. Fang, and J. R. Gong, "Controllable N-Doping of Graphene," *Nano Letters,* vol. 10, p. 4975, 2010.

[39] F. Bonaccorso, Z. Sun, T. Hasan, and A. C. Ferrari, "Graphene photonics and optoelectronics," *Nature Photons,* vol. 4, p. 611, 2010.

[40] J. Wu, H. A. Becerril, Z. Bao, Z. Liu, Y. Chen, and P. Peumans, "Organic solar cells with solution-processed graphene transparent electrodes," *Applied Physics Letters,* vol. 92, p. 263302, 2008.

[41] Q. Lu, X. Dong, L.-J. Li, and X. Hu, "Direct electrochemistry-based hydrogen peroxide biosensor formed from single-layer graphene nanoplatelet–enzyme composite film," *Talanta,* vol. 82, p. 1344, 2010.

[42] N. Mohanty and V. Berry, "Graphene-Based Single-Bacterium Resolution Biodevice and DNA Transistor: Interfacing Graphene Derivatives with Nanoscale and Microscale Biocomponents," *Nano Letters,* vol. 8, p. 4469, 2008.

[43] M. D. Stoller, S. Park, Y. Zhu, J. An, and R. S. Ruoff, "Graphene-based ultracapacitors," *Nano letters,* vol. 8, p. 3498, 2008.

[44] Y.-W. Son, M. L. Cohen, and S. G. Louie, "Half-metallic graphene nanoribbons," *Nature,* vol. 444, p. 347, 2006.

[45] B. Trauzettel, D. V. Bulaev, D. Loss, and G. Burkard, "Spin qubits in graphene quantum dots," *Nature Physics,* vol. 3, pp. 192, 2007.

[46] T. Yokoyama, "Controllable spin transport in ferromagnetic graphene junctions," *Physical Review B,* vol. 77, p. 073413, 2008.

[47] V. Fal'ko, "Graphene: Quantum information on chicken wire," *Nature Physics,* vol. 3, p. 151, 2007.

[48] H. P. Boehm, A. Clauss, G. O. Fischer, and U. Hofmann, "Das Adsorptionsverhalten sehr dünner Kohlenstoff-Folien," *Zeitschrift für anorganische und allgemeine Chemie,* vol. 316, p. 119, 1962.

[49] S. Mouras, A. Hamm, D. Djurado, and J.-C. Cousseins, "Synthesis of first stage graphite intercalation compounds with fluorides," *Revue de chimie minérale,* vol. 24, p. 572, 1987.

[50] P. R. Wallace, "The Band Theory of Graphite," *Physical Review,* vol. 71, p. 622, 1947.

[51] K. Seibert, G. C. Cho, W. Kütt, H. Kurz, D. H. Reitze, M. C. Downer, *et al.*, "Ultrafast Relaxation Processes of Hot Carriers in Graphite," in *Ultrafast Phenomena VII*. vol. 53, C. Harris, E. Ippen, G. Mourou, and A. Zewail, Eds., ed: Springer Berlin Heidelberg, 1990, p. 303.

[52] K. Andre and K. Philip, "Carbon Wonderland," *Scientific American,* vol. 298, p. 90, 2008.

[53] F. Bonaccorso, A. Lombardo, T. Hasan, Z. Sun, L. Colombo, and A. C. Ferrari, "Production and processing of graphene and 2d crystals," *Materials Today,* vol. 15, p. 564, 2012.

[54] A. J. Van Bommel, J. E. Crombeen, and A. Van Tooren, "LEED and Auger electron observations of the SiC(0001) surface," *Surface Science,* vol. 48, p. 463, 1975.

[55] I. Forbeaux, J. M. Themlin, A. Charrier, F. Thibaudau, and J. M. Debever, "Solid-state graphitization mechanisms of silicon carbide 6H–SiC polar faces," *Applied Surface Science,* vol. 162–163, p. 406, 2000.

[56] I. Forbeaux, J. M. Themlin, and J. M. Debever, "Heteroepitaxial graphite on 6H-SiC(0001): Interface formation through conduction-band electronic structure," *Physical Review B,* vol. 58, p. 16396, 1998.

[57] P. Sutter, "Epitaxial graphene: How silicon leaves the scene," *Nature Materials,* vol. 8, p. 171, 2009.

[58] W. A. de Heer, C. Berger, X. Wu, P. N. First, E. H. Conrad, X. Li, *et al.*, "Epitaxial graphene," *Solid State Communications,* vol. 143, p. 92, 2007.

[59] N. Srivastava, H. Guowei, Luxmi, P. C. Mende, R. M. Feenstra, and S. Yugang, "Graphene formed on SiC under various environments: comparison of Si-face and C-face," *Journal of Physics D: Applied Physics,* vol. 45, p. 154001, 2012.

[60] K. V. Emtsev, T. Seyller, L. Ley, A. Tadich, L. Broekman, J. D. Riley, *et al.*, "Electronic properties of clean unreconstructed 6H–SiC surfaces studied by angle resolved photoelectron spectroscopy," *Surface Science,* vol. 600, p. 3845, 2006.

[61] K. V. Emtsev, A. Bostwick, K. Horn, J. Jobst, G. L. Kellogg, L. Ley, *et al.*, "Towards wafer-size graphene layers by atmospheric pressure graphitization of silicon carbide," *Nature Materials,* vol. 8, p. 203, 2009.

[62] C. Riedl, C. Coletti, and U. Starke, "Structural and electronic properties of epitaxial graphene on SiC(0 0 0 1): a review of growth, characterization, transfer doping and hydrogen intercalation," *Journal of Physics D: Applied Physics,* vol. 43, p. 374009, 2010.

[63] G. G. Jernigan, B. L. VanMil, J. L. Tedesco, J. G. Tischler, E. R. Glaser, A. Davidson, *et al.*, "Comparison of Epitaxial Graphene on Si-face and C-face 4H

SiC Formed by Ultrahigh Vacuum and RF Furnace Production," *Nano Letters,* vol. 9, p. 2605, 2009.

[64] F. Schwierz, "Graphene transistors," *Nature Nanotechnology,* vol. 5, p. 487, 2010.

[65] Y.-M. Lin, C. Dimitrakopoulos, K. A. Jenkins, D. B. Farmer, H.-Y. Chiu, A. Grill, *et al.*, "100-GHz Transistors from Wafer-Scale Epitaxial Graphene," *Science,* vol. 327, p. 662, 2010.

[66] Y.-M. Lin, A. Valdes-Garcia, S.-J. Han, D. B. Farmer, I. Meric, Y. Sun, *et al.*, "Wafer-Scale Graphene Integrated Circuit," *Science,* vol. 332, p. 1294, 2011.

[67] X. Li, W. Cai, J. An, S. Kim, J. Nah, D. Yang, *et al.*, "Large-Area Synthesis of High-Quality and Uniform Graphene Films on Copper Foils," *Science,* vol. 324, p. 1312, 2009.

[68] Y. Lee, S. Bae, H. Jang, S. Jang, S.-E. Zhu, S. H. Sim, *et al.*, "Wafer-Scale Synthesis and Transfer of Graphene Films," *Nano Letters,* vol. 10, p. 490, 2010.

[69] X. Li, W. Cai, L. Colombo, and R. S. Ruoff, "Evolution of Graphene Growth on Ni and Cu by Carbon Isotope Labeling," *Nano Letters,* vol. 9, p. 4268, 2009.

[70] S. Lee, K. Lee, and Z. Zhong, "Wafer Scale Homogeneous Bilayer Graphene Films by Chemical Vapor Deposition," *Nano Letters,* vol. 10, p. 4702, 2010.

[71] C. Vo-Van, A. Kimouche, A. Reserbat-Plantey, O. Fruchart, P. Bayle-Guillemaud, N. Bendiab, *et al.*, "Epitaxial graphene prepared by chemical vapor deposition on single crystal thin iridium films on sapphire," *Applied Physics Letters,* vol. 98, p. 181903, 2011.

[72] Y. Miyasaka, A. Nakamura, and J. Temmyo, "Graphite Thin Films Consisting of Nanograins of Multilayer Graphene on Sapphire Substrates Directly Grown by Alcohol Chemical Vapor Deposition," *Japanese Journal of Applied Physics,* vol. 50, p. 04DH12, 2011.

[73] G. Alexander, K. Kurt, and V. V. Denis, "Dynamics of graphene growth on a metal surface: a time-dependent photoemission study," *New Journal of Physics*, vol. 11, p. 073050, 2009.

[74] M. E. Ramón, A. Gupta, C. Corbet, D. A. Ferrer, H. C. P. Movva, G. Carpenter, *et al.*, "CMOS-Compatible Synthesis of Large-Area, High-Mobility Graphene by Chemical Vapor Deposition of Acetylene on Cobalt Thin Films," *ACS Nano*, vol. 5, p. 7198, 2011.

[75] Q. Yu, J. Lian, S. Siriponglert, H. Li, Y. P. Chen, and S.-S. Pei, "Graphene segregated on Ni surfaces and transferred to insulators," *Applied Physics Letters*, vol. 93, p. 113103, 2008.

[76] A. Reina, X. Jia, J. Ho, D. Nezich, H. Son, V. Bulovic, *et al.*, "Large Area, Few-Layer Graphene Films on Arbitrary Substrates by Chemical Vapor Deposition," *Nano Letters*, vol. 9, p. 30, 2008.

[77] P. W. Sutter, J.-I. Flege, and E. A. Sutter, "Epitaxial graphene on ruthenium," *Nature Materials*, vol. 7, p. 406, 2008.

[78] E. Sutter, P. Albrecht, and P. Sutter, "Graphene growth on polycrystalline Ru thin films," *Applied Physics Letters*, vol. 95, p. 133109, 2009.

[79] P. W. Sutter, P. M. Albrecht, and E. A. Sutter, "Graphene growth on epitaxial Ru thin films on sapphire," *Applied Physics Letters*, vol. 97, p. 213101, 2010.

[80] J. Coraux, A. T. N`Diaye, C. Busse, and T. Michely, "Structural Coherency of Graphene on Ir(111)," *Nano Letters*, vol. 8, p. 565, 2008.

[81] T. Oznuluer, E. Pince, E. O. Polat, O. Balci, O. Salihoglu, and C. Kocabas, "Synthesis of graphene on gold," *Applied Physics Letters*, vol. 98, p. 183101, 2011.

[82] B. J. Kang, J. H. Mun, C. Y. Hwang, and B. J. Cho, "Monolayer graphene growth on sputtered thin film platinum," *Journal of Applied Physics,* vol. 106, p. 104309, 2009.

[83] E. V. Rut'kov, A. V. Kuz'michev, and N. R. Gall', "Carbon interaction with rhodium surface: Adsorption, dissolution, segregation, growth of graphene layers," *Physics of the Solid State,* vol. 53, p. 1092, 2011.

[84] S. Roth, J. Osterwalder, and T. Greber, "Synthesis of epitaxial graphene on rhodium from 3-pentanone," *Surface Science,* vol. 605, p. L17, 2011.

[85] S.-Y. Kwon, C. V. Ciobanu, V. Petrova, V. B. Shenoy, J. Bareño, V. Gambin, *et al.*, "Growth of Semiconducting Graphene on Palladium," *Nano Letters,* vol. 9, p. 3985, 2009.

[86] Y. Murata, S. Nie, A. Ebnonnasir, E. Starodub, B. B. Kappes, K. F. McCarty, *et al.*, "Growth structure and work function of bilayer graphene on Pd(111)," *Physical Review B,* vol. 85, p. 205443, 2012.

[87] H. An, W.-J. Lee, and J. Jung, "Graphene synthesis on Fe foil using thermal CVD," *Current Applied Physics,* vol. 11, p. S81, 2011.

[88] P. R. Somani, S. P. Somani, and M. Umeno, "Planer nano-graphenes from camphor by CVD," *Chemical Physics Letters,* vol. 430, p. 56, 2006.

[89] J. H. Hafner, C. L. Cheung, and C. M. Lieber, "Growth of nanotubes for probe microscopy tips," *Nature,* vol. 398, p. 761, 1999.

[90] T. Land, T. Michely, R. Behm, J. Hemminger, and G. Comsa, "STM investigation of single layer graphite structures produced on Pt (111) by hydrocarbon decomposition," *Surface Science,* vol. 264, p. 261, 1992.

[91] A. Nagashima, K. Nuka, H. Itoh, T. Ichinokawa, C. Oshima, and S. Otani, "Electronic states of monolayer graphite formed on TiC (111) surface," *Surface Science,* vol. 291, p. 93, 1993.

[92] Z. Li, P. Wu, c. Wang, X. Fan, W. Zhang, X. Zhai, *et al.*, "Chemical Vapor Deposition Growth of Graphene using Other Hydrocarbon Sources," 2011.

[93] X. Li, C. W. Magnuson, A. Venugopal, J. An, J. W. Suk, B. Han, *et al.*, "Graphene Films with Large Domain Size by a Two-Step Chemical Vapor Deposition Process," *Nano Letters,* vol. 10, p. 4328, 2010.

[94] A. Ismach, C. Druzgalski, S. Penwell, A. Schwartzberg, M. Zheng, A. Javey, *et al.*, "Direct Chemical Vapor Deposition of Graphene on Dielectric Surfaces," *Nano Letters,* vol. 10, p. 1542, 2010.

[95] L. G. De Arco, Z. Yi, A. Kumar, and Z. Chongwu, "Synthesis, Transfer, and Devices of Single- and Few-Layer Graphene by Chemical Vapor Deposition," *Nanotechnology, IEEE Transactions on,* vol. 8, p. 135, 2009.

[96] J. Hamilton and J. Blakely, "Carbon segregation to single crystal surfaces of Pt, Pd and Co," *Surface Science,* vol. 91, p. 199, 1980.

[97] M. Eizenberg and J. Blakely, "Carbon monolayer phase condensation on Ni (111)," *Surface Science,* vol. 82, p. 228, 1979.

[98] F. Himpsel, K. Christmann, P. Heimann, D. Eastman, and P. J. Feibelman, "Adsorbate band dispersions for C on Ru (0001)," *Surface Science Letters,* vol. 115, p. L159, 1982.

[99] N. A. Kholin, E. V. Rut'kov, and A. Y. Tontegode, "The nature of the adsorption bond between graphite islands and iridium surface," *Surface Science,* vol. 139, p. 155, 1984.

[100] A. Reina, S. Thiele, X. Jia, S. Bhaviripudi, M. Dresselhaus, J. Schaefer, *et al.*, "Growth of large-area single- and Bi-layer graphene by controlled carbon precipitation on polycrystalline Ni surfaces," *Nano Research,* vol. 2, p. 509, 2009.

[101] H. Wang, G. Wang, P. Bao, S. Yang, W. Zhu, X. Xie, *et al.*, "Controllable synthesis of submillimeter single-crystal monolayer graphene domains on copper foils by suppressing nucleation," *Journal of the American Chemical Society*, vol. 134, p. 3627, 2012.

[102] Y. Zhang, L. Gomez, F. N. Ishikawa, A. Madaria, K. Ryu, C. Wang, *et al.*, "Comparison of Graphene Growth on Single-Crystalline and Polycrystalline Ni by Chemical Vapor Deposition," *The Journal of Physical Chemistry Letters*, vol. 1, p. 3101, 2010.

[103] Z. Luo, Y. Lu, D. W. Singer, M. E. Berck, L. A. Somers, B. R. Goldsmith, *et al.*, "Effect of Substrate Roughness and Feedstock Concentration on Growth of Wafer-Scale Graphene at Atmospheric Pressure," *Chemistry of Materials*, vol. 23, p. 1441, 2011.

[104] C. S. Ruiz-Vargas, H. L. Zhuang, P. Y. Huang, A. M. van der Zande, S. Garg, P. L. McEuen, *et al.*, "Softened Elastic Response and Unzipping in Chemical Vapor Deposition Graphene Membranes," *Nano Letters*, vol. 11, p. 2259, 2011.

[105] Y. Zhang, T. Gao, Y. Gao, S. Xie, Q. Ji, K. Yan, *et al.*, "Defect-like Structures of Graphene on Copper Foils for Strain Relief Investigated by High-Resolution Scanning Tunneling Microscopy," *ACS Nano*, vol. 5, p. 4014, 2011.

[106] N. Liu, Z. Pan, L. Fu, C. Zhang, B. Dai, and Z. Liu, "The origin of wrinkles on transferred graphene," *Nano Research*, vol. 4, p. 996, 2011.

[107] T. Kobayashi, M. Bando, N. Kimura, K. Shimizu, K. Kadono, N. Umezu, *et al.*, "Production of a 100-m-long high-quality graphene transparent conductive film by roll-to-roll chemical vapor deposition and transfer process," *Applied Physics Letters*, vol. 102, p. 023112, 2013.

[108] Y. Yao and C.-p. Wong, "Monolayer graphene growth using additional etching process in atmospheric pressure chemical vapor deposition," *Carbon,* vol. 50, p. 5203, 2012.

[109] Z.-Y. Juang, C.-Y. Wu, A.-Y. Lu, C.-Y. Su, K.-C. Leou, F.-R. Chen, *et al.*, "Graphene synthesis by chemical vapor deposition and transfer by a roll-to-roll process," *Carbon,* vol. 48, p. 3169, 2010.

[110] A. Reina, H. Son, L. Jiao, B. Fan, M. S. Dresselhaus, Z. Liu, *et al.*, "Transferring and Identification of Single- and Few-Layer Graphene on Arbitrary Substrates," *The Journal of Physical Chemistry C,* vol. 112, p. 17741, 2008.

[111] S. Bae, H. Kim, Y. Lee, X. Xu, J.-S. Park, Y. Zheng, *et al.*, "Roll-to-roll production of 30-inch graphene films for transparent electrodes," *Nature Nanotechnology,* vol. 5, p. 574, 2010.

[112] X. Li, Y. Zhu, W. Cai, M. Borysiak, B. Han, D. Chen, *et al.*, "Transfer of Large-Area Graphene Films for High-Performance Transparent Conductive Electrodes," *Nano Letters,* vol. 9, p. 4359, 2009.

[113] J. Kang, H. Kim, K. S. Kim, S.-K. Lee, S. Bae, J.-H. Ahn, *et al.*, "High-performance graphene-based transparent flexible heaters," *Nano Letters,* vol. 11, p. 5154, 2011.

[114] Y.-Y. Lee, K.-H. Tu, C.-C. Yu, S.-S. Li, J.-Y. Hwang, C.-C. Lin, *et al.*, "Top Laminated Graphene Electrode in a Semitransparent Polymer Solar Cell by Simultaneous Thermal Annealing/Releasing Method," *ACS Nano,* vol. 5, p. 6564, 2011.

[115] N. Espinosa, R. García-Valverde, A. Urbina, and F. C. Krebs, "A life cycle analysis of polymer solar cell modules prepared using roll-to-roll methods under ambient conditions," *Solar Energy Materials and Solar Cells,* vol. 95, p. 1293, 2011.

[116] S. Chen, W. Cai, R. D. Piner, J. W. Suk, Y. Wu, Y. Ren, *et al.*, "Synthesis and Characterization of Large-Area Graphene and Graphite Films on Commercial Cu–Ni Alloy Foils," *Nano Letters,* vol. 11, p. 3519, 2011.

[117] R. S. Weatherup, B. C. Bayer, R. Blume, C. Ducati, C. Baehtz, R. Schlögl, *et al.*, "In Situ Characterization of Alloy Catalysts for Low-Temperature Graphene Growth," *Nano Letters,* vol. 11, p. 4154, 2011.

[118] B. Dai, L. Fu, Z. Zou, M. Wang, H. Xu, S. Wang, *et al.*, "Rational design of a binary metal alloy for chemical vapour deposition growth of uniform single-layer graphene," *Nature Communications,* vol. 2, p. 522, 2011.

[119] Y. S. Woo, D. H. Seo, D.-H. Yeon, J. Heo, H.-J. Chung, A. Benayad, *et al.*, "Low temperature growth of complete monolayer graphene films on Ni-doped copper and gold catalysts by a self-limiting surface reaction," *Carbon,* vol. 64, p. 315, 2013.

[120] Z.-Y. Juang, C.-Y. Wu, C.-W. Lo, W.-Y. Chen, C.-F. Huang, J.-C. Hwang, *et al.*, "Synthesis of graphene on silicon carbide substrates at low temperature," *Carbon,* vol. 47, p. 2026, 2009.

[121] Z. Sun, Z. Yan, J. Yao, E. Beitler, Y. Zhu, and J. M. Tour, "Growth of graphene from solid carbon sources," *Nature,* vol. 468, p. 549, 2010.

[122] C. Orofeo, H. Ago, B. Hu, and M. Tsuji, "Synthesis of large area, homogeneous, single layer graphene films by annealing amorphous carbon on Co and Ni," *Nano Research,* vol. 4, p. 531, 2011.

[123] W. Xiong, Y. S. Zhou, L. J. Jiang, A. Sarkar, M. Mahjouri-Samani, Z. Q. Xie, *et al.*, "Single-Step Formation of Graphene on Dielectric Surfaces," *Advanced Materials,* vol. 25, p. 630, 2013.

[124] M. Zheng, K. Takei, B. Hsia, H. Fang, X. Zhang, N. Ferralis, *et al.*, "Metal-catalyzed crystallization of amorphous carbon to graphene," *Applied Physics Letters*, vol. 96, p. 063110, 2010.

[125] J. H. Seo, H. W. Lee, J.-K. Kim, D.-G. Kim, J.-W. Kang, M.-S. Kang, *et al.*, "Few layer graphene synthesized by filtered vacuum arc system using solid carbon source," *Current Applied Physics*, vol. 12, p. S131, 2012.

[126] E. Moreau, F. Ferrer, D. Vignaud, S. Godey, and X. Wallart, "Graphene growth by molecular beam epitaxy using a solid carbon source," *physica status solidi (a)*, vol. 207, p. 300, 2010.

[127] L. Baraton, Z. B. He, C. S. Lee, C. S. Cojocaru, M. Châtelet, J. L. Maurice, *et al.*, "On the mechanisms of precipitation of graphene on nickel thin films," *EPL (Europhysics Letters)*, vol. 96, p. 46003, 2011.

[128] B. Laurent, H. Zhanbing, L. Chang Seok, M. Jean-Luc, C. Costel Sorin, G.-L. Anne-Françoise, *et al.*, "Synthesis of few-layered graphene by ion implantation of carbon in nickel thin films," *Nanotechnology*, vol. 22, p. 085601, 2011.

[129] S.-J. Byun, H. Lim, G.-Y. Shin, T.-H. Han, S. H. Oh, J.-H. Ahn, *et al.*, "Graphenes Converted from Polymers," *The Journal of Physical Chemistry Letters*, vol. 2, p. 493, 2011.

[130] H.-J. Shin, W. M. Choi, S.-M. Yoon, G. H. Han, Y. S. Woo, E. S. Kim, *et al.*, "Transfer-Free Growth of Few-Layer Graphene by Self-Assembled Monolayers," *Advanced Materials*, vol. 23, p. 4392, 2011.

[131] T. Wu, G. Ding, H. Shen, H. Wang, L. Sun, D. Jiang, *et al.*, "Triggering the Continuous Growth of Graphene Toward Millimeter-Sized Grains," *Advanced Functional Materials*, vol. 23, p. 198, 2013.

[132] Z. Yan, Z. Peng, Z. Sun, J. Yao, Y. Zhu, Z. Liu, *et al.*, "Growth of Bilayer Graphene on Insulating Substrates," *ACS Nano*, vol. 5, p. 8187, 2011.

[133] G. Lippert, J. Dabrowski, M. Lemme, C. Marcus, O. Seifarth, and G. Lupina, "Direct graphene growth on insulator," *physica status solidi (b)*, vol. 248, p. 2619, 2011.

[134] N. Liu, L. Fu, B. Dai, K. Yan, X. Liu, R. Zhao, *et al.*, "Universal Segregation Growth Approach to Wafer-Size Graphene from Non-Noble Metals," *Nano Letters*, vol. 11, p. 297, 2010.

[135] J. Hofrichter, B. u. N. Szafranek, M. Otto, T. J. Echtermeyer, M. Baus, A. Majerus, *et al.*, "Synthesis of Graphene on Silicon Dioxide by a Solid Carbon Source," *Nano Letters*, vol. 10, p. 36, 2009.

[136] C. Y. Kang, L. L. Fan, S. Chen, Z. L. Liu, P. S. Xu, and C. W. Zou, "Few-layer graphene growth on 6H-SiC(0001) surface at low temperature via Ni-silicidation reactions," *Applied Physics Letters*, vol. 100, p. 251604, 2012.

[137] B. Li, G. Pan, M. Heath, D. Horsell, and M. L. Wears, L. A. Taan, " Transfer-free growth of graphene on SiO2 insulator substrate from sputtered carbon and nickel films, Carbon," *Carbon*, vol. 65, p. 349, 2013.

[138] Z. Peng, Z. Yan, Z. Sun, and J. M. Tour, "Direct Growth of Bilayer Graphene on SiO2 Substrates by Carbon Diffusion through Nickel," *ACS Nano*, vol. 5, p. 8241, 2011.

[139] S. Suzuki, Y. Takei, K. Furukawa, and H. Hibino, "Graphene Growth from a Spin-Coated Polymer without a Reactive Gas," *Applied Physics Express*, vol. 4, p. 065102, 2011.

[140] X. Liu, L. Fu, N. Liu, T. Gao, Y. Zhang, L. Liao, *et al.*, "Segregation Growth of Graphene on Cu–Ni Alloy for Precise Layer Control," *The Journal of Physical Chemistry C*, vol. 115, p. 11976, 2011.

[141] H. Sojoudi and S. Graham, "Transfer-Free Selective Area Synthesis of Graphene Using Solid-State Self-Segregation of Carbon In Cu/Ni Bilayers," *ECS Journal of Solid State Science and Technology,* vol. 2, p. M17, 2013.

[142] G. Pan, B. Li, M. Heath, D. Horsell, M. L. Wears, L. Al Taan, *et al.*, "Transfer-free growth of graphene on SiO2 insulator substrate from sputtered carbon and nickel films," *Carbon,* vol. 65, p. 349, 2013.

[143] D. Wang, H. Tian, Y. Yang, D. Xie, T.-L. Ren, and Y. Zhang, "Scalable and Direct Growth of Graphene Micro Ribbons on Dielectric Substrates," *Scitific Report,* vol. 3, 2013.

[144] L. Gao, G.-X. Ni, Y. Liu, B. Liu, A. H. Castro Neto, and K. P. Loh, "Face-to-face transfer of wafer-scale graphene films," *Nature,* vol. 505, p. 190, 2014.

[145] L. Gao, G.-X. Ni, Y. Liu, B. Liu, A. H. Castro Neto, and K. P. Loh, "Face-to-face transfer of wafer-scale graphene films," *Nature,* vol. 505, p. 190, 2014.

[146] J. Kwak, J. H. Chu, J.-K. Choi, S.-D. Park, H. Go, S. Y. Kim, *et al.*, "Near room-temperature synthesis of transfer-free graphene films," *Nature Communication,* vol. 3, p. 645, 2012.

[147] L. Zhang, Z. Shi, Y. Wang, R. Yang, D. Shi, and G. Zhang, "Catalyst-free growth of nanographene films on various substrates," *Nano Research,* vol. 4, p. 315, 2011.

[148] G. Wang, M. Zhang, Y. Zhu, G. Ding, D. Jiang, Q. Guo, *et al.*, "Direct Growth of Graphene Film on Germanium Substrate," *Scitific Report,* vol. 3, 2013.

[149] J.-H. Lee, E. K. Lee, W.-J. Joo, Y. Jang, B.-S. Kim, J. Y. Lim, *et al.*, "Wafer-Scale Growth of Single-Crystal Monolayer Graphene on Reusable Hydrogen-Terminated Germanium," *Science, vol. 344,p.286 ,* 2014.

[150] K. S. Novoselov, V. I. Falko, L. Colombo, P. R. Gellert, M. G. Schwab, and K. Kim, "A roadmap for graphene," *Nature,* vol. 490, p. 192 2012.

[151] Y. Cui, S. N. Kim, S. E. Jones, L. L. Wissler, R. R. Naik, and M. C. McAlpine, "Chemical Functionalization of Graphene Enabled by Phage Displayed Peptides," *Nano Letters,* vol. 10, p. 4559, 2010.

[152] B. C. Brodie, "On the Atomic Weight of Graphite," *Philosophical Transactions of the Royal Society of London,* vol. 149, p. 249, 1859.

[153] L. Staudenmaier, "Verfahren zur Darstellung der Graphitsäure," *Berichte der deutschen chemischen Gesellschaft,* vol. 31, p. 1481, 1898.

[154] U. Hofmann and E. König, "Untersuchungen über Graphitoxyd," *Zeitschrift für anorganische und allgemeine Chemie,* vol. 234, p. 311, 1937.

[155] W. S. Hummers and R. E. Offeman, "Preparation of Graphitic Oxide," *Journal of the American Chemical Society,* vol. 80, p. 1339, 1958.

[156] S. Gilje, S. Han, M. Wang, K. L. Wang, and R. B. Kaner, "A chemical route to graphene for device applications," *Nano letters,* vol. 7, p. 3394, 2007.

[157] Y. Liu, D. Yu, C. Zeng, Z. Miao, and L. Dai, "Biocompatible Graphene Oxide-Based Glucose Biosensors," *Langmuir,* vol. 26, p. 6158, 2010.

[158] Y. Bo, H. Yang, Y. Hu, T. Yao, and S. Huang, "A novel electrochemical DNA biosensor based on graphene and polyaniline nanowires," *Electrochimica Acta,* vol. 56, p. 2676, 2011.

[159] W. Cai, R. D. Piner, F. J. Stadermann, S. Park, M. A. Shaibat, Y. Ishii, *et al.*, "Synthesis and solid-state NMR structural characterization of 13C-labeled graphite oxide," *Science,* vol. 321, p. 1815, 2008.

[160] D. C. Marcano, D. V. Kosynkin, J. M. Berlin, A. Sinitskii, Z. Sun, A. Slesarev, *et al.*, "Improved Synthesis of Graphene Oxide," *ACS Nano,* vol. 4, p. 4806, 2010.

[161] H. He, T. Riedl, A. Lerf, and J. Klinowski, "Solid-state NMR studies of the structure of graphite oxide," *The Journal of Physical Chemistry*, vol. 100, p. 19954, 1996.

[162] H. He, J. Klinowski, M. Forster, and A. Lerf, "A new structural model for graphite oxide," *Chemical Physics Letters*, vol. 287, p. 53, 1998.

[163] T. Kuila, S. Bose, A. K. Mishra, P. Khanra, N. H. Kim, and J. H. Lee, "Chemical functionalization of graphene and its applications," *Progress in Materials Science*, vol. 57, p. 1061, 2012.

[164] W. Gao, L. B. Alemany, L. Ci, and P. M. Ajayan, "New insights into the structure and reduction of graphite oxide," *Nat Chem*, vol. 1, p. 403, 2009.

[165] H. J. H. Fenton, "LXXIII.-Oxidation of tartaric acid in presence of iron," *Journal of the Chemical Society, Transactions*, vol. 65, p. 899, 1894.

[166] S. Teixeira, G. Burwell, A. Castaing, D. Gonzalez, S. Conlan, and O. J. Guy, "Epitaxial graphene immunosensor for human chorionic gonadotropin," *Sensors and Actuators B: Chemical, vol.190, p. 723, 2014*.

[167] W. Li, Y. Bai, Y. Zhang, M. Sun, R. Cheng, X. Xu, *et al.*, "Effect of hydroxyl radical on the structure of multi-walled carbon nanotubes," *Synthetic Metals*, vol. 155, p. 509, 2005.

[168] R. H. Bradley, K. Cassity, R. Andrews, M. Meier, S. Osbeck, A. Andreu, *et al.*, "Surface studies of hydroxylated multi-wall carbon nanotubes," *Aplied Surface Science*, vol. 258, p. 4835, 2012.

[169] G. V. Buxton, C. L. Greenstock, W. P. Helman, and A. B. Ross, "Critical review of rate constants for reactions of hydrated electrons, hydrogen atoms and hydroxyl radicals (· OH/· O− in aqueous solution," *Journal of physical and chemical reference data*, vol. 17, p. 513, 1988.

[170] K. B. Wiberg and K. A. Saegebarth, "The mechanisms of permanganate oxidation. IV. Hydroxylation of olefins and related reactions," *Journal of the American Chemical Society*, vol. 79, p. 2822, 1957.

[171] X.-L. Ling, Y.-Z. Wei, L.-M. Zou, and S. Xu, "Preparation and characterization of hydroxylated multi-walled carbon nanotubes," *Colloids and Surfaces A: Physicochemical and Engineering Aspects*, vol. 421, p. 9, 2013.

[172] S.-Z. Kang, D.-e. Yin, X. Li, and J. Mu, "A facile preparation of multiwalled carbon nanotubes modified with hydroxyl groups and their high dispersibility in ethanol," *Colloids and Surfaces A: Physicochemical and Engineering Aspects*, vol. 384, p. 363, 2011.

[173] D. V. Kosynkin, A. L. Higginbotham, A. Sinitskii, J. R. Lomeda, A. Dimiev, B. K. Price, *et al.*, "Longitudinal unzipping of carbon nanotubes to form graphene nanoribbons," *Nature*, vol. 458, p. 872, 2009.

[174] S. Niyogi, E. Bekyarova, M. E. Itkis, H. Zhang, K. Shepperd, J. Hicks, *et al.*, "Spectroscopy of Covalently Functionalized Graphene," *Nano Letters*, vol. 10, p. 4061, 2010.

[175] S. Park, D. A. Dikin, S. T. Nguyen, and R. S. Ruoff, "Graphene oxide sheets chemically cross-linked by polyallylamine," *The Journal of Physical Chemistry C*, vol. 113, p. 15801, 2009.

[176] M. M. S. Silva, A. C. M. S. Dias, B. V. M. Silva, S. L. R. Gomes-Filho, L. T. Kubota, M. O. F. Goulart, *et al.*, "Electrochemical detection of dengue virus NS1 protein with a poly(allylamine)/carbon nanotube layered immunoelectrode," *Journal of Chemical Technology & Biotechnology*, *vol. 90*, p. 194, 2014.

[177] D. Tasis, N. Tagmatarchis, A. Bianco, and M. Prato, "Chemistry of Carbon Nanotubes," *Chemical Reviews*, vol. 106, p. 1105, 2006.

[178] A. Fedorov, "The all-organic route to doping graphene," *American Physics Society,* vol. 3, p. 46, 2010.

[179] A. Nourbakhsh, M. Cantoro, A. Klekachev, F. Clemente, B. Sorée, M. H. van der Veen, *et al.*, "Tuning the Fermi Level of SiO2-Supported Single-Layer Graphene by Thermal Annealing," *The Journal of Physical Chemistry C,* vol. 114, p. 6894, 2010.

[180] J. Liu, Y. Li, Y. Li, J. Li, and Z. Deng, "Noncovalent DNA decorations of graphene oxide and reduced graphene oxide toward water-soluble metal-carbon hybrid nanostructures via self-assembly," *Journal of Materials Chemistry,* vol. 20, p. 900, 2010.

[181] Y. Xu, Q. Wu, Y. Sun, H. Bai, and G. Shi, "Three-dimensional self-assembly of graphene oxide and DNA into multifunctional hydrogels," *ACS nano,* vol. 4, p. 7358, 2010.

[182] K. V. Emtsev, A. Bostwick, K. Horn, J. Jobst, G. L. Kellogg, L. Ley, *et al.*, "Towards wafer-size graphene layers by atmospheric pressure graphitization of silicon carbide," *Nature materials,* vol. 8, p. 203, 2009.

[183] L. Liao, J. Bai, R. Cheng, Y.-C. Lin, S. Jiang, Y. Huang, *et al.*, "Top-gated graphene nanoribbon transistors with ultrathin high-k dielectrics," *Nano Letters,* vol. 10, p. 1917, 2010.

[184] M. Y. Han, B. Özyilmaz, Y. Zhang, and P. Kim, "Energy band-gap engineering of graphene nanoribbons," *Physical Review Letters,* vol. 98, p. 206805, 2007.

[185] Y. Zhang, T.-T. Tang, C. Girit, Z. Hao, M. C. Martin, A. Zettl, *et al.*, "Direct observation of a widely tunable bandgap in bilayer graphene," *Nature,* vol. 459, p. 820, 2009.

[186] Z. H. Ni, T. Yu, Y. H. Lu, Y. Y. Wang, Y. P. Feng, and Z. X. Shen, "Uniaxial strain on graphene: Raman spectroscopy study and band-gap opening," *ACS Nano,* vol. 2, p. 2301, 2008.

[187] P. Shemella and S. K. Nayak, "Electronic structure and band-gap modulation of graphene via substrate surface chemistry," *Applied Physics Letters,* vol. 94, p. 032101, 2009.

[188] J.-H. Chen, C. Jang, S. Xiao, M. Ishigami, and M. S. Fuhrer, "Intrinsic and extrinsic performance limits of graphene devices on SiO2," *Nature nanotechnology,* vol. 3, p. 206, 2008.

[189] S. Morozov, K. Novoselov, M. Katsnelson, F. Schedin, D. Elias, J. Jaszczak, *et al.*, "Giant intrinsic carrier mobilities in graphene and its bilayer," *Physical Review Letters,* vol. 100, p. 016602, 2008.

[190] S. A. Thiele, J. A. Schaefer, and F. Schwierz, "Modeling of graphene metal-oxide-semiconductor field-effect transistors with gapless large-area graphene channels," *Journal of Applied Physics,* vol. 107, p. 094505, 2010.

[191] A. Venugopal, L. Colombo, and E. M. Vogel, "Contact resistance in few and multilayer graphene devices," *Applied Physics Letters,* vol. 96, p. 013512, 2010.

[192] F. Schedin, A. K. Geim, S. V. Morozov, E. W. Hill, P. Blake, M. I. Katsnelson, *et al.*, "Detection of individual gas molecules adsorbed on graphene," *Nat Mater,* vol. 6, p. 652, 2007.

[193] J. D. Fowler, M. J. Allen, V. C. Tung, Y. Yang, R. B. Kaner, and B. H. Weiller, "Practical Chemical Sensors from Chemically Derived Graphene," *ACS Nano,* vol. 3, p. 301, 2009.

[194] R. S. Sundaram, C. Gómez‐Navarro, K. Balasubramanian, M. Burghard, and K. Kern, "Electrochemical modification of graphene," *Advanced Materials,* vol. 20, p. 3050, 2008.

[195] J. Li, S. Guo, Y. Zhai, and E. Wang, "High-sensitivity determination of lead and cadmium based on the Nafion-graphene composite film," *Analytica Chimica Acta*, vol. 649, p. 196, 2009.

[196] H.-B. Yao, J. Ge, C.-F. Wang, X. Wang, W. Hu, Z.-J. Zheng, *et al.*, "A Flexible and Highly Pressure-Sensitive Graphene–Polyurethane Sponge Based on Fractured Microstructure Design," *Advanced Materials*, vol. 25, p. 6692, 2013.

[197] F. Scheller, R. Hintsche, D. Pfeiffer, F. Schubert, K. Riedel, and R. Kindervater, "Biosensors: fundamentals, applications and trends," *Sensors and Actuators B: Chemical*, vol. 4, p. 197, 1991.

[198] C.-H. Lu, H.-H. Yang, C.-L. Zhu, X. Chen, and G.-N. Chen, "A Graphene Platform for Sensing Biomolecules," *Angewandte Chemie*, vol. 121, p. 4879, 2009.

[199] S. Teixeira, R. S. Conlan, O. J. Guy, and M. G. F. Sales, "Label-free human chorionic gonadotropin detection at picogram levels using oriented antibodies bound to graphene screen-printed electrodes," *Journal of Materials Chemistry B*, vol. 2, p. 1852, 2014.

[200] M. S. Mannoor, H. Tao, J. D. Clayton, A. Sengupta, D. L. Kaplan, R. R. Naik, *et al.*, "Graphene-based wireless bacteria detection on tooth enamel," *Nature Communications*, vol. 3, p. 763, 2012.

[201] X. Kang, J. Wang, H. Wu, I. A. Aksay, J. Liu, and Y. Lin, "Glucose Oxidase–graphene–chitosan modified electrode for direct electrochemistry and glucose sensing," *Biosensors and Bioelectronics*, vol. 25, p. 901, 2009.

[202] X. Wu, Y. Chai, R. Yuan, H. Su, and J. Han, "A novel label-free electrochemical microRNA biosensor using Pd nanoparticles as enhancer and linker," *Analyst*, vol. 138, p. 1060, 2013.

[203] C.-H. Lu, C.-L. Zhu, J. Li, J.-J. Liu, X. Chen, and H.-H. Yang, "Using graphene to protect DNA from cleavage during cellular delivery," *Chemical Communications*, vol. 46, p. 3116, 2010.

[204] D. Grieshaber. (2008). *Biosensor system and components*. Available: http://en.wikipedia.org/wiki/File:Biosensor_System.jpg

[205] P. Jiang and Z. Guo, "Fluorescent detection of zinc in biological systems: recent development on the design of chemosensors and biosensors," *Coordination Chemistry Reviews*, vol. 248, p. 205, 2004.

[206] H. Chang, L. Tang, Y. Wang, J. Jiang, and J. Li, "Graphene Fluorescence Resonance Energy Transfer Aptasensor for the Thrombin Detection," *Analytical Chemistry*, vol. 82, p. 2341, 2010.

[207] N. Varghese, U. Mogera, A. Govindaraj, A. Das, P. K. Maiti, A. K. Sood, *et al.*, "Binding of DNA Nucleobases and Nucleosides with Graphene," *ChemPhysChem*, vol. 10, p. 206, 2009.

[208] S. He, B. Song, D. Li, C. Zhu, W. Qi, Y. Wen, *et al.*, "A Graphene Nanoprobe for Rapid, Sensitive, and Multicolor Fluorescent DNA Analysis," *Advanced Functional Materials*, vol. 20, p. 453, 2010.

[209] H. Shen, L. Zhang, M. Liu, and Z. Zhang, "Biomedical applications of graphene," *Theranostics*, vol. 2, p. 283, 2012.

[210] J. H. Jung, D. S. Cheon, F. Liu, K. B. Lee, and T. S. Seo, "A Graphene Oxide Based Immuno-biosensor for Pathogen Detection," *Angewandte Chemie International Edition*, vol. 49, p. 5708, 2010.

[211] M. Pumera, "Graphene-based nanomaterials and their electrochemistry," *Chemical Society Reviews*, vol. 39, p. 4146, 2010.

[212] O. Niwa, J. Jia, Y. Sato, D. Kato, R. Kurita, K. Maruyama, *et al.*, "Electrochemical Performance of Angstrom Level Flat Sputtered Carbon Film

Consisting of sp2 and sp3 Mixed Bonds," *Journal of the American Chemical Society,* vol. 128, p. 7144, 2006.

[213] T. J. Davies, M. E. Hyde, and R. G. Compton, "Nanotrench Arrays Reveal Insight into Graphite Electrochemistry," *Angewandte Chemie International Edition,* vol. 44, p. 5121, 2005.

[214] Y. Bo, W. Wang, J. Qi, and S. Huang, "A DNA biosensor based on graphene paste electrode modified with Prussian blue and chitosan," *Analyst,* vol. 136, p. 1946, 2011.

[215] F. Liu, J. Y. Choi, and T. S. Seo, "Graphene oxide arrays for detecting specific DNA hybridization by fluorescence resonance energy transfer," *Biosensors and Bioelectronics,* vol. 25, p. 2361, 2010.

[216] J. Zhao, S. Pei, W. Ren, L. Gao, and H.-M. Cheng, "Efficient Preparation of Large-Area Graphene Oxide Sheets for Transparent Conductive Films," *ACS Nano,* vol. 4, p. 5245, 2010.

[217] X. Dong, W. Huang, and P. Chen, "In Situ Synthesis of Reduced Graphene Oxide and Gold Nanocomposites for Nanoelectronics and Biosensing," *Nanoscale Research Letters,* vol. 6, p. 1, 2010.

[218] C. Gómez-Navarro, R. T. Weitz, A. M. Bittner, M. Scolari, A. Mews, M. Burghard, *et al.*, "Electronic transport properties of individual chemically reduced graphene oxide sheets," *Nano letters,* vol. 7, p. 3499, 2007.

[219] Q. Su, S. Pang, V. Alijani, C. Li, X. Feng, and K. Müllen, "Composites of graphene with large aromatic molecules," *Advanced materials,* vol. 21, p. 3191, 2009.

[220] N. A. Kotov, I. Dékány, and J. H. Fendler, "Ultrathin graphite oxide‐polyelectrolyte composites prepared by self‐assembly: Transition between

conductive and non‐conductive states," *Advanced Materials,* vol. 8, p. 637, 1996.

[221] H. J. Shin, K. K. Kim, A. Benayad, S. M. Yoon, H. K. Park, I. S. Jung, *et al.*, "Efficient reduction of graphite oxide by sodium borohydride and its effect on electrical conductance," *Advanced Functional Materials,* vol. 19, p. 1987, 2009.

[222] H. Yao, S. Jenkins, A. Pesce, H. Halsall, and W. Heineman, "Electrochemical homogeneous enzyme immunoassay of theophylline in hemolyzed, icteric, and lipemic samples," *Clinical chemistry,* vol. 39, p. 1432, 1993.

[223] T. M. Anh, S. V. Dzyadevych, M. C. Van, N. J. Renault, C. N. Duc, and J.-M. Chovelon, "Conductometric tyrosinase biosensor for the detection of diuron, atrazine and its main metabolites," *Talanta,* vol. 63, p. 365 2004.

[224] C. Shan, H. Yang, J. Song, D. Han, A. Ivaska, and L. Niu, "Direct Electrochemistry of Glucose Oxidase and Biosensing for Glucose Based on Graphene," *Analytical Chemistry,* vol. 81, p. 2378, 2009.

[225] G. S. Wilson and Y. Hu, "Enzyme-Based Biosensors for in Vivo Measurements," *Chemical Reviews,* vol. 100, p. 2693, 2000.

[226] M. Zhou, Y. Zhai, and S. Dong, "Electrochemical Sensing and Biosensing Platform Based on Chemically Reduced Graphene Oxide," *Analytical Chemistry,* vol. 81, p. 5603, 2009.

[227] C. Shan, H. Yang, D. Han, Q. Zhang, A. Ivaska, and L. Niu, "Graphene/AuNPs/chitosan nanocomposites film for glucose biosensing," *Biosensors and Bioelectronics,* vol. 25, p. 1070, 2010.

[228] K. Chiang Lin, S. Yu Lai, and S. Ming Chen, "A highly sensitive NADH sensor based on a mycelium-like nanocomposite using graphene oxide and multi-walled carbon nanotubes to co-immobilize poly(luminol) and poly(neutral red) hybrid films," *Analyst,* vol. 139, p. 3991, 2014.

[229] P. T. Kissinger and W. R. Heineman, "Cyclic voltammetry," *Journal of Chemical Education,* vol. 60, p. 702, 1983.

[230] J.-H. Ahn, S.-J. Choi, J.-W. Han, T. J. Park, S. Y. Lee, and Y.-K. Choi, "Double-Gate Nanowire Field Effect Transistor for a Biosensor," *Nano Letters,* vol. 10, p. 2934, 2010.

[231] Y. Ohno, K. Maehashi, Y. Yamashiro, and K. Matsumoto, "Electrolyte-Gated Graphene Field-Effect Transistors for Detecting pH and Protein Adsorption," *Nano Letters,* vol. 9, p. 3318, 2009.

[232] X. Dong, Y. Shi, W. Huang, P. Chen, and L.-J. Li, "Electrical Detection of DNA Hybridization with Single-Base Specificity Using Transistors Based on CVD-Grown Graphene Sheets," *Advanced Materials,* vol. 22, p. 1649, 2010.

[233] R. Stine, J. T. Robinson, P. E. Sheehan, and C. R. Tamanaha, "Real-Time DNA Detection Using Reduced Graphene Oxide Field Effect Transistors," *Advanced Materials,* vol. 22, p. 5297, 2010.

[234] S. Mao, G. Lu, K. Yu, Z. Bo, and J. Chen, "Specific Protein Detection Using Thermally Reduced Graphene Oxide Sheet Decorated with Gold Nanoparticle-Antibody Conjugates," *Advanced Materials,* vol. 22, p. 3521, 2010.

[235] Y. Ohno, K. Maehashi, and K. Matsumoto, "Label-Free Biosensors Based on Aptamer-Modified Graphene Field-Effect Transistors," *Journal of the American Chemical Society,* vol. 132, p. 18012, 2010.

[236] M. Yang and S. Gong, "Immunosensor for the detection of cancer biomarker based on percolated graphene thin film," *Chemical Communications,* vol. 46, p. 5796, 2010.

[237] D. Waldmann, J. Jobst, F. Speck, T. Seyller, M. Krieger, and H. B. Weber, "Bottom-gated epitaxial graphene," *Nat Mater,* vol. 10, p. 357, 2011.

[238] P. K. Ang, W. Chen, A. T. S. Wee, and K. P. Loh, "Solution-Gated Epitaxial Graphene as pH Sensor," *Journal of the American Chemical Society,* vol. 130, p. 14392, 2008.

[239] T. Cohen-Karni, Q. Qing, Q. Li, Y. Fang, and C. M. Lieber, "Graphene and Nanowire Transistors for Cellular Interfaces and Electrical Recording," *Nano Letters,* vol. 10, p. 1098, 2010.

[240] L. H. Hess, M. Jansen, V. Maybeck, M. V. Hauf, M. Seifert, M. Stutzmann, *et al.*, "Graphene Transistor Arrays for Recording Action Potentials from Electrogenic Cells," *Advanced Materials,* vol. 23, p. 5045, 2011.

[241] D. A. Armbruster and T. Pry, "Limit of Blank, Limit of Detection and Limit of Quantitation," *The Clinical Biochemist Reviews,* vol. 29, p. S49, 2008.

[242] E. Lindner, K. Tóth, and E. Pungor, "Definition and determination of response time of ion selective electrodes," *Pure and Applied Chemistry,* vol. 58, p. 469, 1986.

[243] Q. Fu, C. Lu, and J. Liu, "Selective coating of single wall carbon nanotubes with thin SiO2 layer," *Nano Letters,* vol. 2, p. 329, 2002.

[244] A. Hozumi, K. Ushiyama, H. Sugimura, and O. Takai, "Fluoroalkylsilane monolayers formed by chemical vapor surface modification on hydroxylated oxide surfaces," *Langmuir,* vol. 15, p. 7600, 1999.

[245] P. Blake, E. W. Hill, A. H. C. Neto, K. S. Novoselov, D. Jiang, R. Yang, *et al.*, "Making graphene visible," *Applied Physics Letters,* vol. 91, p. 063124, 2007.

[246] F. Haber and J. Weiss, "Über die Katalyse des Hydroperoxydes," *Naturwissenschaften,* vol. 20, p. 948, 1932.

[247] G. K. Ramesha and S. Sampath, "Electrochemical Reduction of Oriented Graphene Oxide Films: An in Situ Raman Spectroelectrochemical Study," *The Journal of Physical Chemistry C,* vol. 113, p. 7985, 2009.

[248] F. Liu, Y. H. Kim, D. S. Cheon, and T. S. Seo, "Micropatterned reduced graphene oxide based field-effect transistor for real-time virus detection," *Sensors and Actuators B: Chemical,* vol. 186, p. 252, 2013.

[249] Z.-S. Wu, S. Pei, W. Ren, D. Tang, L. Gao, B. Liu, *et al.*, "Field Emission of Single-Layer Graphene Films Prepared by Electrophoretic Deposition," *Advanced Materials,* vol. 21, p. 1756, 2009.

[250] S. Stankovich, D. A. Dikin, G. H. B. Dommett, K. M. Kohlhaas, E. J. Zimney, E. A. Stach, *et al.*, "Graphene-based composite materials," *Nature,* vol. 442, p. 282, 2006.

[251] M. Dresselhaus, G. Dresselhaus, and M. Hofmann, "Raman spectroscopy as a probe of graphene and carbon nanotubes," *Philosophical Transactions of the Royal Society of London A: Mathematical, Physical and Engineering Sciences,* vol. 366, p. 231-236, 2008.

[252] A. C. Ferrari, J. C. Meyer, V. Scardaci, C. Casiraghi, M. Lazzeri, F. Mauri, *et al.*, "Raman Spectrum of Graphene and Graphene Layers," *Physical Review Letters,* vol. 97, p. 187401, 2006.

[253] C. Casiraghi, A. Hartschuh, H. Qian, S. Piscanec, C. Georgi, A. Fasoli, *et al.*, "Raman Spectroscopy of Graphene Edges," *Nano Letters,* vol. 9, p. 1433, 2009.

[254] D. S. Lee, C. Riedl, B. Krauss, K. von Klitzing, U. Starke, and J. H. Smet, "Raman Spectra of Epitaxial Graphene on SiC and of Epitaxial Graphene Transferred to SiO_2," *Nano Letters,* vol. 8, p. 4320, 2008.

[255] L. G. Cançado, K. Takai, T. Enoki, M. Endo, Y. A. Kim, H. Mizusaki, *et al.*, "General equation for the determination of the crystallite size La of nanographite by Raman spectroscopy," *Applied Physics Letters,* vol. 88, p. 163106, 2006.

[256] E. Zakar, B. M. Nichols, S. Kilpatrick, G. Meissner, R. Fu, and K. Hauri, "Nucleation sites for multilayer graphene on nickel catalyst," in *Nanotechnology (IEEE-NANO), 2011 11th IEEE Conference on*, 2011, p. 1516.

[257] S. Malola, H. Häkkinen, and P. Koskinen, "Structural, chemical, and dynamical trends in graphene grain boundaries," *Physical Review B*, vol. 81, p. 165447, 2010.

[258] S.-E. Zhu, V. E. Calado, L. M. K. Vandersypen, and G. C. A. M. Janssen, "Controllable synthesis of large monlayer and multilayer graphene crystal," 2013.

[259] Q. Jin, J.-P. Eom, S.-G. Lim, W.-W. Park, and B.-S. You, "Grain refining mechanism of a carbon addition method in a Mg–Al magnesium alloy," *Scripta Materialia*, vol. 49, p. 1129, 2003.

[260] P. Y. Huang, C. S. Ruiz-Vargas, A. M. van der Zande, W. S. Whitney, M. P. Levendorf, J. W. Kevek, *et al.*, "Grains and grain boundaries in single-layer graphene atomic patchwork quilts," *Nature*, vol. 469, p. 389, 2011.

[261] A. C. Ferrari and J. Robertson, "Interpretation of Raman spectra of disordered and amorphous carbon," *Physical Review B*, vol. 61, p. 14095, 2000.

[262] P. K. Chu and L. Li, "Characterization of amorphous and nanocrystalline carbon films," *Materials Chemistry and Physics*, vol. 96, p. 253, 2006.

[263] J. C. Shelton, H. R. Patil, and J. M. Blakely, "Equilibrium segregation of carbon to a nickel (111) surface: A surface phase transition," *Surface Science*, vol. 43, p. 493, 1974.

[264] O. Balci and C. Kocabas, "Rapid thermal annealing of graphene-metal contact," *Applied Physics Letters*, vol. 101, p. 243105, 2012.

[265] J. Moser, A. Verdaguer, D. Jimenez, A. Barreiro, and A. Bachtold, "The environment of graphene probed by electrostatic force microscopy," *Applied Physics Letters,* vol. 92, p. 123507, 2008.

[266] M. Okumura, S. Nakamura, S. Tsubota, T. Nakamura, M. Azuma, and M. Haruta, "Chemical vapor deposition of gold on Al_2O_3, SiO_2, and TiO_2 for the oxidation of CO and of H2," *Catalysis Letters,* vol. 51, p. 53, 1998.

[267] K. Nagashio and A. Toriumi, "Density-of-States Limited Contact Resistance in Graphene Field-Effect Transistors," *Japanese Journal of Applied Physics,* vol. 50, p. 6, 2011.

[268] B. Dlubak, P. Seneor, A. Anane, C. Barraud, C. Deranlot, D. Deneuve, *et al.*, "Are Al_2O_3 and MgO tunnel barriers suitable for spin injection in graphene?," *Applied Physics Letters,* vol. 97, p. 092502, 2010.

[269] H. M. Mohammad, K. Fang-Ling, M. Kristopher, H. Junyeon, B. Rajarshi, and D. S. Nigel, "The influence of high dielectric constant aluminum oxide sputter deposition on the structure and properties of multilayer epitaxial graphene," *Nanotechnology,* vol. 22, p. 205703, 2011.

[270] F. Miriam, W. Mirosław, M. André, W. Stefan, D. Thorsten, W. Thomas, *et al.*, "Versatile sputtering technology for Al_2O_3 gate insulators on graphene," *Science and Technology of Advanced Materials,* vol. 13, p. 025007, 2012.

[271] M. Quintana, E. Vazquez, and M. Prato, "Organic Functionalization of Graphene in Dispersions," *Accounts of Chemical Research,* vol. 46, p. 138, 2013.

[272] C.-T. Chen, E. A. Casu, M. Gajek, and S. Raoux, "Low-damage high-throughput grazing-angle sputter deposition on graphene," *Applied Physics Letters,* vol. 103, p. 033109, 2013.

[273] X. P. Qiu, Y. J. Shin, J. Niu, N. Kulothungasagaran, G. Kalon, C. Qiu, *et al.*, "Disorder-free sputtering method on graphene," *AIP Advances*, vol. 2, p. 032121, 2012.

[274] J. A. Robinson, M. LaBella, M. Zhu, M. Hollander, R. Kasarda, Z. Hughes, *et al.*, "Contacting graphene," *Applied Physics Letters*, vol. 98, p. 053103, 2011.

[275] J. T. Smith, A. D. Franklin, D. B. Farmer, and C. D. Dimitrakopoulos, "Reducing Contact Resistance in Graphene Devices through Contact Area Patterning," *ACS Nano*, vol. 7, p. 3661, 2013.

[276] K. I. Bolotin, K. Sikes, Z. Jiang, M. Klima, G. Fudenberg, J. Hone, *et al.*, "Ultrahigh electron mobility in suspended graphene," *Solid State Communications*, vol. 146, p. 351, 2008.

[277] X. Lu, H. Huang, N. Nemchuk, and R. S. Ruoff, "Patterning of highly oriented pyrolytic graphite by oxygen plasma etching," *Applied Physics Letters*, vol. 75, p. 193, 1999.

[278] J. Li, T.-F. Chung, Y. P. Chen, and G. J. Cheng, "Nanoscale Strainability of Graphene by Laser Shock-Induced Three-Dimensional Shaping," *Nano Letters*, vol. 12, p. 4577, 2012.

[279] D. C. Bell, M. C. Lemme, L. A. Stern, J. R. Williams, and C. M. Marcus, "Precision cutting and patterning of graphene with helium ions," *Nanotechnology*, vol. 20, p. 455301, 2009.

[280] L. Zhang, S. Diao, Y. Nie, K. Yan, N. Liu, B. Dai, *et al.*, "Photocatalytic patterning and modification of graphene," *Journal of the American Chemical Society*, vol. 133, p. 2706, 2011.

[281] P. Blake, R. Yang, S. Morozov, F. Schedin, L. Ponomarenko, A. Zhukov, *et al.*, "Influence of metal contacts and charge inhomogeneity on transport properties

of graphene near the neutrality point," *Solid State Communications*, vol. 149, p. 1068, 2009.

[282] C. Vo-Van, A. Kimouche, A. Reserbat-Plantey, O. Fruchart, P. Bayle-Guillemaud, N. Bendiab, *et al.*, "Epitaxial graphene prepared by chemical vapor deposition on single crystal thin iridium films on sapphire," *Applied Physics Letters*, vol. 98, p. 181903, 2011.

[283] K. Nagashio, T. Nishimura, K. Kita, and A. Toriumi, "Metal/graphene contact as a performance Killer of ultra-high mobility graphene analysis of intrinsic mobility and contact resistance," in *Electron Devices Meeting (IEDM), 2009 IEEE International*, 2009, p. 1.

[284] W. S. Leong, C. T. Nai, and J. T. Thong, "What Does Annealing Do to Metal–Graphene Contacts?," *Nano letters*, vol. 14, p. 3840, 2014.

[285] M. Lafkioti, B. Krauss, T. Lohmann, U. Zschieschang, H. Klauk, K. v. Klitzing, *et al.*, "Graphene on a Hydrophobic Substrate: Doping Reduction and Hysteresis Suppression under Ambient Conditions," *Nano Letters*, vol. 10, p. 1149, 2010.

[286] Z. Cheng, Q. Zhou, C. Wang, Q. Li, C. Wang, and Y. Fang, "Toward Intrinsic Graphene Surfaces: A Systematic Study on Thermal Annealing and Wet-Chemical Treatment of SiO2-Supported Graphene Devices," *Nano Letters*, vol. 11, p. 767, 2011.

[287] A. D. Franklin, H. Shu-Jen, A. A. Bol, and V. Perebeinos, "Double Contacts for Improved Performance of Graphene Transistors," *Electron Device Letters, IEEE*, vol. 33, p. 17, 2012.

[288] Y. Shao, J. Wang, H. Wu, J. Liu, I. A. Aksay, and Y. Lin, "Graphene based electrochemical sensors and biosensors: a review," *Electroanalysis*, vol. 22, p. 1027, 2010.

[289] Y. Li, L. Tang, and J. Li, "Preparation and electrochemical performance for methanol oxidation of pt/graphene nanocomposites," *Electrochemistry Communications,* vol. 11, p. 846, 2009.

[290] J. Li, S. Guo, Y. Zhai, and E. Wang, "Nafion–graphene nanocomposite film as enhanced sensing platform for ultrasensitive determination of cadmium," *Electrochemistry Communications,* vol. 11, p. 1085, 2009.

[291] Q. Zhang, Q. Ren, Y. Miao, J. Yuan, K. Wang, F. Li, *et al.*, "One-step synthesis of graphene/polyallylamine–Au nanocomposites and their electrocatalysis toward oxygen reduction," *Talanta,* vol. 89, p. 391, 2012.

[292] M. Pumera, "Graphene in biosensing," *Materials Today,* vol. 14, p. 308-315, 2011.

[293] K. Erickson, R. Erni, Z. Lee, N. Alem, W. Gannett, and A. Zettl, "Determination of the local chemical structure of graphene oxide and reduced graphene oxide," *Advanced Materials,* vol. 22, p. 4467, 2010.

[294] H. J. Kim, S.-M. Lee, Y.-S. Oh, Y.-H. Yang, Y. S. Lim, D. H. Yoon, *et al.*, "Unoxidized Graphene/Alumina Nanocomposite: Fracture- and Wear-Resistance Effects of Graphene on Alumina Matrix," *Scitific Report,* vol. 4, 2014.

[295] M. M. Lucchese, F. Stavale, E. Ferreira, C. Vilani, M. Moutinho, R. B. Capaz, *et al.*, "Quantifying ion-induced defects and Raman relaxation length in graphene," *Carbon,* vol. 48, p. 1592, 2010.

[296] J. Hu, B. He, J. Lu, L. Hong, J. Yuan, J. Song, *et al.*, "Facile Preparation of Pt/polyallylamine/reduced graphene oxide composites and their application in the electrochemical catalysis on methanol oxidation," *International Journal of Electrochem Science,* vol. 7, p. 10094, 2012.

[297] B. Li, G. Pan, N. D. Avent, R. B. Lowry, T. E. Madgett, and P. L. Waines, "Graphene electrode modified with electrochemically reduced graphene oxide

for label-free DNA detection," *Biosensors and Bioelectronics,* vol. 72, p. 313, 2015.

[298] A. J. Bard and L. R. Faulkner, *Electrochemical methods: fundamentals and applications* vol. 2: Wiley New York, 1980.

[299] N. D. Avent, T. E. Madgett, D. G. Maddocks, and P. W. Soothill, "Cell-free fetal DNA in the maternal serum and plasma: current and evolving applications," *Current Opinion in Obstetrics and Gynecology,* vol. 21, p. 175, 2009.

[300] L.-M. Houdebine, "Transgenic Animal Models in Biomedical Research," in *Target Discovery and Validation Reviews and Protocols*. vol. 360, M. Sioud, Ed., ed: Humana Press, 2007, p. 163.

[301] V. G. Gavalas, S. A. Law, J. Christopher Ball, R. Andrews, and L. G. Bachas, "Carbon nanotube aqueous sol-gel composites: enzyme-friendly platforms for the development of stable biosensors," *Analytical biochemistry,* vol. 329, p. 247, 2004.

[302] M. M. S. Silva, A. C. M. S. Dias, B. V. M. Silva, S. L. R. Gomes-Filho, L. T. Kubota, M. O. F. Goulart, *et al.*, "Electrochemical detection of dengue virus NS1 protein with a poly(allylamine)/carbon nanotube layered immunoelectrode," *Journal of Chemical Technology & Biotechnology,* vol. 90, p. 194, 2015.

[303] D. Pandey, R. Reifenberger, and R. Piner, "Scanning probe microscopy study of exfoliated oxidized graphene sheets," *Surface Science,* vol. 602, p. 1607, 2008.

[304] M. Du, T. Yang, and K. Jiao, "Immobilization-free direct electrochemical detection for DNA specific sequences based on electrochemically converted gold nanoparticles/graphene composite film," *Journal of Materials Chemistry,* vol. 20, p. 9253, 2010.

[305] A. J. Patil, J. L. Vickery, T. B. Scott, and S. Mann, "Aqueous Stabilization and Self-Assembly of Graphene Sheets into Layered Bio-Nanocomposites using DNA," *Advanced Materials,* vol. 21, p. 3159, 2009.

[306] H. Lei, L. Mi, X. Zhou, J. Chen, J. Hu, S. Guo, *et al.*, "Adsorption of double-stranded DNA to graphene oxide preventing enzymatic digestion," *Nanoscale,* vol. 3, p. 3888, 2011.

[307] N. Zhu, Z. Chang, P. He, and Y. Fang, "Electrochemically fabricated polyaniline nanowire-modified electrode for voltammetric detection of DNA hybridization," *Electrochimica Acta,* vol. 51, p. 3758, 2006.

[308] J. Zhao, G. Chen, L. Zhu, and G. Li, "Graphene quantum dots-based platform for the fabrication of electrochemical biosensors," *Electrochemistry Communications,* vol. 13, p. 31, 2011.

[309] A.-L. Liu, G.-X. Zhong, J.-Y. Chen, S.-H. Weng, H.-N. Huang, W. Chen, *et al.*, "A sandwich-type DNA biosensor based on electrochemical co-reduction synthesis of graphene-three dimensional nanostructure gold nanocomposite films," *Analytica Chimica Acta,* vol. 767, p. 50, 2013.

[310] L. Zhu, L. Luo, and Z. Wang, "DNA electrochemical biosensor based on thionine-graphene nanocomposite," *Biosensors and Bioelectronics,* vol. 35, p. 507, 2012.